

# Doctoral Thesis

Generation and Propagation of Jovian Quasi-Periodic  
Low Frequency Radio Bursts

Tomoki Kimura

Department of Geophysics  
Graduate School of Science  
Tohoku University

2009

## Thesis Committee Members

Associate Professor Hiroaki Misawa (Supervisor)  
Professor Yasumasa Kasaba (Chair)  
Professor Shoichi Okano  
Professor Takayuki Ono  
Associate Professor Atushi Kumamoto



# 博士論文

木星準周期的低周波電波バースト現象の励起と伝搬

東北大学理学研究科  
地球物理学専攻

木村 智樹

平成21年

## 論文審査委員

三澤 浩昭 准教授（指導教員）  
笠羽 康正 教授（主査）  
岡野 章一 教授  
小野 高幸 教授  
熊本 篤志 准教授



*I do not know what I may appear to the world  
but to myself I seem to have been only like a boy playing on the seashore,  
and diverting myself in now and then finding a smoother pebble or a prettier shell than  
ordinary, whilst the great ocean of truth lay all undiscovered before me.*

*Isaac Newton*



# Acknowledgements

The present thesis was achieved in doctor's course of Department of Geophysics in Graduate School of Science, Tohoku University. Firstly, I would like to thank Associate Prof. Hiroaki Misawa for being a supervisor. I really appreciate his constructive advice, careful guidance with deep insights into my study, and his ray tracing system, which brought the most important results in this thesis.

Professor emeritus Akira Morioka and Dr. Fuminori Tsuchiya have always supported me with hearty help and encouragement since I was assigned to our lab. Their continued supports over 6 years are greatly appreciated.

I would like to thank Dr. Philippe Zarka and Dr. Baptiste Cecconi for a lot of their assistance in analyzing polarization data of Cassini. I was highly motivated by lectures and discussions with them at l'Observatoire de Paris in spring 2009.

Ulysses' polarization data in non-public domain were analyzed thanks to Dr. Bob MacDowall and Dr. Roger Hess in Goddard Space Flight Center, NASA. I feel very honored to collaborate with them.

I am grateful for Prof. Yasumasa Kasaba for being a cool second supervisor. Frank exchange of views with him was exciting for me. Dr. A. Kumamoto, Dr. Y. Katoh, and Dr. Y. Nishimura supported me especially in the theoretical work in the present study.

My colleagues, Satoshi Kimura, Hiroyasu Tadokoro, and Yuka Sato have been encouraging me over 7 years (whether they realized it or not...). I express my special thanks to younger colleagues in our lab, especially to M. Yoneda, T. Kobuna, K. Iwai, S. Kurita, K. Akisato, K. Masunaga, and K. Kaneko, who assisted in writing my doctoral thesis. I also

express my gratitude to staffs and seniors in the lab, Ms. M. Sato, Ms. A. Koiwa, Dr. M. Kagitani, Dr. H. Nozawa, Dr. Y. S. Miyoshi, Dr. F. Nakagawa, and L. Miyamoto for their continuous assistance and guidance.

Prof. S. Okano, and Dr. T. Sakanoi gave me many beneficial advices and asked sharp questions about my study in weekly seminars. Prof. T. Ono, Dr. N. Terada, Dr. I. Murata, and Dr. H. Fujiwara gave me careful suggestions in C-group seminars.

Friends in the orchestra and strings encouraged me with their hearty music. I never forget ensembles and concerts with them.

Finally, I present this thesis to my wife and parents, who have always supported and encouraged me throughout my life.

Tomoki Kimura

# Abstract

Jovian quasi-periodic (QP) bursts were discovered by Voyager (*Kurth et al.*, 1989) and named “Jovian Type III bursts” due to their dispersive spectral nature. Their occurrence characteristics were investigated in detail based on Ulysses’ observations. During Ulysses’ first Jovian flyby in 1992, two kinds of QP bursts were identified (*MacDowall et al.*, 1993): one with a periodicity of around 15 min during the inbound phase and the other with a periodicity of  $\sim$ 40 min during the outbound phase. They were named “QP15” and “QP40” bursts, respectively. The Ulysses/COSPIN observations during the outbound pass indicated that energetic ( $> 9$  MeV) electron outbursts with a 40-min period were correlated with the QP40 radio bursts (*McKibben et al.*, 1993). The Chandra X-ray Observatory observed an X-ray “hot spot” pulsating with an approximately 45-min period (*Gladstone et al.*, 2002), and it has been suggested that the emissions are excited by precipitations of relativistic heavy magnetospheric ions (e.g., *Cravens et al.*, 2003; *Elsner et al.*, 2005). These observations imply the relativistic particle acceleration processes in the Jovian polar region, accompanied by quasi-periodic radio and auroral emissions. This thesis addressed the propagation and generation process of quasi-periodic radio bursts. We discussed the magnetospheric dynamics responsible for the particle acceleration process based on the radio emission studies. The following conclusions were obtained in the present study.

## Occurrence Characteristics

Occurrence characteristics of QP bursts were investigated based on the wave data observed by Ulysses at the northern high latitudes and Galileo at the low latitudes. Statistics

based on the Ulysses' wave data indicated that QP bursts observed at high latitudes are excited in a particular rotational phase ( $\text{SSL}=90^\circ\text{--}300^\circ$ ) in the high latitudinal region ( $+30^\circ\text{--}+90^\circ$ ). QP bursts observed at the low latitudes were also found to be excited in a particular rotational phase ( $\text{SSL}=300^\circ\text{--}480^\circ$ ). Thus, it was concluded that QP bursts observed at low and high latitudes have “clock modulations” which are internally driven in a particular rotational phase with a similar manner to the phenomena found in Saturn's magnetosphere. It was also revealed that the meridional distribution of QP bursts forms a shadow zone in the equatorial region ( $|\text{MLAT}| < 10^\circ$ ) of less than 30 Jovian radii from Jupiter where QP bursts are quenched. Statistics based on the Lomb-Scargle analysis indicated that the period of “ $\sim 40 \text{ min}$ ” is the most dominant in amplitudes at all latitudes.

## **Polarization Properties**

Polarization properties and source directions of QP bursts were investigated based on the wave data observed by Ulysses at the northern high latitudes and Cassini at the low latitudes. It was indicated that QP bursts observed at the northern high latitudes are left-handed (LH) circular polarized waves (the Stokes parameters,  $V = +0.7\text{--}+0.8$ ,  $Q = 0\text{--}+0.4$ , and  $U = 0\text{--}+0.2$ ). In addition, statistics of the Stokes parameters confirmed that QP bursts observed at the low latitudes are also LH circular polarized ( $V = 0\text{--}0.6$ ,  $Q, U \sim 0$ ). The direction findings at the low latitudes were performed based on the data observed by Cassini during the closest approach to Jupiter. It was found that some QP bursts have arrival directions at a distance of  $\sim 50 \text{ R}_J$  from Jupiter with  $\sim 20 \text{ R}_J$  ambiguity.

## **Interpretation of the Observation Results Based on the Ray Tracing**

We discussed the source location, directivity, and propagation process of QP bursts based on the ray tracing analysis, comparing with the observation results. The parametric survey suggested that QP bursts observed at high latitudes have the source region located at  $f \sim f_p$  (plasma frequency) surface ( $1.3\text{--}1.4 \text{ R}_J$ ) along high-latitudinal field lines. It was suggested that these QP bursts are left-handed ordinary (L-O) mode waves with signifi-

cantly broadened beaming patterns like a “filled cone”. On the other hand, the ray tracing suggested that QP bursts observed in the equatorial region are right-handed extraordinary (R-X) mode wave emitted from  $f \sim f_{RX}$  (cutoff frequency of R-X mode) surface ( $\sim 10$ – $20 R_J$ ) along high-latitudinal field lines ( $L > \sim 20$ ). They are emitted from a restricted L-value range with “filled cone” like beaming patterns. These results imply that QP bursts have two kinds of sources: one has higher altitudes ( $f_{RX}$  surface) emitting R-X mode waves and the other has lower altitudes ( $f_p$  surface) emitting L-O mode waves. Based on the ray tracing with the magnetosheath plasma model, we interpreted the direction finding results by Cassini as meaning that QP bursts from the polar region were scattered and reached to the apparent altitudes ( $\sim 50 R_J$ ) by the local density fluctuations in the magnetosheath and interplanetary space, and/or they have the real source region in the magnetosheath.

### **Microscopic Generation of Quasi-Periodic Bursts**

Two possible scenarios were proposed for the microscopic generation mechanism of QP bursts: the “direct generation scenario” and “indirect generation scenario”. They were examined based on the theoretical approaches. The growth rate calculations were performed to examine the direct generation scenario at low ( $\sim 2 R_J$ ) and high ( $\sim 10 R_J$ ) source altitudes. The results suggested that free-space O mode (i.e., L-O mode) waves are directly excited by relativistic electron beams via the Cyclotron Maser Instability (CMI). On the other hand, it was indicated that free-space X mode waves (i.e., R-X mode) waves are not excited effectively. This means that the observed shadow zone is not formed by the R-X mode waves. Ray tracing and theoretical study suggested that the O mode waves could propagate in the magnetosphere forming the observed shadow zone. The indirect generation scenario was examined referring to the previous theoretical study. It was concluded that the following mode conversion scenario is also possible at low and high source altitudes: (1) Z mode waves propagating toward Jupiter are excited at low and high altitudes via the cyclotron resonance, and (2) they are converted to free-space O mode waves at the density boundary where  $f \sim f_p$ . The growth rate calculation under conditions of the

magnetosheath revealed that both of the direct and indirect processes are unreasonable in the magnetosheath. Thus, we interpreted the direction finding results by Cassini as the scattering process in the magnetosheath and interplanetary space.

## **Macroscopic Generation of QP Phenomena**

Two possible scenarios were proposed for the relativistic particle acceleration process of the quasi-periodic phenomena: the “flux transfer event (FTE) scenario” and “field line resonance (FLR) scenario”. The scenarios were examined based on *in-situ* and remote observations of plasma, magnetic field, and wave data performed by Galileo and Ulysses. The FTE scenario was examined based on observations of magnetic fields, solar wind, and QP bursts. It was confirmed that FTE signals at Jupiter’s magnetopause were not accompanied with periodic features similar to the QP phenomena. In addition, it was indicated that QP bursts do not respond significantly to any solar wind parameters. Thus, we concluded that the FTE scenario is not feasible for the relativistic particle acceleration process of QP phenomena. The FLR scenario was investigated based on the *in-situ* magnetic field data in the middle and outer magnetosphere. The results indicated that linear Alfvén waves with a period of tens of minutes were propagating quasi-parallel with the background field lines in the middle magnetosphere. In addition, the Alfvén waves were suggested to be propagating to the polar region accompanied with the relativistic electron bursts and QP radio bursts. Thus, we concluded that the Alfvén waves propagating between the equatorial and polar region could be a generator of QP accelerations in the Jovian polar region.

There still remain some unsolved problems on the Jovian QP phenomena: e.g., the internal initiator of the Alfvén waves, “40-min period”, and energy budget. This thesis proposed observational requirements to solve these problems as concluding remarks. The observations should be performed based on multi-spacecraft exploration with a full set of equipments in two kinds of orbital regimes: the “polar regime” and “equatorial regime”. In the polar regime, the exploration is performed by a spacecraft in the cusp or polar

magnetopause and another spacecraft at the magnetic footprint in the polar region. In the equatorial regime, the exploration is performed by a spacecraft in the distant tail region and another spacecraft at the magnetic footprint in the polar region. These observations are expected to reveal the relativistic quasi-periodic acceleration process and relevant internal magnetospheric dynamics.



# Contents

<b>Acknowledgements</b>	i
<b>Abstract</b>	iii
<b>1 Introduction</b>	1
1.1 Jovian Magnetosphere . . . . .	1
1.2 Jovian Radio Emissions . . . . .	10
1.3 Quasi-Periodic Phenomena . . . . .	14
1.3.1 Quasi-Periodic Radio Bursts . . . . .	14
1.3.2 Relativistic Particle Bursts . . . . .	22
1.3.3 Polar Auroral Hot Spots . . . . .	25
1.4 Purpose of This Thesis . . . . .	32
<b>2 Instrumentation and Datasets</b>	35
2.1 Instrumentation . . . . .	35
2.1.1 Ulysses Spacecraft . . . . .	35
2.1.2 Galileo Spacecraft . . . . .	39
2.1.3 Cassini Spacecraft . . . . .	42
2.2 Datasets . . . . .	43
2.2.1 Ulysses Spacecraft . . . . .	43
2.2.2 Galileo Spacecraft . . . . .	46
2.2.3 Cassini Spacecraft . . . . .	47

<b>3 Occurrence Characteristics</b>	<b>49</b>
3.1 Detection of QP Bursts . . . . .	49
3.1.1 Detection from Ulysses' Data . . . . .	49
3.1.2 Detection from Galileo's Data . . . . .	50
3.2 Occurrence Dependence on Longitude and Latitude . . . . .	51
3.2.1 Occurrence Dependence Observed by Ulysses . . . . .	51
3.2.2 Occurrence Dependence Observed by Galileo . . . . .	53
3.3 Occurrence Dependence on Radial Distance and Latitude . . . . .	57
3.4 Discussion—Occurrence Dependence on Geometric Parameters . . . . .	59
3.5 Periodicity . . . . .	60
3.5.1 Description of the Lomb-Scargle Periodogram analysis . . . . .	60
3.5.2 Periodicity Analysis Results . . . . .	63
3.6 Brief Summary . . . . .	68
<b>4 Polarization Properties</b>	<b>71</b>
4.1 Description of Polarization Measurements and Direction Finding . . . . .	71
4.2 Polarization Measurements at High Latitudes . . . . .	78
4.3 Polarization Measurements and Direction Finding at Low Latitudes . . . . .	90
4.3.1 Polarization Measurements at Low Latitudes . . . . .	90
4.3.2 Direction Finding at Low latitudes . . . . .	97
4.4 Brief Summary . . . . .	107
<b>5 Interpretation of Observational Results Based on Propagation Analysis</b>	<b>111</b>
5.1 Description of Ray Tracing Method . . . . .	111
5.1.1 Ray Tracing Equations . . . . .	111
5.1.2 Parameters for Ray Tracing . . . . .	114
5.2 QP Bursts Observed by Ulysses at High Latitudes . . . . .	121
5.2.1 Assumptions and Calculation Conditions . . . . .	121
5.2.2 Ordinary Mode . . . . .	122

5.2.3	Dependence on the Planetary Rotational Phase . . . . .	126
5.2.4	Dependence of the Observable Region on Other Parameters . . . . .	126
5.2.5	Summary and Discussion: Radiation Characteristics of QP bursts Observed at High Latitudes . . . . .	128
5.3	QP Bursts Observed by Galileo at Low Latitudes . . . . .	130
5.3.1	Assumptions and Calculation Conditions . . . . .	130
5.3.2	Ordinary Mode . . . . .	132
5.3.3	Extraordinary Mode . . . . .	134
5.3.4	Summary and Discussion: Radiation Characteristics of QP bursts Observed at Low Latitudes . . . . .	140
5.4	QP Bursts Observed by Cassini at Low Latitudes . . . . .	143
5.4.1	Assumptions and Calculation Conditions . . . . .	143
5.4.2	Ordinary mode . . . . .	144
5.4.3	Extraordinary mode . . . . .	146
5.4.4	Summary and Discussion: Propagation of QP bursts in the Magne- tosheath and Interplanetary Space . . . . .	147
5.5	Brief Summary . . . . .	150
<b>6</b>	<b>Generation Mechanism of Quasi-Periodic Bursts</b>	<b>153</b>
6.1	Microscopic Generation Mechanisms of Quasi-Periodic Bursts . . . . .	153
6.1.1	Scenario 1: Direct Generation . . . . .	154
6.1.2	Scenario 2: Indirect Generation . . . . .	178
6.1.3	Brief Summary . . . . .	189
6.2	Macroscopic Generation Process of Quasi-Periodic Phenomena . . . . .	192
6.2.1	Scenario 1: External Process . . . . .	192
6.2.2	Scenario 2: Internal Process . . . . .	207
6.2.3	Brief Summary . . . . .	223
<b>7</b>	<b>Summary and Conclusions</b>	<b>225</b>

7.1	Summary and Conclusions . . . . .	225
7.2	Open Issues and Requirements . . . . .	230
<b>References</b>		<b>236</b>

# List of Figures

1.1	A schematic of Jupiter's magnetosphere showing the noon-midnight meridian and equatorial cross section . . . . .	3
1.2	Sketch of the Jovian magnetosphere showing the principal features of the inner and middle magnetosphere . . . . .	4
1.3	The strength of the various current systems in Earth's and Jupiter's magnetosphere . . . . .	5
1.4	Plasma loading process in the Jovian magnetotail . . . . .	6
1.5	First order anisotropy vectors of protons (80–220 keV) in the Jovian magnetosphere . . . . .	7
1.6	Data from Galileo orbit G2 inside the Jovian magnetosphere . . . . .	8
1.7	Hubble Space Telescope STIS UV image of Jupiter's northern aurora taken in November 1997 . . . . .	9
1.8	Sketch of radio source locations in the Earth's and Jupiter's magnetosphere	11
1.9	Frequency variations of characteristic frequencies and ranges of the four main electromagnetic modes . . . . .	13
1.10	Spectra of Jovian radio components plus auroral radio emissions from the other radio planets . . . . .	14
1.11	Jovian low-frequency radio emissions as detected by Cassini-RPWS . . . . .	15
1.12	QP bursts observed by Voyager . . . . .	15
1.13	Dynamic spectra displays showing QP15 and QP40 bursts . . . . .	17
1.14	Histograms showing the delays between successive QP bursts event . . . . .	18

1.15	Histograms showing the QP bursts distributions in sub-spacecraft longitude	18
1.16	Plot of QP-40 burst source directions derived for several bursts on 9 February 1992	19
1.17	Frequency-time spectrograms showing QP bursts detected by Cassini and Galileo	20
1.18	A plot of the apparent direction of arrival of QP bursts observed by Galileo on DOY 357, 2002, at $\sim$ 20 kHz	21
1.19	Longitudinal distribution for QP-burst groups observed by Galileo	22
1.20	Comparison of occurrence characteristics between JAC and QP bursts	23
1.21	Radio and electron observations for a period including the large 40-min pe- riodic electron bursts	24
1.22	Polar projections of X-rays seen by Chandra and simultaneous far-ultraviolet images obtained by the Hubble Space Telescope	26
1.23	Light-curve and power-spectrum data for the auroral hot spot	27
1.24	The rapidly evolving auroral flare observed poleward of Jupiter's auroral oval	28
1.25	The sum of the EUV and FUV H <sub>2</sub> bands counts from the northern auroral zone are compared with the Galileo PWS radio signal	29
1.26	Evolution of the morphology of the nightside polar spot (NPS) in the STIS data set obtained on 18 December 2000	30
1.27	North-polar projection of temperatures shows a hot spot high in the strato- sphere	31
2.1	A schematic of the Ulysses spacecraft and spacecraft coordinate	36
2.2	A schematic of the Galileo spacecraft	41
2.3	A schematic of the Cassini spacecraft	42
2.4	Orbital parameters of Ulysses in 1991–1992	44
2.5	Orbital parameters of Ulysses in 2004	45
2.6	Orbital parameters of Galileo	46
2.7	Orbital parameters of Cassini	47

3.1	Typical events of QP bursts observed by Ulysses . . . . .	50
3.2	Typical events of QP bursts observed by Galileo . . . . .	51
3.3	Occurrence dependence of QP bursts on longitudes and latitudes . . . . .	54
3.4	Occurrence dependence of QP bursts on longitudes and local time . . . . .	55
3.5	Meridional distribution of QP bursts . . . . .	58
3.6	Periodgram of QP bursts observed by Ulysses during the first encounter . .	64
3.7	Periodgram of QP bursts observed by Ulysses during the second encounter	65
3.8	Periodgram of QP bursts observed by Galileo at low latitudes . . . . .	66
3.9	Histogram of QP bursts' periodicity . . . . .	67
4.1	RPWS antenna system on the Cassini spacecraft . . . . .	72
4.2	Coordinate systems used for the direction finding analysis . . . . .	73
4.3	Spherical triangle solved by the law of cosines . . . . .	74
4.4	Histogram of the received intensity observed by Ulysses . . . . .	79
4.5	Dynamic spectrograms showing QP bursts on 19 Feb. 2004 . . . . .	81
4.6	Stokes parameters at 52 kHz on 19 Feb. 2004 . . . . .	82
4.7	Stokes parameters at 52 kHz at 7–10 h on 19 Feb. 2004 . . . . .	83
4.8	Dynamic spectrograms showing QP bursts on 2 Mar. 2004 . . . . .	84
4.9	Stokes parameters at 52 kHz on 2 Mar. 2004 . . . . .	85
4.10	Stokes parameters at 52 kHz at 11–13 h on 2 Mar. 2004 . . . . .	86
4.11	Dynamic spectrograms showing QP bursts on 18 Feb. 2004 . . . . .	87
4.12	Stokes parameters at 52 kHz at 0–9 h on 18 Feb. 2004 . . . . .	88
4.13	Stokes parameters at 52 kHz at 5–8 h on 18 Feb. 2004 . . . . .	89
4.14	Dynamic spectra observed by RPWS on 22 Dec. 2000 . . . . .	91
4.15	Stokes parameters observed at 1–2 h on 22 Dec. 2000 . . . . .	93
4.16	Statistical distribution of Stokes parameters of QP bursts . . . . .	94
4.17	Dependence of QP bursts' Stokes parameters on CML . . . . .	95
4.18	Dependence of QP bursts' Stokes parameters on SSL . . . . .	96
4.19	Dynamic spectra observed by RPWS on 7 Jan. 2001 . . . . .	98

4.20	Polarization and direction finding results at 675 kHz on 7 Jan. 2001 . . . . .	99
4.21	Polarization and direction finding results at 675 kHz on 7 Jan. 2001 ( $Q, U = 0$ )	100
4.22	Polarization and direction finding results at 116.6 kHz on 7 Jan. 2001 . . . . .	101
4.23	Polarization and direction finding results at 116.6 kHz on 7 Jan. 2001 ( $Q, U = 0$ ) . . . . .	102
4.24	Polarization and direction finding results at 25.9 kHz on 22 Dec. 2000 . . . . .	105
4.25	Polarization and direction finding results at 25.9 kHz on 22 Dec. 2000 ( $Q, U = 0$ ) . . . . .	106
4.26	Dynamic spectra observed by RPWS on 23 Dec. 2000 . . . . .	107
4.27	Polarization and direction finding results at 14.7 kHz on 23 Dec. 2000 . . . . .	108
4.28	Polarization and direction finding results at 14.7 kHz on 23 Dec. 2000 ( $Q, U = 0$ ) . . . . .	109
5.1	A schematic of a boundary defined by quadratic functions . . . . .	115
5.2	Electron density distribution from the Divine-Garrett model . . . . .	116
5.3	Electron density distribution from the plasma models . . . . .	117
5.4	Magnetic field distribution from the VIP4-CS model . . . . .	118
5.5	Ray tracing results for the case of Ulysses (L-O mode) . . . . .	125
5.6	$f_p$ and $f_c$ profile along $L = 30$ magnetic field line . . . . .	127
5.7	Ray tracing results for the case of Ulysses (R-X mode) . . . . .	129
5.8	$f_p$ and $f_c$ distribution in a meridian plane . . . . .	133
5.9	Ray tracing results for the case of Galileo (L-O mode) . . . . .	135
5.10	$f_{RX}$ and $f_p/f_c$ distribution in a meridian plane . . . . .	136
5.11	Ray tracing results for the case of Galileo (R-X mode) . . . . .	137
5.12	Relationship between half-cone angles and minimum radial distances . . . . .	139
5.13	Ray tracing results for the case of Cassini (L-O mode) . . . . .	145
5.14	Ray tracing results for the case of Cassini (R-X mode) . . . . .	146
5.15	Typical example of LF bursts . . . . .	147
5.16	Results of the ray tracing in Steinberg et al. (2004) . . . . .	149

6.1	Direct generation scenario of QP bursts . . . . .	155
6.2	A schematic showing parallel-beam distribution function and resonance curve in a momentum space . . . . .	161
6.3	Growth rate for the case of O mode where $\omega_p/\omega_c = 10^{-3}$ , $n = 2$ , $u_{\parallel 0} \sim 1$ MeV, $u_{\perp 0} = 0$ eV, and $a_{\parallel} = a_{\perp} \sim 300$ keV . . . . .	162
6.4	Growth rate for the case of X mode where $\omega_p/\omega_c = 10^{-3}$ , $n = 2$ , $u_{\parallel 0} \sim 1$ MeV, $u_{\perp 0} = 0$ eV, and $a_{\parallel} = a_{\perp} \sim 300$ keV . . . . .	164
6.5	Growth rate for the case of O mode where $\omega_p/\omega_c = 10^{-3}$ , $n = 1$ , $u_{\parallel 0} \sim 15$ MeV, $u_{\perp 0} = 0$ eV, and $a_{\parallel} = a_{\perp} \sim 300$ keV . . . . .	165
6.6	Growth rate for the case of X mode where $\omega_p/\omega_c = 10^{-3}$ , $n = 1$ , $u_{\parallel 0} \sim 15$ MeV, $u_{\perp 0} = 0$ eV, and $a_{\parallel} = a_{\perp} \sim 300$ keV . . . . .	166
6.7	Momentum distribution function of a beam of electrons viewed from a generation site above an active region . . . . .	168
6.8	A schematic showing ring-beam distribution function and resonance curve in a momentum space . . . . .	169
6.9	Growth rate for the case of O mode where $\omega_p/\omega_c = 10^{-3}$ , $n = 1$ , $u_{\parallel 0} \sim 15$ MeV, $u_{\perp 0} \sim 4$ eV, and $a_{\parallel} = a_{\perp} \sim 300$ keV . . . . .	170
6.10	Growth rate for the case of X mode where $\omega_p/\omega_c = 10^{-3}$ , $n = 1$ , $u_{\parallel 0} \sim 15$ MeV, $u_{\perp 0} \sim 4$ MeV, and $a_{\parallel} = a_{\perp} \sim 300$ keV . . . . .	171
6.11	Ray tracing results for the cases of L-O and R-X mode waves from high source altitudes . . . . .	172
6.12	Growth rate for the case of O mode where $\omega_p/\omega_c = 10^{-2}$ , $n = 1$ , $u_{\parallel 0} \sim 15$ MeV, $u_{\perp 0} \sim 4$ MeV, and $a_{\parallel} = a_{\perp} \sim 300$ keV . . . . .	174
6.13	Growth rate for the case of X mode where $\omega_p/\omega_c = 10^{-2}$ , $n = 1$ , $u_{\parallel 0} \sim 15$ MeV, $u_{\perp 0} \sim 4$ MeV, and $a_{\parallel} = a_{\perp} \sim 300$ keV . . . . .	175
6.14	Growth rate for the case of X mode where $\omega_p/\omega_c \sim 42$ , $n = 1$ , $u_{\parallel 0} \sim 15$ MeV, $u_{\perp 0} \sim 4$ MeV, and $a_{\parallel} = a_{\perp} \sim 300$ keV . . . . .	176
6.15	Indirect generation scenario of QP bursts . . . . .	179

6.16 Density boundary with Cartesian coordinate . . . . .	180
6.17 A schematic of the mode conversion model in the present calculation . . . . .	182
6.18 Profiles of plasma and cyclotron frequencies along a field line of the apex located at a distance of $30 R_J$ . . . . .	183
6.19 Profile of electron density gradients along a field line of the apex located at a distance of $30 R_J$ . . . . .	184
6.20 Energy conversion rate of the reflected ordinary mode wave $K_{REO}$ vs the angle $\theta_H$ . . . . .	185
6.21 Energy conversion rate of the reflected ordinary mode wave $K_{REO}$ vs the incident angle $\theta_{IE}$ . . . . .	187
6.22 Polar diagram to indicate the $K_{REO}(\theta)$ as the function of $\theta$ . . . . .	188
6.23 Frequency profiles showing the conversion process of L-O mode waves from Z mode waves . . . . .	190
6.24 Stream lines and field aligned currents in the cusp region . . . . .	193
6.25 Flux transfer event scenario of QP phenomena . . . . .	196
6.26 A schematic of a flux transfer event . . . . .	198
6.27 Magnetic field components in boundary normal coordinates on 24 Oct, 2001	200
6.28 Solar wind parameters and QP bursts' occurrence . . . . .	202
6.29 Cross correlation between solar wind and QP bursts . . . . .	203
6.30 Solar wind parameters and intensities of high-latitude bKOM . . . . .	205
6.31 Cross correlation between solar wind and bKOM . . . . .	206
6.32 Example of a pulsating AKR event on 6 August 1997 2005–2105 UT . . . . .	209
6.33 Correlation between AKR pulsation frequencies and FLRs frequencies . . . . .	210
6.34 Magnetic field, riometer, and wave data presented by Nosé <i>et al.</i> (1998) . . . . .	212
6.35 Relative occurrence of magnetic and riometer Pc5 pulsations . . . . .	213
6.36 Field line resonance scenario of QP phenomena . . . . .	214
6.37 Dynamic spectra of the perturbation fields on 1 Apr, 1997 . . . . .	216
6.38 Averaged spectra of the perturbation fields at 7–9 h on 1 Apr, 1997 . . . . .	217

6.39	Hodograph of the perturbation field vector at 8–9 h on 1 Apr, 1997 . . . . .	219
6.40	Dynamic spectra of the periodic magnetic fields and MeV electrons observed by Ulysses . . . . .	221
6.41	Hodograph of the perturbation field vector at 5.8–6.4 h on 12 Feb (Day 43), 1992 . . . . .	222
7.1	A picture of Jovian quasi-periodic phenomena . . . . .	231



# List of Tables

1.1	Characteristics of Jovian radio components . . . . .	12
1.2	Summary of Jovian quasi-periodic radio bursts observations by Ulysses in 1991–1992 . . . . .	16
2.1	Characteristics of URAP . . . . .	37
2.2	Characteristics of Ulysses' magnetometer . . . . .	39
2.3	Characteristics of PWS . . . . .	40
2.4	Characteristics of Galileo's magnetometer . . . . .	41
2.5	Characteristics of RPWS . . . . .	43
3.1	Chi-Square Values of Longitudinal Dependence of QP Bursts . . . . .	56
4.1	Significance level of the received power of URAP/RAR . . . . .	80
4.2	Accuracy of the direction finding at 675 kHz on 7 Jan. 2001 (no assumption) . . . . .	103
4.3	Accuracy of the direction finding at 675 kHz on 7 Jan. 2001 ( $Q, U = 0$ ) . . . . .	103
4.4	Accuracy of the direction finding at 116.6 kHz on 7 Jan. 2001 (no assumption) . . . . .	103
4.5	Accuracy of the direction finding at 116.6 kHz on 7 Jan. 2001 ( $Q, U = 0$ ) . . . . .	103
5.1	Parameters for the ray tracing . . . . .	120
5.2	Calculation conditions of the ray tracing for the case of Ulysses . . . . .	122
5.3	Calculation conditions of the ray tracing for the case of Galileo . . . . .	131
5.4	Calculation conditions of the ray tracing for the case of Cassini . . . . .	144

6.1	Characteristics of the quasi-periodic electron outbursts in a relativistic energy range . . . . .	158
6.2	Calculation conditions for the linear wave growth rate . . . . .	160
6.3	Responses of Jovian radio components to the solar wind . . . . .	207
7.1	Observational requirements proposed by the present thesis . . . . .	235

# Chapter 1

## Introduction

### 1.1 Jovian Magnetosphere

Jupiter has strong magnetic moment ( $\sim 1.56 \times 10^{20} \text{ T} \cdot \text{m}^3$ ) with a tilt angle of  $\sim 10^\circ$  to the rotational axis. The large magnetic moment corresponds to a surface magnetic field of  $\sim 4$  gauss in the equatorial region. This strong magnetic field and Jupiter's rapid rotation (period  $\sim 9$  h 55 min) create the characteristic magnetosphere which is the largest and most dynamic in the planets of our solar system. The Jovian magnetosphere expands up to a distance of  $\sim 100 R_J$  ( $R_J$ : Jovian radius, 71492 km) in the sub solar direction, and its size is variable depending on the solar wind fluctuations: sometimes it is compressed to a sub solar distance of  $\sim 45 R_J$ .

Another unique characteristic of the Jovian magnetosphere is the fact that Jupiter's moon, Io, works as the dominant plasma source, which is located at the inner region ( $\sim 6 R_J$ ) of the magnetosphere. Io provides heavy plasma consisting of sulfur and oxygen to the magnetosphere at a rate of  $\sim 1000$  kg per second. These heavy ions and electrons are picked up by the strong magnetic fields in the inner magnetosphere and corotate with Jupiter. The corotating plasma is distributed circularly around Jupiter, which is termed as the "Io plasma torus" or simply "plasma torus". Heavy plasma from the plasma torus diffuses radially outward from the inner magnetosphere to the outer magnetosphere. Centrifugal

force and thermal pressure of the internal heavy plasma have a quite large influence on dynamics of the whole Jovian magnetosphere. Configurations of the Jovian magnetosphere are illustrated in Figure 1.1.

The unique configurations of the Jovian magnetosphere are responsible for characteristic current systems in the magnetosphere. The picked-up heavy plasma in the middle magnetosphere bends magnetic fields in radial directions by its centrifugal force. The radially stretched fields of the middle magnetosphere are equivalent to azimuthal currents in the equatorial region called the “current sheet”. In the current sheet region, there also exist the radial currents resulted from the magnetosphere-ionosphere coupling process as shown in Figure 1.2 (Cowley and Bunce, 2001). Corotating plasma in the middle magnetosphere bends magnetic field lines back to the direction of sub-corotation due to the plasma’s inertial force or conservation of angular momentum. The angular velocity of a magnetic field shell  $\omega$  falls below the angular velocity of the neutral upper atmosphere in the Pedersen layer of the ionosphere  $\Omega_J^*$ . The angular velocity  $\Omega_J^*$  is expected to lie between  $\omega$  and the angular velocity of the planetary rotation  $\Omega_J$  because of the frictional torque on the atmosphere due to ion-neutral collisions. The oppositely-directed frictional torque on the magnetospheric flux tube is communicated to the equatorial plasma by the magnetosphere-ionosphere coupling current system, which is indicated by the arrowed dashed lines in Figure 1.2. The current system was named the “Hill current system” after the theoretical framework established by *Hill* (1979).

The current sheet and Hill current system have an large effect on the dynamics of the Jovian magnetosphere, contrasting remarkably with the current systems at Earth. This fact indicates an importance of the Jovian magnetosphere in terms of the comparative planetology. Global view of the current systems at Jupiter and Earth are summarized in Figure 1.3.

On the other hand, the Jovian magnetosphere has similar dynamics to those at Earth: plasmoid ejections associated with tail reconnections as one of the examples. Figure 1.4 indicates plasma loading process in the Jovian magnetotail region. The outward diffusing

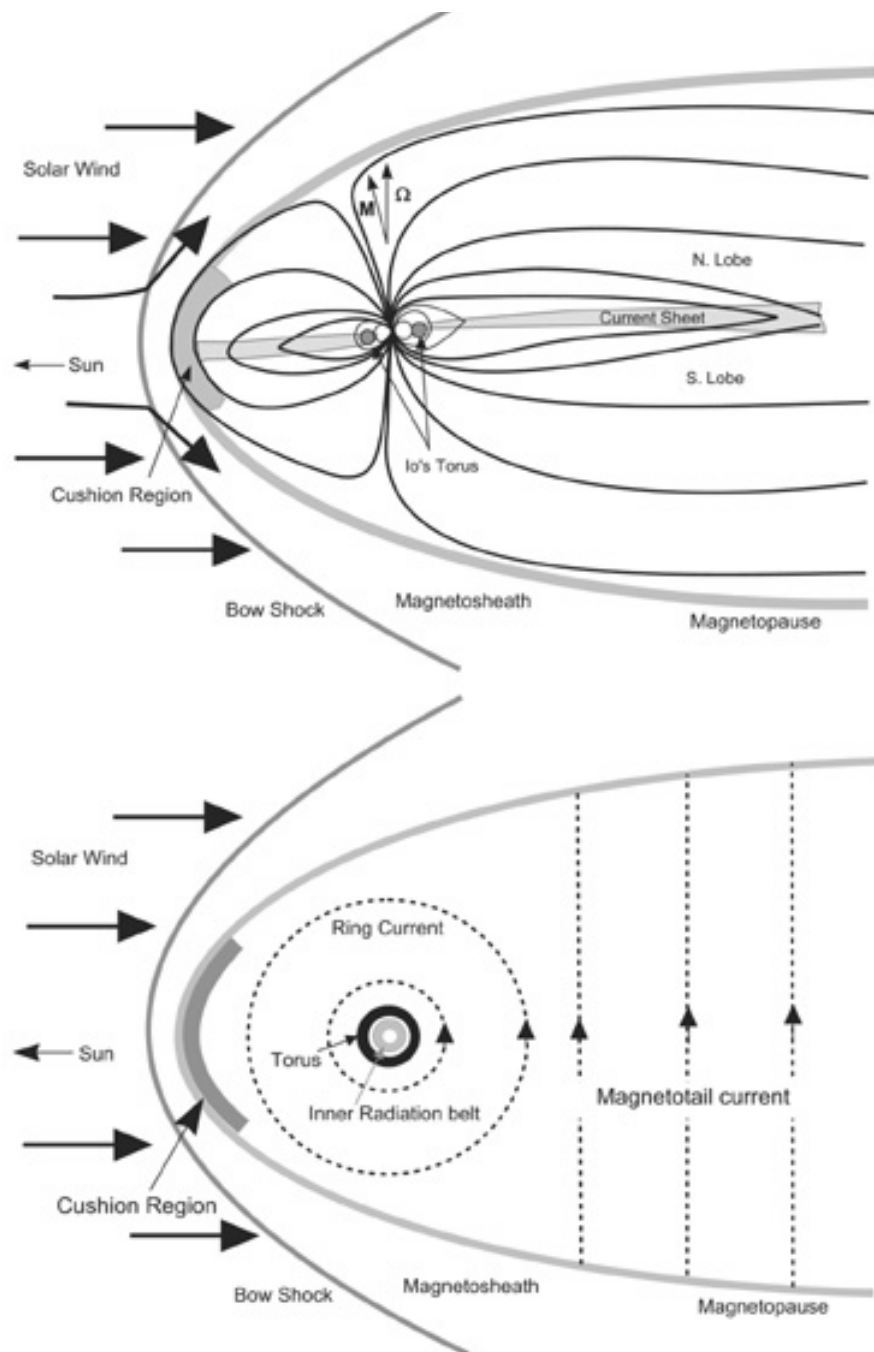


**Figure 1.1:** A schematic of Jupiter's magnetosphere showing the noon-midnight meridian (top) and the equatorial cross section (bottom) (after Khurana et al., 2004).

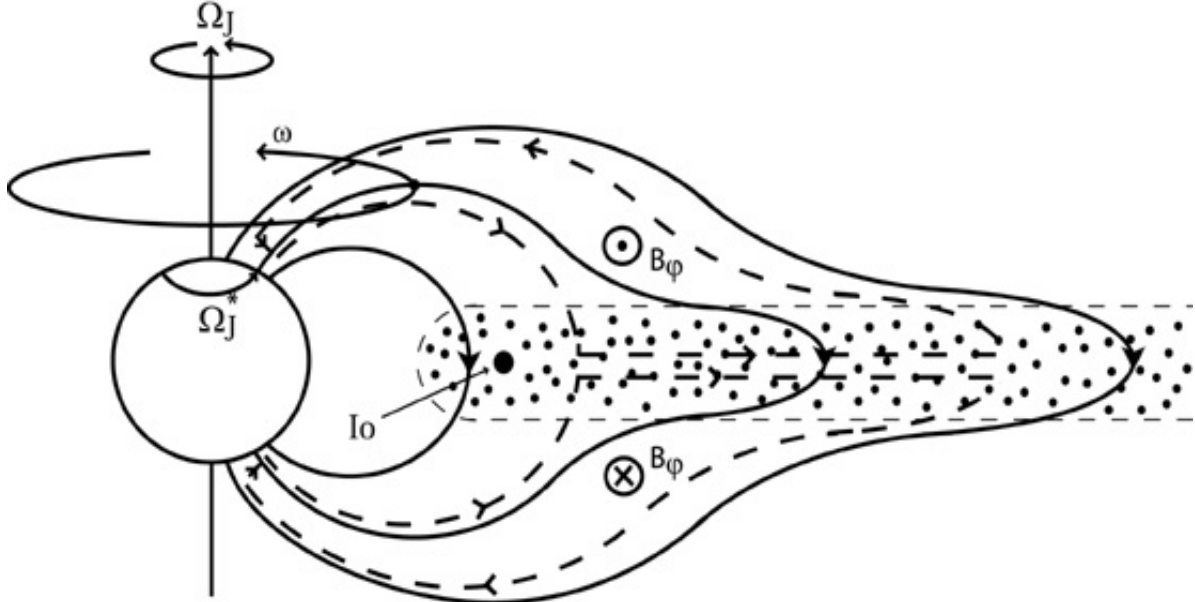


**Figure 1.2:** Sketch of a meridian cross section through the Jovian magnetosphere, showing the principal features of the inner and middle magnetosphere regions (Cowley and Bunce, 2001). The arrowed solid lines indicate magnetic field lines, which are distended outwards in the middle magnetosphere region by azimuthal currents in the current sheet. The current sheet plasma originates mainly at Io, which orbits in the inner magnetosphere at  $\sim 6 R_J$  as indicated, liberating  $\sim 1000 \text{ kg s}^{-1}$  of sulfur and oxygen plasma. This plasma is shown by the dotted region, which rotates rapidly with the planetary field due to magnetosphere-ionosphere coupling, while more slowly diffusing outwards. Three separate angular velocities associated with this coupling are indicated. These are the angular velocity of the planet  $\Omega_J$ , the angular velocity of a particular shell of field lines  $\omega$ , and the angular velocity of the neutral upper atmosphere in the Pedersen layer of the ionosphere  $\Omega_J^*$ . The latter is expected to lie between  $\omega$  and  $\Omega_J$  because of the frictional torque on the atmosphere due to ion-neutral collisions. The oppositely-directed frictional torque on the magnetospheric flux tube is communicated to the equatorial plasma by the current system indicated by the arrowed dashed lines, shown here for the case of sub-corotation of the plasma (i.e.,  $\omega \leq \Omega_J$ ). This “lagging” configuration, associated with the azimuthal field components  $B_\phi$  shown.

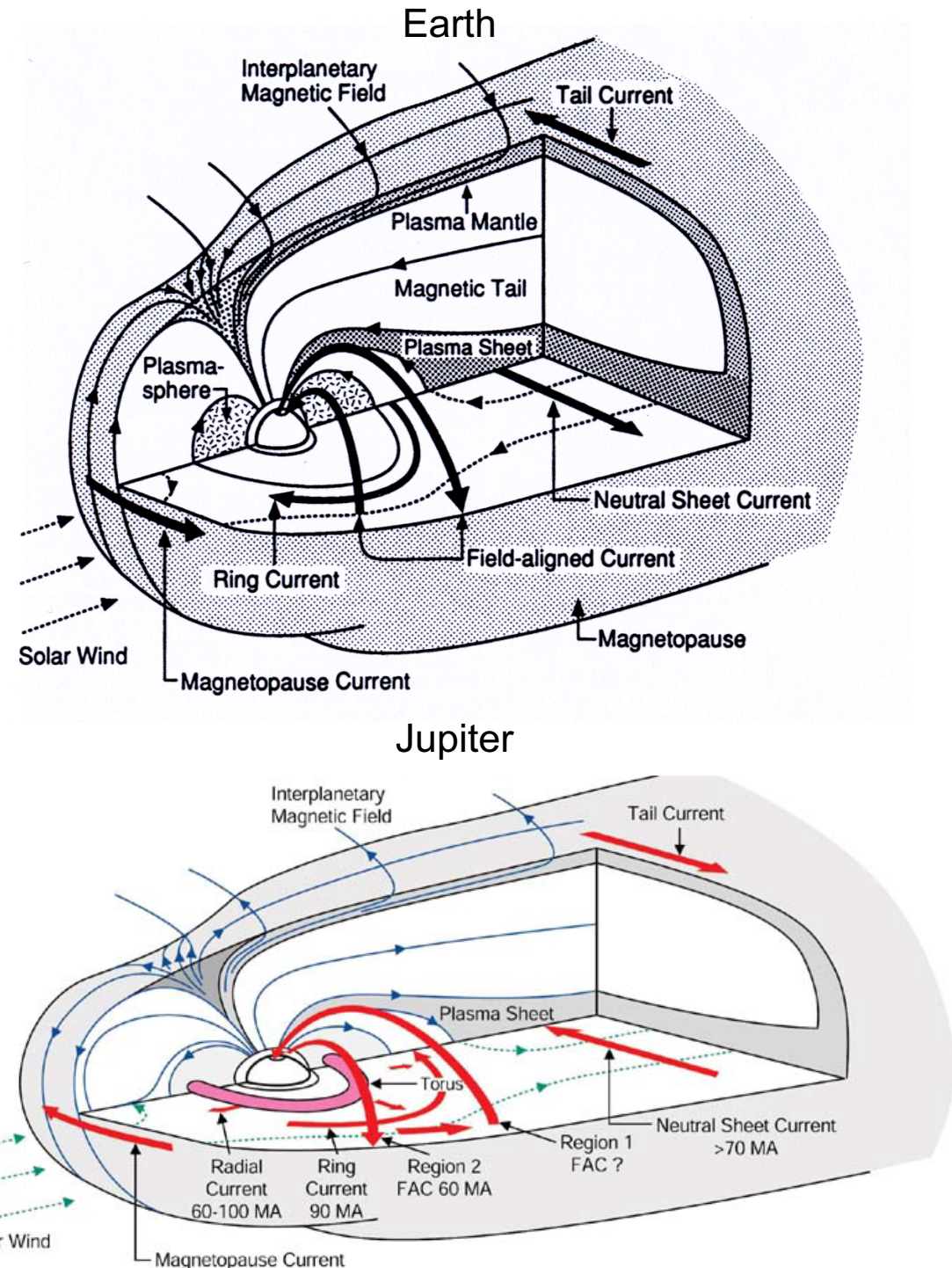


**Figure 1.3:** The strength of the various current systems in Earth's and Jupiter's magnetosphere (Kivelson and Russell, 1995; Khurana, 2004).

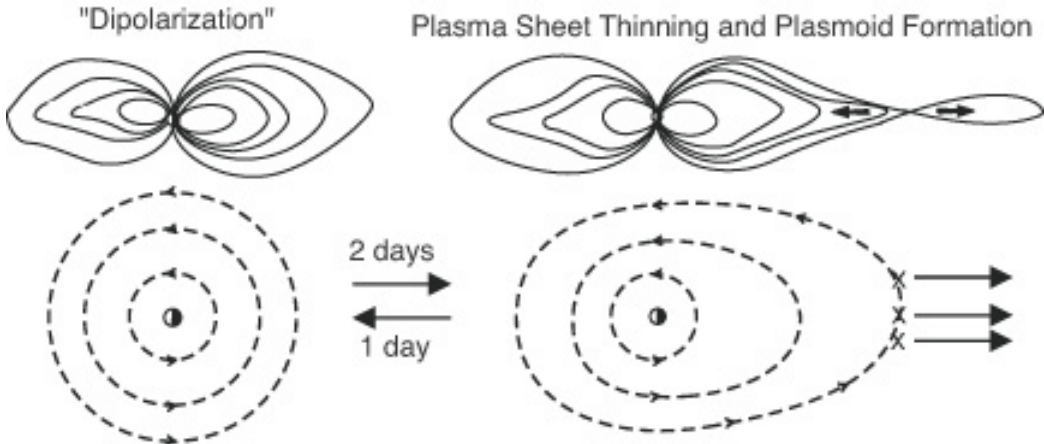


**Figure 1.4:** Plasma loading in the Jovian magnetotail (Woch et al., 1998) from a more dipolar configuration state (left) to a stretched configuration (right). (top) Field lines in the noon-midnight plane and (bottom) flow pattern in the equatorial plane.

plasma thins and stretches the plasma sheet, and finally it initiates magnetic reconnections in the distant tail region (right figure). Then, plasmoids are ejected tailward from Jupiter and dipolarization phase is commenced (left figure). Some previous observations (e.g., Krupp et al., 1998) suggested that the two phases of plasma loading are cycling with a period of  $\sim 3$  days, accompanying with energetic features in particle, wave, and magnetic fields (see Figure 1.5 and 1.6). The behavior of the Jovian magnetosphere is quite similar to the magnetospheric substorm at Earth. This similarity implies that Jupiter also have the dynamic and intermittent energy release process similar to the terrestrial magnetosphere. However, it should be noted that the driver is quite different each other: the internal plasma from Io for Jupiter and solar wind for Earth. The cyclic substorm-like process in the Jovian magnetosphere was named the “Vasyliunas cycle” after the theoretical work by Vasyliunas (1983).

These current systems and dynamics of the Jovian magnetosphere are accompanied with energetic particle accelerations in various parts of the magnetosphere, followed by radiative phenomena: auroral and radio emissions. Particularly, the field aligned currents connected to the polar ionosphere generate bright auroral emissions accompanying with intense radio emissions. Figure 1.7 indicates auroras in ultraviolet wavelengths (Clarke et

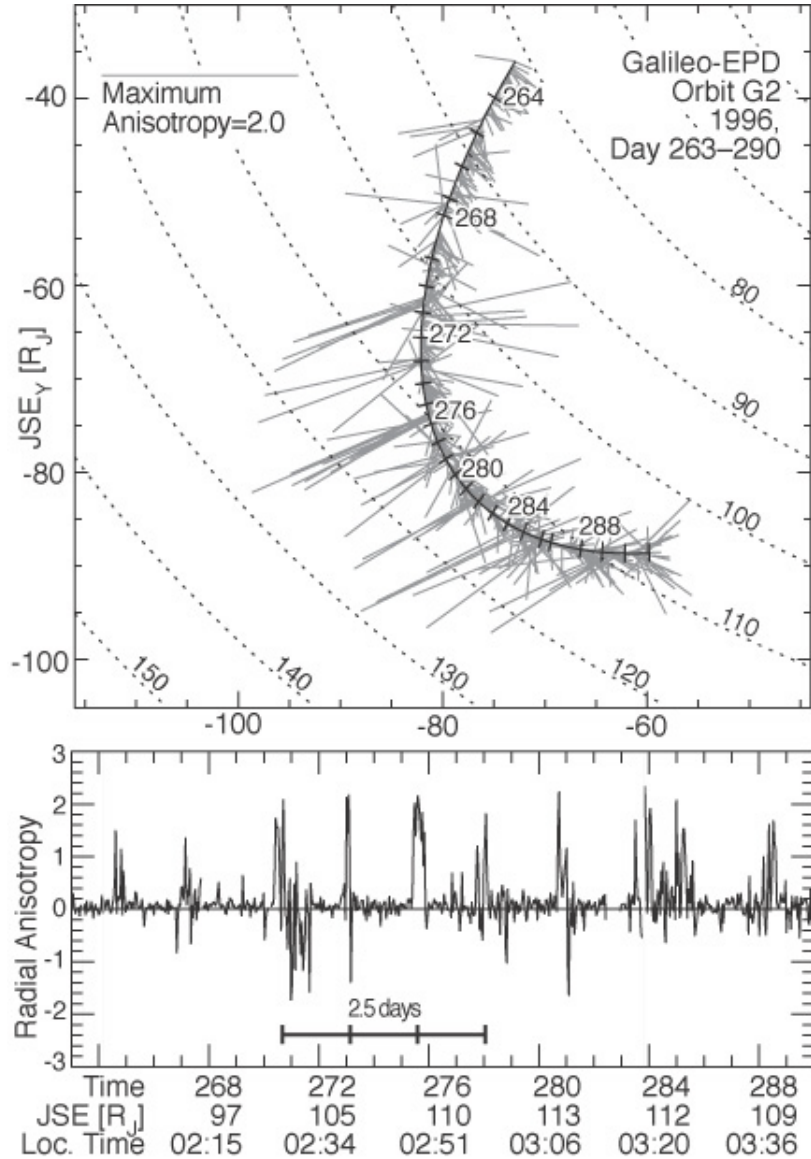


**Figure 1.5:** First order anisotropy vectors of protons (80–220 keV) (Krupp et al., 1998). (top) Anisotropy vector projected on to Jupiter's equatorial plane. The vectors are plotted along the Galileo trajectory of orbit G2 in 1996 (days 263–290) in the pre-dawn section of the Jovian magnetosphere. (bottom) Radial anisotropy component as a function of time for the same interval shown in the top panel. The 2.5–3 day modulation is very obvious.

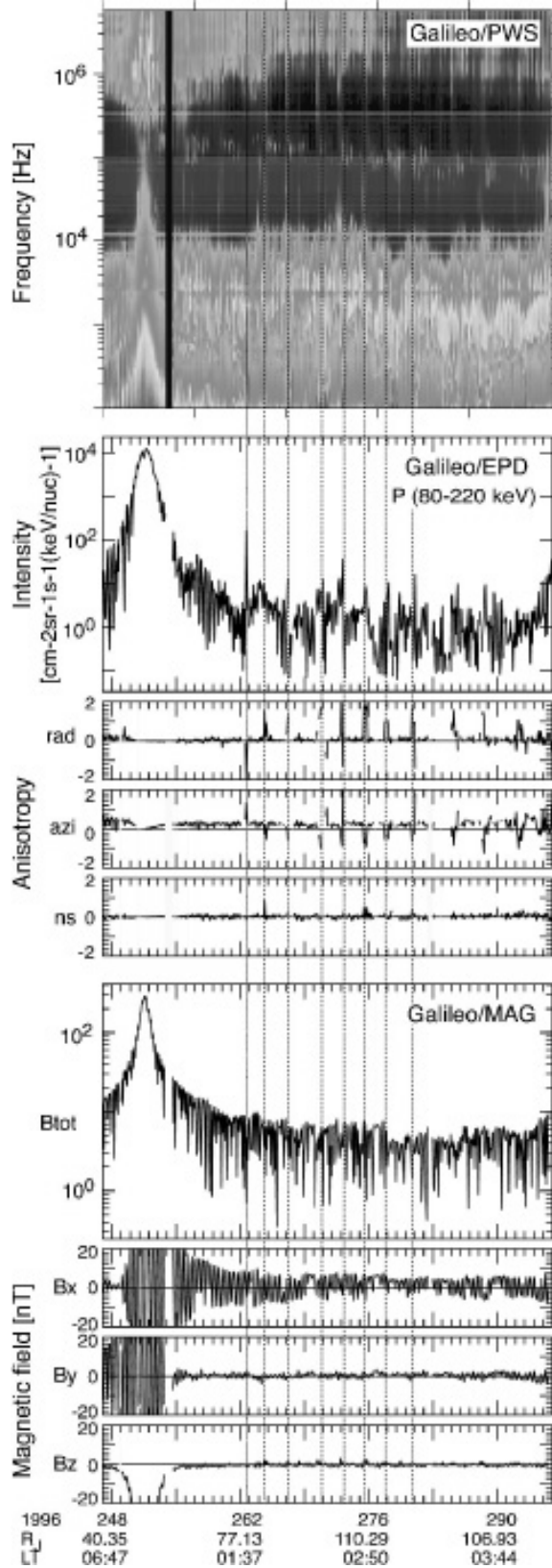


**Figure 1.6:** Data from Galileo orbit G2 in 1996 inside the Jovian magnetosphere (Krupp et al., 2004). From top to bottom, radio emissions, two-hour averaged intensity and relative anisotropy components of protons (80–220 keV), total magnetic field strength and magnetic field components in the JSE coordinate system ( $x$  axis towards the Sun,  $y$  axis towards dusk,  $z$  axis towards north). Horizontal axis is date (day of year) with radial distance ( $R_J$ ) and solar local time (hour:minute).

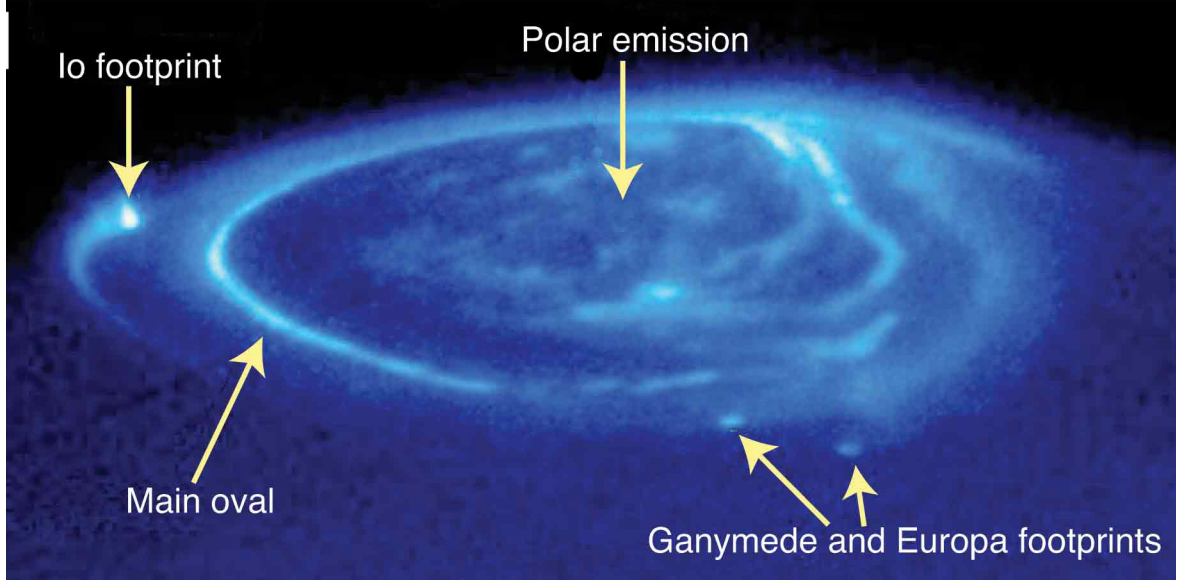


**Figure 1.7:** Hubble Space Telescope (HST) Space Telescope Imaging Spectrograph (STIS) UV image of Jupiter’s northern aurora taken in November 1997, showing the 3 different emission regions: the main oval, the satellite footprints, and the polar emissions (Clarke et al., 2004). The image has been scaled with a logarithmic stretch in intensity to make clear the faint emissions next to brighter ones. Note the resolved auroral curtain above the limb, particularly in Io’s magnetic footprint.

al., 2004), which are resulted from the magnetospheric current systems such as the Hill system. At Jupiter, morphologies of auroral emissions are roughly categorized into three kinds: the main oval, satellite footprints, and polar emissions. The main oval are generated by the precipitating electrons which are energized by the Hill current system. The satellite footprints are associated with the field aligned currents induced by the magnetosphere-satellite interaction process. The polar emissions are relevant to the distant tail region, open-closed boundary, or cusp region of the Jovian magnetosphere. The three kinds of auroras are brightened by the energetic particles which are accelerated downward by the field aligned potentials.

The particles which are energized in planetary magnetospheres have the free energies responsible for local plasma waves and the free-space waves termed the “planetary radio emissions”. These radio emissions at Jupiter are called “Jovian radio emissions”, which are generated in the polar region associated with the auroral field aligned currents, and also in

the equatorial region associated with the radiation belts and the intermittent energization phenomena named “injections”. The injections are possibly related to the substorm-like phenomena as indicated above. Thus, the planetary radio emissions, particularly Jovian radio emissions, are good candidates for the “probe” which can explore the particle accelerations relevant to the dynamics in various parts of planetary magnetospheres.

## 1.2 Jovian Radio Emissions

Jovian radio emissions have more various morphologies and source regions than those of terrestrial radio components. For instance, auroral radio emissions observed in the terrestrial magnetosphere have only two main components: auroral kilometric radiation (AKR) and high-frequency (HF) roar (see Figure 1.8a). These emissions are emitted from the terrestrial polar ionosphere in kilometric and hectometric wavelengths. On the other hand, auroral radio emissions at Jupiter have multiple components: Io-related and non-Io-related decametric radiations (Io-DAM and non-Io-DAM), hectometric radiations (HOM), broadband kilometric radiations (bKOM), and possibly quasi-periodic bursts (QP bursts). These ratio components are termed based on the wavelengths, spectral characteristics, and temporal behavior. The source regions of each component are different in latitudes, altitudes, and corresponding magnetospheric regions. The source region of Io-DAM is considered to be located along the flux tube connecting between Io and the polar ionosphere, i.e.,  $L$ -value of the source field line is  $\sim 6$ , and the radio component is related to the Io footprint aurora (see Figure 1.7). The source location of non-Io DAM has not been identified yet but considered to be associated with auroral emissions like the main oval. *Ladreiter et al.* (1994) performed direction findings for the emissions of HOM and bKOM observed by the Ulysses spacecraft at southern high latitudes during its first encounter with Jupiter. They suggested the source  $L$ -values of HOM and bKOM to be in a range of  $L = 7 - 11$  and  $9 - 15$ , respectively. The source location of Quasi-periodic radio bursts, which is the main subject in the present study, has not been clearly revealed yet but believed to be at high latitudes in the polar region (*MacDowall et al.*, 1993). Correspondence between each

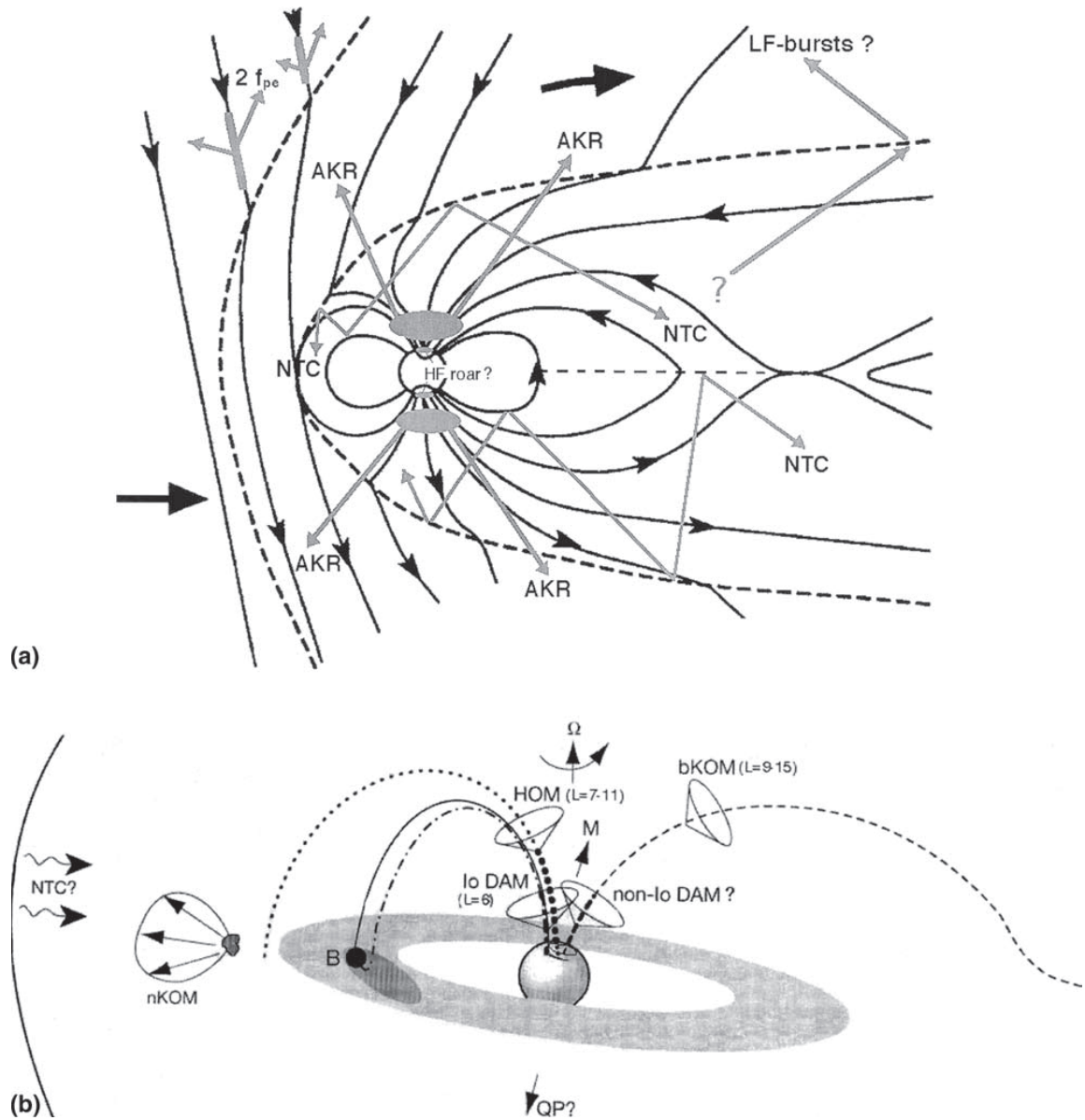


**Figure 1.8:** (a) Sketch of radio source locations in the Earth's magnetosphere and (b) sketch of radio source locations in the Jovian magnetosphere (Zarka et al., 2004).

**Table 1.1:** Characteristics of Jovian radio components (*Kaiser, 1993*)

Component Name	Frequency Range	Radiated Power	Source Location	Comments
DIM	~80 MHz - 300 GHz	2 GW	radiation belts	
DAM	2 - 40 MHz	400 GW	Io torus field lines	
HOM	0.2 - 2 MHz	1 GW*	auroral field lines	
bKOM	10 - 1000 kHz	500 MW	Io torus or auroral	
nKOM	40 - 200 kHz	100 MW	Io torus	
Continuum	0.1 - 30 kHz	100 GW	outer magnetosphere	steep ( $f^{-4}$ ) spectrum
Fast drift	1 - 500 kHz	large	?	

\* From *Desch and Kaiser [1984]*. All other table values after *Carr et al. [1983]*.

(Fast drift: corresponding to QP bursts)

radio component and auroral emission is still unclear except for Io-DAM. However, previous multi-spectral observations and direction findings suggested that the source of bKOM (and possibly non-Io-DAM) is associated with the middle to external magnetosphere (e.g., Zarka *et al.*, 2001; Prangé *et al.*, 2001), and that of HOM is related to the external region of the plasma torus (e.g., Ladreiter *et al.*, 1994). The source location and auroral correspondence of QP bursts are also still unclear, which are the main subjects of the present thesis and thoroughly discussed in the following chapters.

Radio emissions other than the auroral components are also excited in the Jovian magnetosphere: e.g., Synchrotron radiations (or decimetric radiations, DIM) are generated by relativistic electrons in the radiation belts, and narrowband kilometric radiations (nKOM) are considered to have the sources in outer regions of the plasma torus (*Reiner et al.*, 1993). Some previous studies suggested that intensification of nKOM is related to the energetic particle injections accompanying with the large magnetospheric disturbances in the outer region of the plasma torus named “energetic events” (*Louarn et al.*, 2001). Schematics of the planetary radio emissions at Earth and Jupiter are illustrated in Figure 1.8. *Kaiser* (1993) summarized the frequency range, radiated power, and source location of the Jovian radio components as indicated in Table 1.1.

Previous theoretical studies predicted that free-space waves are excited at the altitudes where emission frequencies are close to the local cutoff frequencies in each mode (e.g., Wu

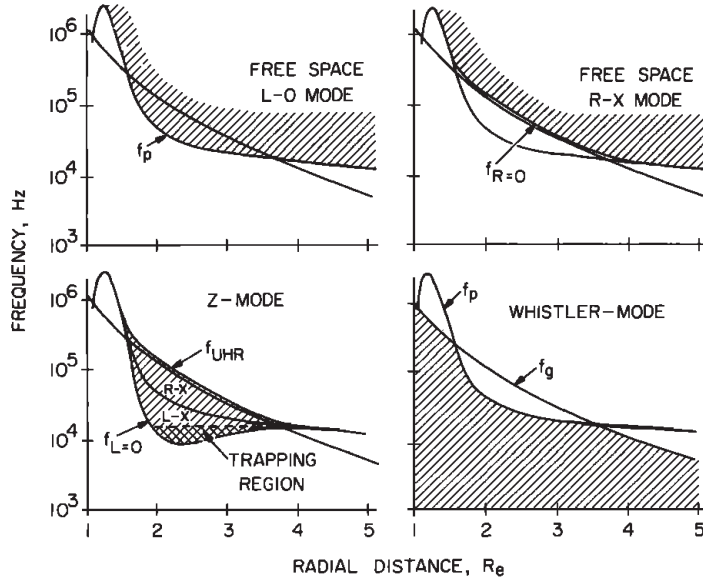


**Figure 1.9:** Frequency variations of characteristic frequencies and ranges of the four main electromagnetic modes versus distance in a magnetized plasma representative of the Earth's auroral regions (Gurnett et al., 1983).

and Lee, 1979). For example, free-space waves in left-handed ordinary (L-O) mode at a frequency  $f$  are excited at the altitudes of  $f \sim f_p$  where  $f_p$  is the local plasma frequency. Meanwhile, right-handed extraordinary (R-X) mode waves are excited at the altitude of  $f \sim f_{RX}$  where  $f_{RX}$  is the local cutoff frequency of R-X mode waves. Figure 1.9 represents the characteristic frequencies  $f_p$  and  $f_{RX}$  in Earth's auroral region (Gurnett et al., 1983). Source regions of Jovian radio components are also defined by these characteristic frequencies. These source characteristics lead to the spectral structures of radio components, which reflect the spatial expansion of source region, temporal variation of energy source (i.e., energetic particle or local plasma wave), and other factors relevant to the magnetospheric dynamics.

Figure 1.10 indicates various spectral structures of Jovian radio components with other planetary radio emissions (Zarka, 2004). The horizontal and vertical axes show frequency in Hz and the flux densities normalized at a distance of 1 AU from radio sources ( $\text{W m}^{-2} \text{ Hz}^{-1}$ ), respectively. As is evident from Figure 1.10, Jovian radio components have significantly larger intensities than the other planetary radio emissions. This means that the Jovian mag-

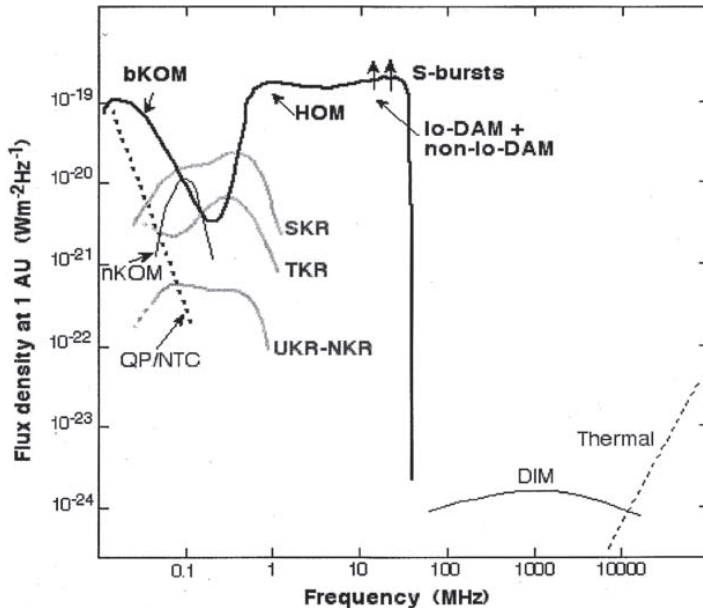


**Figure 1.10:** Spectra of Jovian radio components and auroral radio emissions from the other radio planets (Zarka, 2004).

netosphere has the significantly larger free energies responsible for the radio components than the other magnetospheres. Frequency-time (*f-t*) structures of Jovian radio emissions also show multiple natures in dynamic spectra as indicated in Figure 1.11. Variations of the *f-t* structures reflect the propagation processes and generation mechanisms of the radio emissions: e.g., source locations, directivity at the sources, ray paths, and temporal variations of the energy sources.

## 1.3 Quasi-Periodic Phenomena

### 1.3.1 Quasi-Periodic Radio Bursts

Jovian quasi-periodic (QP) radio bursts were discovered by Voyager (Kurth et al., 1989) and named “Jovian Type III bursts” due to their dispersive spectral nature as shown in Figure 1.12. Their occurrence characteristics have been investigated in detail using Ulysses’ observations. During Ulysses’ first Jovian flyby in 1992, two kinds of QP bursts were

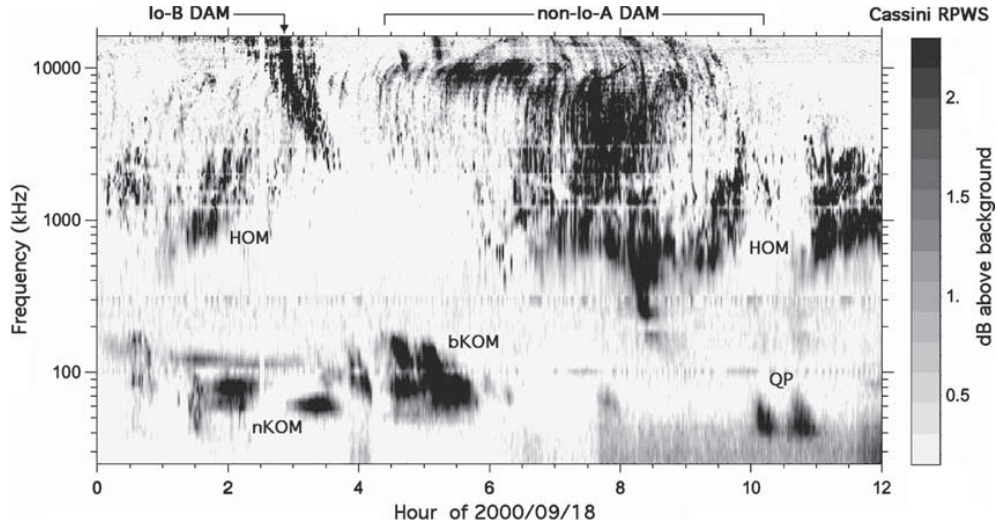


**Figure 1.11:** Jovian low-frequency radio emissions as detected by Cassini-RPWS from  $1350 R_J$  range from Jupiter (Zarka, 2004).

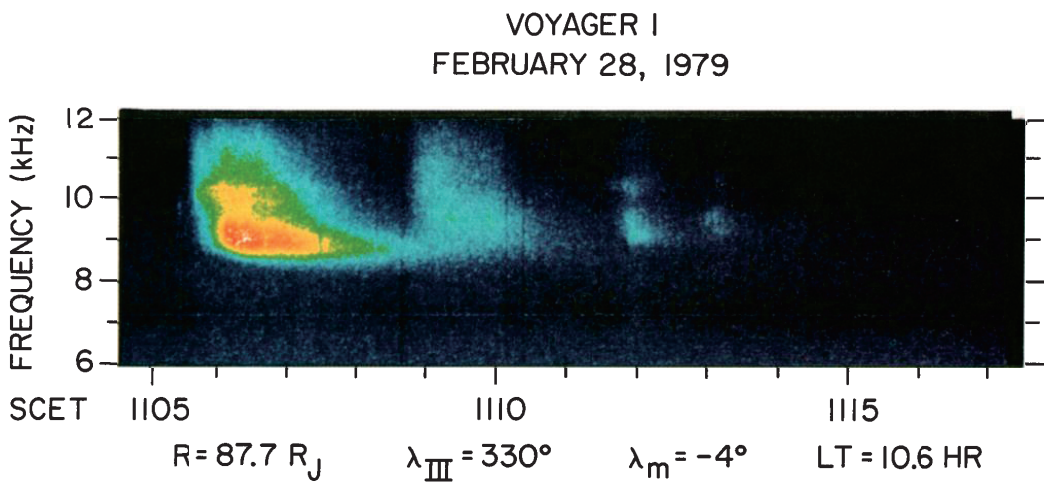


**Figure 1.12:** A plot of dynamic spectra showing the remarkable similarity in the appearance of QP radio bursts to solar type III bursts (Kurth et al., 1989).

**Table 1.2:** Summary of Jovian quasi-periodic radio bursts observations by Ulysses in 1991–1992 (*MacDowall et al.*, 1993).

Observation	QP-15 bursts	QP-40 bursts
Quasiperiodicity	10–20 min	40–50 min
Observing geometry	Predominantly inbound ; some outbound	Almost exclusively outbound
Dependence on sub-spacecraft longitude	Abrupt onset at $\sim 0^\circ$ longitude	Weakly correlated with longitude ; most likely at $\sim 20^\circ$
Typical frequency range	$\sim 1\text{--}50 \text{ kHz}$	$\sim 1\text{--}200 \text{ kHz}$ ; several events reach 700 kHz
Spectral behavior	Power flux density $\sim f^{-3}\text{--}f^{-6}$ or steeper	Variable (see text)
Typical emitted power	$10^7 \text{ W}$	$10^8 \text{ W}$
Duration	2–5 min	5–10 min
Source location	Uncertain	Near South Pole
Polarization	Unknown	Right-hand circular (Stokes $V \sim -0.6$ ) ; emission is L-O
Associated electrons	No 15 min periodicity reported	Correlated with keV and MeV electron bursts (outbound in magnetosphere)
Correlation with solar wind parameters	26 (or 13) day variability	Good correlation with solar wind velocity

identified based on analysis of time intervals of each QP burst pulse (*MacDowall et al.*, 1993): one with a periodicity of around 15 min during the inbound phase and the other with a periodicity of  $\sim 40$  min during the outbound phase (see Figures 1.13 and 1.14). They were named “QP15” and “QP40” bursts, respectively. The two burst groups were typically observed in the frequency range of 1–50 kHz (QP15) and 1–200 kHz (QP40). *MacDowall et al.* (1993) showed that the occurrence of QP15 and QP40 depends on the central meridian longitude of System III (CML) of Ulysses as shown in Figure 1.15. When the spacecraft was at the southern high latitudes ( $\sim -40^\circ$ ) near the dusk terminator of Jupiter during the outbound pass, direction-finding analyses were performed to reveal the wave mode and source region of QP40. Results of the direction findings are indicated in Figure 1.16, which suggested that QP40 bursts are L-O mode waves emitted from the polar region. Table 1.2 summarizes the observation results of the QP bursts observed by Ulysses during the first encounter (*MacDowall et al.*, 1993).

QP bursts were also detected by the Galileo and Cassini spacecraft. *Kaiser et al.*

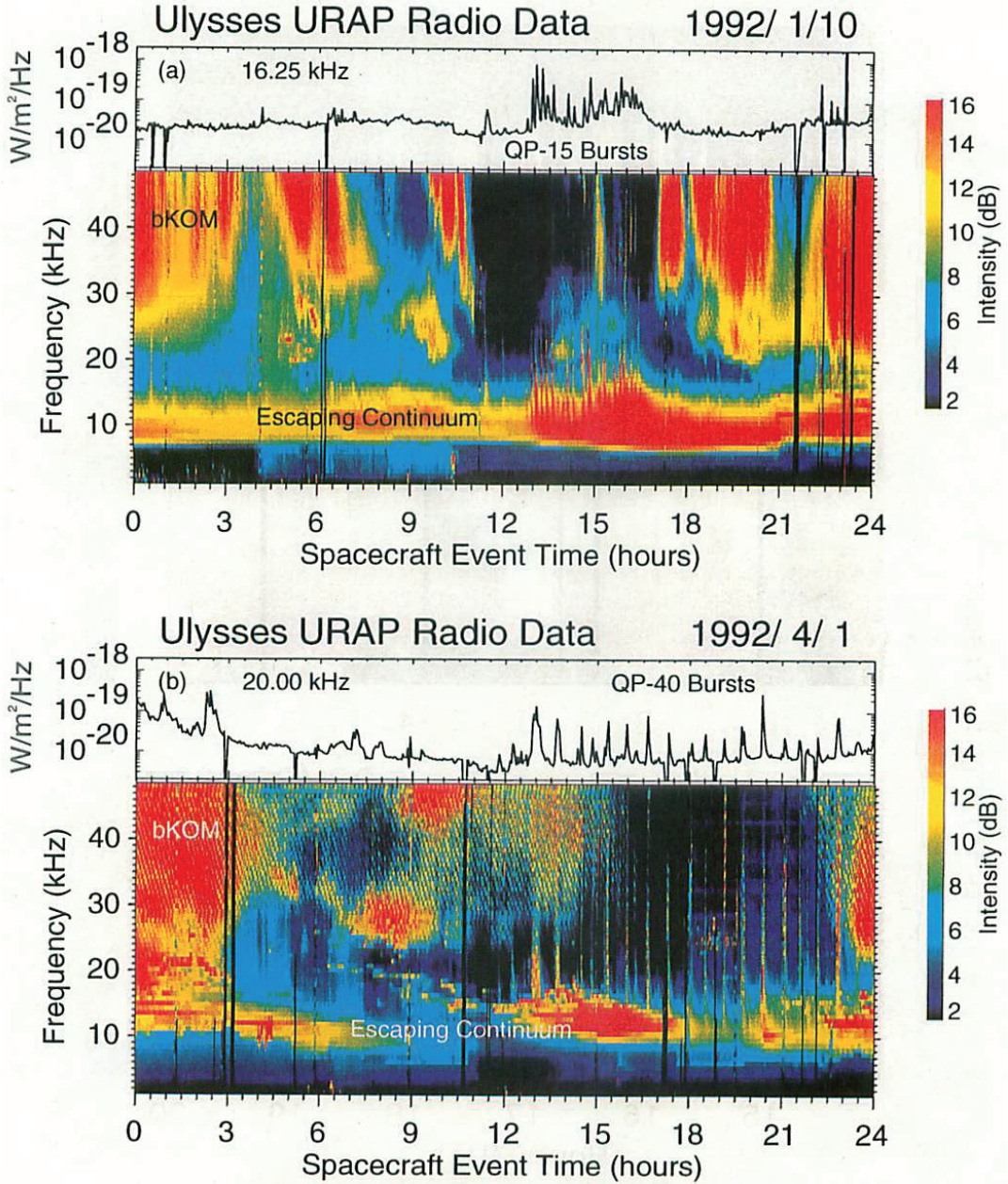


**Figure 1.13:** Dynamic spectra showing QP15 bursts observed inbound on 10 January 1992, from 13:00 to 17:00 UT (panel (a)) and QP40 bursts observed outbound on 1 April 1992, from 12:00 to 24:00 (panel (b)) (MacDowall *et al.*, 1993). Only data from the low band of the RAR are presented. In panel (b), the mottled appearance of the QP40 bursts results from modulation of the signal due to changes in antenna orientation as the spacecraft spins. A single frequency plot is also displayed for each panel, showing the periodic nature of the QP bursts.

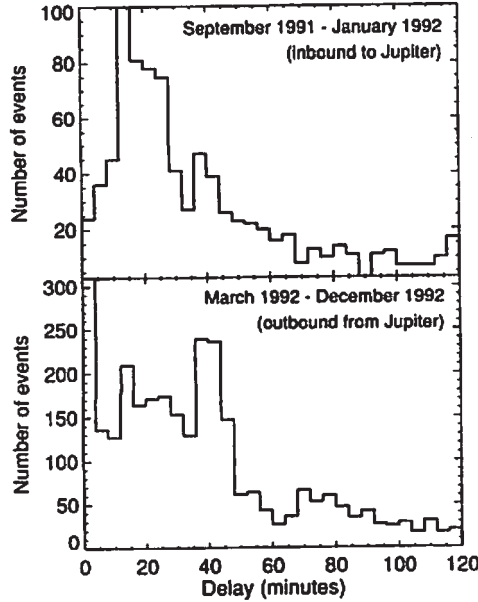


**Figure 1.14:** Histograms showing the delays between successive events in the computer-generated QP burst event list (MacDowall et al., 1993). (a) September 1992 through January 1992 (inbound), (b) March 1992 through December 1992 (outbound).

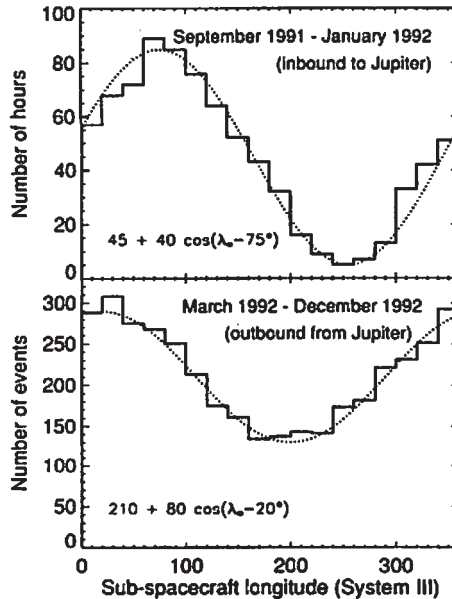


**Figure 1.15:** Histograms showing the distributions in sub-spacecraft longitude for QP bursts events (MacDowall et al., 1993). (a) September 1992 through January 1992 (inbound), (b) March 1992 through December 1992 (outbound). The dotted lines are fitted sinusoids.

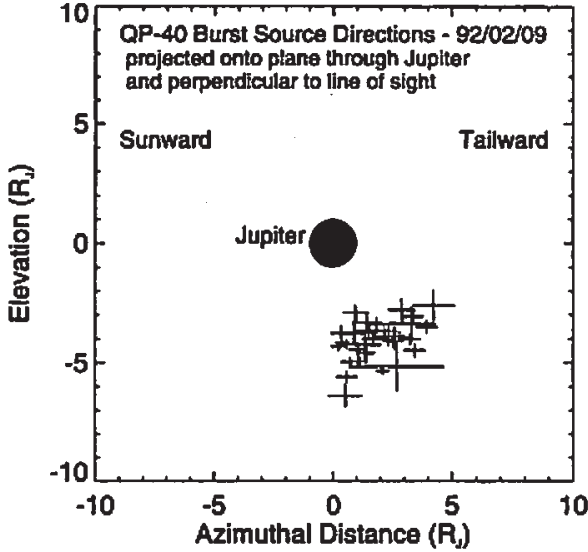


**Figure 1.16:** Plot of QP-40 burst source directions derived for several bursts on 9 February 1992 (MacDowall *et al.*, 1993). The source directions are projected onto the plane containing Jupiter and perpendicular to the line of sight from Ulysses to Jupiter. Ulysses is at approximately  $-30^{\circ}$ S Jovigraphic latitude and at 19.8 h LT (i.e., beyond the dusk meridian). The size of the cross is an estimate of the uncertainty in the location.

(2001) compared the observations during the Ulysses' first flyby era with those during the Cassini and Galileo era and concluded that there is a difference between each era: in the Ulysses data, QP bursts appeared with clear periodicities ( $\sim 15$  and  $\sim 40$  min), however, in the Galileo and Cassini data, these periodicities were broadly dispersed (a few to tens of minutes).

Simultaneous observations using Galileo and Cassini were analyzed by Hospodarsky *et al.* (2004). Figure 1.17 indicates the comparison of QP bursts observed by Galileo with those observed by Cassini. When these events were observed, Cassini and Galileo were located at local time of 20.5 and 16.9, respectively. Hospodarsky *et al.* (2004) showed many events with similar characteristics to Figure 1.17 and concluded that beaming patterns of QP bursts observed at low latitudes have a large solid angle with a ‘strobe’ like manner. They also performed direction-finding analyses from Cassini as shown in Figure 1.18. This result indicates that QP bursts have apparent directions significantly distant from Jupiter

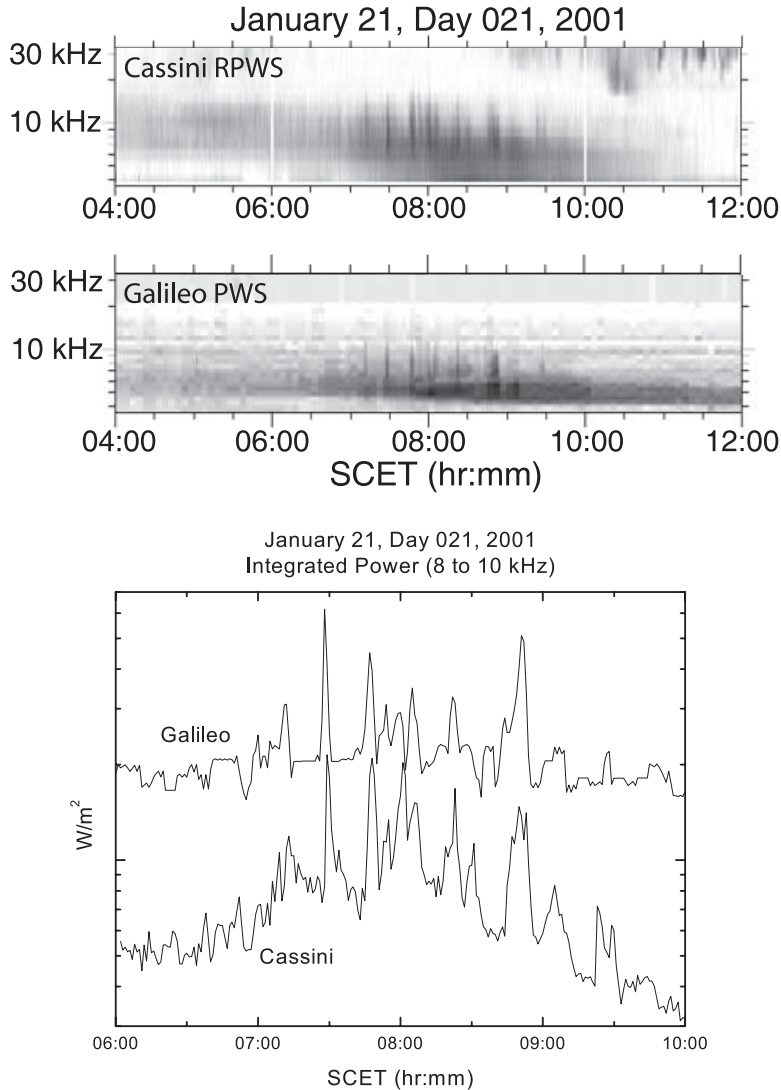


**Figure 1.17:** Frequency-time spectrograms showing QP bursts detected by Cassini (top panel) and Galileo (middle panel) from 21 January 2001, when both spacecraft are in the solar wind. QP bursts are detected by both spacecraft from about 0700 to 1000 SCET. The QP bursts detected by both spacecraft range in frequency from about 5 kHz to 15 kHz. Cassini is located about  $320 R_J$  from Jupiter and at 20.5 hours LT, while Galileo was about  $144 R_J$  from Jupiter and at 16.9 hours LT. (bottom) A plot of the integrated power flux from 8 to 10 kHz (1 min averages) of the QP emissions as measured by Galileo (top curve) and Cassini (bottom curve) for 21 January 2001. The Cassini data has been shifted downward to allow more easy comparison of the data. In this example, the Cassini data has not been shifted “earlier” (to the left) to account for the difference in the light time from Jupiter to each of the spacecraft (actual difference is  $\sim 42$  s, or 0.7 min). As can be seen, the QP bursts observed by the two spacecraft are very similar, though the Cassini peaks occur slightly after the Galileo peaks.

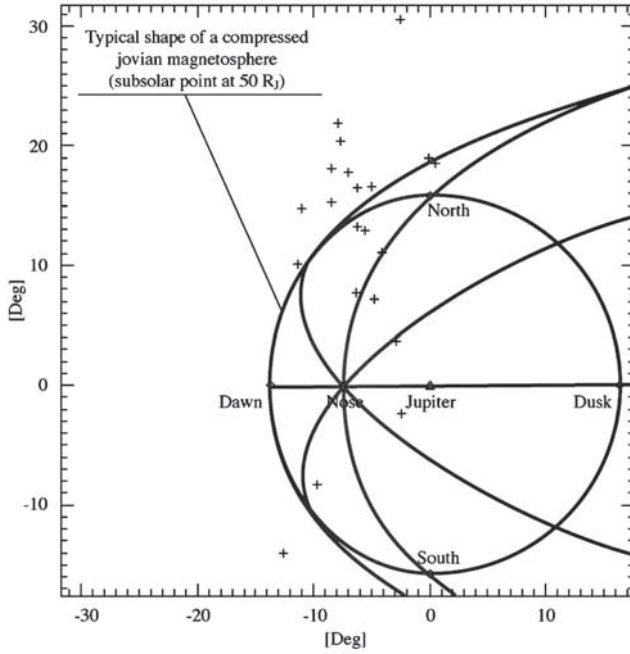


**Figure 1.18:** A plot of the apparent direction of arrival of QP bursts from DOY 357, 2002, at  $\sim 20$  kHz, projected (the crosses) on the plane of the sky (Hospodarsky et al., 2004). The axes are the azimuth and colatitude in a Jupiter-centered XYZ frame, with Z along the Jupiter to Cassini axis, Y is the plane containing Jupiter's rotation axis and Z, pointing in Jupiter's north pole direction, and X completes the right-hand triad. Superimposed is the sketch of the orientation and size of the Jovian magnetosphere as seen from Cassini in the same reference frame. The magnetosphere is seen from the dayside, slightly off the Sun-planet axis. Remarkable points (dawn and dusk terminators, north and south pole directions, and the magnetosheath nose) are represented for a compressed magnetopause with a sub solar point at  $50 R_J$ .

seen from Cassini. They interpreted that the QP bursts at low frequencies were dispersed at the magnetosheath and escaped from the high latitudinal region of the magnetosheath into the interplanetary space.

Morioka et al. (2006) showed that the trigger of QP burst pulse groups depends on the phase of Jovian rotation using data obtained from Galileo. Figure 1.19 indicates the dependence on longitude of sub solar point (SSL) and CML with solid and broken lines, respectively. The sub solar longitude corresponds to a representative for rotational phase of Jupiter. They concluded that the SSL dependence is more significant than the CML dependence because of the higher occurrence peak in the SSL dependence. In addition, the

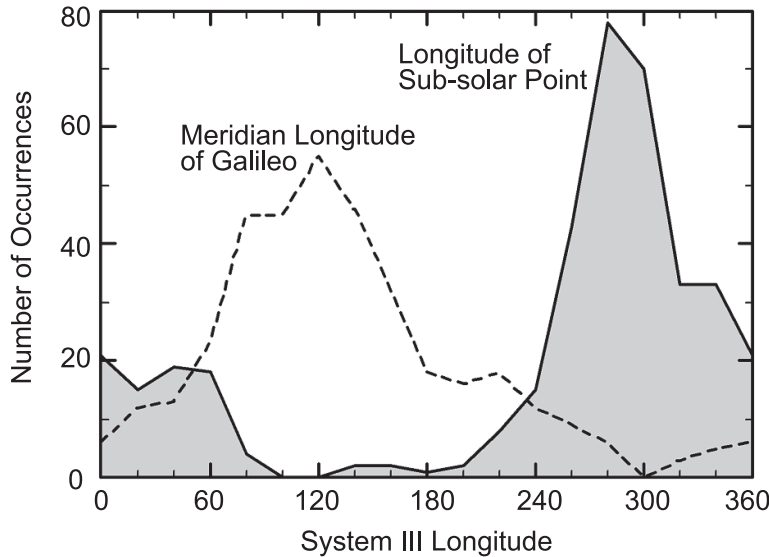


**Figure 1.19:** Longitudinal distribution for QP burst groups (*Morioka et al.*, 2006). The solid line indicates longitude of sub solar point at time of QP-burst group commencements and the broken line indicates central meridian longitude of Galileo at time of QP-burst group commencements.

SSL dependence of QP burst groups coincides with that of the Jovian anomalous continuum (JAC) indicated by *Morioka et al.* (2004). Figure 1.20 shows the comparison of occurrence characteristics between JAC detected from the Ulysses observation and QP burst groups from the Galileo observation. The very similar distribution of both phenomena with a unique occurrence peak at around System III longitude of  $260^\circ$ – $320^\circ$  supports that QP bursts and JAC are generated by “recurrent disturbances” once a planetary rotation which are excited when Jupiter has a particular rotational phase with respect to the solar wind direction (i.e., with respect to the magnetosphere).

Although several spacecraft have observed QP bursts in detail as indicated above, the statistical picture of occurrence, source location, propagation process, and generation mechanism of the emissions are still unclear.

### 1.3.2 Relativistic Particle Bursts

The Cosmic Ray and Solar Particle Investigation (COSPIN) onboard Ulysses observed energetic (more than 9 MeV) electron outbursts with a 40-min period, which were correlated

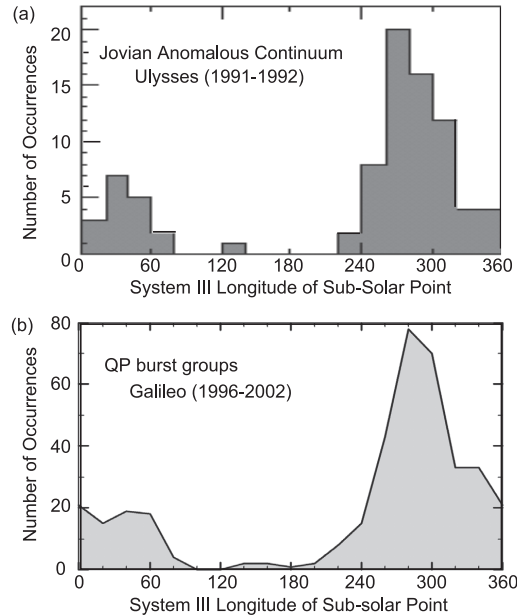


**Figure 1.20:** Comparison of occurrence characteristics between (a) JAC detected from the Ulysses observation and (b) QP-burst groups from the Galileo observation (Morioka et al., 2006). The horizontal axis is System III longitude of sub solar point when JAC and QP-burst groups are detected.

with the QP40 radio bursts at high latitudes in the dusk terminator during the outbound pass (McKibben et al., 1993; Zhang et al., 1995). Figure 1.21 represents the observation results observed on day 41, 1992. The top panels show 64-s average anisotropy amplitudes for more than  $\sim 3$  MeV electrons, based on a fit to a function of the form  $C = C(0)[1 + C(1) \cos(\phi - \phi_1) + C(2) \cos 2(\phi - \phi_2)]$ , where  $\phi$  is a pitch angle of particles,  $\phi_1$  and  $\phi_2$  are directions of the first and second order anisotropies. The anisotropy amplitudes are plotted only if the amplitude differs from zero by more than  $3\sigma$  as determined from the fit. The unidirectional amplitude  $C(1)$  indicates the particle anisotropy directed parallel to the background magnetic field. The bidirectional amplitude  $C(2)$  represents the bi-directional anisotropy with respect to the background field. The analysis results indicated that the periodic electron bursts were accelerated outward from the Jovian polar region, accompanied with QP radio bursts with 40 minutes periodicity. Zhang et al. (1995) also detected relativistic proton populations with the anisotropy outward from Jupiter.

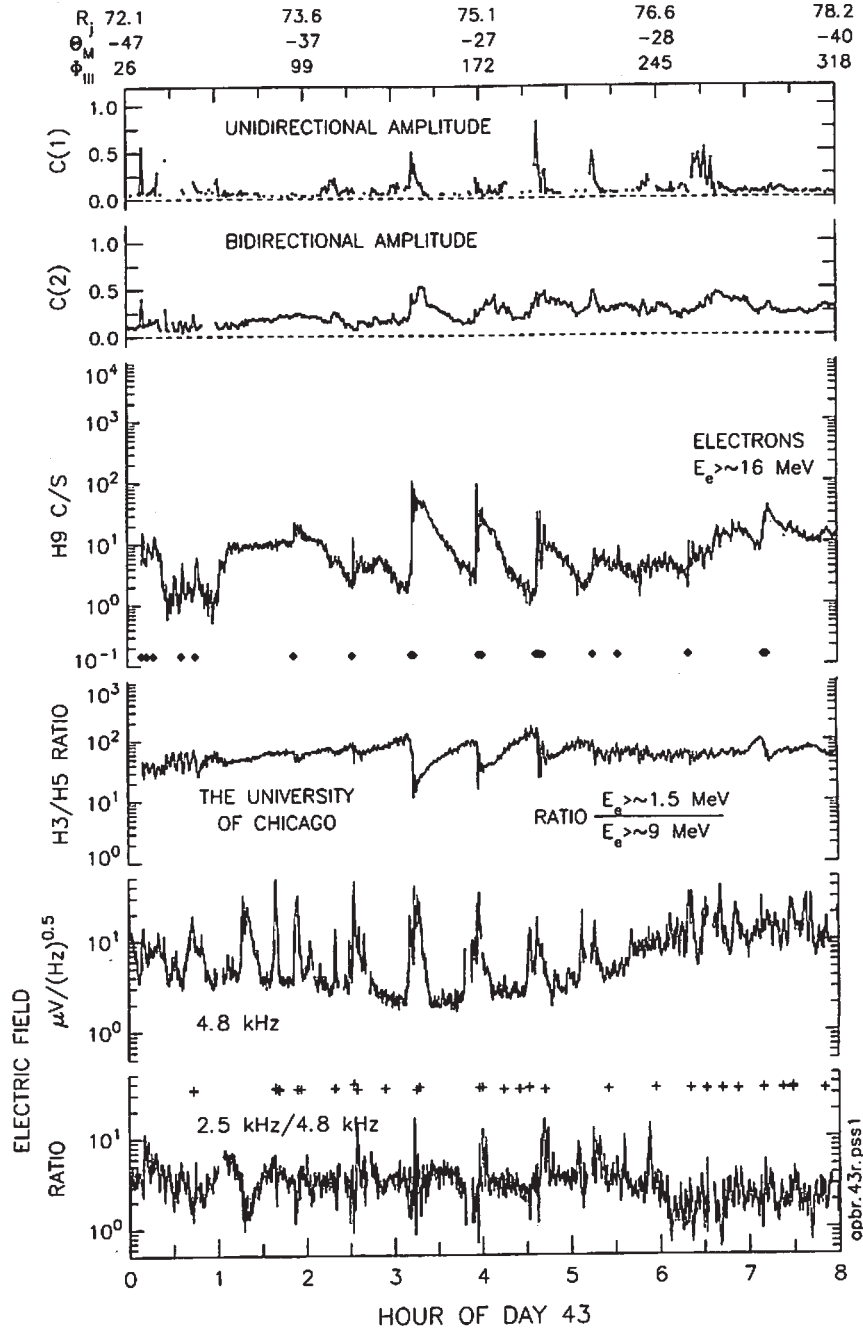


**Figure 1.21:** Radio and electron observations for a period including the large 40-min periodic electron bursts (McKibben et al., 1993). The H9 counting rate corresponds to electrons more than 16 MeV, and the H3/H5 ratio corresponds to the ratio of counting rates for electrons more than 1.5 MeV (H3) and more than 9 MeV (H5). Each measurement is accumulated over an average of 16-s period. The two top panels show 64-s average anisotropy amplitudes for more than  $\sim 3$  MeV electrons (H7S), based on a fit to a function of the form  $C = C(0)[1 + C(1) \cos(\phi - \phi_1) + C(2) \cos 2(\phi - \phi_2)]$ . Anisotropy amplitudes are plotted only if the amplitude differs from zero by more than  $3\sigma$  as determined from the fit. Diamonds indicate times for electron bursts identified as discussed in the text, and plus signs (+) indicate times for radio bursts as identified by MacDowall et al. (1993). Radio observations are shown in the lower two panels as the magnitude of the measured oscillating electric field at a frequency of  $\sim 4.8$  kHz in units of  $\mu\text{V}\text{Hz}^{-1/2}$  and the ratio of the measured field at  $\sim 2.5$  kHz to that at  $\sim 4.8$  kHz

They suggested that the particles were energized by strong field-aligned potential drops, which were directed upward and downward from Jupiter, or wave heating in the polar magnetosphere.

### 1.3.3 Polar Auroral Hot Spots

The Chandra X-ray Observatory observed an X-ray “hot spot” pulsating with an approximately 45-min period (*Gladstone et al.*, 2002). Figure 1.22 represents polar projections of X-rays seen by Chandra and simultaneous far-ultraviolet images obtained by HST in *Gladstone et al.* (2002). The X-ray hot spot in the northern hemisphere is located significantly poleward inside the main oval, where magnetic field lines are connected to the outermost or external region of the magnetosphere. Light-curve and power-spectrum data are plotted in Figure 1.23, which indicates brightness variations in the northern hot spot. Spectral analyses revealed that the X-ray hot spot was pulsating with a period of  $\sim$ 45 minutes, which is close to the period of QP40 bursts. Studies based on theoretical approaches and X-ray spectroscopic observations suggested that the hot spot is excited by precipitations of the relativistic heavy magnetospheric ions (e.g., O<sup>6+</sup> and O<sup>7+</sup>) which are energized by large potential drops of more than 8 MV (*Cravens et al.*, 2003; *Elsner et al.*, 2005).

Based on the HST data, *Waite et al.* (2001) indicated a spot-like UV auroral “flare”, which was located at the polar cap region quite close to the spot in X-ray wavelengths. As indicated in Figure 1.24, the flare was brightened transiently to a peak brightness of 37 MR followed by an exponential decline on a time scale of tens to hundreds of seconds. It should be noted that periodicity of the brightness was not detected due to short observation windows of a few minutes.

*Pryor et al.* (2005) performed simultaneous observations of ultraviolet spectroscopy for polar UV aurora with the Jovian VLF radio emissions by using the Ultraviolet Imaging Spectrograph (UVIS) onboard Cassini and the Plasma Wave Subsystem (PWS) onboard Galileo. Positive correlations were detected between QP bursts at VLF range and polar

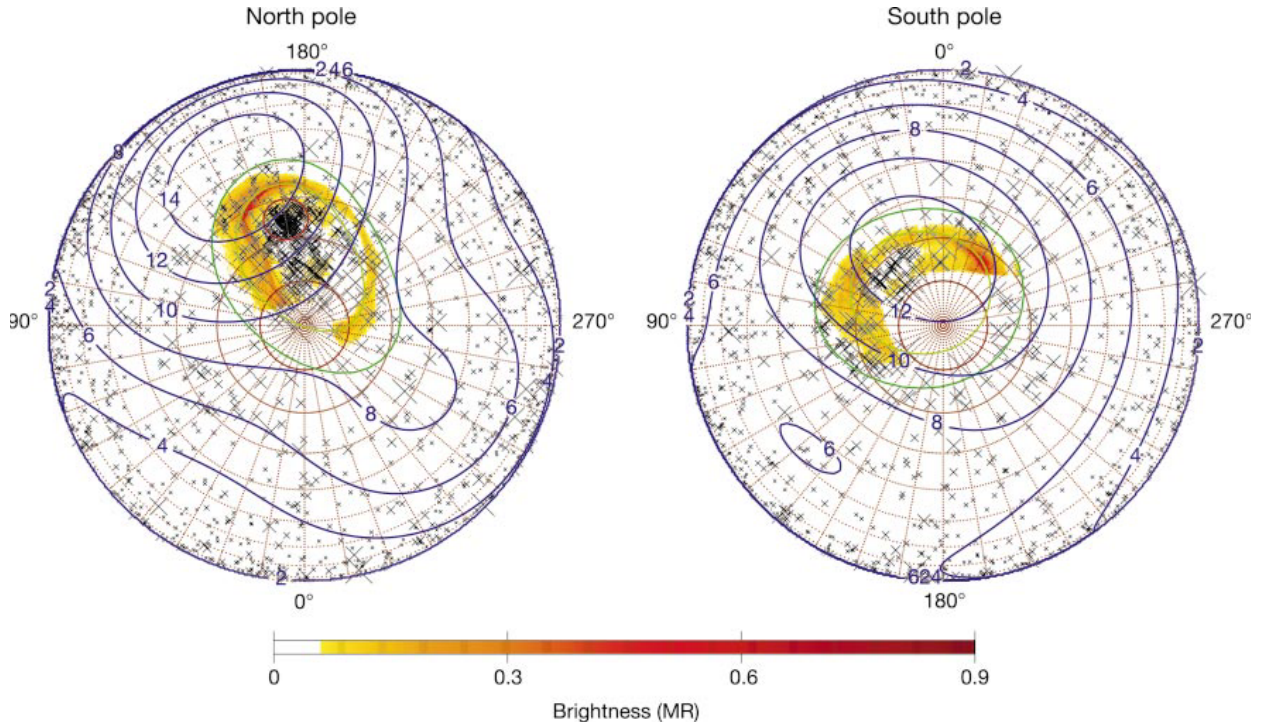


**Figure 1.22:** Polar projections of X-rays seen by Chandra and simultaneous far-ultraviolet images obtained by the Hubble Space Telescope (Gladstone et al., 2002). The mapped locations of individual X-ray photons (crosses) are overlaid on averages of several northern (left) and southern (right) auroral images made with the Hubble Space Telescope imaging spectrograph (HST-STIS) during 10–20 UT on 18 December 2000. The mapping assumes that the X-ray and ultraviolet auroras peak in emission at 240 km above the 1-bar pressure level. The size of each cross gives an approximate indication of the uncertainty in location of the corresponding X-ray photon, and only photons with emission angles of  $<85^\circ$  are shown. The HST-STIS images made with the 25MAMA filter are displayed in false color with auroral H<sub>2</sub> emission brightnesses in megarayleighs (MR) as indicated by the color bar. Surface VIP4 model magnetic field strength contours are shown for comparison (dark blue). The  $L = 5.9$  and  $L = 30$  footprints of the VIP4 model magnetosphere are also included (outer and inner green ovals, respectively), and a  $10^\circ$  graticule (brown dotted lines) with system III longitudes labeled. Most of the northern auroral X-rays are unexpectedly located well within the main far-ultraviolet oval and are coincident with the polar-cap far-ultraviolet emissions. The red circle in the northern auroral plot (left) shows the region defined for the hot spot used in the timing analysis. The apparent increase in X-rays toward the equator is an artifact of the polar projection.

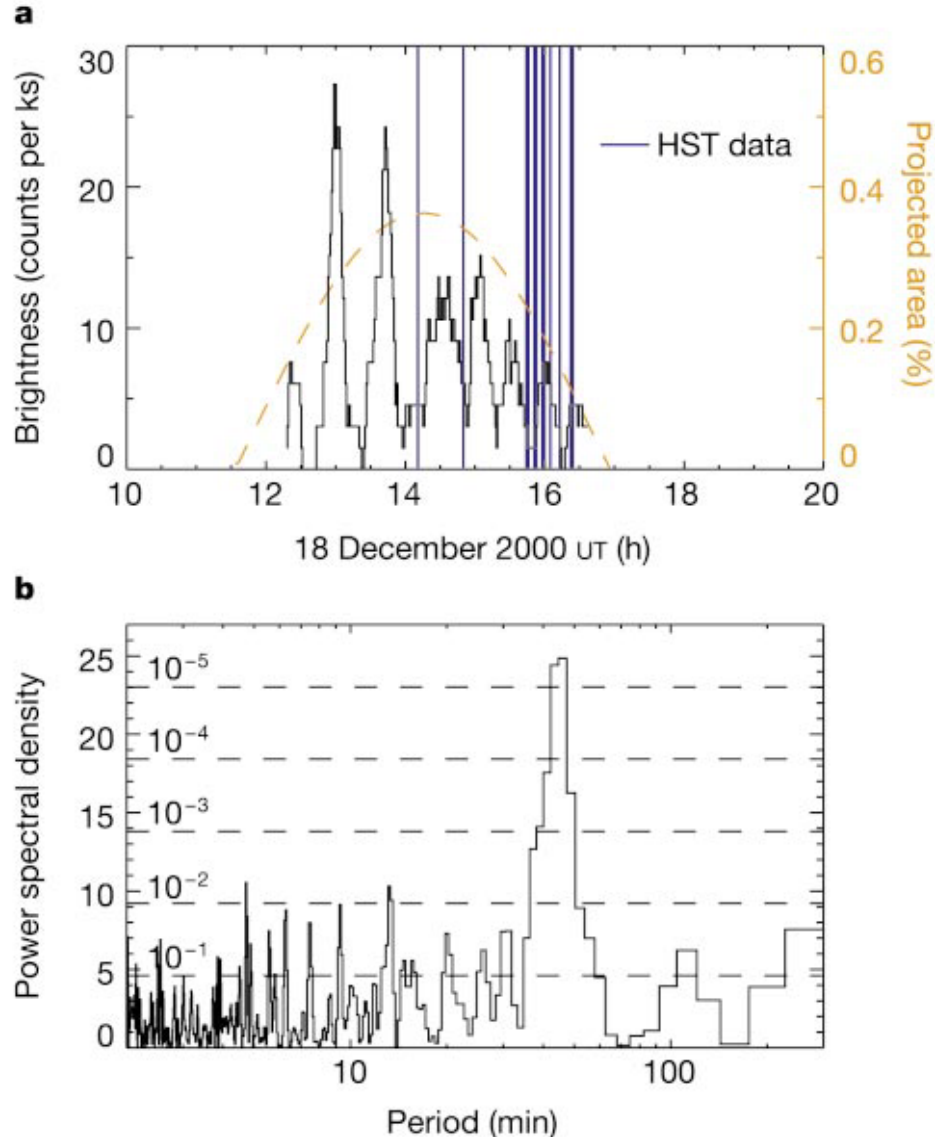


**Figure 1.23:** Light-curve and power-spectrum data for the auroral hot spot (Gladstone et al., 2002). (a) Light curve showing the X-ray count rate measured by Chandra as a function of time for the auroral hot spot. Here we defined the hot spot region to include only those X-rays emitted within a  $5^{\circ}$ -radius circle centered on a latitude of  $65^{\circ}$  and a system III longitude of  $170^{\circ}$  (as shown by the red circle in Figure 1.22). The total number of X-rays emitted from this region is 113, and the plot shows an 11-min boxcar smoothing of a 1-min binning of the data. The orange dashed line shows the projected area of the hot spot (as a percentage of the projected area of Jupiter). The times of the HST-STIS northern auroral region images shown in Figure 1.22 are indicated by vertical purple lines. Unfortunately, no images were obtained during any of the bright X-ray pulses. (b) Power spectrum of the hot spot signal, normalized so that, if the photons were randomly distributed over the visibility period, the mean power spectral density of any particular frequency bin would be expected to have a value of 2. The peak at a period of approximately 45 min is clearly seen. The peak at 300 min is associated with the approximately 600-min rotation period of Jupiter. The dashed lines are labeled with the probability of a random signal exceeding that level in a particular frequency bin (for example, the 45-min period peak has a  $4 \times 10^{-6}$  likelihood of having been attained at random).

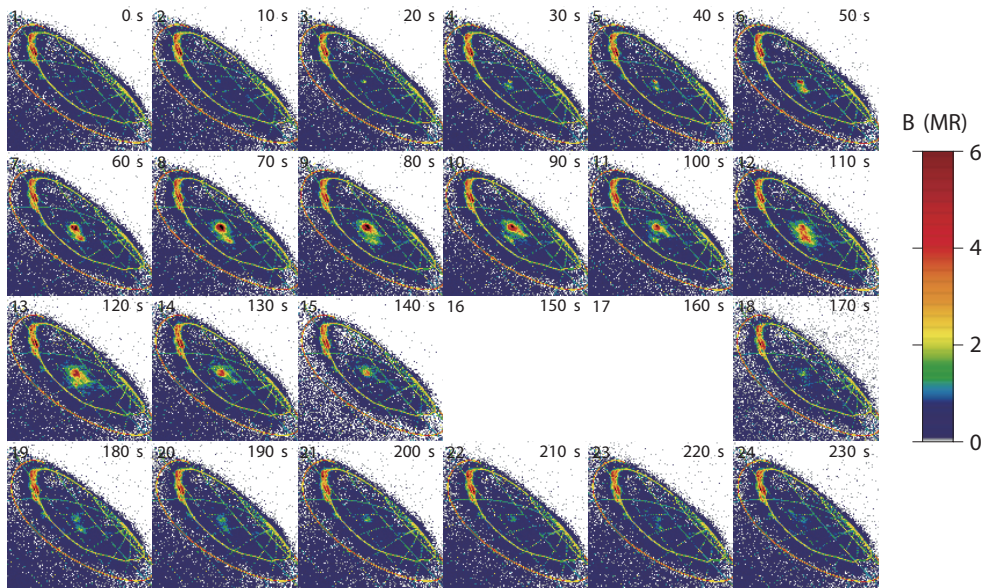


**Figure 1.24:** The rapidly evolving auroral flare observed poleward of Jupiter’s auroral oval (Waite et al., 2001). The time series shows the evolution of the flare beginning at 21:04:50 UT on 21 September. Ten-second frames are used, and the brightness scale is as indicated (with brightnesses clipped at 6 MR). The peak brightness of the flare at the 70-s frame is 37 MR (total H<sub>2</sub> + H emissions).

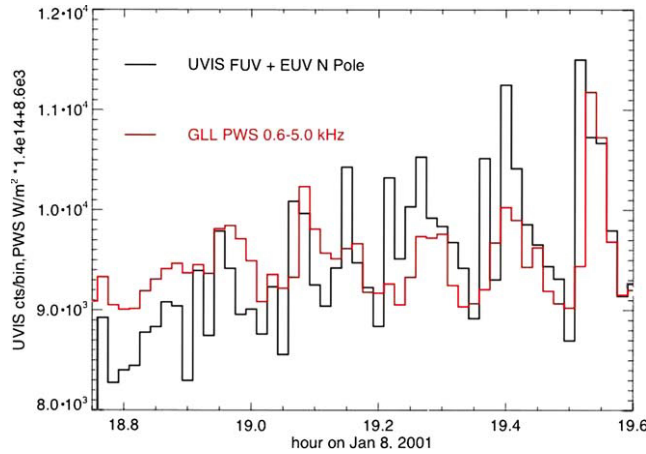


**Figure 1.25:** The sum of the EUV and FUV H<sub>2</sub> bands counts from the northern auroral zone are compared with the Galileo PWS radio signal from 0.6 to 5.0 kHz for the period 2001 day 8 18.75–19.6 h (Pryor et al. (2005)).

UV brightness (see Figure 1.25).

Grodent et al. (2004) also detected UV auroral spots in the nightside polar cap region (Figure 1.26). They indicated the multiple spots brightened in a similar manner to the flare in Waite et al. (2001) and suggested that source field lines of these UV spots are located at the distant tail region of the magnetosphere, where the plasmoid ejections are initiated by the tail reconnections as indicated in Section 1.1. The periodicity was also not detected because of the short observation windows.

Flasar et al. (2004) and Kunde et al. (2004) represented the spectroscopic imaging in mid-infrared (mid-IR) wavelengths performed by the Composite Infrared Spectrometer (CIRS) onboard Cassini during Cassini’s closest approach to Jupiter. They retrieved vertical profiles of atmospheric temperature from the mid-infrared spectrum of Jovian atmosphere by means of a constrained inversion. Figure 1.27 show the retrieved temperature maps at altitudes of 1-mbar (a) and 4-mbar (b) level. This result indicates that a spot of thermal-infrared emission is localized in the polar region at an altitude of the stratosphere. Kunde et al. (2004) suggested that the thermal emission spot corresponds to hydrocarbon atmospheres (e.g., methane CH<sub>4</sub>, acetylene C<sub>2</sub>H<sub>2</sub>) heated by the precipitating particles into the stratosphere or Joule heating by the ionospheric currents which are responsible for

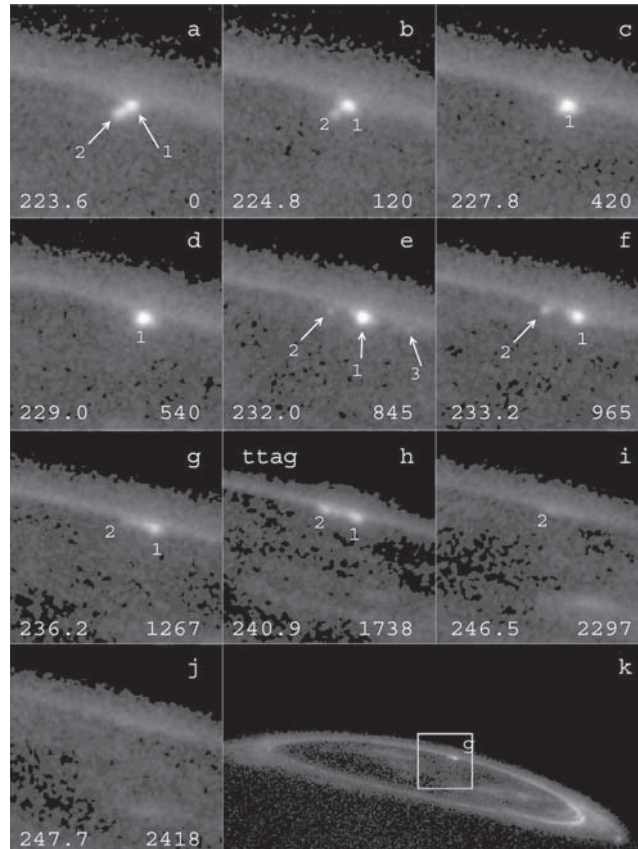


**Figure 1.26:** Evolution of the morphology of the nightside polar spot (NPS) in the STIS data set obtained on 18 December 2000 (Grodent *et al.*, 2004). Distinct spots are marked with ID numbers 1, 2, and 3. The number in the bottom left corner of each panel is the CML at mid exposure, and the bottom right corner number gives the time spanned (in seconds) since the first image of the series (panel (a)). The image displayed in panel (h) was obtained in time tagged mode with an additional filter. Panel (k) shows the limits of the zoomed sector appearing in panel (g).

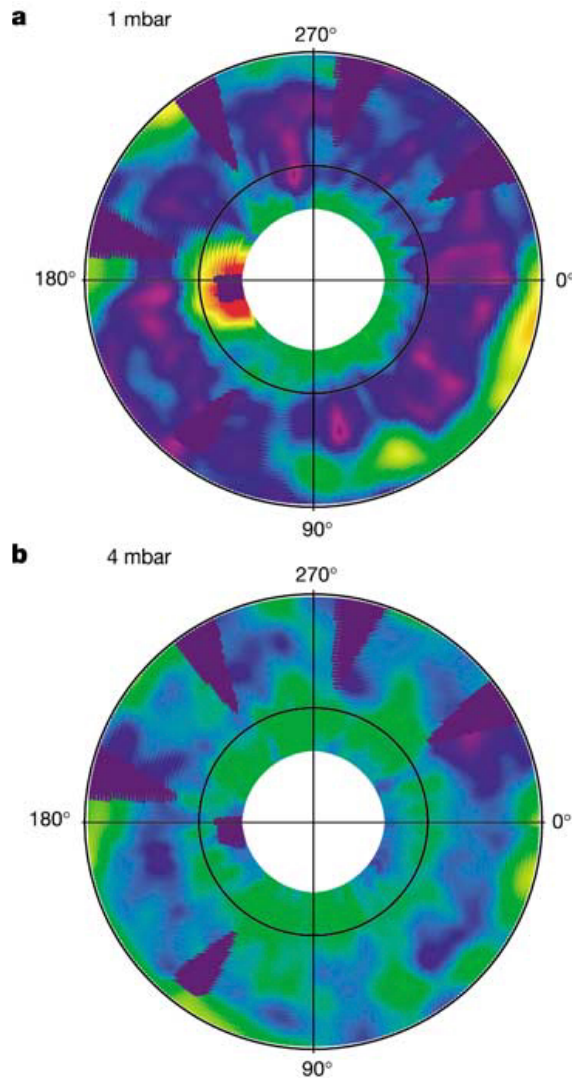


**Figure 1.27:** North-polar projection of temperatures shows a hot spot high in the stratosphere (Flasar et al., 2004). The hot spot is seen at the 1-mbar level (a), but not at the 4-mbar level (b). This is from the 1 January 2001 mapping sequence. Latitude circles are at 60° N and 30° N. In the rainbow color scale, red to purple span 185 K to 160 K. Although the hot spot is strongly evident in the 1-mbar map, there is an ambiguity as to whether it actually extends down to this level. This is because the emission in the Q-branch of the  $\nu_4$  band of CH<sub>4</sub> near 1,304 cm<sup>-1</sup>, used in the temperature retrievals, can be markedly influenced by hotter temperatures at altitudes up to the 1-mbar level. Hence, the black region within the hot spot reflects this ambiguity and not a lack of data.

auroral emissions. The IR hot spot is also close to the X-ray and UV hot spots. It should be noted that no periodicity was detected in the IR hot spot because of long integration time of the CIRS.

## 1.4 Purpose of This Thesis

This thesis aims to associate properties of planetary radio emissions with particle accelerations and dynamics of planetary magnetospheres. As indicated in Section 1.3, the observations of electrons, protons, and auroras in multi-spectra (X-ray, ultraviolet, and infrared) imply existence of relativistic particle acceleration processes, which are possibly accompanied by quasi-periodic radio emissions in the polar region of Jupiter. Although the detailed observations and theoretical studies have been performed, the following problems are still outstanding:

1. Source location of quasi-periodic radio bursts
2. Propagation process of quasi-periodic radio bursts
3. Microscopic wave generation mechanism of quasi-periodic radio bursts
4. Periodic particle acceleration process in a relativistic energy range responsible for the quasi-periodic phenomena
5. Corresponding macroscopic dynamics of the Jovian magnetosphere

This thesis addressed the problems based on the following approaches:

- Analyze dependence of QP radio bursts' occurrence on geometric parameters using wave data from Ulysses, Galileo, and Cassini (Chapter 3)
- Analyze polarization properties and source directions using the data measured by Ulysses and Cassini (Chapter 4)

- Interpret the source location and propagation process of the observed QP bursts using the modeling technique of ray paths; i.e., ray tracing (Chapter 5)
- Propose microscopic scenarios for the generation mechanisms of QP radio bursts and verify the scenarios based on wave generation theories (Section 6.1)
- Propose macroscopic scenarios for the quasi-periodic particle acceleration and verify the scenarios based on *in-situ* observation data of Galileo and Ulysses (Section 6.2)

The approaches are expected to reveal the propagation and generation of quasi-periodic radio bursts and to constrain the relativistic particle acceleration process. In addition, this thesis contributes to giving further significance of the planetary radio emissions as probes for dynamics and particle accelerations in the planetary magnetospheres and to discussions on universal particle accelerations in the space plasmas.



# Chapter 2

## Instrumentation and Datasets

### 2.1 Instrumentation

#### 2.1.1 Ulysses Spacecraft

##### The URAP

Data used in the present study are spectral densities observed by the Radio Astronomy Receiver (RAR) of the Unified Radio And Plasma Wave Experiment (URAP) onboard Ulysses (Stone *et al.*, 1992). RAR consists of two receivers: one is the low frequency receiver with a frequency range of 1.25–48.5 kHz and the other is the high frequency receiver with a range of 52–940 kHz. Spectrum from 1.25 to 940 kHz is obtained every 144 sec. The wave spectral data are available from the Ulysses Data System (UDS), ESA. Direction finding and polarization measurements were performed with use of RAR and antenna system of Ulysses. Polarization and source direction data and analysis tool were provided by courtesy of Dr. R. MacDowall, Principal Investigator of URAP, and Dr. R. Hess at Goddard Space Flight Center, NASA. Detailed principles of direction finding and polarization measurement of RAR are described in the appendix of Ladreiter *et al.* (1994).

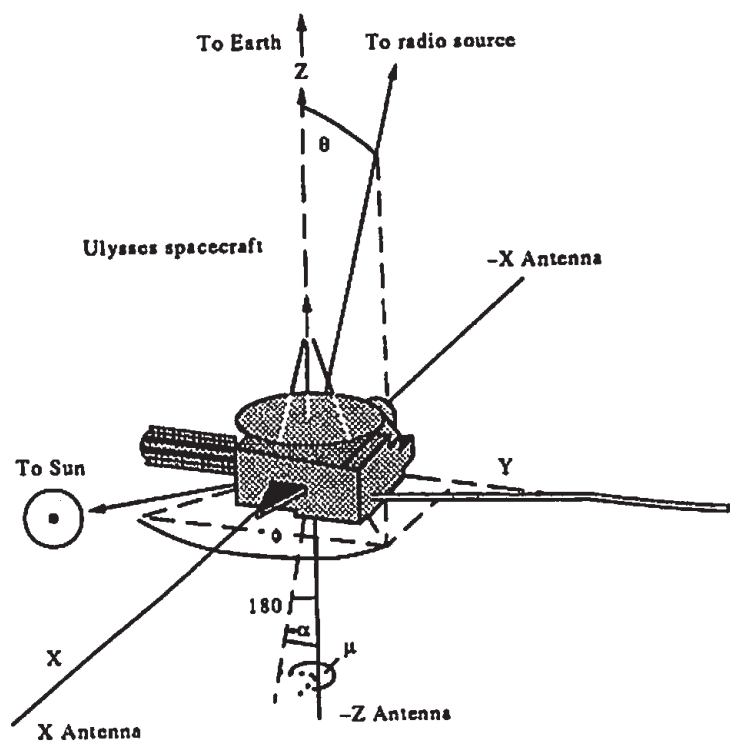


**Figure 2.1:** A schematic of the Ulysses spacecraft and spacecraft coordinate (Ladreiter et al., 1994).

**Table 2.1:** Characteristics of the Unified Radio and Plasma experiment (Stone et al., 1992)

### The SWOOPS

Solar wind parameters are also used in this study, obtained by the instrument of the Solar Wind Observations Over the Poles of the Sun (SWOOPS) (*Bame et al.*, 1992). Bulk velocity, number density, and temperature are derived from the velocity distribution of solar wind plasma observed by SWOOPS. These data are also available from the UDS. In the present analysis, these solar wind parameters were plotted as average values with a time resolution of 1 hour.

For the direct comparison of daily solar wind fluctuations with Jovian radio components, the propagation time of the solar wind from an observer to Jupiter was extrapolated. The extrapolation was performed based on the ballistic method adopted by *Morioka and Tsuchiya* (1996). Solar wind data was corrected by the following equation:

$$\Delta t = \frac{\Delta R}{V_{SW}} + \frac{\Delta\phi}{\Omega_S} \quad (2.1)$$

where  $\Delta R$  is radial distance of an observer from Jupiter's orbit,  $\Delta\phi$  is angular separation between the observer and Jupiter in heliocentric longitude,  $V_{SW}$  is radial velocity of the solar wind, and  $\Omega_S$  is angular velocity of solar rotation( $14.1^\circ/\text{day}$ ). The time when solar wind arrived at Jupiter is extrapolated by adding  $\Delta t$  to the observation time of solar wind.

### The FGM/VHM

Data of the interplanetary magnetic field (IMF) were observed by the Vector Helium Magnetometer/Flux Gate Magnetometer (VHM/FGM) of Ulysses (*Balogh et al.*, 1992). One minute averages of the magnetic field are available from the UDS. Dynamic range and resolution of VHM/FGM are summarized in Table 2.2. One-hour averaged data were plotted with the solar wind data observed by SWOOPS in the present analysis.

**Table 2.2:** Performance characteristics of Ulysses' magnetometer (*Balogh et al.*, 1992)

INSTRUMENT	RANGES	RESOLUTION
Vector Helium Magnetometer	+/- 8.192 nT +/- 65.52 nT	4.0 pT 32.0 pT
Fluxgate Magnetometer	+/- 8.00 nT +/- 64.0 nT +/- 2.048 μT +/- 44.0 μT	3.9 pT 31.2 pT 1.0 nT 21.5 nT

### 2.1.2 Galileo Spacecraft

#### The PWS

The Plasma Wave Subsystem (PWS) (*Gurnett et al.*, 1992) onboard the Galileo spacecraft has three spectrum analyzers (low-, medium-, and high-frequency bands), which provide survey spectra of the wave electric field from 5.6 Hz to 5.6 MHz with a time resolution of 18.67 sec. Characteristics of PWS are summarized in Table 2.3. We used the PWS data available from the Planetary Data System (PDS), NASA.

#### The MAG

Fluctuation of the Jovian magnetosphere relevant to the QP phenomena was investigated based on the magnetic field observed by the Magnetometer (MAG) (*Kivelson et al.*, 1992) onboard Galileo. The MAG data are also available from the PDS. Most of the data used for the present analysis corresponds to Real-Time Survey (RTS) data, which were typically sampled every 24 seconds in the magnetospheric survey mode of Galileo. For spectral investigation, we calculated the data with an average time resolution of 1 min from the RTS data. Table 2.4 indicates characteristics of MAG including the dynamic range.

**Table 2.3:** Characteristics of the Plasma Wave Subsystem (*Gurnett et al.*, 1992)

Plasma wave instrument characteristics		
Parameter	Characteristic	
Frequency range, electric	5.62 Hz to 5.65 MHz	
Frequency range, magnetic	5.62 Hz to 160 kHz	
Frequency resolution	(Low freq.) 5.62 Hz to 31.1 Hz, $\Delta f/f \simeq 67\%$ (Med. freq.) 40 Hz to 160 kHz, $\Delta f/f \simeq 8\%$ (High freq.) 100 kHz to 5.65 MHz, $\Delta f/f \simeq 10\%$	
Time resolution	(Low freq.) 5.62 Hz to 31.1 Hz, $\Delta t = 2.67$ s (Med. freq.) 40 Hz to 160 kHz, $\Delta t = 18.67$ s (High freq.) 100 kHz to 5.65 MHz, $\Delta t = 18.67$ s	
Sensitivity, electric	$E/\sqrt{\Delta f} \simeq 15$ nV m <sup>-1</sup> Hz <sup>-1/2</sup> at $\sim 10$ kHz	
Sensitivity, magnetic	$B/\sqrt{\Delta f} \simeq 50$ $\mu\gamma$ Hz <sup>-1/2</sup> at $\sim 100$ Hz decreasing to $\simeq 3$ $\mu\gamma$ Hz <sup>-1/2</sup> at 20 kHz	
Dynamic range	5.62 Hz to 31.1 Hz, 110 db 40 Hz to 5.65 MHz, 100 db	
Wideband waveform modes	Mode 1, 50 Hz to 10 kHz Mode 2, 50 Hz to 80 kHz Mode 3, 5 Hz to 1 kHz	
Waveform resolution	Mode 1, 4-bits, 25 200 samples s <sup>-1</sup> Mode 2, 4-bits, 201 600 samples s <sup>-1</sup> Mode 3, 4-bits, 3150 samples s <sup>-1</sup>	
Mass	Main electronics box	3.94 kg
	Search coil	1.52
	Electric antenna	1.68
	Total	7.14 kg
Power	6.80 W, heater power 3.0 W	

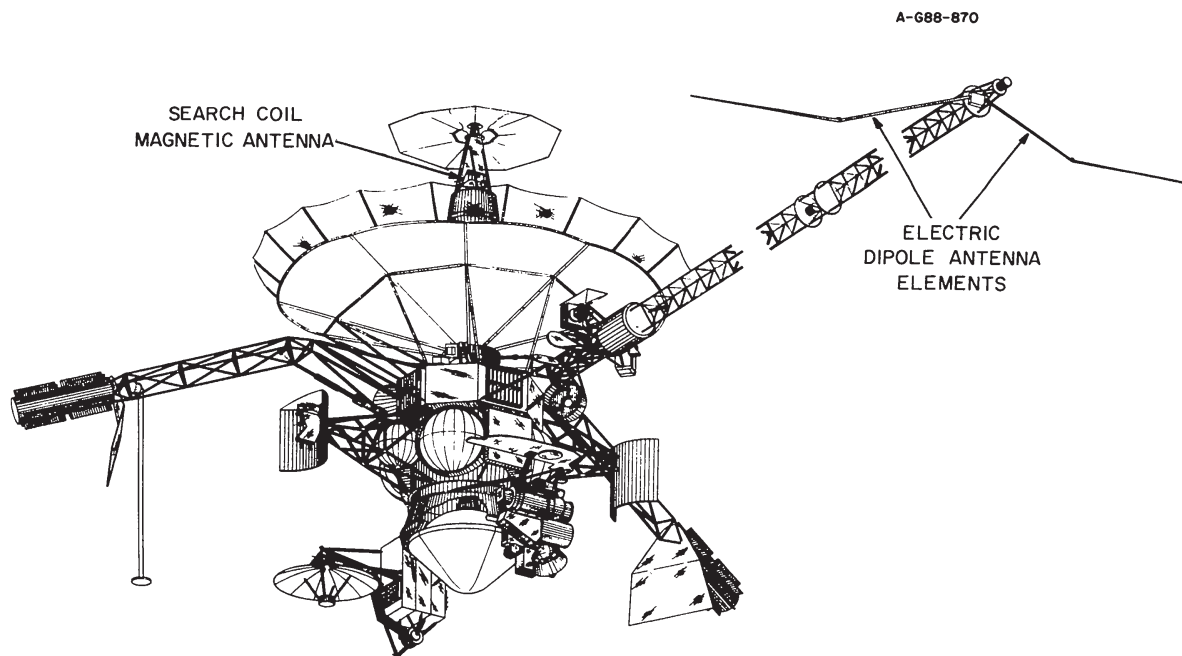


**Figure 2.2:** A schematic of the Galileo spacecraft and electric dipole antenna elements of PWS (Gurnett et al., 1992).

**Table 2.4:** Characteristics of Galileo's magnetometer (Kivelson et al., 1992)

Sensors	
Mass	0.72 kg
Dimensions	8.1 cm (diameter), 16.0 cm (length)
Power	4.35 W for 4 min to activate flip
Electronics	
Mass	3.98 kg
Volume	14.6 × 17.8 × 41.8 (cm) <sup>3</sup>
Power	3.9 W
Dynamic Range	
Inboard magnetometer	± 512 nT and ± 16,384 nT
Outboard magnetometer	± 32 nT and ± 512 nT

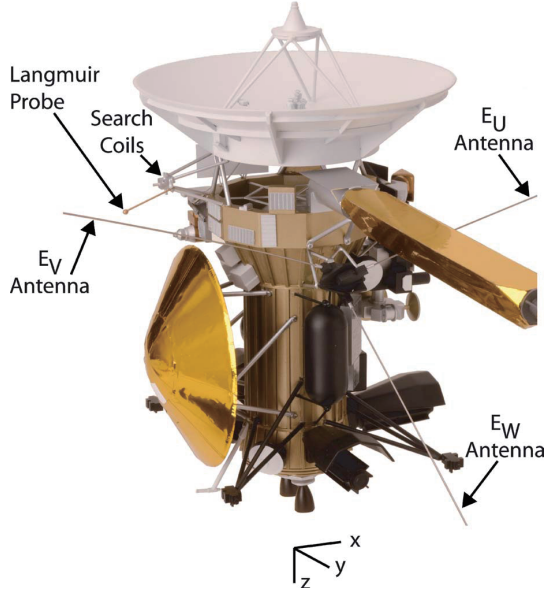


**Figure 2.3:** A schematic of the Cassini spacecraft and its electric monopole antenna system (Gurnett *et al.*, 2004). Three axes of the spacecraft coordinate are depicted below the spacecraft.

### 2.1.3 Cassini Spacecraft

#### The RPWS

The Radio and Plasma Wave Science Investigation (RPWS) has the High Frequency Receiver (HFR), which measures electric field spectra over a frequency range from 3.5 kHz to 16.125 MHz with three monopole electric antennae ( $E_u, E_v, E_w$ ). The time resolution is ranging from 0.1 to 10 sec per one spectrum. The HFR derives polarization and arrival directions of electromagnetic waves from measurements of complex auto- and cross-correlation functions between  $E_x$  ( $x = u, v$ ) and  $E_w$  antennae. Spectrum, polarization, and source direction data were provided by courtesy of Dr. P. Zarka, co-investigator of the RPWS, and Dr. B. Cecconi at Observatoire de Paris. Details for polarization and source direction measurements of Cassini are described in Chapter 4 and are also explained in *Ladreiter et al.* (1995).

**Table 2.5:** Characteristics of RPWS (*Gurnett et al., 2004*)

Receiver section	Measurements	Spectral range	Spectral resolution	Temporal resolution
High frequency receiver (HFR)	$E_1 = E_u, E_v$ or $E_x$ $E_2 = E_w;  E_1 ^2,  E_2 ^2, \text{Re}(E_1 \bullet E_2^*), \text{Im}(E_1 \bullet E_2^*)$	3.5–318 kHz 0.125–16.125 MHz	$\Delta f/f = 5, 10, 20\%$ (log); $\Delta f = 3.1$ kHz to $n \times 25$ kHz (linear)	0.1–10 s/spectrum
Medium frequency receiver (MFR)	One of: $E_x, E_u, E_v, E_w, B_x, B_z$	24–180 Hz; 180 Hz–1.5 kHz; 1.5–12 kHz	$\Delta f/f \approx 13\%$ ; $\Delta f/f \approx 7\%$ ; $\Delta f/f \approx 7\%$	16 s/spectrum; 16 s/spectrum; 8 s/spectrum
Five-channel waveform receiver (WFR)	Five of: $E_x, E_u, E_v, E_w, B_x, B_y, B_z$ , LP	$\sim 1$ –26 Hz; 3 Hz–2.5 kHz	0.2 Hz, typical; 3.5 Hz typical	1 data set/5 min, typical, 1 data set/16 s, max
Low frequency receiver (LFR)	Two of: $E_x, E_u, E_v, E_w, B_x, B_y, B_z$ , LP	$\sim 1$ –26 Hz	$\Delta f/f = 12\%$	$1E + 1B$ spectrum/16s, typical
Wideband receiver (WBR)	One of: $E_x, E_u, E_v, E_w, B_x$ , LP	60 Hz–10.5 kHz; 0.8–75 kHz	13.6 Hz, typical; 109 Hz, typical	125ms/spectrum, typical

## 2.2 Datasets

### 2.2.1 Ulysses Spacecraft

#### The first encounter with Jupiter

Ulysses, which is the spacecraft for exploration of the space above the poles of the sun, launched in October 1990. On 8 February, 1992, it made the first closest approach to Jupiter at the radial distance of  $\sim 6R_J$ , and entered the polar orbit of the sun by taking advantage of a gravity assist of the planet. Before the closest approach, Ulysses approached to Jupiter from the Jovian equatorial region in the noon sector (Jovigraphic latitude, JLAT $\sim 2^\circ$  and local time, LT $\sim 11$  hr), and after the closest approach, it fled away from the southern high latitudinal region of Jupiter in the dusk sector (JLAT $\sim -38^\circ$  and LT $\sim 18$  hours). The present analysis period spans  $\sim 1$  year from 1 September, 1991 to 1 September, 1992.

Ulysses' orbital parameters around the closest approach are plotted in Figure 2.4. The

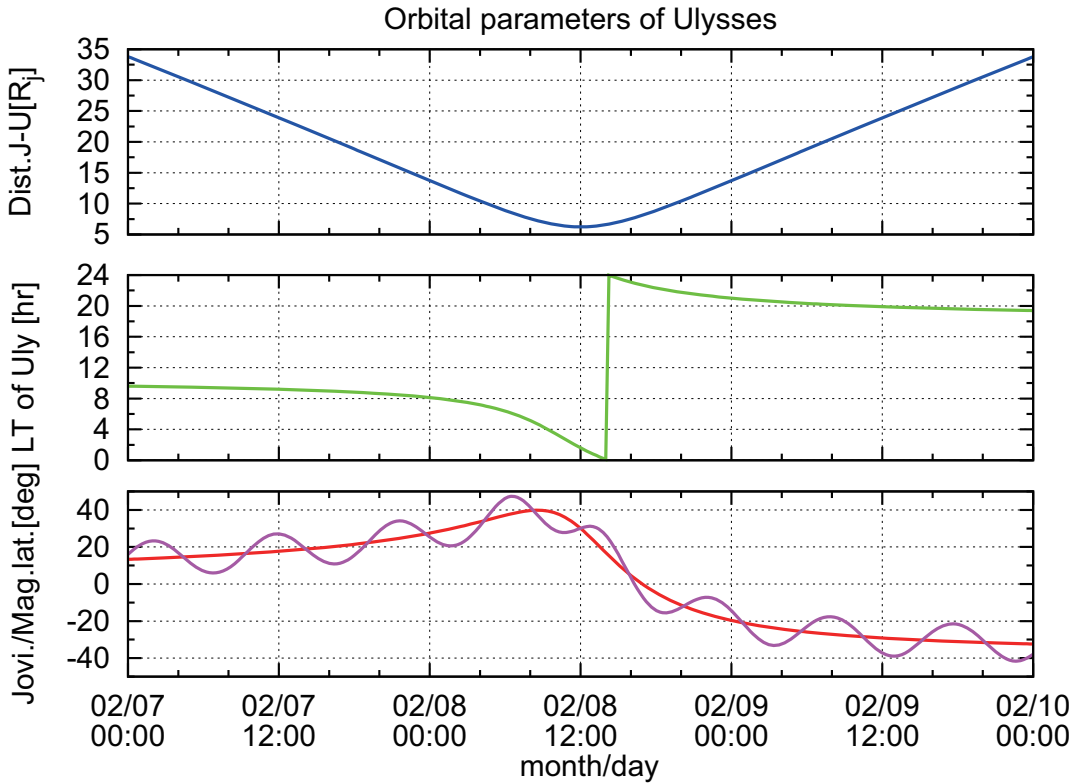


**Figure 2.4:** Orbital parameters of Ulysses during the first encounter with Jupiter in 1992. (top) Distance between Ulysses and Jupiter in Jovian radii,  $R_J$ . (middle) Local time seen from Jupiter and (bottom) Jovicentric (red line) and magnetic (violet) latitudes.

top panel represents the distance of Ulysses from Jupiter in Jovian radii,  $R_J$ . The green solid line in the middle panel corresponds to the local time of Ulysses as seen from Jupiter. The red and violet lines in the bottom panel are Jovicentric and magnetic latitudes of Ulysses.

### The second encounter with Jupiter

The analysis period for the observations at high latitudes spans 7 months from November 1, 2003 to May 31, 2004, and it included Ulysses' second closest encounter with Jupiter. Figure 2.5 shows the orbital parameters of Ulysses from November 1, 2003 to May 31, 2004. During this period, Ulysses flew at a distance of 0.80–1.22 AU from Jupiter, in the region of 11.1 to 17.5 hours local time. As is evident from Figure 2.5, Ulysses had an orbit from which it viewed Jupiter from north to the equatorial plane in the noon-dusk quadrant.

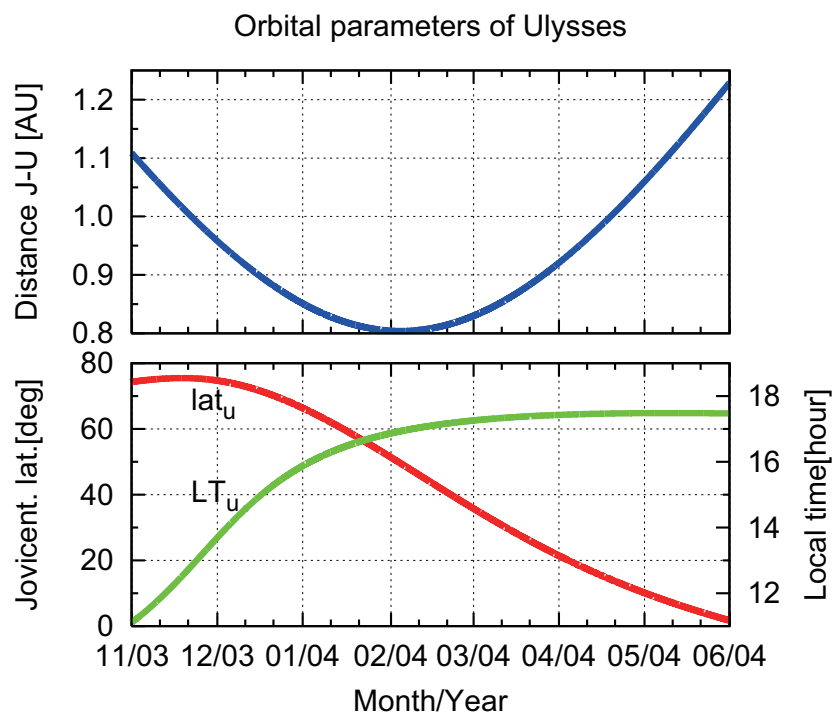


**Figure 2.5:** Orbital parameters of Ulysses during the second encounter with Jupiter in 2004. (top) Distance between Ulysses and Jupiter in AU. (bottom) Local time (green line) and Jovigraphic latitude (red line) of Ulysses seen from Jupiter.

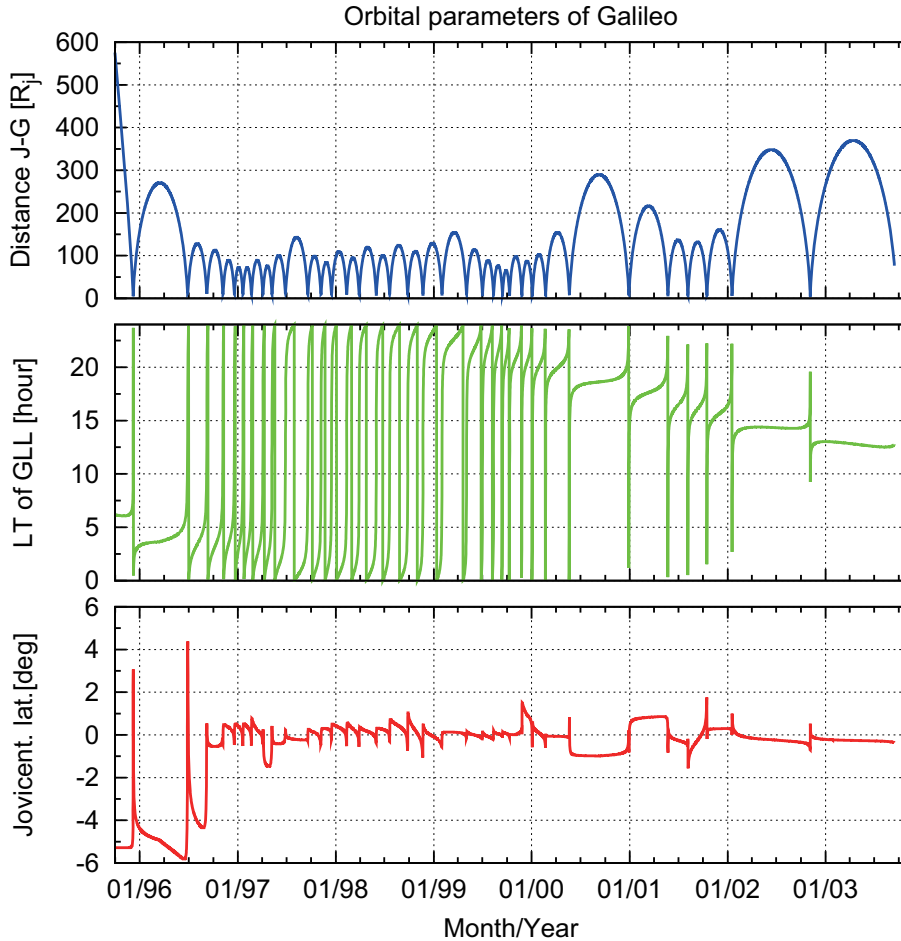


**Figure 2.6:** Orbital parameters of Galileo during its Jovian mission from 1995 to 2003. (top) Distance between Galileo and Jupiter in Jovian radii. (middle) Local time and (bottom) Jovigraphic latitude of Galileo seen from Jupiter.

## 2.2.2 Galileo Spacecraft

The period of analysis in this study includes all the orbits of Galileo around Jupiter (J00-J35) from December 1995 to September 2003. Orbital parameters of Galileo are plotted in Figure 2.6. During the Jovian mission of Galileo, it explored all local time in the equatorial region (Jovigraphic latitude within  $5^\circ$ ) at radial distances from  $\sim 2 R_J$  to  $\sim 370 R_J$ , however, the bulk of observations were performed in the nightside magnetosphere.

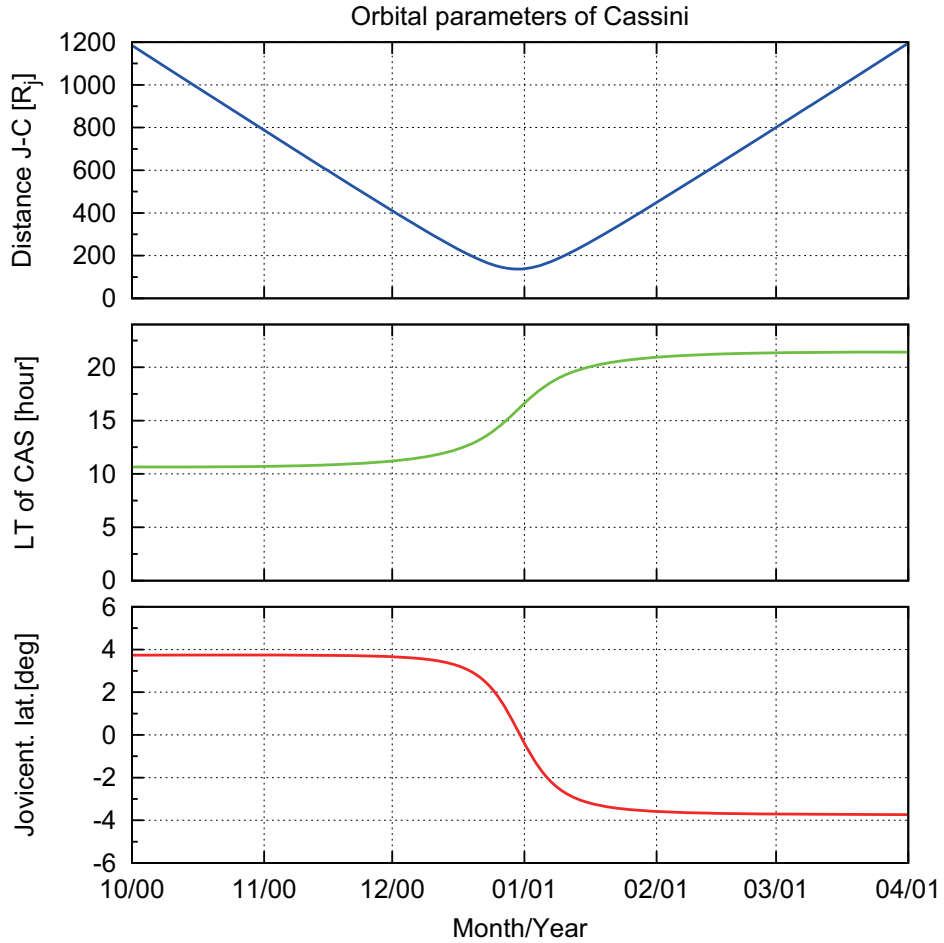


**Figure 2.7:** Orbital parameters of Cassini around its closest approach to Jupiter. (top) Distance between Cassini and Jupiter in Jovian radii. (middle) Local time and (bottom) Jovigraphic latitude of Cassini seen from Jupiter.

### 2.2.3 Cassini Spacecraft

The period of analysis for the Cassini data spans  $\sim$ 6 months from 1 October, 2000 to 31 March, 2001 including its closest approach to Jupiter. Figure 2.7 shows orbital parameters of Cassini. Cassini made the closest approach to Jupiter at the distance of  $137 R_J$  on 30 December, 2000 during its interplanetary cruise to Saturn. In the present analysis period, Cassini approached to Jupiter from the pre-noon sector ( $LT \sim 11$ ) and fled away from Jupiter in the pre-midnight sector ( $LT \sim 21$ ). Cassini was at Jovigraphic latitudes of  $|JLAT| < 4^\circ$  during the analysis period.



# Chapter 3

## Occurrence Characteristics

### 3.1 Detection of QP Bursts

#### 3.1.1 Detection from Ulysses' Data

To investigate the latitudinal and longitudinal distributions of the QP burst groups, the occurrence probabilities of the pulse groups were mapped with respect to geometric and temporal parameters. In this study, QP bursts were detected by visual inspections from dynamic spectrograms. Figure 3.1 is a dynamic spectrogram showing typical events of QP bursts observed by Ulysses at high latitudes. As is evident from Figure 3.1, QP bursts form groups of successive pulses. A group of QP burst pulses was treated as one event in a similar way to that of Morioka *et al.* (2006).

The analysis procedure was as follows: (1) a data point when QP burst groups were occurring was counted as one event, and a data point when URAP was operating was counted as one observation, (2) the number of event and the number of URAP operation were plotted on a map corresponding to the magnetic latitude and the System III longitude of the observer, (3) the occurrence probability with respect to a  $5^\circ \times 5^\circ$  bin was derived by dividing the number of event by the number of URAP operation. The detection criteria of a QP burst group were follows: (1) the peak spectral density of the pulse was 15 dB higher than the background level, (2) the width of the frequency range where the peak spectral

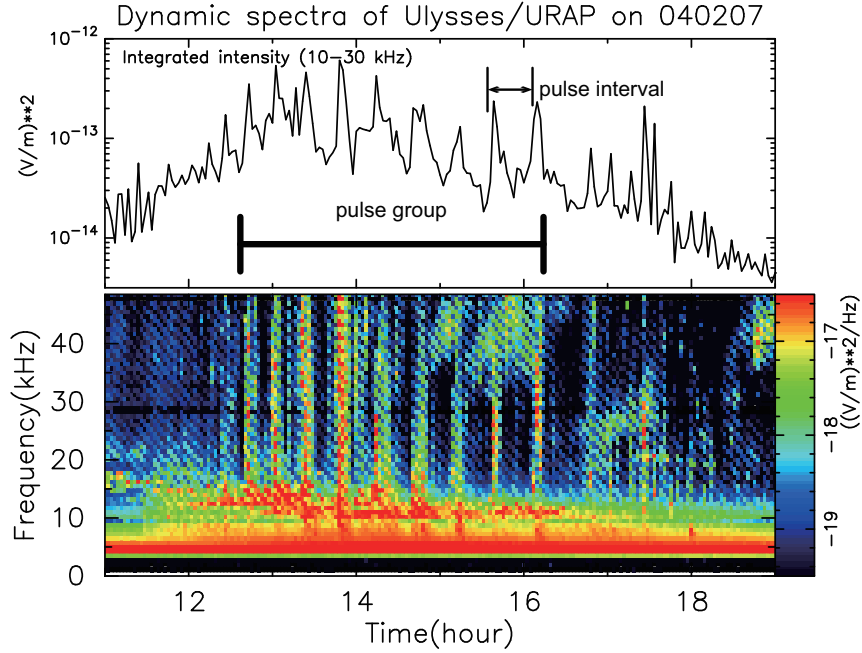


**Figure 3.1:** Dynamic spectrogram obtained by Ulysses/URAP on February 7, 2004. The lower spectrogram includes a typical example of quasi-periodic bursts forming a pulse group. The upper panel indicates the integrated spectral density plot in the frequency range of 10–30 kHz (Kimura et al., 2008b).

density is 15 dB higher than the background was more than 15 kHz. Based on these criteria, visual inspections identified 106 groups of QP bursts during the second encounter event and 147 events during the first encounter with Jupiter, corresponding to a cumulative visible time of  $\sim$ 17 and  $\sim$ 32 days for each.

### 3.1.2 Detection from Galileo's Data

Similar to the case for Ulysses, we counted a pulse group, which satisfies the following criteria, as one event: the spectral density of each pulse was 15 dB higher than the background noise level within a frequency range from 3 to 10 kHz. This frequency range is just above that of the trapped continuum, which are emitted from the inner magnetosphere with steep plasma density gradients and is trapped in the magnetosphere due to its frequency being lower than the plasma frequency at the magnetosheath (e.g., Kurth, 1992b). Thus, we consider that QP bursts detected in this study were not trapped in the magnetosphere

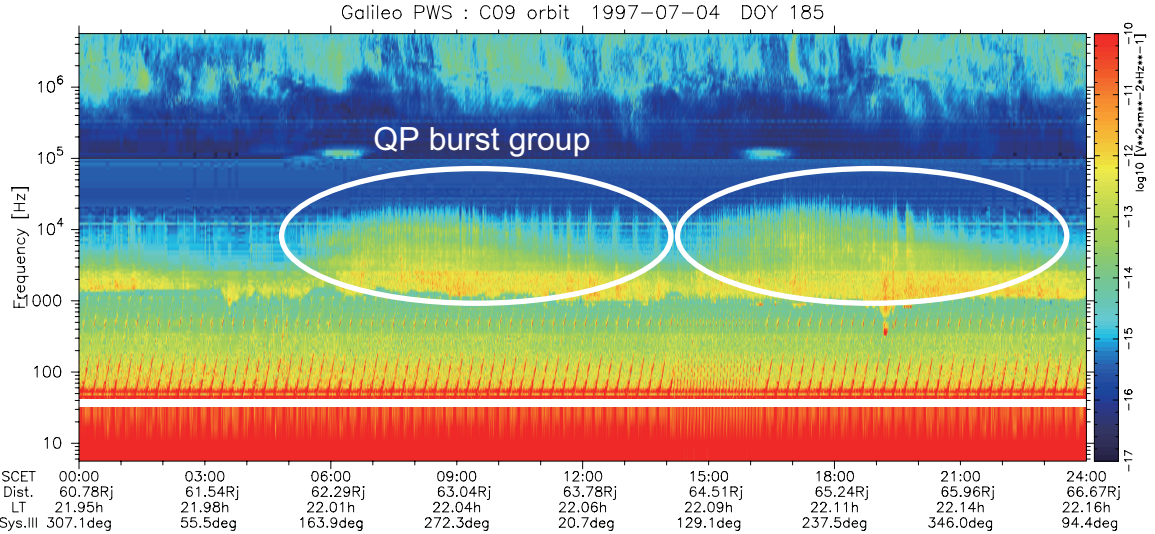


**Figure 3.2:** Dynamic spectrogram showing typical events of QP bursts forming pulse groups. Vertical and horizontal axes are frequency and time, respectively. Colors show the received spectral densities of wave electric field normalized to source location at  $10 R_J$  from Jupiter. Under spacecraft event times in the horizontal axis, orbital parameters of Galileo are indicated (Kimura et al., in press).

and could escape into the interplanetary space. Based on these criteria, we detected 214 groups of QP bursts corresponding to a cumulative visible time of  $\sim 44$  days. Figure 3.2 shows typical events of QP bursts observed by Galileo in the Jovian magnetosphere.

Distributions of the occurrence probability with respect to geometric parameters were calculated by dividing the number of events of the observed QP bursts by the data number of PWS operations. The derived occurrence probability is equivalent to the ratio of the QP bursts' visible time to the operation time of the PWS.

## 3.2 Occurrence Dependence on Longitude and Latitude

### 3.2.1 Occurrence Dependence Observed by Ulysses

Figure 3.3 shows the occurrence probability map obtained from Ulysses' data during the second encounter event. The horizontal axis in Figure 3.3a indicates the CML of Ulysses.

The upper panel shows the occurrence probability distribution with respect to the CML of the observer, and the lower panel shows the occurrence probability map with respect to the CML and the magnetic latitude of the observer. The color indicates the occurrence probability level. The black regions in the lower panel correspond to no observations, whereas the blue (red) regions indicate the lowest (highest) probability. The format of Figure 3.3b is similar to that of Figure 3.3a, except for the horizontal axis, which indicates the sub solar longitude (SSL) when the QP burst groups were observed. The SSL corresponds to the phase of planetary rotation with respect to the sun. As is evident from the upper panels, the occurrence probability distribution with respect to the CML exhibits roughly sinusoidal variations (the main component is in the range  $30^\circ < \text{CML} < 240^\circ$ ). However, the dependence on the SSL obviously has a rectangular distribution: the abrupt increase around  $\text{SSL} \sim 90^\circ$  remains quasi-constant till  $300^\circ$  and starts decreasing at  $300^\circ$ .

We did a  $\chi^2$  test under a null hypothesis that the occurrence dependence on each longitude has a flat distribution (i.e., the events at each longitude always occur with the same probability): the  $\chi^2$  value was 2170 for the case of CML and 2350 for the case of SSL (the degrees of freedom were 72, and the  $\chi^2$  values were derived from the distribution of the number of events). This result indicates that the dependence on the SSL is more deviated from a flat distribution than that of the CML: i.e., the QP burst groups are more dependent on the SSL than on the CML.

We consider the sinusoidal variation of the occurrence dependence on the CML resulted from the local time of the observer and the SSL dependence. During the second encounter event, Ulysses had a large amount of URAP operating time in the dayside, whereas in the nightside, it had little operation time. The relationship between the CML and SSL at a certain moment is given as follows:

$$\text{CML} = \text{SSL} - (LT - 12) \times 15^\circ \quad (3.1)$$

where LT is the local time of the observer in hours, and the CML and SSL are given in degrees. If observations are statistically performed in a particular LT sector, the angular

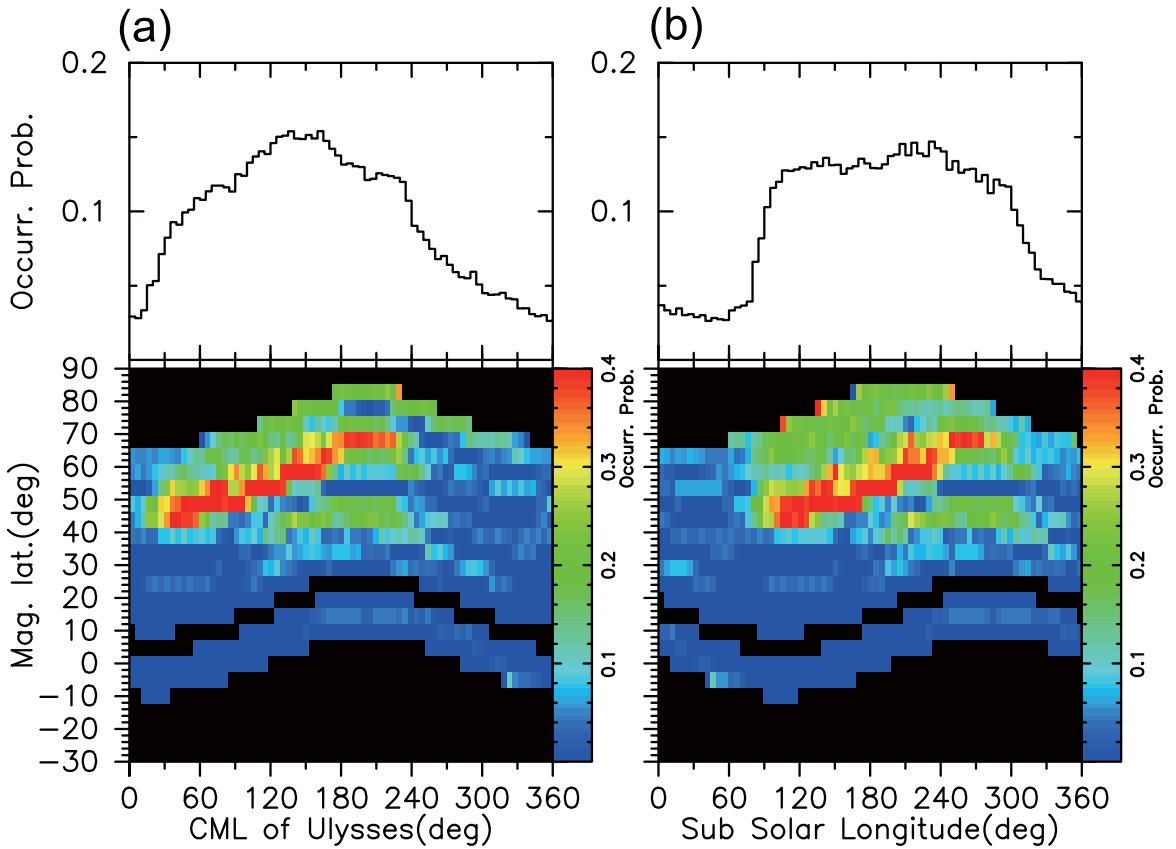
difference between the CML and SSL remains constant. Thus, we conclude that the CML dependence is an apparent variation, which resulted from the observational bias in local time and the SSL dependence. Thus, we interpret the sinusoidal CML distribution as an apparent one due to the SSL dependence and constant local time of the observer.

The lower panels of Figure 3.3 also show that the QP burst group is observed in latitudinal ranges from  $+30^\circ$  to  $\sim +90^\circ$ . It is speculated that the source location, directivity, and propagation process of QP bursts result in forming the latitudinal structure. In Chapter 5, we discuss these radiation conditions by comparing the observed latitudinal structure with the ray paths modeled using the ray tracing analysis.

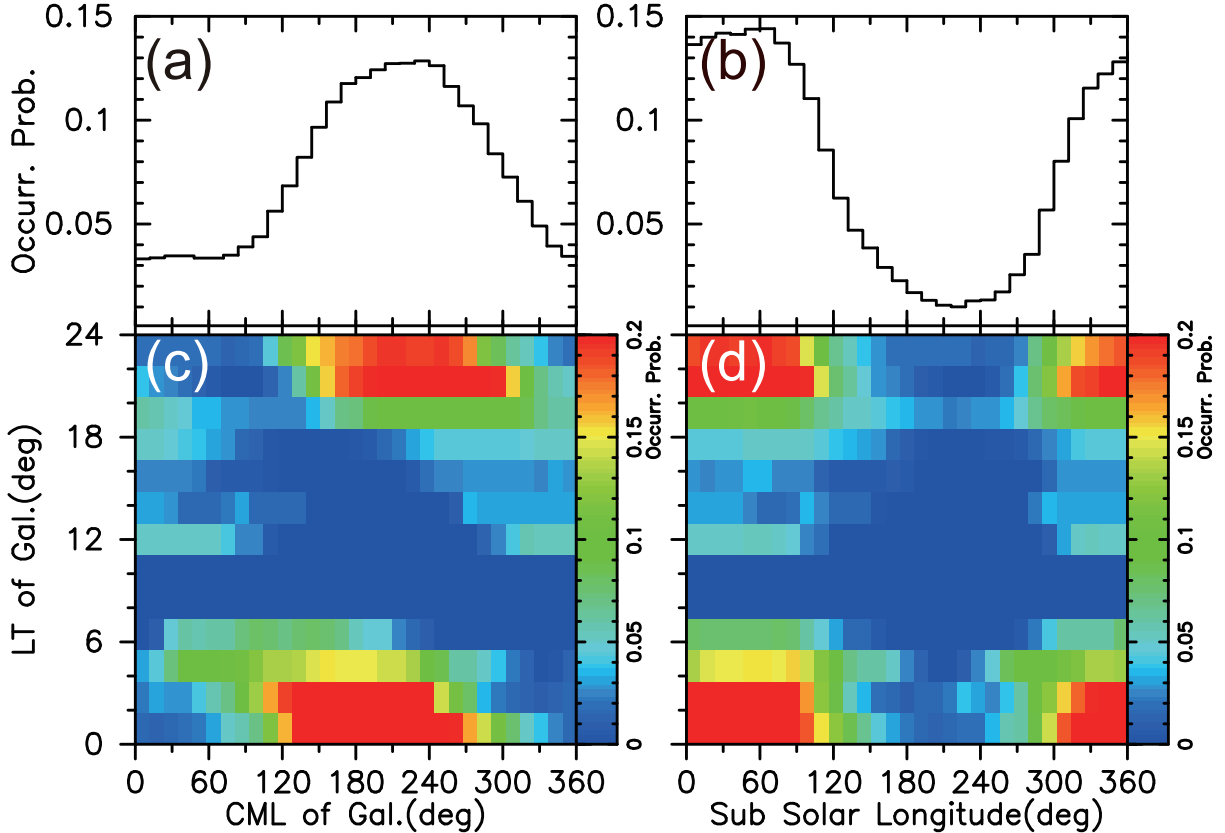
### 3.2.2 Occurrence Dependence Observed by Galileo

Figure 3.4a shows the occurrence probabilities with respect to the CML of the observer, and Figure 3.4b shows those with respect to SSL when QP bursts were observed. Longitudinal resolution was set to  $12^\circ$  in each panel. The sum of the PWS operating times at each bin is equivalent to  $\sim 19$  days. The visible time of QP bursts is derived by multiplying the operating time by the occurrence probability. Both distributions show quasi-sinusoidal dependencies with respect to the System III longitudes. Each distribution has high probabilities in a range of  $120^\circ$ – $330^\circ$  for the CML and  $300^\circ$ – $480^\circ$  for the SSL with a peak at  $CML \sim 210^\circ$  and  $SSL \sim 50^\circ$ . However, the difference between the maximum and minimum probabilities in the SSL dependence is relatively larger than that of the CML dependence (SSL: 0.134 and CML: 0.096).

We did a  $\chi^2$  test under a null hypothesis that the occurrence dependence on each longitude has a flat distribution in a similar way to that for the case of Ulysses. The  $\chi^2$  value was about 48,000 for CML and about 95,000 for SSL (the degrees of freedom were 29, and the  $\chi^2$  values were derived from the distribution of the number of events). These results indicate that the QP burst groups observed in the equatorial region are also more dependent on the planetary rotational phase than on the geometric relation between the observer and Jupiter. During the Jovian mission, Galileo had a large amount of PWS



**Figure 3.3:** A map of occurrence probability of the QP burst groups. (a) The horizontal axis in each panel indicates the CML of Ulysses. The upper panel shows the CML distribution of the probability of the QP burst groups. The lower panel is the CML vs. the magnetic latitude map of the occurrence probability. The color indicates the occurrence probability. The black regions correspond to the lack of observation, whereas the blue regions indicate the lowest probability. Figure 3.3b has a similar format to that of Figure 3.3a, but the horizontal axis is the sub solar Longitude (SSL) (Kimura et al., 2008b).



**Figure 3.4:** Distribution of QP bursts' occurrence probability with respect to temporal and geometric parameters. (a) Distribution with respect to CML of the observer and (b) that to subsolar longitude when QP bursts were observed. (c) A plot of occurrence probability with respect to CML and local time of the observer and (d) that to subsolar longitude and local time. Colors indicate occurrence probability. Blue region is the lowest probability (*Kimura et al., in press*).

**Table 3.1:** Chi-Square Values Derived from Longitudinal Dependence of QP Bursts

	Galileo (low lat.)	Ulysses (high lat.)
CML dependence	48,000	2,170
SSL dependence	95,000	2,350

operating time in the nightside, whereas in the dayside, it had less operation time (e.g., the operation time in 19–21 LT sector is equivalent to  $\sim$ 70 days, whereas 8.7 days in 9–11 LT sector). Thus, we conclude that the CML dependence in the equatorial region is also an apparent variation, which resulted from the observational bias in local time and the SSL dependence. Results of the  $\chi^2$  test for the case of Ulysses and Galileo were summarized in Table 3.1.

Figure 3.4c and d are plots indicating the distribution of occurrence probability with respect to the longitudes (CML and SSL) and local time of the observer. The colors indicate the occurrence probability, and the blue region is the lowest probability. Note that the QP bursts are absent not only in the pre-noon sector but rather in a 08h to 18h sector of local time. One can see that the peak of the SSL dependence remains constant (SSL $\sim$ 50°) with respect to the local time of the observer, while that of the CML dependence drifts continuously in local time. These figures indicate that occurrence of QP bursts is better organized by the SSL rather than by the CML. These results support the idea described in Section 3.2.1 that the CML dependence is an apparent variation resulting from the SSL dependence.

We interpret the absence of QP bursts in the dayside as caused by the “shadow zone” at a radial distance of  $<30 R_J$  and in the observations around noon, which were mostly conducted in the shadow zone (see the next section for more detail).

### 3.3 Occurrence Dependence on Radial Distance and Latitude

Figure 3.5a-c show the distribution of the occurrence probability of QP bursts plotted in a meridian plane. The vertical and horizontal axes in Figure 3.5a are parallel to the magnetic axis and magnetic equator, respectively. The colored portion indicates the occurrence probability, and the black region corresponds to the lack of observations. The spatial grid was set to  $3 \times 3 R_J$  in Figure 3.5a. Figure 3.5b indicates the distribution of the occurrence probability with respect to the radial distance, and Figure 3.5c is the distribution in the north-south direction. The spatial grids of these figures are also equivalent to  $3 R_J$ . Figure 3.5d-f show the number of data points of PWS operation time with similar formats to those of Figure 3.5a-c ( $\sim 4600$  data points in a bin correspond to an operation time of 1 day).

As is evident from Figure 3.5b and Figure 3.5e, QP bursts were not observed in a region within  $30 R_J$  at  $|MLAT| < 10^\circ$ , although the number of observations is large in the inner and middle magnetospheres. This corresponds to the so-called “shadow zone” region, which has been detected by previous observations of Jovian hectometric (HOM) radio emissions (e.g., *Ladreiter and Leblanc*, 1990a, b, 1991; *Nakagawa*, 2001). In the previous section, it was indicated that no QP bursts were observed in the pre-noon sector. Most observations around noon were performed in the region of  $< 30 R_J$ . In addition, we confirmed that there is no significant tendency showing day-night asymmetry of the shadow zone (not shown). Therefore we interpret the absence of QP bursts in the pre-noon sectors as caused by the longitudinally symmetric shadow zone and the bias of observations in local time.

As shown in Figure 3.5c, the occurrence probabilities are significantly higher at  $Z > 0$  than those at  $Z < 0$ , i.e., the observer can often observe QP bursts in the northern hemisphere. The peak around  $Z \sim -30 R_J$  is insignificant because the operating time is nearly zero at  $Z \sim -30 R_J$  as indicated in Figure 3.5f. We interpret the higher probabilities at the northern hemisphere as a result of apparent CML dependence. As described in Section 3.2, the occurrence probability has an apparent peak around  $CML \sim 200^\circ$  due to the rota-

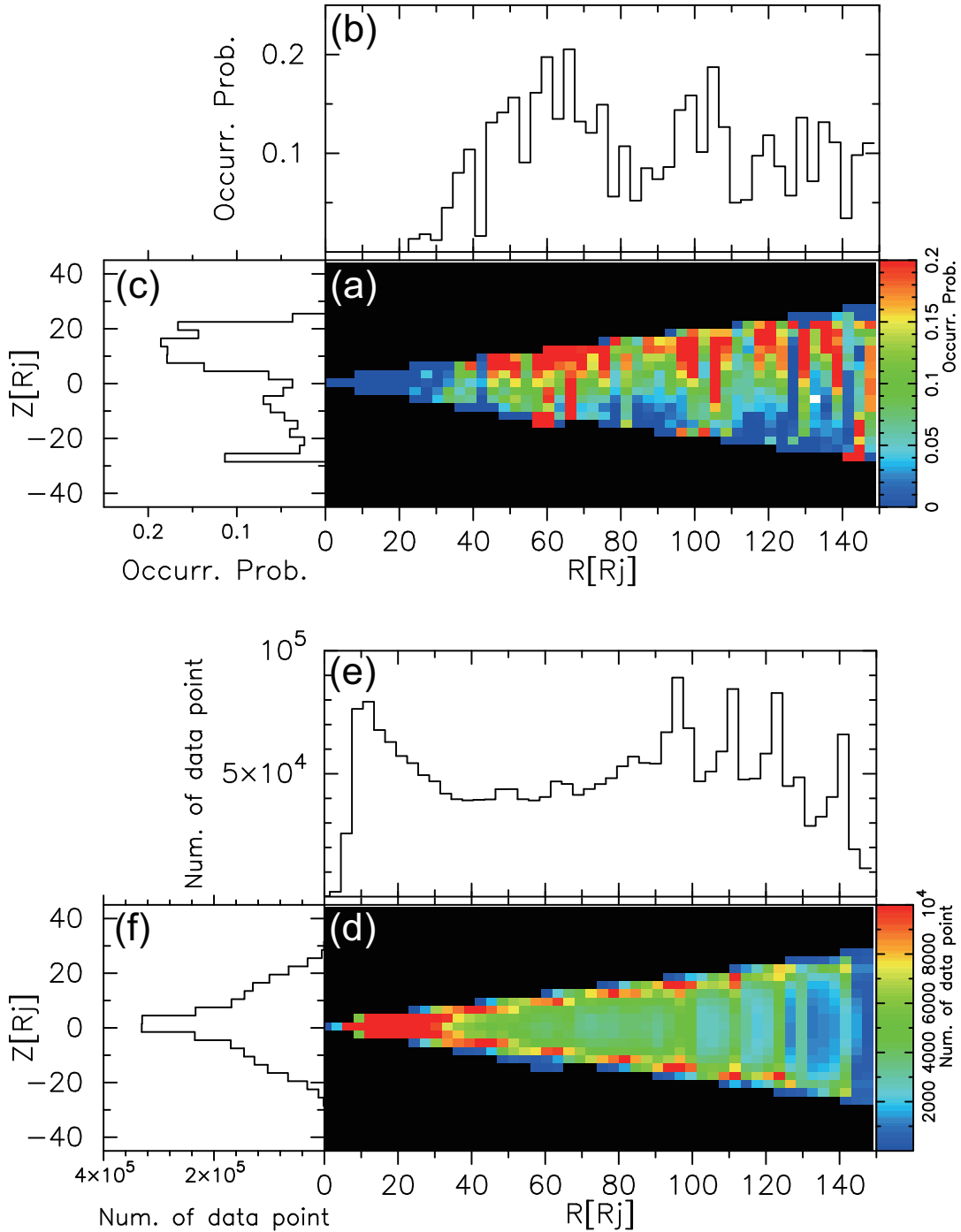


**Figure 3.5:** (a) Distribution of QP bursts' occurrence probability in a meridian plane. Vertical and horizontal axes in Figure 3.5a are parallel to magnetic axis and magnetic equator, respectively. Colored section indicates occurrence probability. Black region corresponds to lack of observations. Spatial resolution is equivalent to  $3 \times 3 R_J$  at each bin. (b) Radial distribution of occurrence probability. (c) Distribution of occurrence probability in north-south direction. Spatial resolutions of these panels are also  $3 R_J$ . (d) Distribution of PWS operating time in a meridian plane in the similar format to that of Figure 3.5a, but colors indicate number of data points when PWS was operating during the analysis period. About 4600 data points correspond to 1 day of operating time. (e) Radial distribution and (f) north-south distribution of operating time. They are also shown in formats to those of Figure 3.5b and c, respectively (Kimura et al., in press).

tional phase dependence and the observational bias in the LT direction (see Figure 3.4a). Because the magnetic axis is tilted to the CML $\sim 200^\circ$  meridian, the observer is located at the northern hemisphere when observer's CML is around  $200^\circ$  with higher probabilities.

## 3.4 Discussion—Occurrence Dependence on Geometric Parameters

We obtained the dependence of QP bursts occurrence on the SSL and CML. Statistical tests indicated that the occurrence dependence on the SSL is more significant than that on the CML. This suggests that QP bursts are excited in a particular SSL ranges. This is consistent with the results from Morioka *et al.* (2006), who stated that QP burst groups have their onset around SSL $\sim 260^\circ$ – $320^\circ$  based on the Galileo's observations. It should be noted that the rotational phase dependence in the equatorial region shows the opposite of that observed at the northern high latitudes by Ulysses (Figures 3.3 and 3.4). The SSL range is  $90^\circ$ – $300^\circ$  at the northern high latitudes, while the SSL range at low latitudes is  $300^\circ$ – $480^\circ$ . This means that QP bursts observed at the northern high latitudes are excited when the northern magnetic pole (System III longitude $\sim 200^\circ$ ) is directed sunward and those at low latitudes are excited when the southern magnetic pole (System III longitude $\sim 20^\circ$ ) is directed sunward.

The dependence on the rotational phase has been reported in other magnetospheric phenomena. Kaiser *et al.* (1993b) and Morioka *et al.* (2004) showed the rotational phase dependence of Jovian Anomalous Continuum (JAC). Statistical analyses by Morioka *et al.* (2004) indicated that JAC is triggered around SSL $\sim 270^\circ$ . In addition, Voyager observations showed that the “clock modulation” of the spectral index of the MeV electrons has a peak at SSL $\sim 240^\circ$  (Schardt *et al.*, 1981). It is still unclear why QP bursts, JAC, and MeV electrons have the SSL dependence and why the occurrence phase differs in each. We need to consider a model of these phenomena with reference to that of Saturn kilometric radiation (SKR) and magnetospheric structure proposed by recent observations and theories (e.g.,

Cecconi and Zarka, 2005; Zarka et al., 2007; Southwood and Kivelson, 2007; Gurnett et al., 2007; Goldreich and Farmer, 2007; Andrews et al., 2008; Provan et al., 2009), which claim that periodic intensity variation of SKR is driven by the modulation in solar wind velocities, corotating heavy sector of outflowing plasma from the inner magnetosphere, or longitudinally-asymmetric magnetic field structure resulted from a field aligned current system. An analogous mechanism with the periodic behavior of SKR might work as the clock modulation mechanism of QP bursts.

We first detected the “shadow zone” of QP bursts based on the data from Galileo in the Jovian magnetosphere (Figure 3.5). In the equatorial region at  $|MLAT| < 10^\circ$ , the shadow zone appeared at a radial distance of  $< 30 R_J$ . Voyager and Galileo also observed the shadow zone of HOM at  $< 20 R_J$  in the equatorial region (Ladreiter and Leblanc, 1990a, b, 1991; Nakagawa, 2001). The ray tracing results from Ladreiter and Leblanc (1990a, b, 1991) confirmed that the null region of HOM results from the high latitudinal source and propagation process from the polar region to the equatorial region. Thus, it was suggested that the source of QP bursts is in the polar region, and this suggestion was demonstrated using the ray tracing method in Chapter 5.

## 3.5 Periodicity

### 3.5.1 Description of the Lomb-Scargle Periodogram analysis

Previous studies performed periodicity analyses of QP bursts by counting temporal intervals between individual pulses (MacDowall et al., 1993; Kimura et al., 2008b). These studies indicated that QP bursts observed at high and low latitudes (both in the northern and southern hemispheres) are categorized into two kinds of periodicity: one having  $\sim 15$  min periodicity at low latitudes and the other with  $\sim 40$  min periodicity at high latitudes. There have been, however, no discussions about spectral nature of the periodicity: i.e., it is still unclear which periodicity has larger amplitudes of pulses. In this study, periodicity analyses for QP bursts’ spectral densities were investigated based on the “*Lomb-Scargle*

*periodogram*" technique, which was adopted to validate periods of some magnetospheric activities: e.g., variation in the Io plasma torus brightness or Energetic Neutral Atom (ENA) emissions from the inner magnetosphere of Saturn (Woodward *et al.*, 1992, 1994; Nozawa *et al.*, 2004; Carberry *et al.*, 2007, 2008, 2009).

This technique can be applied to a set of the data points which are unequally sampled in time, and can find spectral power at any frequencies below the *Nyquist frequency*, above which spectral power of sampled signal is not evaluated correctly due to the aliasing effect. The Nyquist frequency is described as

$$\omega_c \equiv \frac{\pi}{t_i - t_{i-1}} \quad (3.2)$$

where  $t_i$  and  $t_{i-1}$  are the time of  $i$ -th and  $(i-1)$ -th data points, thus the Nyquist frequency is equivalent to a half of the sampling frequency.

A spectral power at frequency  $\omega$ ,  $P(\omega)$ , in the Lomb-Scargle periodogram developed by Scargle (1982) is written as

$$P(\omega) = \frac{1}{2\sigma^2} \left\{ \frac{\left[ \sum_{i=1}^N y_i \cos \omega(t_i - \tau) \right]^2}{\sum_{i=1}^N \cos^2 \omega(t_i - \tau)} + \frac{\left[ \sum_{i=1}^N y_i \sin \omega(t_i - \tau) \right]^2}{\sum_{i=1}^N \sin^2 \omega(t_i - \tau)} \right\} \quad (3.3)$$

with  $\tau$  which is defined by

$$\tan 2\omega\tau = \frac{\sum_{i=1}^N y_i \sin 2\omega t_i}{\sum_{i=1}^N y_i \cos 2\omega t_i} \quad (3.4)$$

where  $y_i$  is  $i$ -th value in  $N$  data points, and  $\sigma^2$  is a variance of the data set.

Significance of the spectral power is discussed based on the false-alarm test. Following Horne and Baliunas (1986) and Koen (1990), this thesis defined the probability density

function of  $F$  distribution ( $F_{2,N-1}$ ) as the false-alarm probability at single-frequency:

$$Pr(z) = \left(1 + \frac{2z}{N-1}\right)^{-(N-1)/2} \quad (3.5)$$

where  $Pr(z)$  shows the probability that random noise could reach to a spectral height of  $z$  at single-frequency. Equation 3.5 becomes approximately equivalent to  $e^{-z}$ , i.e., Gaussian noise, for the case of  $z \ll N$  and  $N \gg 1$ . In the present analysis, the number of data points  $N$  is sufficiently larger than  $z$  and unity, thus,  $Pr(z) \sim e^{-z}$ . For the periodogram performed at independent frequencies, the false-alarm probability  $FA(z)$  is expressed as

$$FA(z) = 1 - [1 - Pr(z)]^{N_i} \quad (3.6)$$

where  $N_i$  is the number of frequencies checked in the periodogram analysis. See Scargle (1982), Hrone and Baliunas (1986), and appendix in Woodward (1992) for detailed derivation of above equations.

Periodicity of QP bursts was investigated by the following procedures:

1. The observed spectral densities of QP burst groups were integrated in a frequency range of 10–30 kHz for Ulysses and 8–12 kHz for Galileo.
2. Short-term variations (a few to tens of minutes) were obtained by subtracting long-term variations, which were fitted to 4th polynomial function, from the integrated spectral densities
3. The Lomb-Scargle periodograms were computed from the short-term variations based on Equations 3.3 and 3.4
4. False-alarm probabilities were calculated from Equations 3.5 and 3.6

These analyses were applied to all of the QP burst events observed by Ulysses and Galileo.

### 3.5.2 Periodicity Analysis Results

Figure 3.6 shows a periodogram analysis result of QP bursts observed by Ulysses at southern high latitudes ( $\sim -38^\circ$ ) after the first encounter with Jupiter. Figure 3.6a shows short-term variations of spectral densities derived by subtracting long-term variations evaluated by polynomial fitting from the observed spectral density. Figure 3.6b and c are the Lomb-Scargle periodograms in minutes and mHz, respectively. As is evident from Figure 3.6b, spectral power of the periodogram has a primary peak at  $\sim 40$  min with  $FA < 0.1$ . This indicates that the QP burst group of this event has significant periodicity of 40 min. A peak at  $\sim 20$  min with  $FA \sim 0.5$  is interpreted as insignificant periodicity because the secondary peak has a half period of 40 min: i.e., a harmonic of the primary spectral peak.

Periodogram of QP bursts observed at northern high latitudes ( $\sim +48^\circ$ ) is shown in Figure 3.7. Formats of Figure 3.7 are the same as those of Figure 3.6. This result indicates that this event has no significant periodicity except for a peak at  $\sim 30$  min.

The periodogram analyses were also performed for the QP bursts observed at low latitudes. Figure 3.8 is a periodogram derived from observations by Galileo in the equatorial region of the magnetosphere. Formats are also the same as those of Figure 3.6. Multiple periodicity appears significantly in the periodogram from a few to tens of minutes because of high spectral resolution: i.e., observations by PWS were performed with higher time resolution (18.67 sec) than that of URAP (144 sec).

Statistical analysis was performed to investigate averaged periodicity of QP bursts at high and low latitudes. Data points of the periodogram which exceed a level of  $FA = 0.5$  were counted at each frequency for all the QP burst groups. Figure 3.9a-d show results of the statistics for each geometry. Histograms of Figure 3.9a and b are derived from the observations by Ulysses during the inbound (Jovigraphic latitude, JLAT $\sim 0^\circ$ ) and outbound phase (JLAT $\sim -40^\circ$ ) of the first encounter with Jupiter, respectively. Figure 3.9c is the result from Ulysses' observations during the second encounter (JLAT:  $+80^\circ - +10^\circ$ ), and Figure 3.9d is the result from Galileo in the equatorial region (JLAT $\sim 0^\circ$ ) of the magnetosphere.

One can find significant peaks around tens of minutes for each geometry except for

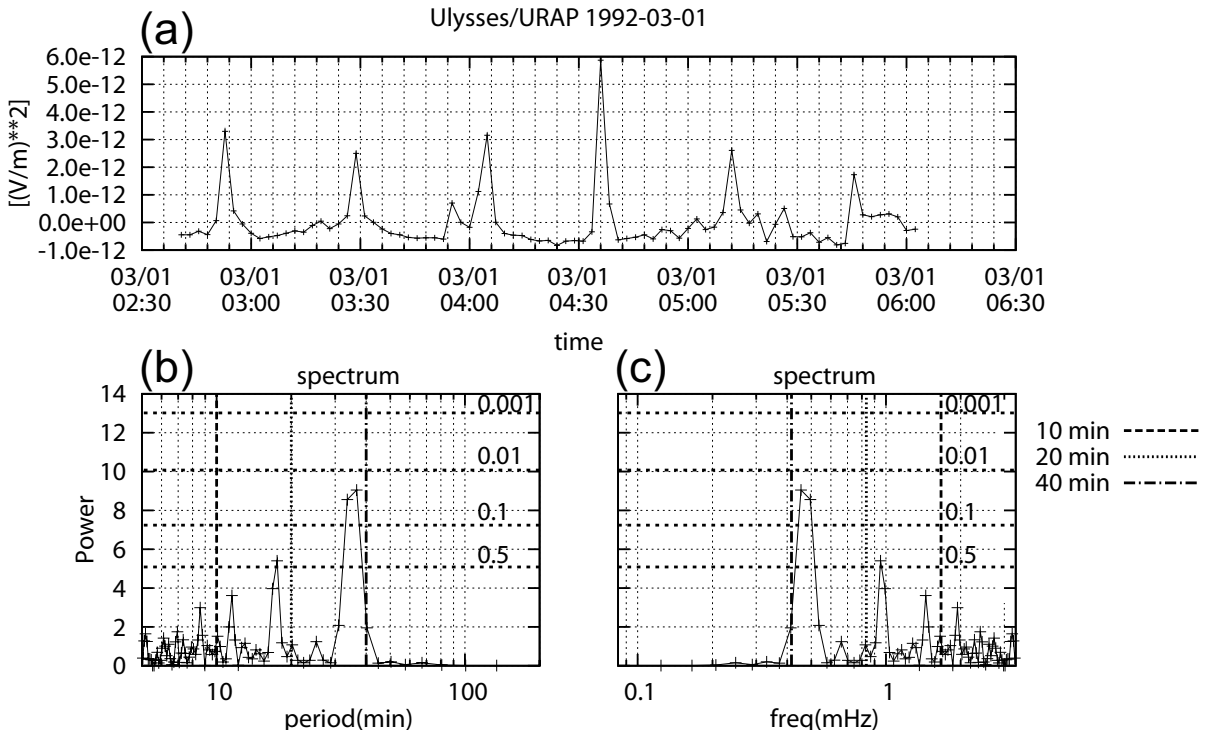


**Figure 3.6:** Periodogram of a QP burst group observed by Ulysses at high latitudes ( $\sim 38^\circ$ ) on March 1, 1992 after the first encounter with Jupiter. (a) Short-term variations of spectral densities, which are sometimes reduced to negative values because of subtracting long-term variations. (b) Lomb-Scargle periodgram of the burst group. Horizontal axis shows periods in minutes and vertical axis shows relative spectral power. Horizontal dotted lines correspond to spectral levels of the false-alarm probabilities of 0.001, 0.01, 0.1, and 0.5. Vertical dotted and dashed lines annotate the periods of interest (5, 10, 20, and 40 minutes). (c) Lomb-Scargle periodgram with a similar format to that of (b), but horizontal axis shows frequencies in mHz.

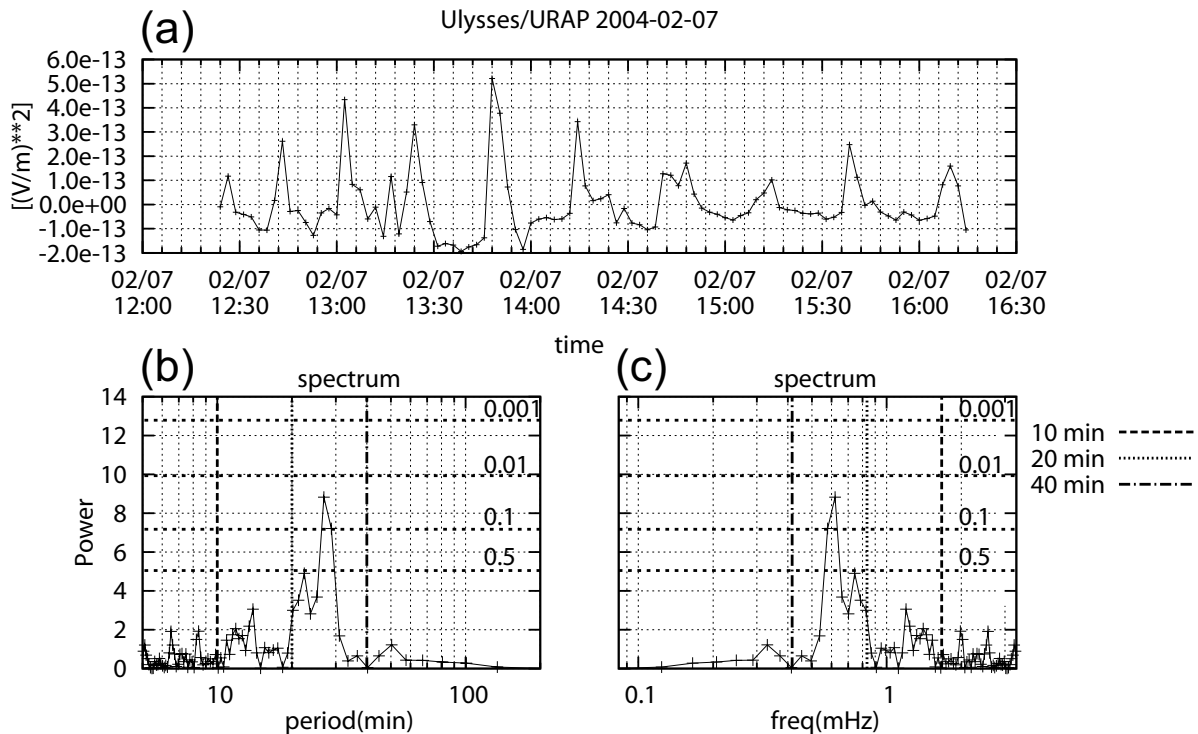


**Figure 3.7:** Periodogram of a QP burst group observed by Ulysses at high latitudes ( $\sim +48^\circ$ ) on February 7, 2004 during the second encounter with Jupiter with the same format as that of Figure 3.6.

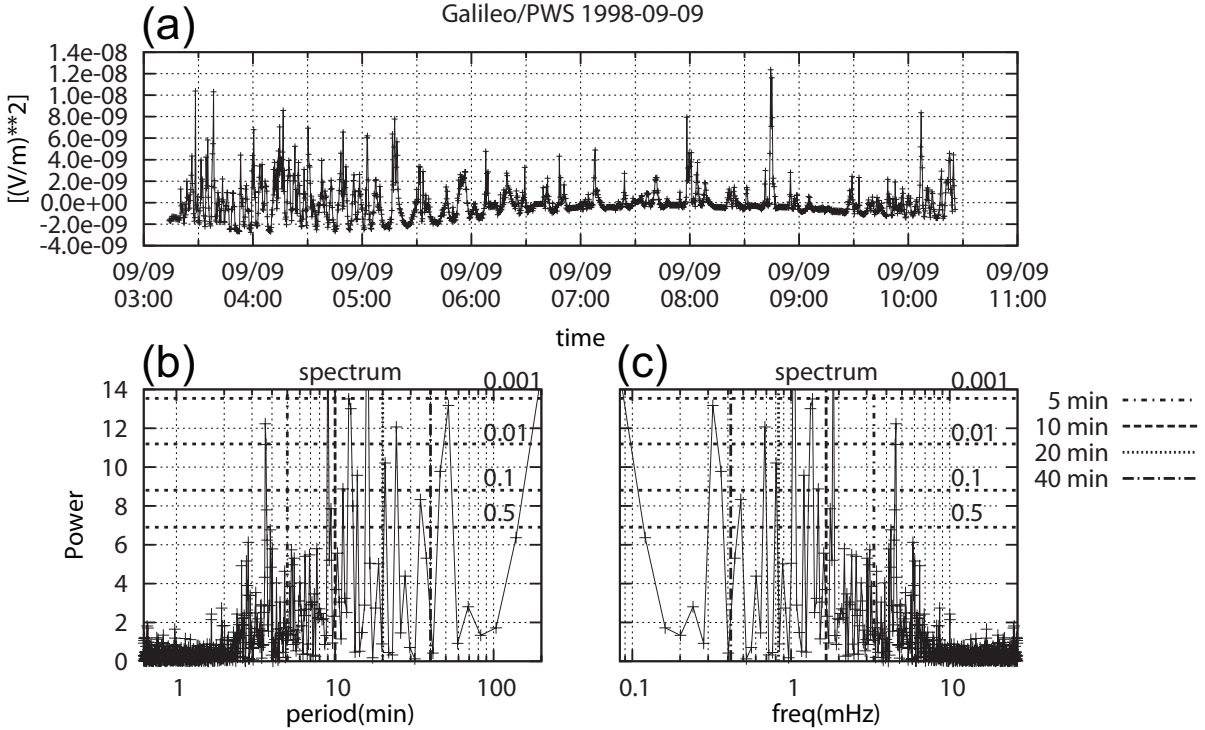


**Figure 3.8:** Periodogram of a QP burst group observed by Galileo at low latitudes on September 9, 1998 with the same format as that of Figure 3.6.

the result of Ulysses' first inbound. We consider that the absence of dominant periodicity during the inbound is resulted from the low frequency range of QP bursts at low latitudes and local thermal noise of solar wind plasma: *MacDowall et al.* (1993) reported that QP bursts observed at low latitudes have lower frequency range (1–50 kHz) than those at high latitudes (1–200 kHz). On the other hand, in the interplanetary space, quasi-thermal noise (see, e.g., *Hoang et al.*, 1992) of solar wind plasma has comparable or larger intensities than those of QP bursts at VLF range (3–30 kHz). Thus, we infer that periodicity of QP bursts during the inbound were contaminated with the thermal noise in solar wind, and dominant periodicity of QP bursts disappeared.

Figure 3.9d indicates that Galileo observed two components of periodicity:  $\sim 30$  min and  $\sim 100$  min. We interpret the longer period at  $\sim 100$  min as fluctuations of local magnetospheric plasma. In the middle magnetosphere, i.e., the magnetodisk region, magnetospheric plasma is corotating or sub-corotating with Jupiter. A spacecraft in the equatorial region

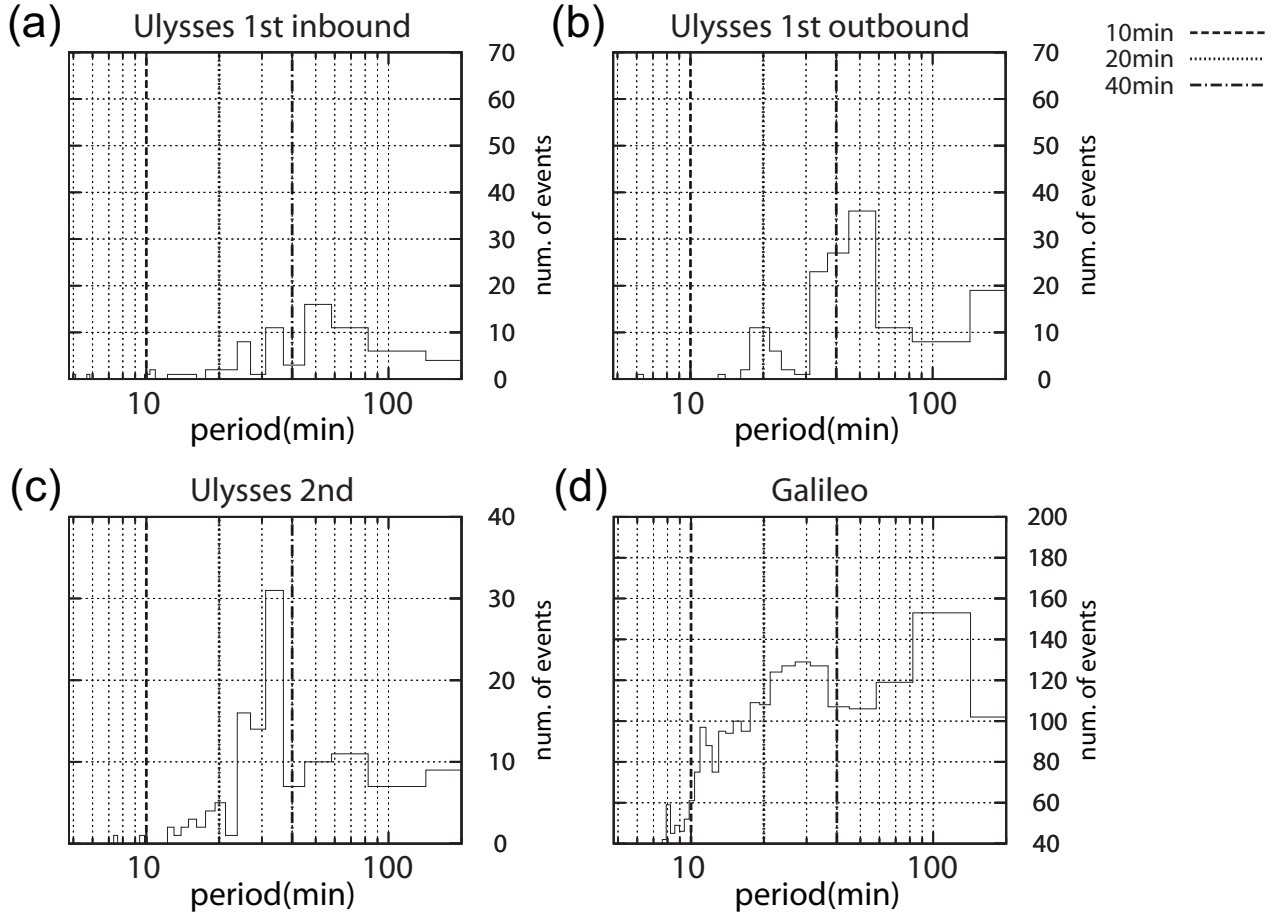


**Figure 3.9:** Histogram of averaged periodicity of QP bursts. Horizontal axes are period in minutes, and vertical axes are the number of spectral data points which exceed a level of  $FA = 0.5$ . Vertical dotted and dashed lines annotate the periods of interests (10, 20, and 40 min). (a) and (b) are derived from the observations by Ulysses during the inbound (Jovigraphic latitude,  $JLAT \sim 0^\circ$ ) and outbound phases ( $JLAT \sim -40^\circ$ ) of the first encounter with Jupiter, respectively. (c) is the result from Ulysses' observations during the second encounter ( $JLAT: +80^\circ - +10^\circ$ ), and (d) is the result from Galileo in the equatorial region ( $JLAT \sim 0^\circ$ ) of the magnetosphere.

can detect local plasma or magnetic field variations with rotational period or a half of the period because it moves in and out of the magnetodisk structure. Local plasma waves (e.g., trapped continuum, Kurth, 1992b) also vary with large amplitudes accompanying with rotational plasma at similar periods. We infer that spectral contamination of these waves are detected as the longer-period component in the periodgram of Figure 3.9d.

For these reasons, we conclude that following periods are significant periodicity of QP bursts:  $\sim 50$  min of Ulysses' first outbound (high latitudes),  $\sim 35$  min of Ulysses' second encounter (high latitudes), and  $\sim 30$  min of Galileo (low latitudes). It is obvious that there is no shorter periods than 30 minutes at all latitudes. This means that QP15 bursts, which were observed frequently at low latitudes and less at high latitudes (MacDowall et al., 1993), are insignificant in amplitudes of pulses, but QP40 bursts are dominant at all latitudes. This statistical results suggest that " $\sim 40$  min" is the key periodicity, which is possibly associated with the energy source of QP bursts and relevant particle acceleration process.

## 3.6 Brief Summary

In this chapter, occurrence characteristics of QP bursts were investigated based on the wave data observed by Ulysses at the northern high latitudes and Galileo at the low latitudes. It was indicated that the occurrence probabilities of QP bursts have dependence on geometric parameters (latitudes, longitudes, and radial distance) as follows:

1. QP bursts are frequently observed in the northern latitudinal ranges from  $+30^\circ$  to  $\sim +90^\circ$  (Figure 3.3)
2. QP bursts are excited in a particular rotational phase ( $\text{SSL}=90^\circ\text{--}300^\circ$  at the high latitudes and  $300^\circ\text{--}480^\circ$  at the low latitudes), corresponding to the so-called "clock modulations" which are internally driven in a particular rotational phase with a similar manner to the phenomena found in Saturn's magnetosphere (Figures 3.3 and 3.4)

3. QP bursts have the “shadow zone” in a region within  $30 R_J$  at  $|MLAT| < 10^\circ$  (Figure 3.5)

Statistics based on the Lomb-Scargle analysis presented the remarkable characteristic of QP bursts’ periodicity:

4. QP bursts with the “40 min” periodicity are more dominant in amplitudes than QP “15 min” bursts at all latitudes, suggesting that “ $\sim 40$  min” is the key periodicity for QP bursts and relevant phenomena (Figure 3.9)



# Chapter 4

## Polarization Properties

### 4.1 Description of Polarization Measurements and Direction Finding

In this section, we describe techniques of the direction finding analysis with use of triaxial antenna systems of RPWS on the Cassini spacecraft (*Ladreiter et al.*, 1995; *Vogl et al.*, 2004). The RPWS antenna system (u, v, and w antennae) and cartesian axes ( $x$ ,  $y$ , and  $z$  axes) of Cassini are indicated in Figure 4.1. Two of the antenna elements (u, v) are extended with a  $60^\circ$  angular separation from the  $y$ - $z$  plane, and the u, v plane inclined by  $37^\circ$  relative to the  $x$ - $y$  plane of the spacecraft cartesian axes. The third element, w antenna, is extended in the  $y$ - $z$  plane at an angle of  $37^\circ$  from the  $z$ -axis.

Coordinate systems for the direction finding are shown in Figure 4.2. First, we derive the modeled quantity of the received voltage of electromagnetic waves, which arrives from the colatitude of  $\theta$  and azimuth of  $\phi$  in the spacecraft coordinate ( $o, x, y, z$ ). The Stokes parameters which indicate polarization characteristics of the electromagnetic waves in the wave coordinate ( $O, X_w, Y_w, Z_w$ ) are also derived from the modeled voltage.

The modeled quantity is defined by

$$\langle V_n V_k^* \rangle^{\text{mod}} = \langle (\mathbf{h}_n \mathbf{E})(\mathbf{h}_k \mathbf{E})^* \rangle \quad (4.1)$$

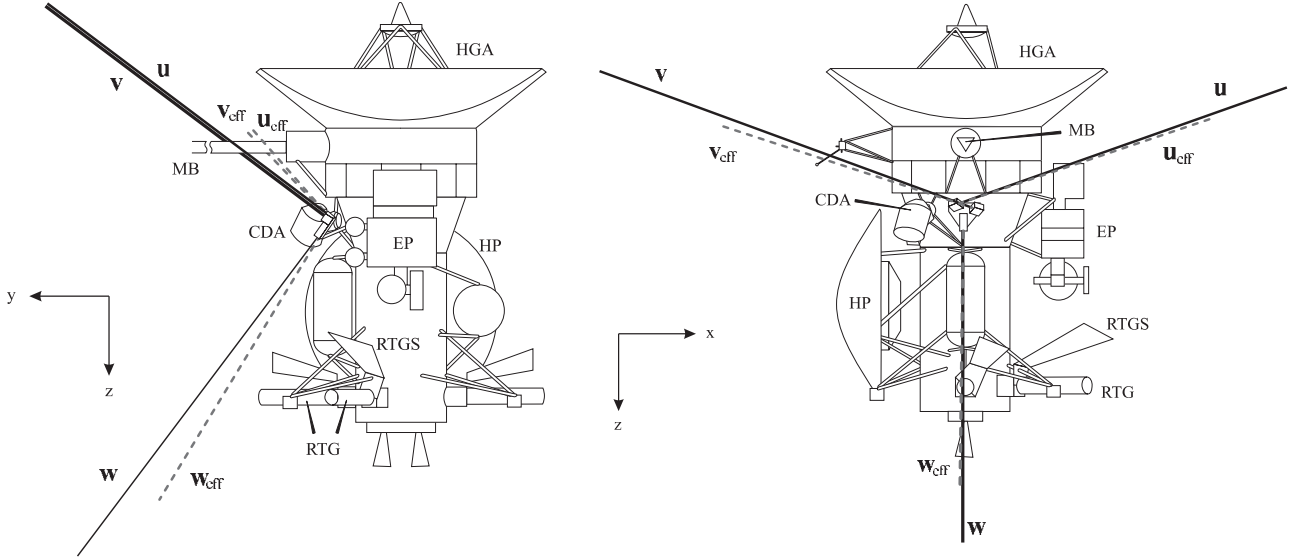


**Figure 4.1:** RPWS antenna system on the Cassini spacecraft and associated coordinate system used for direction finding and polarization measurements (Vogl et al., 2004). The angles  $\theta = 90^\circ - \arctan(z/\sqrt{x^2 + y^2})$  (colatitude) and  $\phi = \arctan(y/x)$  (azimuth) refer to a spherical coordinate system based on the cartesian axes  $x, y, z$  as shown.

where  $\langle V_n V_k^* \rangle^{mod}$  is the cross correlation signal between the complex voltage received by  $n$ -th antenna  $V_n$  and the conjugate of the  $k$ -th voltage  $V_k^*$  ( $n, k = 1, 2, 3$  or  $u, v, w$ ), and  $\mathbf{E}$  is the electric field of the incident wave, and  $\mathbf{h}_n$  is an effective height of the  $n$ -th antenna. The components of the effective height  $\mathbf{h}_n$  in the wave coordinate are defined by

$$h_{n,X_w} = h_n \sin \beta \cos \vartheta \quad (4.2)$$

$$h_{n,Y_w} = h_n \sin \beta \sin \vartheta \quad (4.3)$$

where  $h_n$  is the modulus of  $\mathbf{h}_n$ . Introducing a spherical law of cosines in the spherical trigonometry,

$$\cos a = \cos b \cos c + \sin b \sin c \cos A \quad (4.4)$$

where the angles  $a, b, c$ , and  $C$  are defined in Figure 4.3, we obtain the following relations

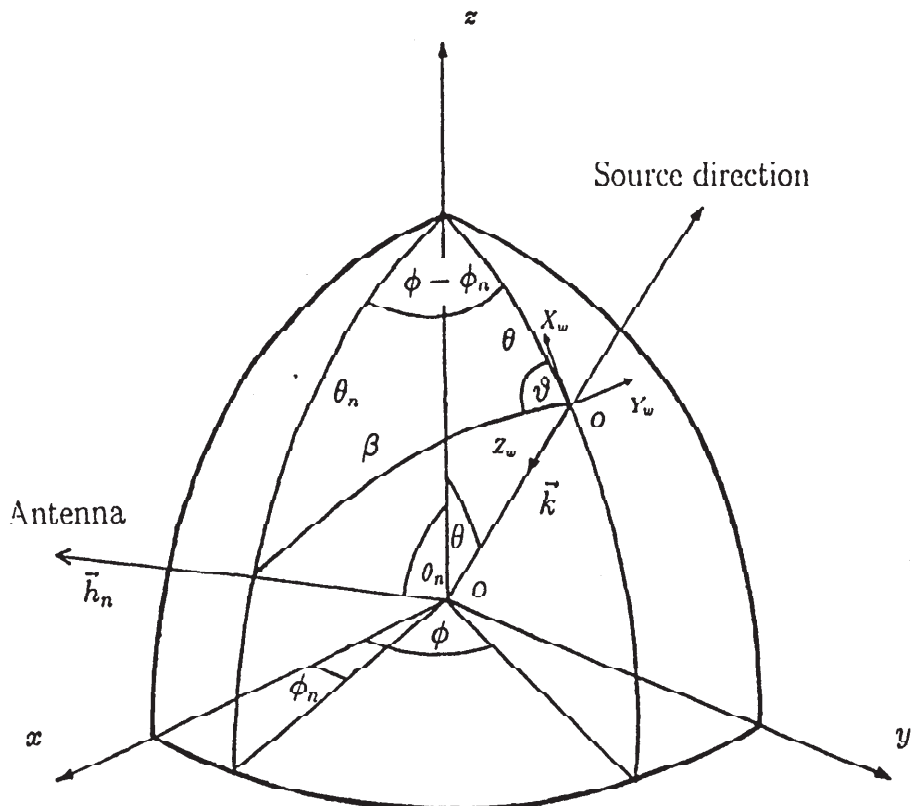


**Figure 4.2:** Coordinate systems used for derivation of the modeled antenna signals of RPWS (Ladreiter et al., 1995). Coordinate  $(o, x, y, z)$  is the antenna system and  $(O, X_w, Y_w, Z_w)$  is the wave system. Here  $\theta_n$  and  $\phi_n$  define the effective height direction of  $n$ -th antenna.  $\theta$  and  $\phi$  are the source direction angles.

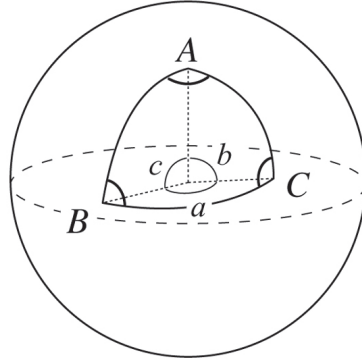


**Figure 4.3:** Spherical triangle solved by the law of cosines (<http://wwwsoc.nii.ac.jp/geod-soc/web-text/part4/4-2/4-2.html>).

between the directions of wave source and  $n$ -th antenna:

$$\cos \beta = \cos \theta_n \cos \theta + \sin \theta_n \sin \theta \cos(\phi - \phi_n) \quad (4.5)$$

$$\cos \theta_n = \cos \beta \cos \theta + \sin \beta \sin \theta \cos \vartheta. \quad (4.6)$$

By using Equations 4.5 and 4.6, the  $\mathbf{h}_n$  components in the wave coordinate are rewritten as

$$h_{n,X_w} = h_n [\cos \theta_n \sin \theta - \sin \theta_n \cos \theta \cos(\phi - \phi_n)] \quad (4.7)$$

$$h_{n,Y_w} = -h_n \sin \theta_n \sin(\phi - \phi_n). \quad (4.8)$$

These components are expressed by directions of the antenna  $(\theta_n, \phi_n)$  and the wave source  $(\theta, \phi)$ .

To characterize the electric field of the waves, we assume the incoming wave is the plane wave defined by

$$E_{X_w} = a_1 e^{i\omega t} \quad (4.9)$$

$$E_{Y_w} = a_2 e^{i(\omega t - \delta)} \quad (4.10)$$

where  $\omega$  is the angular frequency of the wave and  $\delta$  is the phase shift between the  $E_{X_w}$  and  $E_{Y_w}$  components with wave amplitudes of  $a_1$  and  $a_2$ .  $Z_w$  component is zero because the plane containing the wave electric field (i.e.,  $X_w$ - $Y_w$  plane in Figure 4.2) is perpendicular to the wave normal direction  $Z_w$ , which is parallel to the wave number vector  $\vec{k}$ . Using Equations 4.7, 4.8, 4.9, and 4.10, the complex voltage received by the antenna  $n$  is rewritten as

$$\begin{aligned} V_n &= h_{n,X_w} \cdot E_{X_w} + h_{n,Y_w} \cdot E_{Y_w} \\ &= h_n \left( a_1 e^{i\omega t} [\cos \theta_n \sin \theta - \sin \theta_n \cos \theta \cos(\phi - \phi_n)] - a_2 e^{i(\omega t - \delta)} \sin \theta_n \sin(\phi - \phi_n) \right). \end{aligned} \quad (4.11)$$

Multiplying the  $n$ -th voltage by the conjugate of  $k$ -th voltage and averaging over a time of  $T \gg 2\pi/\omega$  yield real and imaginary parts of the modeled cross correlation function

$$\begin{aligned} \text{Re} < V_n V_k^* >^{\text{mod}} &= \frac{Sh_n h_k}{2} \left( (1+Q)\Omega_n \Omega_k \right. \\ &\quad - U (\sin \theta_k \sin(\phi - \phi_k) \Omega_n + \sin \theta_n \sin(\phi - \phi_n) \Omega_k) \\ &\quad \left. + (1-Q) \sin \theta_n \sin \theta_k \sin(\phi - \phi_n) \sin(\phi - \phi_k) \right) \end{aligned} \quad (4.12)$$

$$\text{Im} < V_n V_k^* >^{\text{mod}} = \frac{Sh_n h_k}{2} V (\sin \theta_n \sin(\phi - \phi_n) \Omega_k - \sin \theta_k \sin(\phi - \phi_k) \Omega_n) \quad (4.13)$$

where  $\Omega_n = \cos \theta_n \sin \theta - \sin \theta_n \cos \theta \cos(\phi - \phi_n)$ , and  $S, Q, U, V$  are the Stokes parameters, which indicate polarization characteristics of an incident plane wave defined by Kraus

(1982) as

$$S = \langle a_1^2 + a_2^2 \rangle \quad (4.14)$$

$$Q = \frac{\langle a_1^2 - a_2^2 \rangle}{S} \quad (4.15)$$

$$U = \frac{2 \langle a_1 a_2 \cos \delta \rangle}{S} \quad (4.16)$$

$$V = \frac{2 \langle a_1 a_2 \sin \delta \rangle}{S}. \quad (4.17)$$

$S$  is derived by multiplying the modulus of the Poynting vector  $\vec{P}$  by the antenna impedance  $Z$ : i.e.,  $S = Z|\vec{P}|$ .  $Q$  and  $U$  indicate degree of linear polarization, and  $V$  is that of circular polarization of an electromagnetic wave. For example, when  $(Q, U, V) = (0, 0, +1)$  or  $(0, 0, -1)$ , the received wave is completely left-handed (LH) or right-handed (RH) circular polarized in the wave electric field plane with respect to  $\vec{k}$  or  $Z_w$  axis. On the other hand, if  $(Q, U, V) = (\pm 1, 0, 0)$  or  $(0, \pm 1, 0)$ , the waves are completely linearized in the wave electric field plane.

It should be noted that the modeled quantity  $\langle V_n V_k^* \rangle^{mod}$  is a function depending on six wave parameters  $\mathbf{X} \equiv (S, Q, U, V, \theta, \phi)$ . Thus, one can find the wave parameters of the incoming electromagnetic waves by setting the modeled voltage  $\langle V_n V_k^* \rangle^{mod}$  equal to the  $\langle V_n V_k^* \rangle^{obs}$  observed by the RPWS experiment.

A solution of the wave parameter vector  $\mathbf{X}$  can be found when the weighted residual sum of squares between the RPWS observations  $y_i^{obs}$  and the predicted values  $y_i^{mod}$  becomes a minimum:

$$\chi^2 = \sum_{i=1}^N W_i (y_i^{obs} - y_i^{mod}(\mathbf{X}))^2 = \text{Min}. \quad (4.18)$$

The observed quantities  $y_i^{obs}$  correspond to  $\langle V_1 V_1^* \rangle$ ,  $\langle V_2 V_2^* \rangle$ ,  $\langle V_3 V_3^* \rangle$ ,  $Re \langle V_1 V_3^* \rangle$ ,  $Re \langle V_2 V_3^* \rangle$ ,  $Im \langle V_1 V_3^* \rangle$ , and  $Im \langle V_2 V_3^* \rangle$  derived from triaxial antenna observations of RPWS. The weights  $W$  reflect the uncertainty of each observed value, corresponding to standard deviations  $1/\sigma^2$  which contains the intrinsic receiver noise level.  $N$  is the total number of the observed auto-correlation and cross-correlation signals.

The solution of Equation 4.18,  $\mathbf{X}$ , is found when derivation of  $\chi^2$  with respect to the components  $X_j$  of the vector  $\mathbf{X}$  ( $X_1, \dots, X_6 = S, Q, U, V, \theta, \phi$ ) becomes zero:

$$\frac{\partial \chi^2}{\partial X_j} = 0 \quad (4.19)$$

or

$$\frac{\partial \chi^2}{\partial \mathbf{X}} = 0. \quad (4.20)$$

Taylor expansion of Equation 4.19 around the initial vector  $\mathbf{X}^0$  yields

$$0 = \frac{\partial \chi^2}{\partial \mathbf{X}} \sim \frac{\partial \chi^2}{\partial \mathbf{X}} \Big|_{\mathbf{x}^0} + \frac{\partial}{\partial \mathbf{X}'} \frac{\partial \chi^2}{\partial \mathbf{X}} \Big|_{\mathbf{x}^0} \cdot (\mathbf{X}' - \mathbf{X}^0). \quad (4.21)$$

Thus, linearization of Equation 4.19 becomes

$$\frac{\partial \chi^2}{\partial \mathbf{X}} \Big|_{\mathbf{x}^0} = - \frac{\partial}{\partial \mathbf{X}'} \frac{\partial \chi^2}{\partial \mathbf{X}} \Big|_{\mathbf{x}^0} \cdot \Delta \mathbf{X}' \quad (4.22)$$

where  $\Delta \mathbf{X} = \mathbf{X} - \mathbf{X}^0$ , and each component is expressed as

$$\frac{\partial \chi^2}{\partial X_j} \Big|_{\mathbf{x}^0} = - \frac{\partial^2 \chi^2}{\partial X_j \partial X_k} \Big|_{\mathbf{x}^0} \cdot \Delta X_k. \quad (4.23)$$

Equation 4.22 can be written in a matrix form

$$b_j = A_{jk} \Delta X_k \quad (4.24)$$

or

$$\mathbf{b} = \mathbf{A} \Delta \mathbf{X} \quad (4.25)$$

where we rewrite  $\Delta \mathbf{X}'$  as  $\Delta \mathbf{X}$ . Applying singular-value decomposition (see *Ladreiter et al*, 1995 for details), we obtain the solution  $\Delta \mathbf{X}$ :

$$\Delta \mathbf{X} = V \Lambda^{-1} U^T \mathbf{b} \quad (4.26)$$

where the matrix  $V$  and  $U$  satisfy the following relations

$$A = U\Lambda V^T \quad (4.27)$$

$$A^T = V\Lambda U^T \quad (4.28)$$

$\Lambda$  is a diagonal matrix containing the singular values of  $A$ :

$$\Lambda = \begin{pmatrix} \lambda_1 & 0 & \dots & \dots \\ 0 & \lambda_1 & \dots & \dots \\ \vdots & \vdots & \ddots & \dots \\ \vdots & \vdots & \vdots & \lambda_n \end{pmatrix}. \quad (4.29)$$

The singular values  $\lambda_i$  of  $A$  correspond to the square root of eigenvalues of the matrix  $AA^T$  or  $A^TA$ . From  $\Delta\mathbf{X}$  and the initial vector  $\mathbf{X}^0$ , the wave parameter vector  $\mathbf{X}$  is derived.

## 4.2 Polarization Measurements at High Latitudes

Polarization characteristics of QP bursts were investigated by *MacDowall et al.* (1993) based on the wave data observed by Ulysses during its first encounter with Jupiter. They reported that QP bursts observed at southern high latitudes were RH circular polarized and suggested that these QP bursts are left-handed ordinary (L-O) mode waves emitted from the southern polar region, which have LH polarized electric field with respect to the local magnetic fields around the source region. There has been, however, no additional discussion about the polarization characteristics of QP bursts after *MacDowall et al.* (1993).

For further discussions about generation mechanisms of QP bursts, we investigated polarization characteristics of the QP bursts observed at northern high latitudes during Ulysses' second encounter with Jupiter. Summed-modes of RAR, which correspond to the polarization measurements and direction finding mode, were operated in the period from 9 February to 16 March, 2004 in the high band receiver (52–940 kHz).

First, to detect sufficiently-intense signals of QP bursts, we subtracted the background

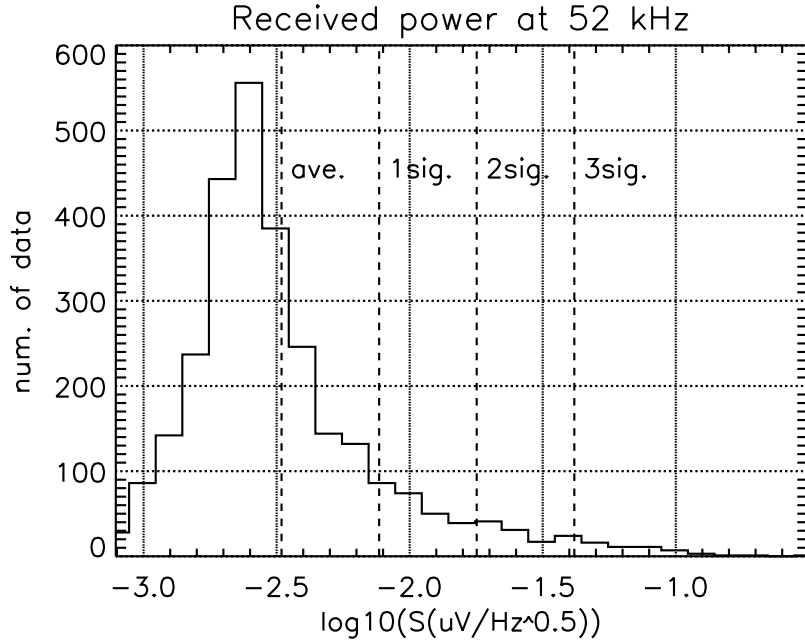


**Figure 4.4:** Histogram of the received power at 52 kHz observed by Ulysses during 19–24 Feb. 2004. Horizontal axis indicates the received power given in ten base logarithm of square-root of spectral density ( $\log_{10}(\mu V/\sqrt{Hz})$ ) and vertical axis shows the number of the data points. Vertical dotted lines indicate the average power and significance level of  $1\sigma$ ,  $2\sigma$ , and  $3\sigma$  from the average where  $\sigma$  is standard deviation of the observed power. Values of the significance level are summarized in Table 4.1

receiver noise from the observed power and took the statistic for the received power. The statistic determined the significance level of the observations by RAR during the analysis period. Figure 4.4 indicates histogram of the received intensity at 52 kHz observed during 19–24 Feb. 2004. The horizontal axis indicates the received power given in ten base logarithm of square-root of spectral density ( $\log_{10}(\mu V/\sqrt{Hz})$ ) and the vertical axis shows the number of the data points. The vertical dotted lines indicate the average power and significance level of  $1\sigma$ ,  $2\sigma$ , and  $3\sigma$  from the average where  $\sigma$  is standard deviation of the observed power.

Typical events of QP bursts observed by RAR during the analysis period are indicated in Figure 4.5. These events were observed on 19 February 2004 when Ulysses was located at  $+41^\circ$  Jovigraphic latitude in a local time of 17.1 h at a distance of 0.81 AU from Jupiter.

**Table 4.1:** Significance level of the received intensity during 19–24 Feb. 2004

significance level	ave.	$1\sigma$	$2\sigma$	$3\sigma$
value ( $\log_{10}(\mu V/\sqrt{Hz})$ )	-2.48	-2.11	-1.75	-1.38

Note that broadband frequency expansion of QP burst pulses up to a few hundred kHz was observed at 8–9 h and 15–18 h. Figure 4.6 indicates a 24-hour plot of Stokes parameters measured on the same day. From the top panel, Stokes parameters  $S$ ,  $V$ ,  $Q$ , and  $U$  defined in Equations 4.14–4.17 are plotted. In the top panel, one can find a intense pulse around 8 h with a peak of  $S \sim -1.2$  (a significance level is equal to  $\sim 3.5\sigma$ ), corresponding to the broadband QP bursts shown in Figure 4.5. Stokes parameters around the QP pulse event are plotted in Figure 4.7. When  $S$  had a peak of  $\sim -1.2$  around 08:20,  $V$  rose to  $\sim +0.8$ , while  $Q$  and  $U$  dropped to  $\sim 0$ . This means that the received electric field of the QP burst pulse is strongly LH circular polarized with respect to the wave number vector  $\vec{k}$ .

Second example of QP bursts is indicated in Figure 4.8. These events were observed on 2 March, 2004 when Ulysses was located at  $+35^\circ$  Jovigraphic latitude in a local time of 17.3 h at a distance of 0.83 AU from Jupiter. Stokes parameters on 2 March are shown in Figures 4.9 and 4.10 with the same formats as those of Figures 4.6 and 4.7. These figures indicate that  $(V, Q, U)$  approximately is equal to  $(+0.7, +0.4, +0.2)$ , when a pulse of QP bursts was observed around 12:30 with a significance level of  $\sim 1.3\sigma$ . This tendency of Stokes parameters means that the observed QP bursts on 2 March were partial LH circular waves.

Figure 4.11 shows third example of QP bursts observed on 18 Feb. when Jovigraphic latitude, local time, and a distance of Ulysses seen from Jupiter were  $+42^\circ$ , 17.1 h, and 0.81 AU, respectively. A QP burst pulse was observed around 6 h with a  $1.3\sigma$  significance as indicated in Figure 4.12. Figure 4.13 indicates that Stokes parameters  $V$ ,  $Q$ , and  $U$  when the QP pulse was observed were  $\sim +0.7$ ,  $\sim +0.1$ , and  $\sim 0.0$ , respectively. This result also corresponds to the fact that QP bursts observed on 18 Feb. was also partially LH circular polarized.

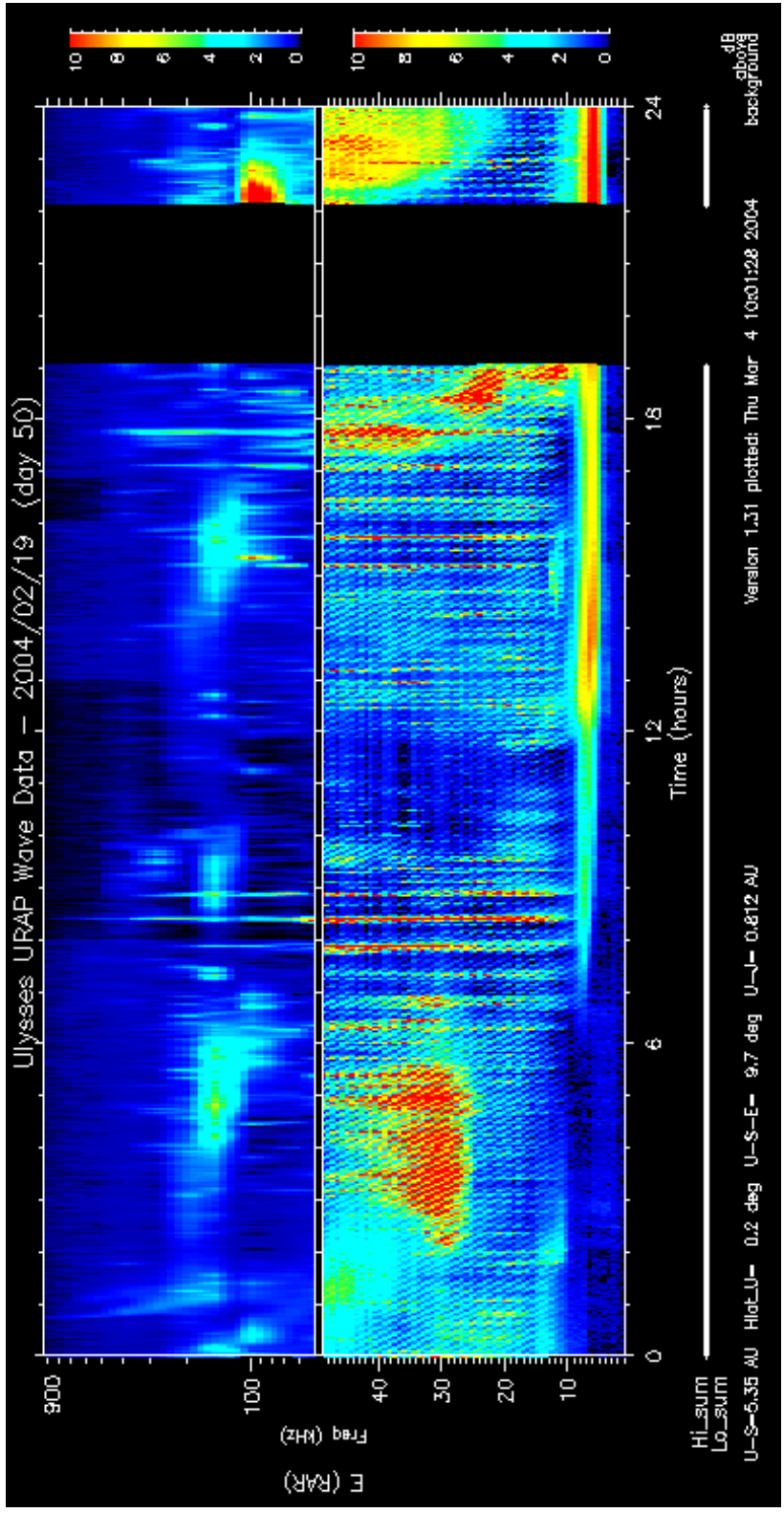


**Figure 4.5:** A 24-hour plot of dynamic spectra showing the QP bursts observed by RAR on 19 Feb. 2004 ([http://urap.gsfc.nasa.gov/data\\_access.html](http://urap.gsfc.nasa.gov/data_access.html)). (top) Spectra observed at high band (52–940 kHz) of RAR and (bottom) those at low band (1.25–48.5 kHz). Colors show intensities of the received power in dB. Jovigraphic latitude, local time, and a distance of Ulysses from Jupiter were  $+41^\circ$ , 17.1 h, and 0.81 AU, respectively.

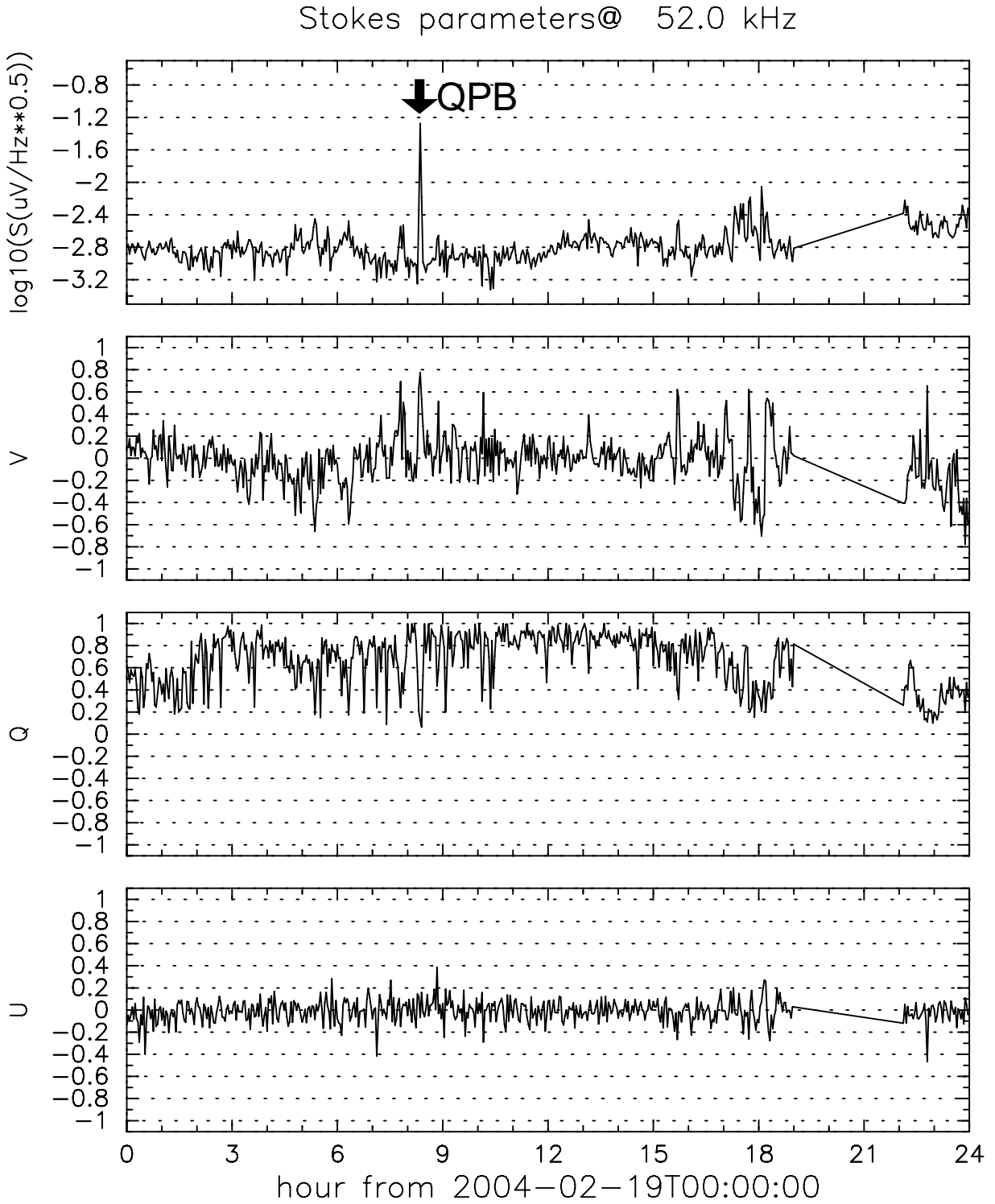


**Figure 4.6:** Stokes parameters at 52 kHz observed by RAR on 19 Feb. 2004. Horizontal axis shows the time of 24 hours. From the top panel, Stokes parameters  $S$ ,  $V$ ,  $Q$ , and  $U$  are plotted. The received power  $S$  is given in ten base logarithm of square-root of spectral density (i.e.,  $\log_{10}(\mu\text{V}/\sqrt{\text{Hz}})$ ). An QP burst (QPB) appeared around 08:20.

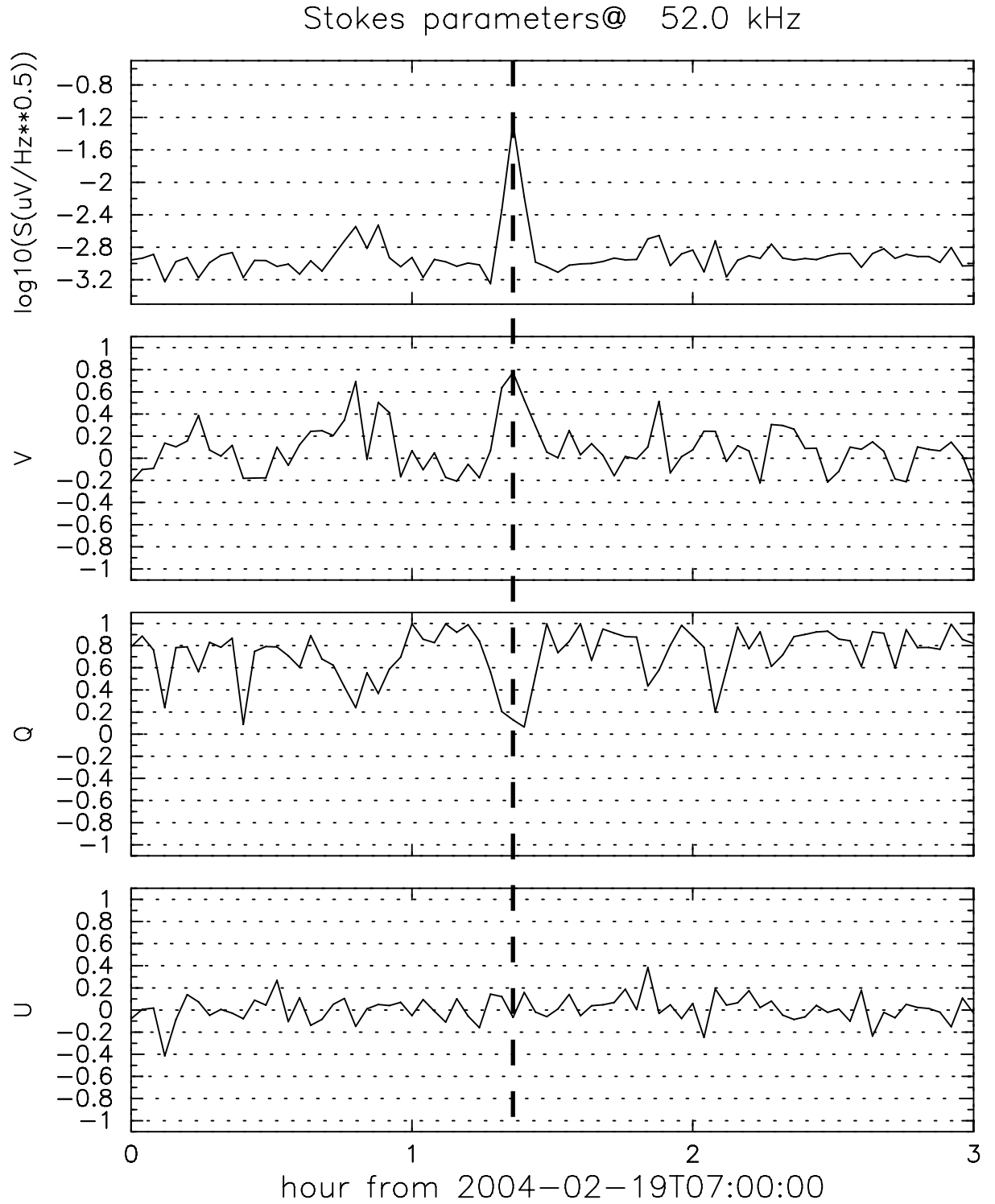


**Figure 4.7:** Stokes parameters at 52 kHz observed by RAR at 7–10 h on 19 Feb. 2004. Format of this figure is the same as that of Figure 4.6 except for the horizontal axis, which indicates the time of 3 hours from 7 h on 19 Feb. Vertical broken line shows the time when the intensity of a QP burst pulse reached the maximum.

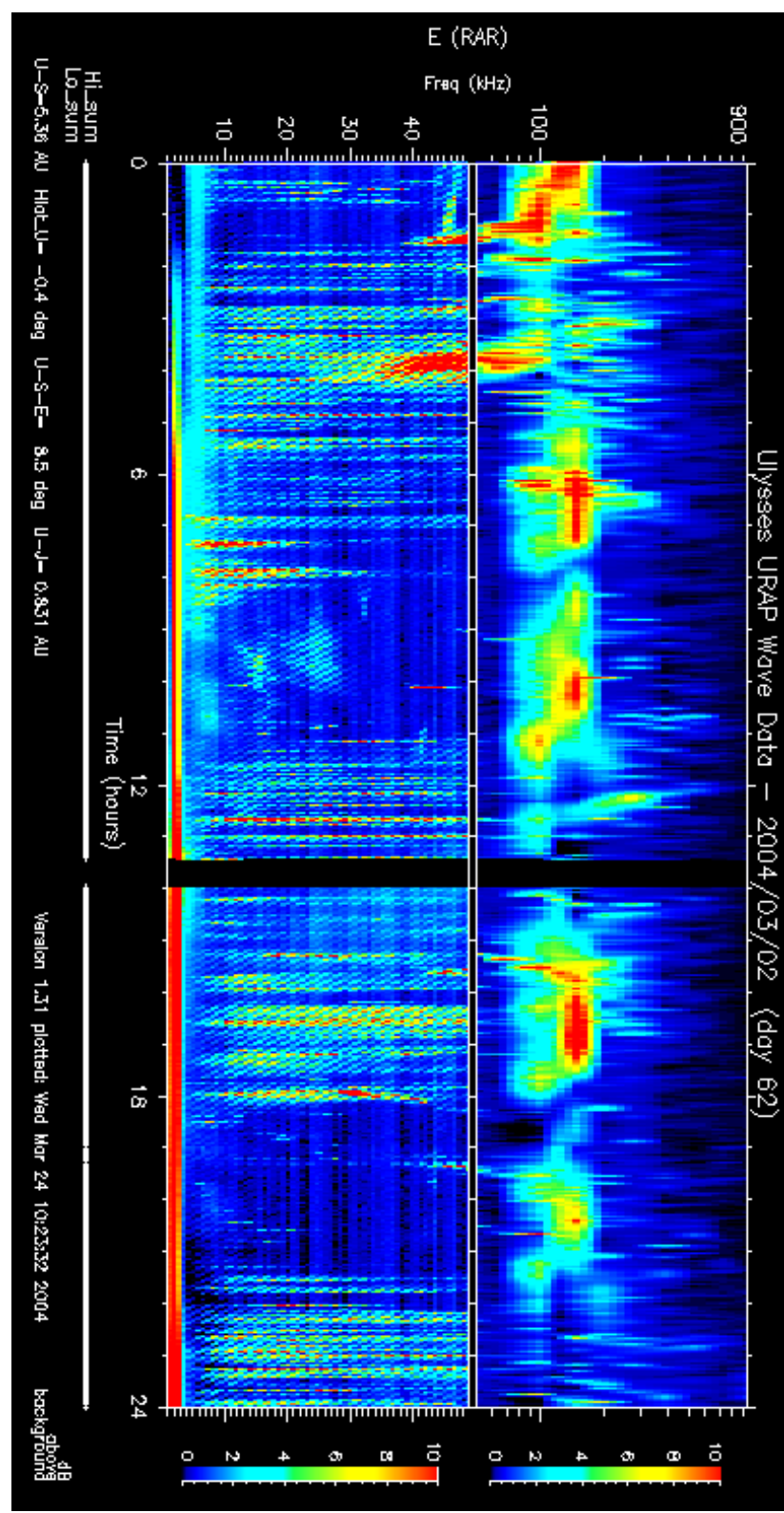


**Figure 4.8:** Dynamic spectra showing the QP bursts observed by Ulysses on 2 Mar. 2004 with the same format as that of Figure 4.5 ([http://urap.gsfc.nasa.gov/data\\_access.html](http://urap.gsfc.nasa.gov/data_access.html)). Jovigraphic latitude, local time, and a distance of Ulysses from Jupiter were  $+35^\circ$ , 17.3 h, and 0.83 AU, respectively.

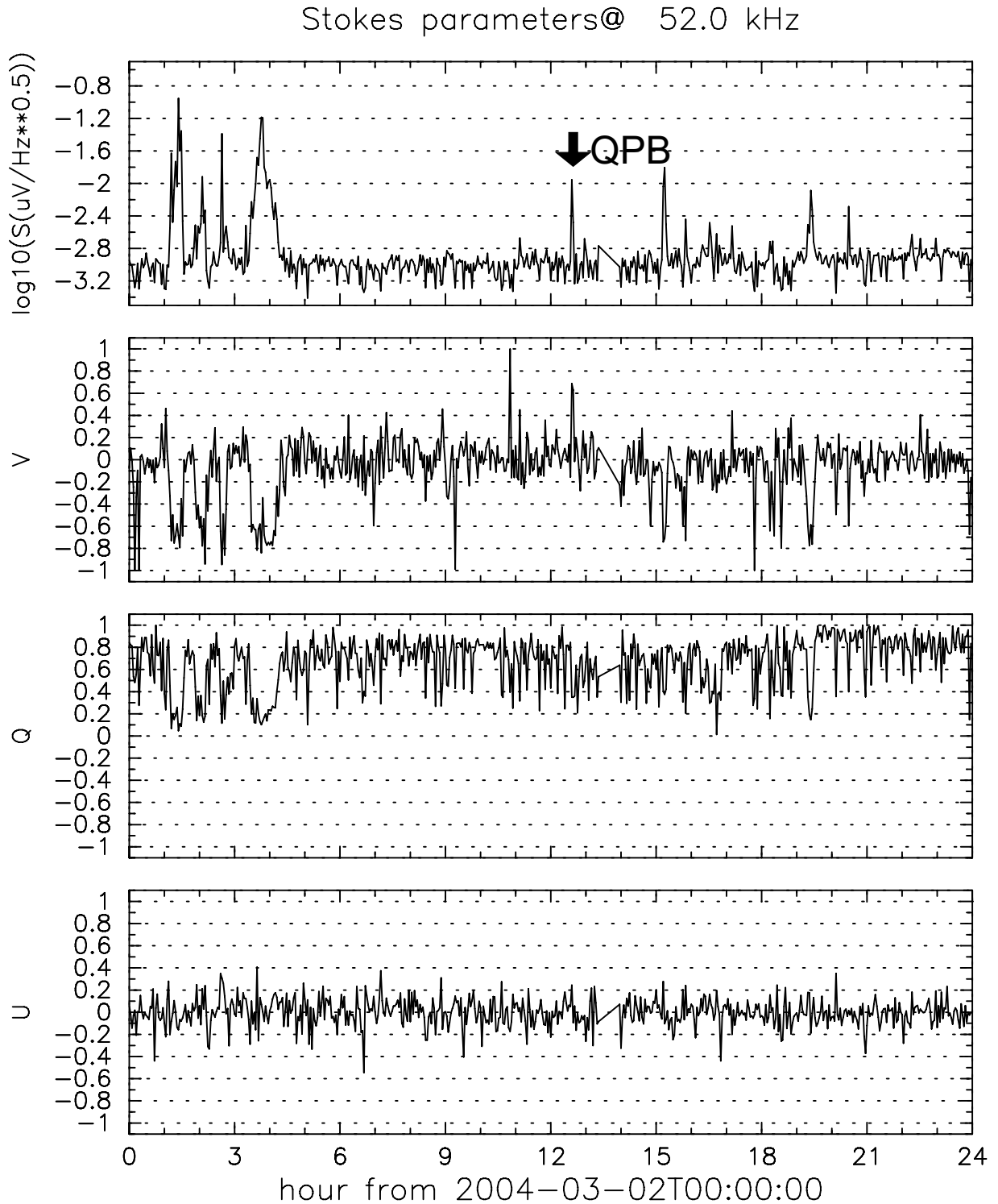


**Figure 4.9:** A plot of Stokes parameters at 52 kHz observed by RAR on 2 Mar. 2004 with the same format as that of Figure 4.6.

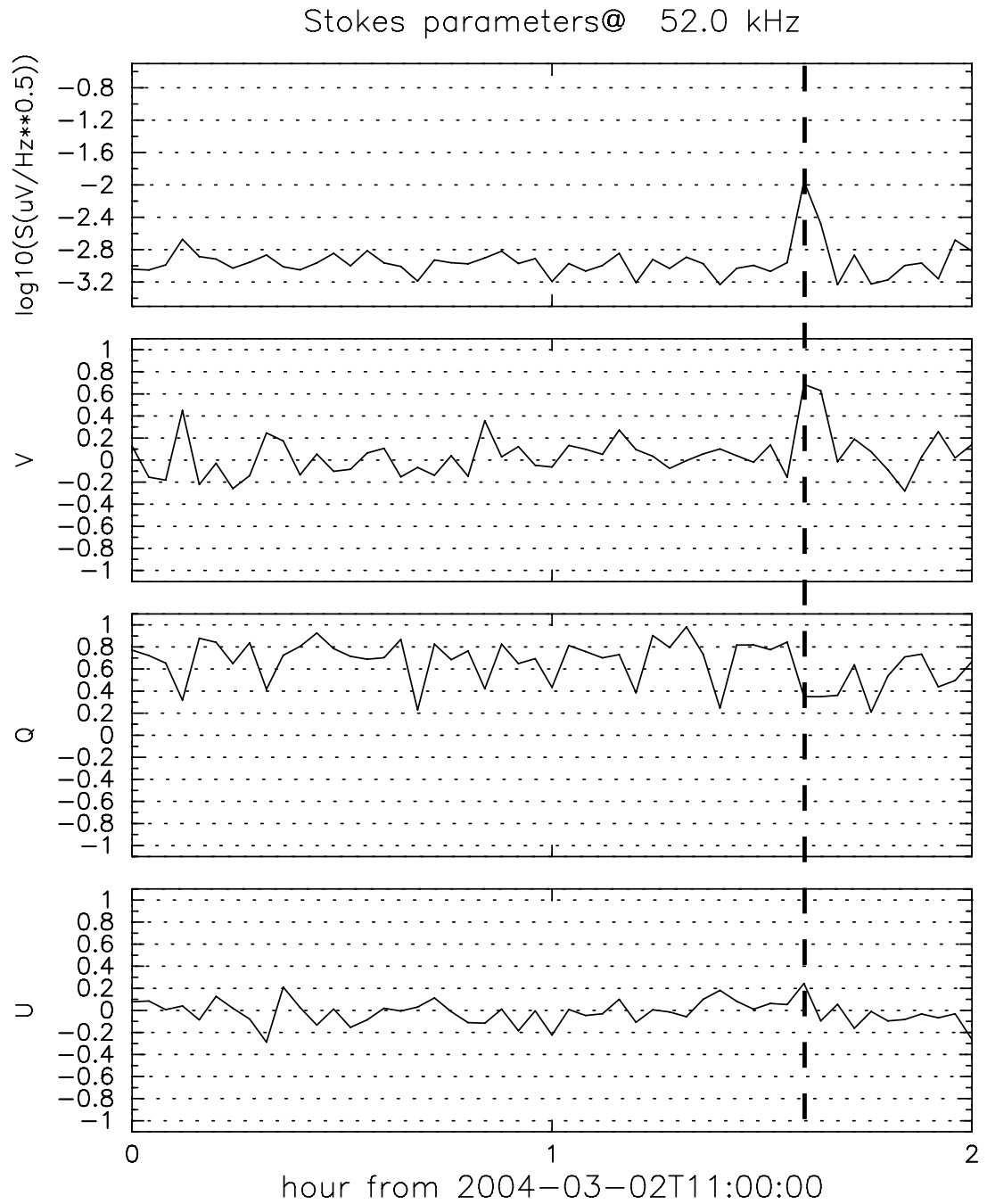


**Figure 4.10:** A plot of Stokes parameters at 52 kHz observed by RAR on 2 Mar. 2004 with the same format as that of Figure 4.7 except for horizontal axis showing the time of 2 hours from 11 h on 2 Mar.

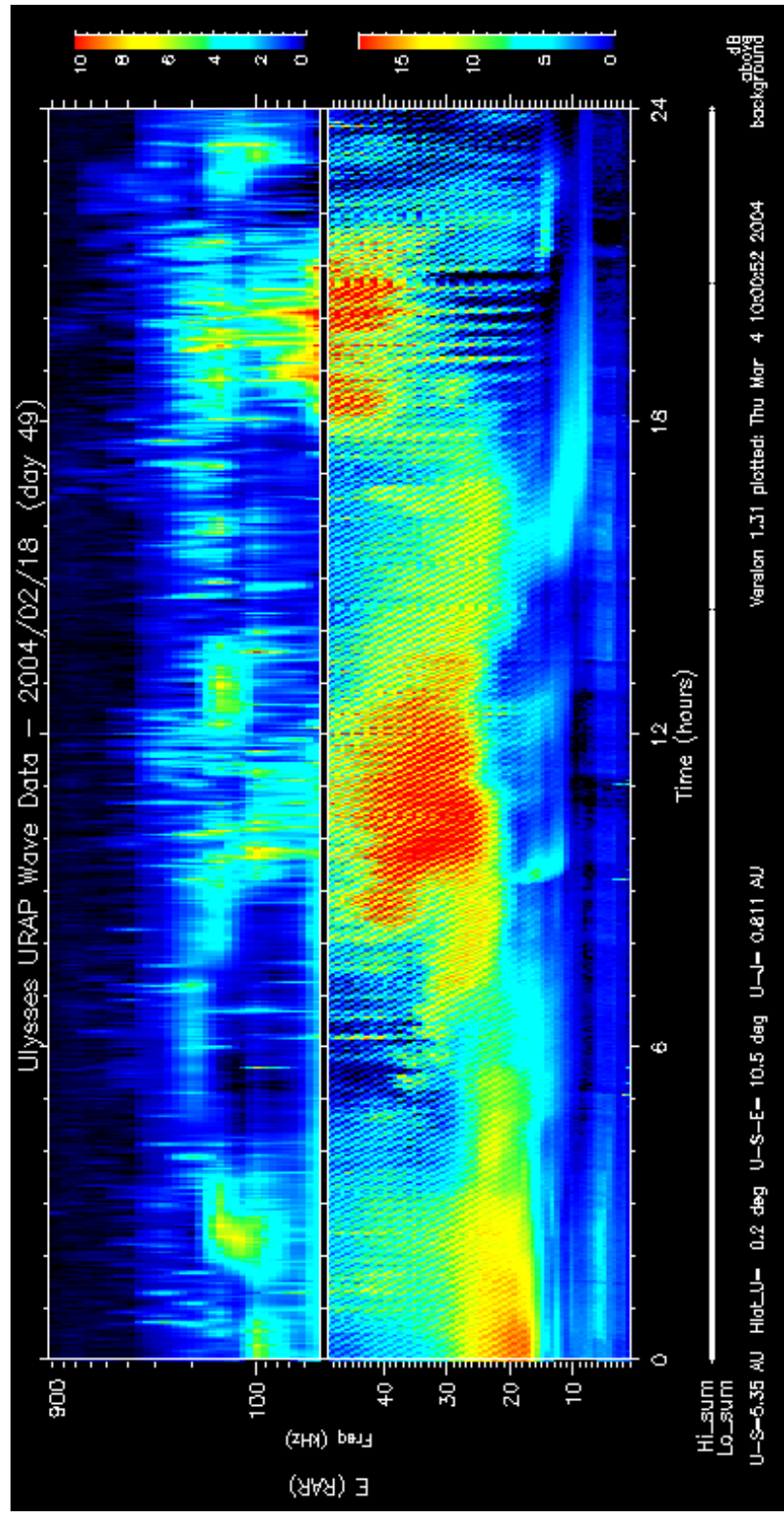


**Figure 4.11:** Dynamic spectra showing the QP bursts observed by Ulysses on 18 Feb. 2004 with the same format as that of Figure 4.5 (<http://urap.gsfc.nasa.gov/data.access.html>). Jovigraphic latitude, local time, and a distance of Ulysses seen from Jupiter were  $+42^\circ$ , 17.1 h, and 0.81 AU, respectively.

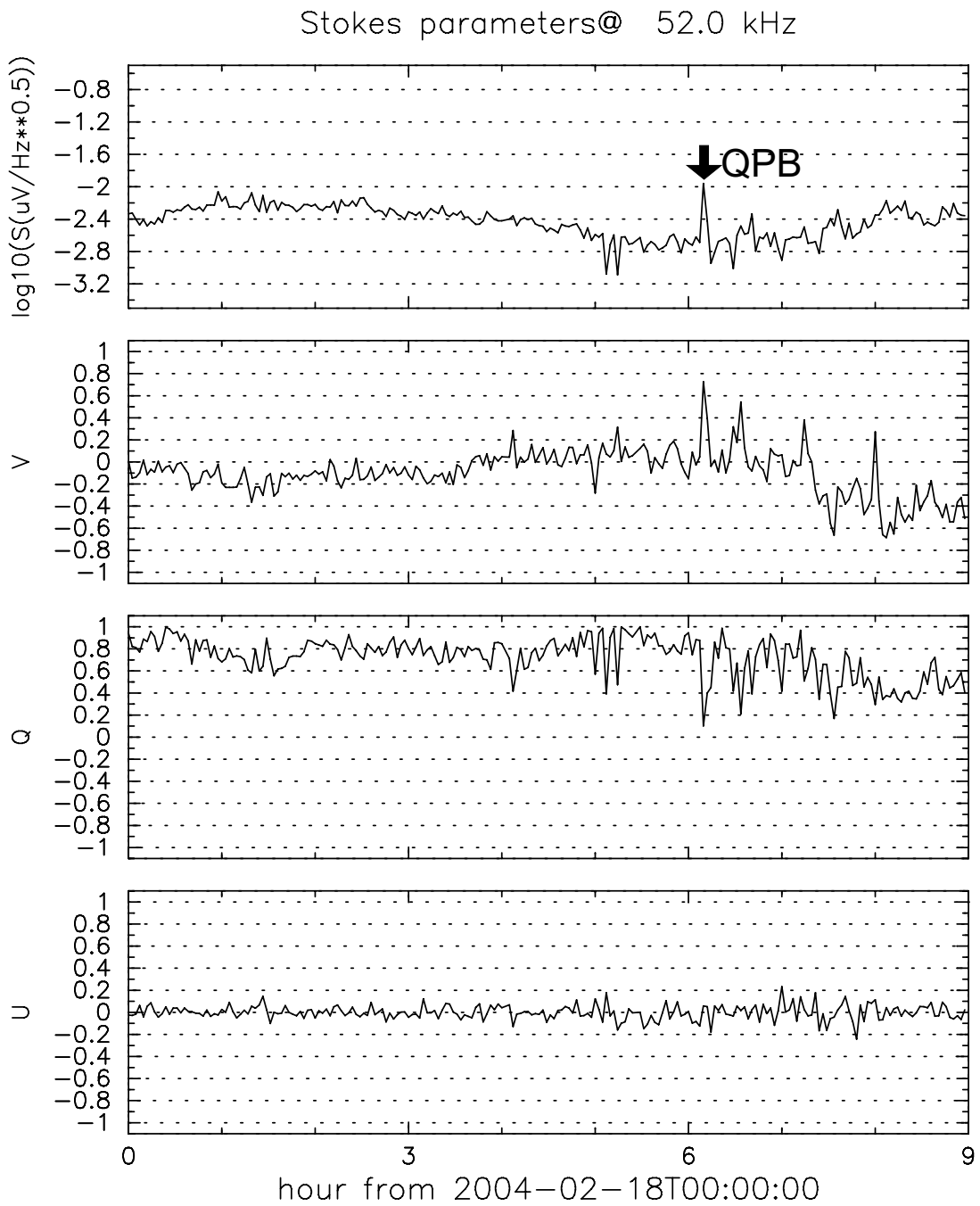


**Figure 4.12:** A plot of Stokes parameters at 52 kHz observed by RAR on 18 Feb. 2004 with the same format as that of Figure 4.6 except for horizontal axis showing the time of 9 hours from 0 h on 18 Feb.

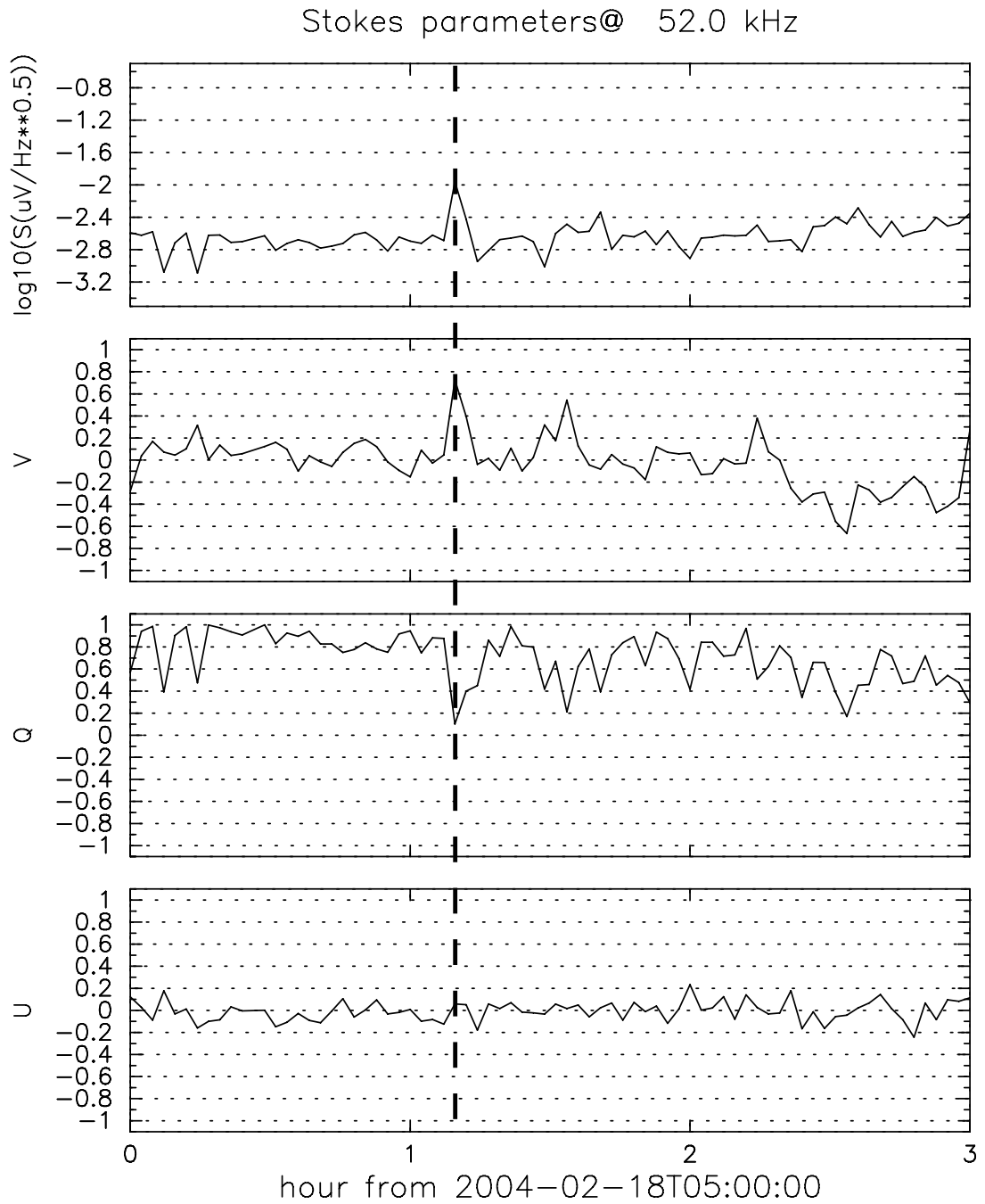


**Figure 4.13:** A plot of Stokes parameters at 52 kHz observed by RAR on 18 Feb. 2004 with the same format as that of Figure 4.7 except for horizontal axis showing the time of 3 hours from 5 h to 8 h on 18 Feb.

In the present analysis, three events of QP bursts observed at northern high latitudes were analyzed. It was confirmed that these QP bursts were observed with a significance level of  $\sigma = 1.3\text{--}3.5$  and Stokes parameters of these events were  $V = +0.7\text{--}+0.8$ ,  $Q = 0\text{--}+0.4$ , and  $U = 0\text{--}+0.2$ . This means that QP bursts observed at northern high latitudes were LH circular polarized. These results suggest that QP bursts observed at northern high latitudes are L-O mode waves emitted from the north polar region, being consistent with the observed QP bursts from the southern hemisphere (MacDowall *et al.*, 1993). In Chapter 5, this suggestion is examined based on the ray tracing analysis, and in Chapter 6, the generation mechanisms of QP bursts are further discussed based on the theoretical approach.

## 4.3 Polarization Measurements and Direction Finding at Low Latitudes

### 4.3.1 Polarization Measurements at Low Latitudes

Figure 4.14 represents the dynamic spectra showing a typical event of the QP bursts observed by RPWS during Cassini's interplanetary cruise to Saturn just before the closest approach to Jupiter. On 22 Dec. 2000, QP bursts were observed at 20–30 kHz from 0 h to 6 h when Cassini was located at a distance of  $\sim 175 R_J$  from Jupiter in a local time of 13.3 h. The top panel of Figure 4.14 shows the dynamic spectra observed by RPWS at 0–8 h on 22 Dec. and the bottom panel is the spectral data with a signal-to-noise ratio of  $S/N > 20$  dB showing a QP burst event at 1–2 h. In this section, we analyzed such sufficiently-intense spectral signals, which have a signal-to-noise ratio larger than 20 dB as plotted in Figure 4.14.

Applying the polarization and direction finding techniques in Section 4.1 to these QP bursts, we derived four Stokes parameters as shown in Figure 4.15 corresponding to the event in the bottom panel of Figure 4.14. Stokes parameters  $V$  and  $Q$  at 25.9 kHz are plotted in the top panel and  $U$  and  $S$  are in the bottom panel. While significantly intense

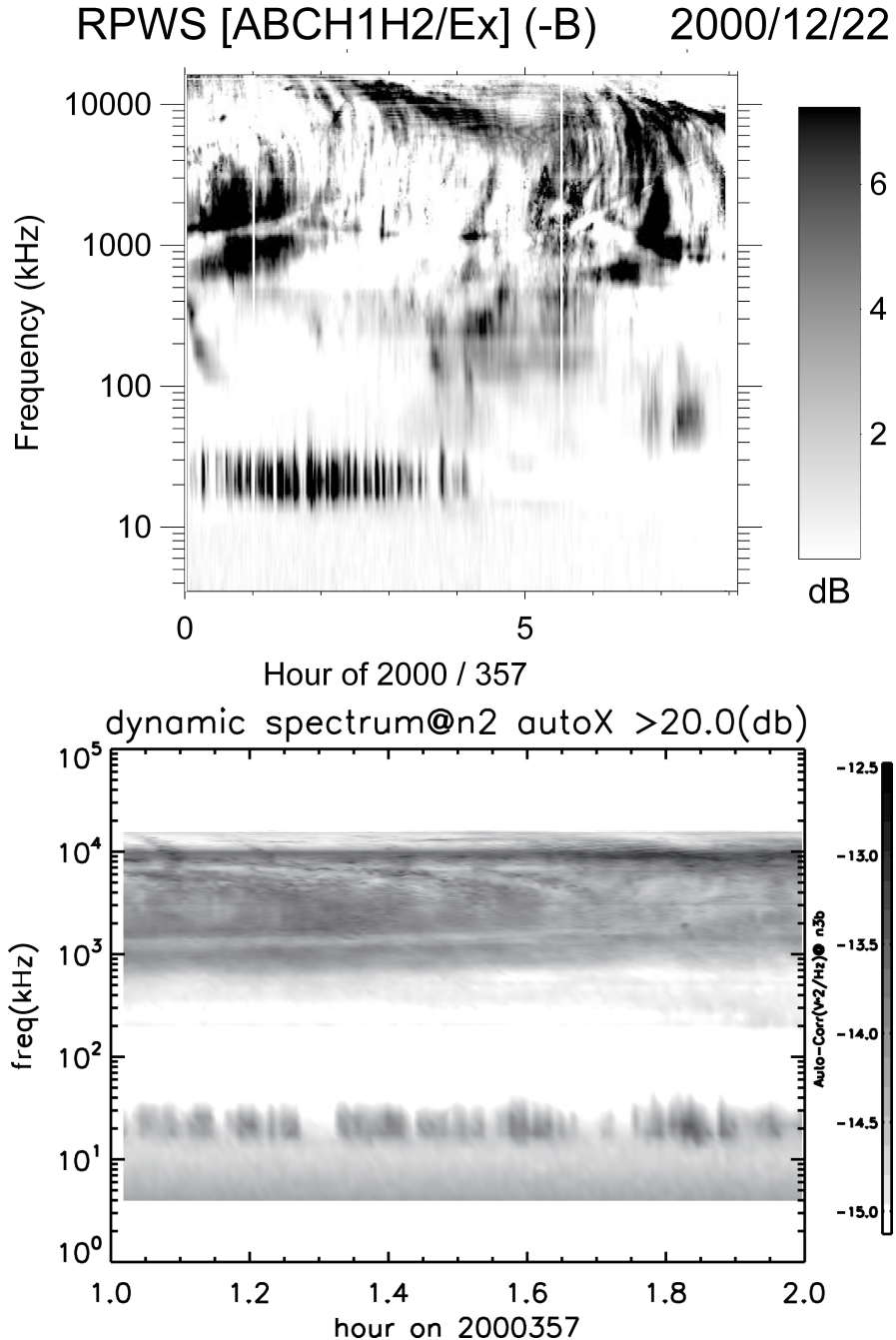


**Figure 4.14:** (top) Dynamic spectra observed by RPWS at 0–8 h on 22 Dec. 2000 during Cassini’s interplanetary cruise to Saturn, and (bottom) those with a signal-to-noise ratio of  $S/N > 20$  dB indicating a QP burst event at 1–2 h. Cassini was located at a distance of  $\sim 175 R_J$  from Jupiter in a local time of 13.3 h. Horizontal axes show time in hour and the vertical axes show frequencies in kHz. Black and white colors indicate the received power in dB.

QP bursts were observed, Stokes parameters  $V$ ,  $Q$ , and  $U$  were in the following range:  $V = +0.1 - +0.7$ ,  $Q = -0.4 - +0.2$ , and  $U = -0.5 - +0.1$ . These results indicate that QP bursts in this event were partially LH circular polarized.

Long-term observations by RPWS around the closest approach allowed us to take statistics of QP bursts' Stokes parameters. We detected QP bursts from the data points which had intense spectral signals with a signal-to-noise ratio of  $S/N > 20$  dB in a frequency range of 10–30 kHz. It was assumed that arrival directions of rays were located at the center of Jupiter because during almost all the analysis period, Cassini was far from Jupiter sufficiently to regard Jupiter as a point radio source. 44 pulse groups of QP bursts were identified during the analysis period from 1 Oct. 2000 to 31 Mar. 2001. Distribution of the detected data points with respect to the four Stokes parameters are plotted in Figure 4.16. The vertical axes indicate the number of the data and the horizontal axes show Stokes parameters. From the panel of  $S$ , it was found that the received power was the most frequently observed at  $-145 - -140$  dB, which is significantly higher than the background level ( $\sim -170$  dB). The panels of  $Q$  and  $U$  indicate that they were almost always equal to zero, thus the received waves were *not* linearly polarized. We interpreted the bimodal distribution in the panel  $V$  as the result that the data of each QP pulse were observed at  $V \sim +1$  and the data of interpulse period were observed at  $V \sim 0$ . Thus, we conclude that QP bursts observed by Cassini at low latitudes have the complete LH circular polarization (i.e.,  $(Q, U, V) = (0, 0, +1)$ ) in the statistics.

Figure 4.17 represents the dependence of Stokes parameters with respect to the Central Meridian Longitude (CML) of Cassini when QP bursts were observed. The same data sets as those in Figure 4.16 were used in this statistics. It should be noted that the received power  $S$  is significantly dependent on CML and the  $S$  values are large in a range of  $CML=180^\circ - 360^\circ$ . This characteristic is similar to that observed by Galileo at low latitudes in the Jovian magnetosphere (see Figure 3.4a). On the other hand,  $Q$  and  $U$  are constantly equal to zero at all the longitudes and  $V$  is mostly in a range of  $V = 0 - +0.6$ . This result means that intensities of QP bursts are dependent on CML and the polarizations

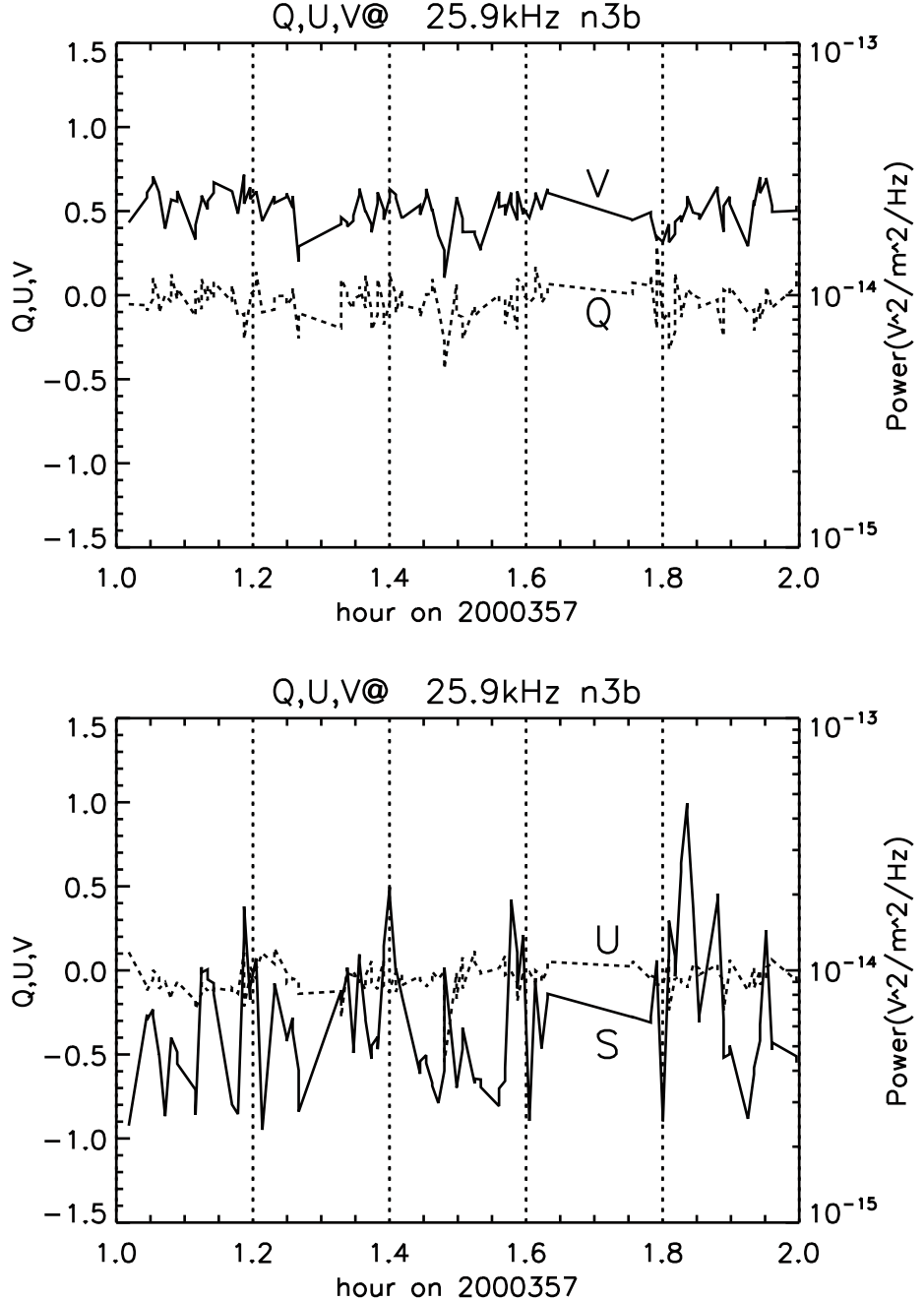


**Figure 4.15:** Stokes parameters of the QP bursts at 25.9 kHz observed at 1–2 h on 22 Dec. 2000 corresponding to the event in Figure 4.14. Solid and dotted lines in the top panel are  $V$  and  $Q$ , and those in the bottom panel are  $S$  and  $U$ , respectively. Signals with a signal-to-noise ratio of  $S/N > 20$  dB are plotted.

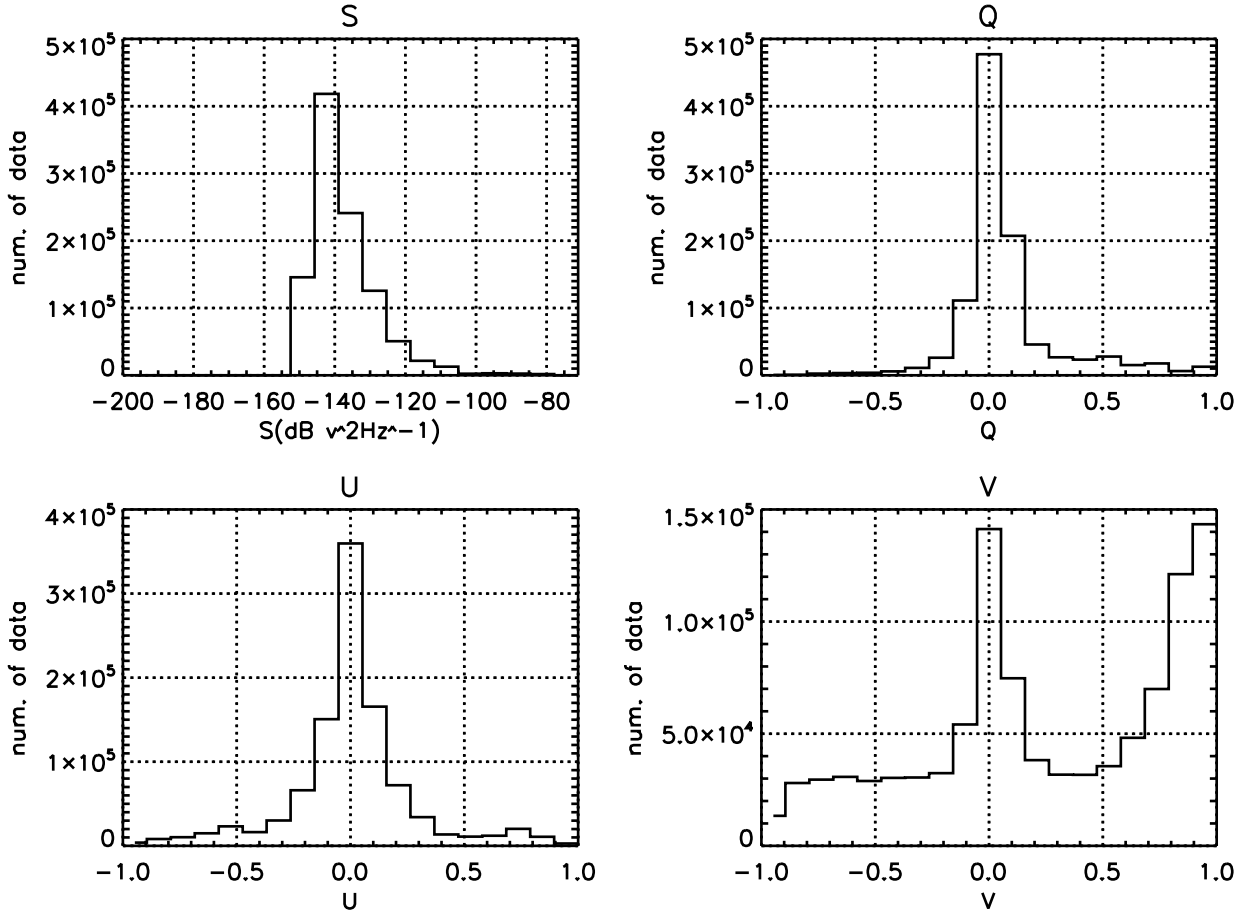


**Figure 4.16:** Histograms indicating Stokes parameter data of QP bursts, which were observed at 10–30 kHz with a signal-to-noise ratio of  $S/N > 20$  dB. 44 events were detected during the period in a period from 1 Oct. 2000 to 31 Mar. 2001. It was assumed that arrival directions of rays were located at the center of Jupiter because Cassini was far from Jupiter sufficiently to regard Jupiter as a point radio source during almost all the analysis period. Vertical axes indicate the number of the data and horizontal axes show Stokes parameters.

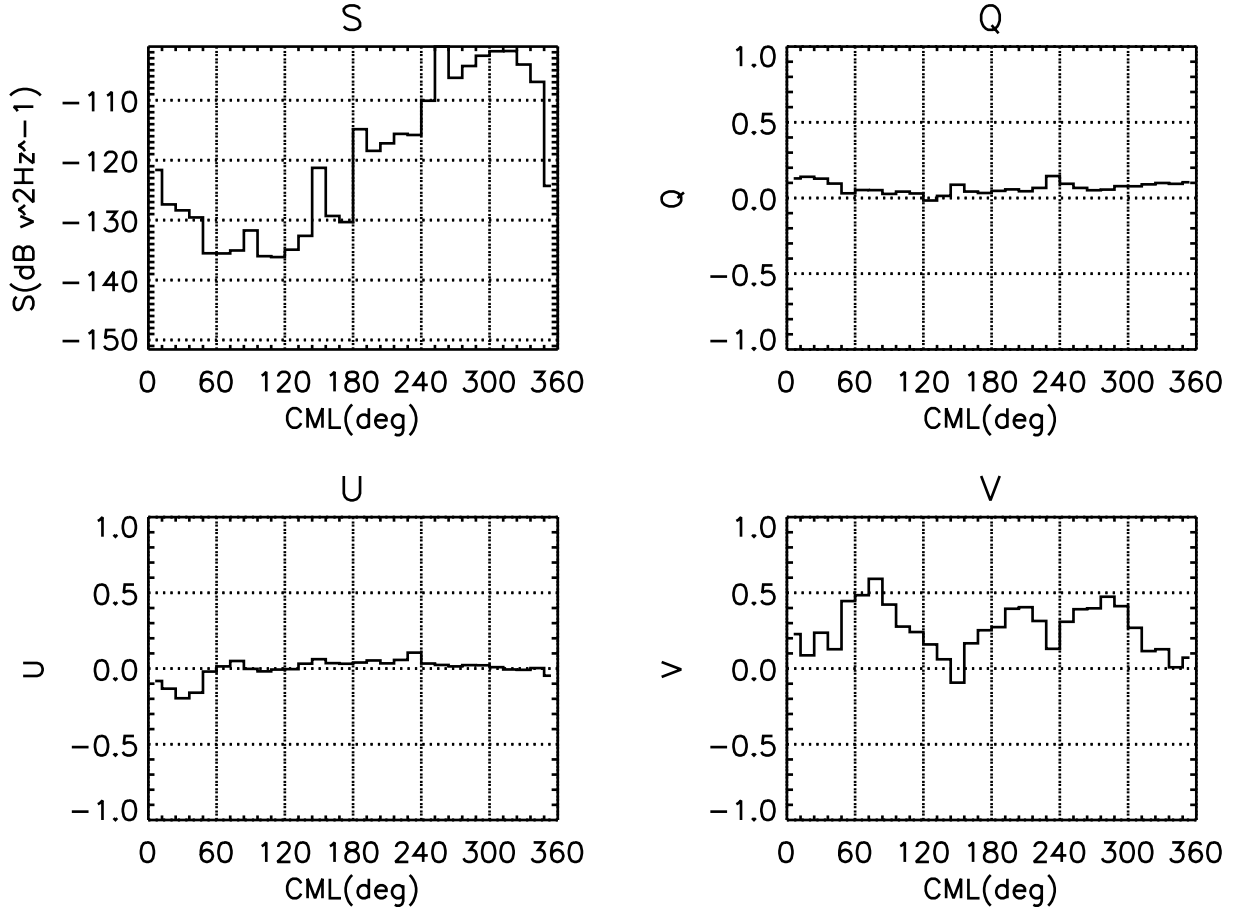


**Figure 4.17:** Statistical distribution of Stokes parameters with respect to the Central Meridian Longitude (CML) of Cassini when QP bursts were observed. The same data sets as those in Figure 4.16 are used in this statistics. Horizontal axes are CML of Cassini, and vertical axes indicate Stokes parameters.

are always LH circular at all longitudes.

Figure 4.18 represents the dependence of Stokes parameters on the sub-solar longitude (SSL) when QP bursts were observed in a similar format to that of Figure 4.17. The same data sets as those in Figure 4.16 were used in this statistics. It is obvious that  $S$  is significantly dependent on SSL with the large values in a range of  $SSL=310^\circ\text{--}490^\circ$ . This phase is almost the same as that of QP bursts observed by Galileo ( $SSL=300^\circ\text{--}480^\circ$ , see Figure 3.4b). Characteristics of  $Q$ ,  $U$ , and  $V$  are similar to those in Figure 4.17.

From these statistics, it is concluded that QP bursts observed by Cassini at low latitudes

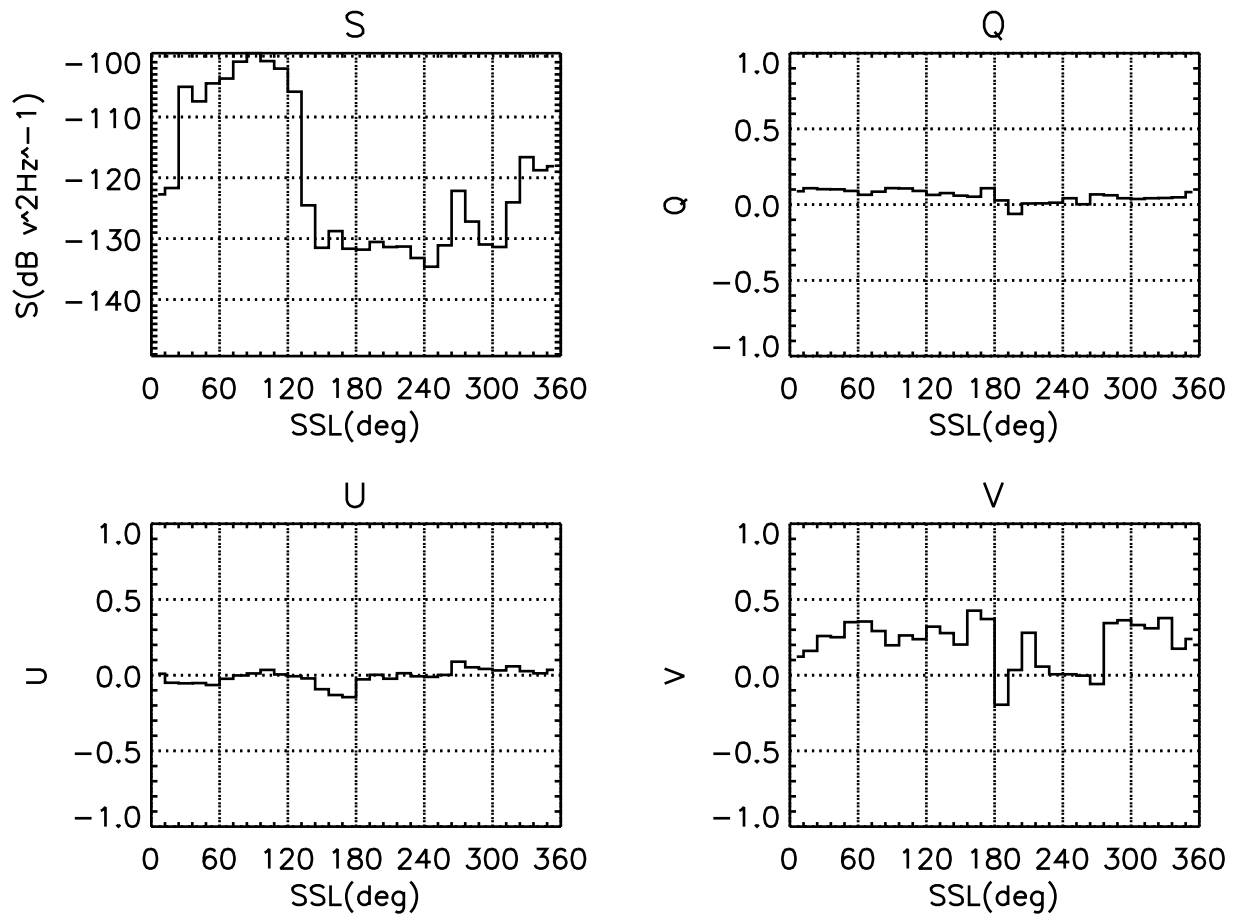


**Figure 4.18:** Statistical distribution of Stokes parameters with respect to the sub-solar longitude (SSL) when QP bursts were observed. The same data sets as those in Figure 4.16 are used in this statistics. Horizontal axes are SSL when QP bursts were observed, and vertical axes indicate Stokes parameters.

are always LH circular polarized without any dependence on CML and SSL, and they have the same SSL dependence as those observed by Galileo. This result imply that the rotational phase when QP bursts are generated is always constant, not changed in long-term period such as an annual time scale.

### 4.3.2 Direction Finding at Low latitudes

#### Angular Error Estimation

Before making the direction finding of QP bursts, we estimated angular errors of the direction finding based on the observations of the other Jovian radio components: Hectometric radiations (HOM) and narrowband kilometric radiations (nKOM). These two components were adopted because they have relatively larger intensities and source locations near Jupiter (see also Figure 1.10). Hectometric radiations are the MF range (0.3–3 MHz) radiations supposed to be emitted from the polar  $f_c$  surface, where the emission frequencies are approximately equal to the local cyclotron frequencies (a few  $R_J$  altitudes from Jovian surface in the MF range), and some supportive observation results have been reported (e.g., *Ladreiter et al.*, 1994). While, source regions of nKOM were found to be located in the outer edge of the Io plasma torus at a distance of 7–13  $R_J$  based on the direction findings by Ulysses (*Reiner et al.*, 1993). We performed the direction findings of HOM and nKOM when Cassini is far from Jupiter, regarding source regions of these radio components as a point radio source at Jupiter.

Dynamic spectra observed on 7 January 2001 are shown in Figure 4.19 including HOM and nKOM events. For the angular error estimation, We used the event of the intensification of HOM around 1 MHz at 1–3 h and that of nKOM around 150 kHz at 8–11 h.

Figure 4.20 represents the results of polarization measurements and direction findings of HOM. Figures 4.20a and b show dynamic spectra observed by RPWS and Stokes parameters at 675 kHz measured at 1.6–2.3 h on 7 January 2001 when Cassini was located at a distance of  $\sim 170 R_J$  from Jupiter in a local time of 18.5 h. Figure 4.20c is a result of the direction finding at 675 kHz performed at 1.6–2.3 h. The horizontal axis shows

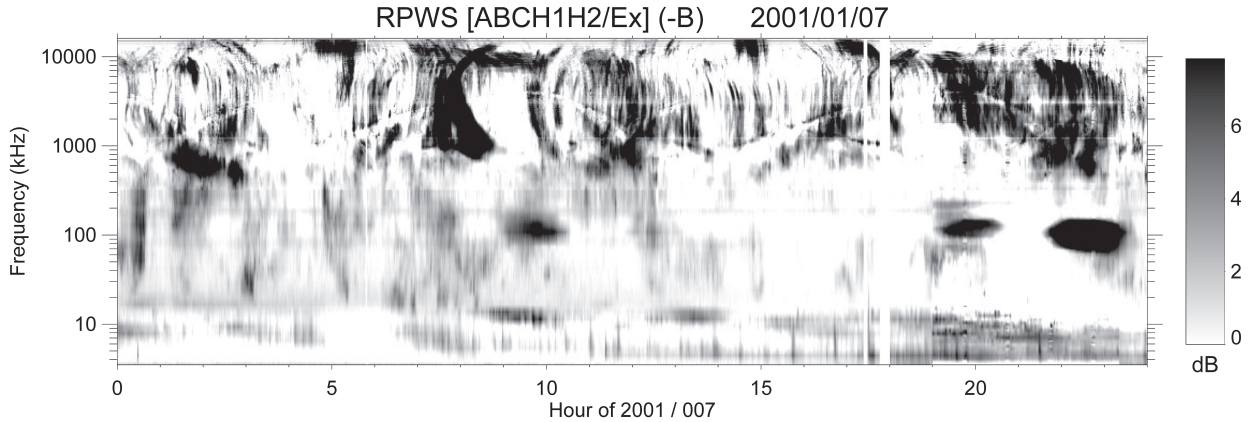


**Figure 4.19:** Dynamic spectra of Jupiter’s radio emissions observed by RPWS on 7 Jan. 2001.

angular distances (arcmin) from Jupiter in the east-west direction and the vertical axis is those in the north-south direction. Jupiter is located at the origin (0,0). One Jovian radius ( $=71492\text{ km}$ ) corresponds to an apparent diameter of 20.1 arcmin seen from Cassini. Figure 4.20d indicates the histograms showing the distribution of arrival directions of rays at 675 kHz. The horizontal axis is angular distances between the arrival direction of rays and Jupiter in arcmin, and vertical axis is the number of the data. Solid line indicates the absolute angular distances from Jupiter with the error bar annotated “total” corresponding to  $\pm 1\sigma$  ( $\sigma$ :standard deviation) and the average value of the arrival directions marked “\*”. Broken and dotted lines indicate the angular distances in the longitudinal and latitudinal directions (i.e., east-west and north-south directions), respectively. From Figure 4.20d, we found that arrival directions of the HOM event have some errors: e.g., the total angular distances have an offset error, which corresponds to the average direction of  $\sim 350$  arcmin ( $\sim 18 R_J$ ) from Jupiter, and a random error with a spread of  $\sigma \sim \pm 210$  arcmin ( $\sim \pm 10 R_J$ ). In the longitudinal and latitudinal directions, the offset errors are relatively small ( $\sim 10$  and -30 arcmin, respectively) and the random errors were  $\sim \pm 370$  arcmin ( $\sim \pm 18 R_J$ ) in longitudes and  $\sim \pm 180$  arcmin ( $\sim \pm 9 R_J$ ) in latitudes.

For reduction of the direction finding error, we assumed Stokes parameters  $Q$  and  $U$  to be zero (i.e., complete circular polarized) based on the statistics of the Stokes parameters

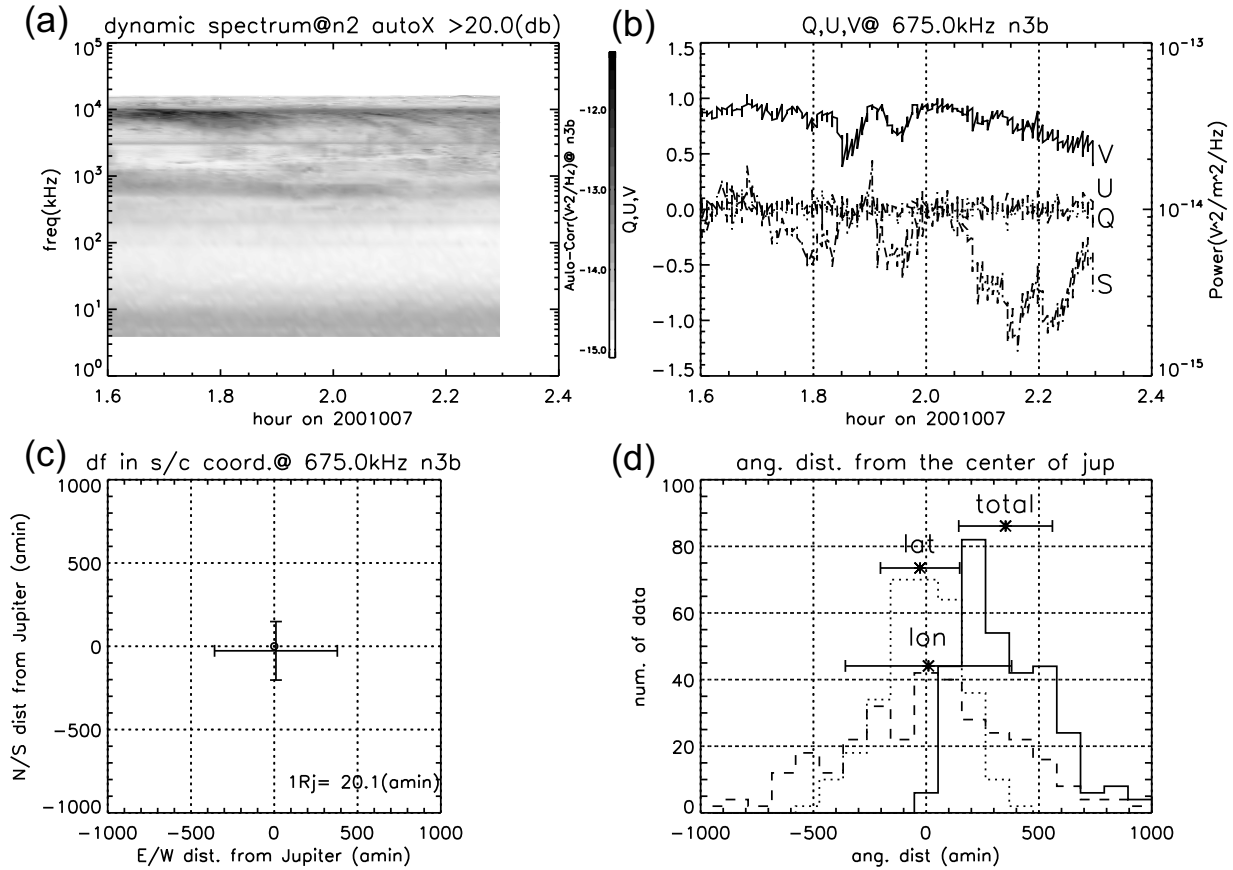


**Figure 4.20:** (a) Dynamic spectra observed by RPWS at 1.5–2.3 h on 7 Jan. 2001 when Cassini was located at a distance of  $\sim 170 R_J$  from Jupiter in a local time of 18.5 h. (b) Stokes parameters at 675 kHz measured at 1.6–2.3 h on 7 Jan. 2001. (c) A result of the direction finding at 675 kHz performed at 1.6–2.3 h on 7 Jan. 2001. Horizontal axis shows angular distances (arcmin) from Jupiter in the east-west direction and vertical axis is those in the north-south direction. One Jovian radius ( $=71492$  km) corresponds to an apparent diameter of 20.1 arcmin seen from Cassini. (d) Histograms showing the distribution of arrival directions at 675 kHz observed at 1.6–2.3 h on 7 Jan. 2001. Horizontal axis is angular distances between the arrival direction of rays and Jupiter in arcmin, and vertical axis is the number of the data. Solid line indicates the total angular distances from Jupiter with the error bar annotated “total” corresponding to  $\pm 1\sigma$  and the average value of the arrival directions marked “\*”. Broken and dotted lines indicate the angular distances in the longitudinal and latitudinal directions (i.e., east-west and north-south directions).

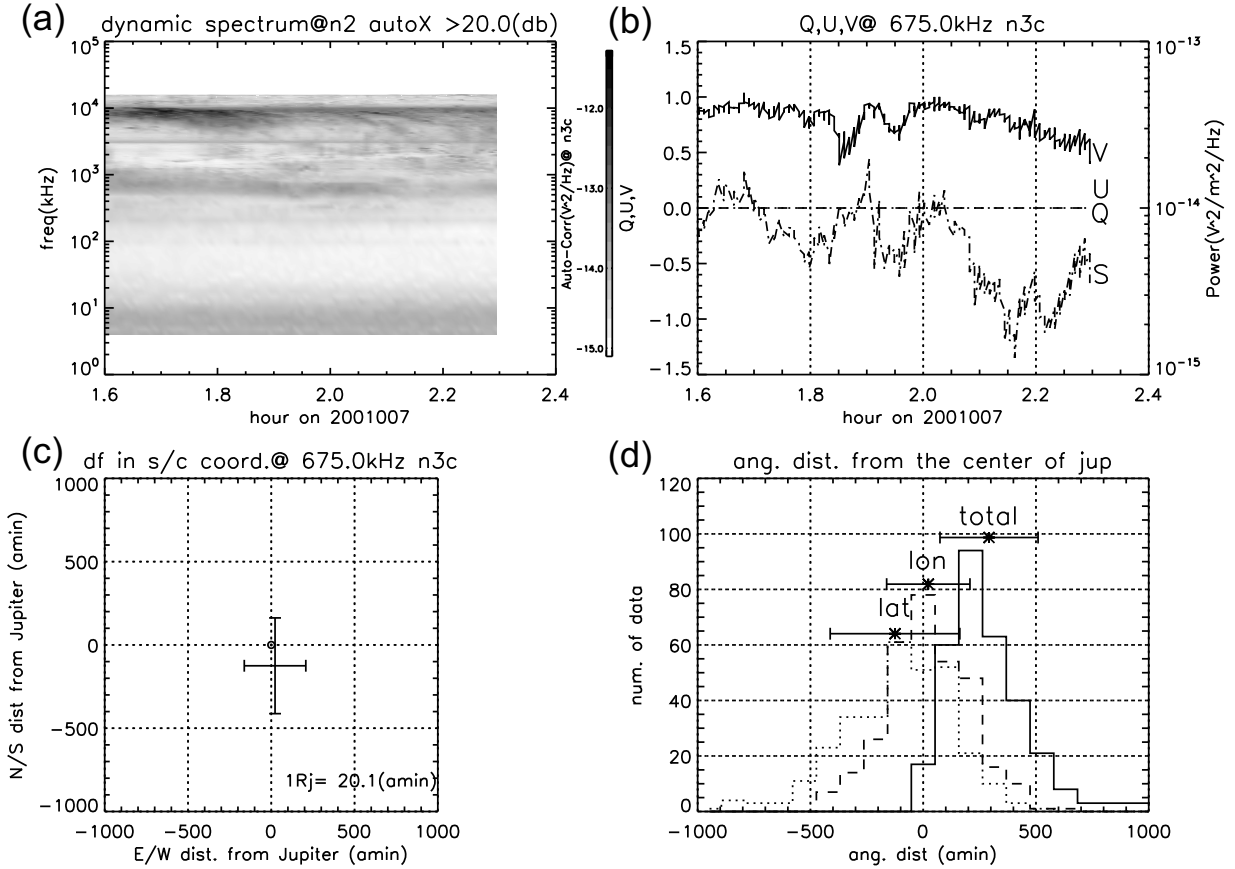


**Figure 4.21:** Polarization measurements and direction finding results at 675 kHz observed on 7 Jan. 2001 with the same format as Figure 4.20. Note that the polarization measurements and direction findings were performed assuming to be  $Q, U = 0$ : i.e., the received waves are completely circular polarized.

shown in Figure 4.16 in Section 4.3.1. This assumption reduces the free components of the wave parameter vector  $\mathbf{X} = (S, Q, U, V, \theta, \phi)$  to  $(S, V, \theta, \phi)$  and improve the accuracy of the direction finding. The improved results are represented in Figure 4.21 with the same format as Figure 4.20. It is notable that the offset error of the total angular distances was reduced from  $\sim 350$  arcmin to  $\sim 290$  arcmin, and the random error of the longitudinal errors was also dropped from  $\sim 370$  arcmin to  $\sim 180$  arcmin.

Figure 4.22 and 4.23 are the results of polarization measurements and direction findings performed for nKOM at 116.6 kHz on 7 January 2001. In LF range (30–300 kHz), where RPWS gives the best performance in the direction finding, the offset errors and random

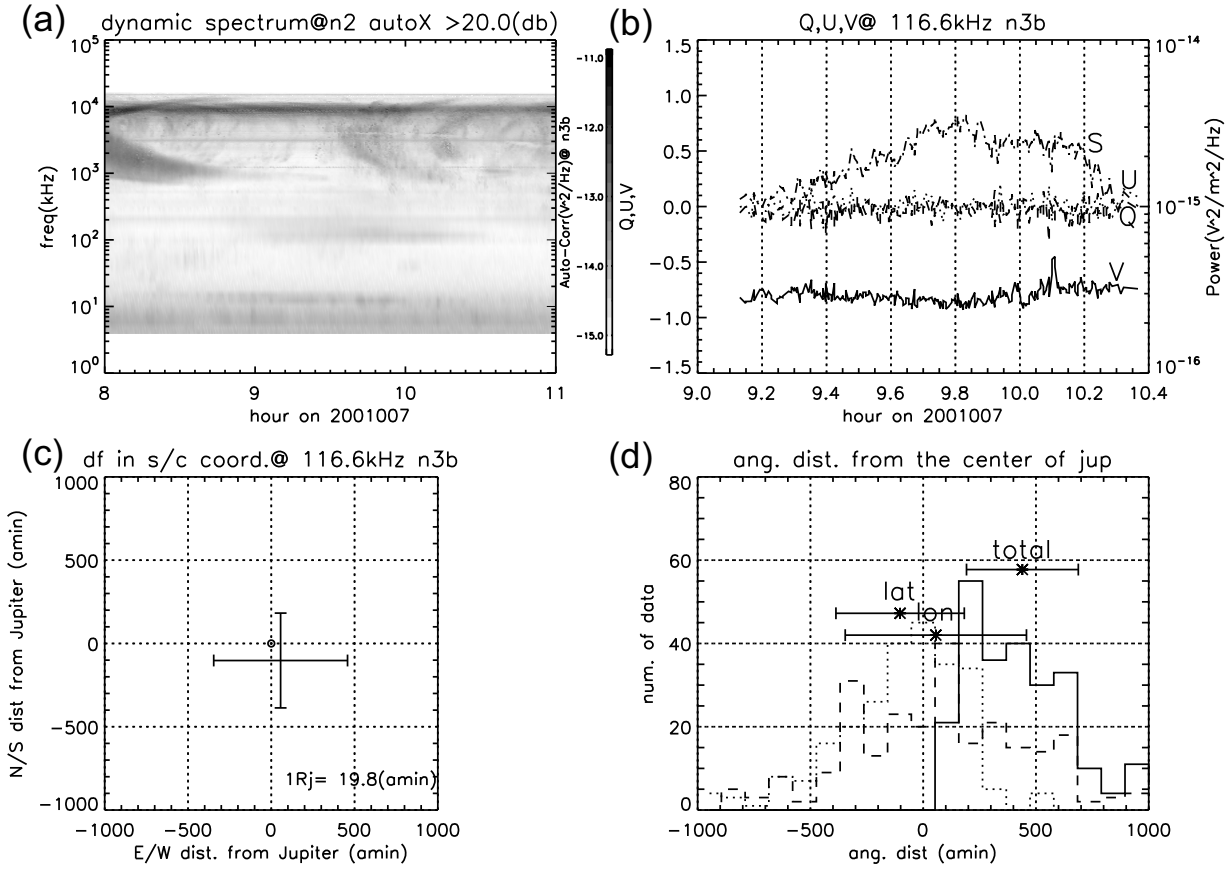


**Figure 4.22:** Polarization measurements and direction finding results at 116.6 kHz observed on 7 Jan. 2001 with the same format as Figure 4.20.

errors were also improved significantly under the assumption of  $Q, U = 0$ . For the total angular distance of nKOM, the offset error was reduced from 440 arcmin to 290 arcmin, and the random error was improved from  $\pm 250$  arcmin to  $\pm 140$  arcmin. The random error in longitudes and latitudes were also reduced from  $\pm 400$  to  $\pm 210$  arcmin and from  $\pm 280$  to  $\pm 230$ , respectively.

Tables 4.2–4.5 summarize the errors of the direction finding for each radio component derived from the observations on 7 January 2001. From these results, we conclude that direction finding errors are improved significantly if Stokes parameters  $Q$  and  $U$  are assumed to be zero: i.e., completely circular polarized waves. Particularly, the offset and random errors of the total angular distance are reduced to 290 arcmin and less than 220 arcmin,

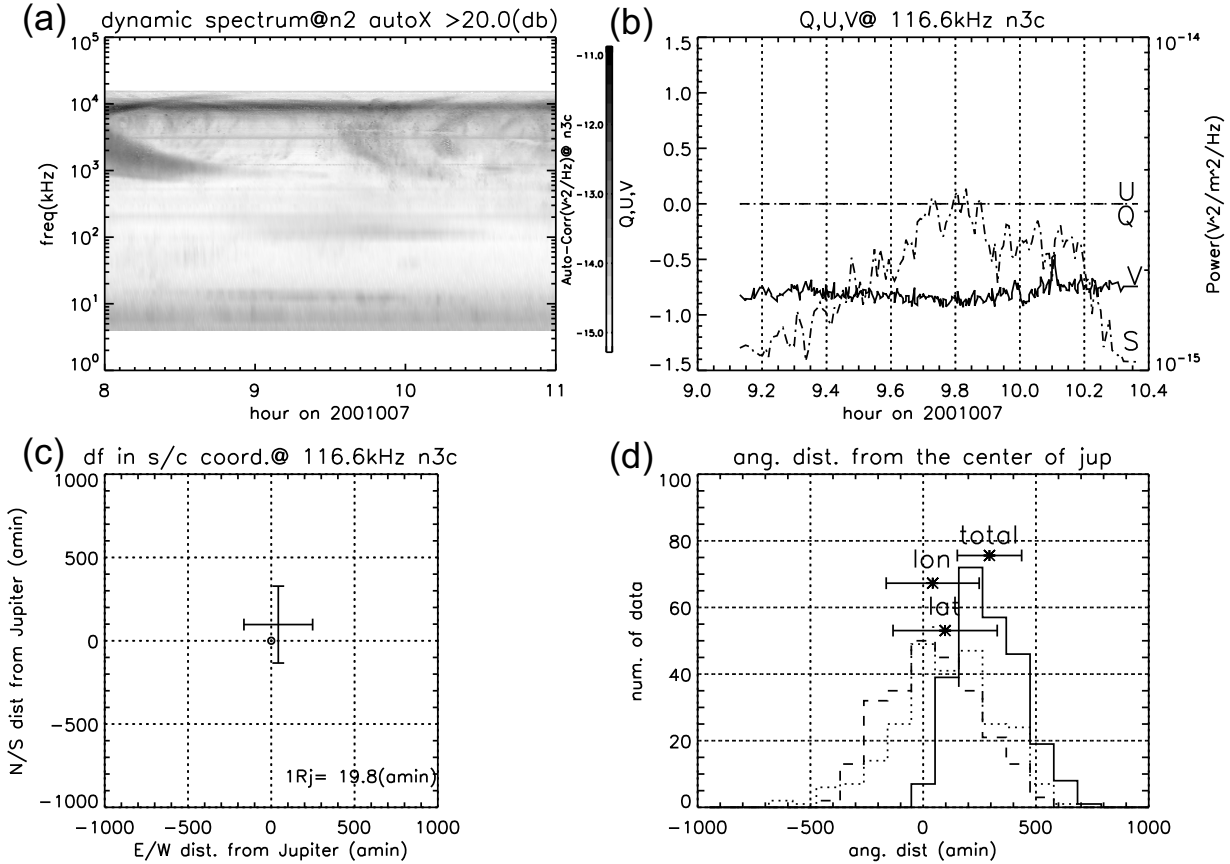


**Figure 4.23:** Polarization measurements and direction finding results at 116.6 kHz observed on 7 Jan. 2001 with the same format as Figure 4.20. Note that the polarization measurements and direction findings were performed assuming to be  $Q, U = 0$ : i.e., the received waves are completely circular polarized.

**Table 4.2:** Accuracy of the direction finding at 675 kHz on 7 Jan. 2001 under no assumption

$f = 675 \text{ kHz}, Q, U \neq 0$		
	offset (arcmin)	$1\sigma$ (arcmin)
total	350	210
longitude	+10	370
latitude	-30	180

**Table 4.4:** Accuracy of the direction finding at 116.6 kHz on 7 Jan. 2001 under no assumption

$f = 116.6 \text{ kHz}, Q, U \neq 0$		
	offset (arcmin)	$1\sigma$ (arcmin)
total	440	250
longitude	+60	400
latitude	-100	280

**Table 4.3:** Accuracy of the direction finding at 675 kHz on 7 Jan. 2001 under the assumption of  $Q, U = 0$ 

$f = 675 \text{ kHz}, Q, U = 0$		
	offset (arcmin)	$1\sigma$ (arcmin)
total	290	220
longitude	+20	180
latitude	-120	290

**Table 4.5:** Accuracy of the direction finding at 116.6 kHz on 7 Jan. 2001 under the assumption of  $Q, U = 0$ 

$f = 116.6 \text{ kHz}, Q, U = 0$		
	offset (arcmin)	$1\sigma$ (arcmin)
total	290	140
longitude	+40	210
latitude	+100	230

respectively.

### Direction Finding of QP bursts

Figure 4.24 represents a direction finding result of the QP bursts at 25.9 kHz observed on 22 Dec. 2000, corresponding to the same event as that in Figure 4.14 and 4.15. Formats of Figure 4.24 are the same as panel (c) and (d) in Figure 4.20. It should be noted that the direction finding analysis of this event was performed in *Hospodarsky et al.* (2004), however, the accuracy of arrival directions was not discussed. On the other hand, this study discusses the accuracy of arrival direction of QP bursts comparing with the point radio sources described above.

Because Cassini was located in a local time of 13.3 h at a distance of  $\sim 175 R_J$  from Jupiter during the event, negative longitudes (left side of the top panel in Figure 4.24) correspond to the sunward direction, and positive longitudes (right side) to the tailward direction. Figure 4.24 indicates that apparent arrival directions of QP bursts are deviated toward the north-west direction from Jupiter: i.e., they apparently arrived from dayside of

the high latitudinal region of Jupiter.

We applied the assumption of  $Q, U = 0$  to the direction finding for QP bursts because those radio components are almost completely circular polarized in statistics as shown in Section 4.3.1. Under the assumption, errors in the arrival directions are considerably reduced as shown in Figure 4.25. The average of the total angular distances between Jupiter and rays is  $\sim 850$  arcmin, which corresponds to an apparent diameter of  $\sim 46R_J$ . From the results of error estimations described above, this average direction far exceeds the estimated offset error of 290 arcmin (see Tables 4.3 and 4.5). In addition, spreads of the arrival directions are  $\sim \pm 280$  arcmin ( $\sim \pm 14 R_J$ ) in longitudes and  $\sim \pm 190$  ( $\sim \pm 10 R_J$ ) arcmin in latitudes (a spread in total angular distances is  $\sim 180$  arcmin), which are comparable to the direction errors of HOM and nKOM as indicated in Tables 4.3 and 4.5. This means that QP bursts of this event apparently arrived from the restricted region significantly distant from Jupiter ( $\sim 46R_J$ ) seen from Cassini.

Direction finding results of another QP burst event are shown in Figures 4.26–4.28. This event was observed when Cassini was at a distance of  $166 R_J$  from Jupiter in a local time of 13.6 h on 23 Dec. 2000. Under the assumption of  $Q, U = 0$ , the average value and spreads of the total angular distance were found to be  $\sim 1200$  arcmin ( $\sim 58 R_J$ ) and  $\sim \pm 410$  ( $\sim \pm 20 R_J$ ) arcmin, respectively.

From above direction finding results, we conclude that QP bursts which were observed at low latitudes in the interplanetary space have the arrival directions significantly distant from Jupiter. Previous theoretical studies proposed that some planetary radio emissions, such as auroral radio emissions from the polar region, are generated at the characteristic altitudes where the local cyclotron frequency ( $f_c$ ) or plasma frequency ( $f_p$ ) equal to the emission frequencies (e.g., Wu and Lee, 1979; Oya, 1974). However, the directions of QP bursts were at a distance of  $46 R_J$  (at 25.9 kHz) or  $58 R_J$  (at 14.7 kHz) from Jupiter, which are quite higher than the characteristic altitudes: e.g., magnetic field and plasma distribution models of the Jovian magnetosphere predict that the altitude of  $f_c = 20$  kHz is about  $\sim 10 R_J$  and the altitude of  $f_p = 20$  kHz is  $\sim 2 R_J$ , respectively.

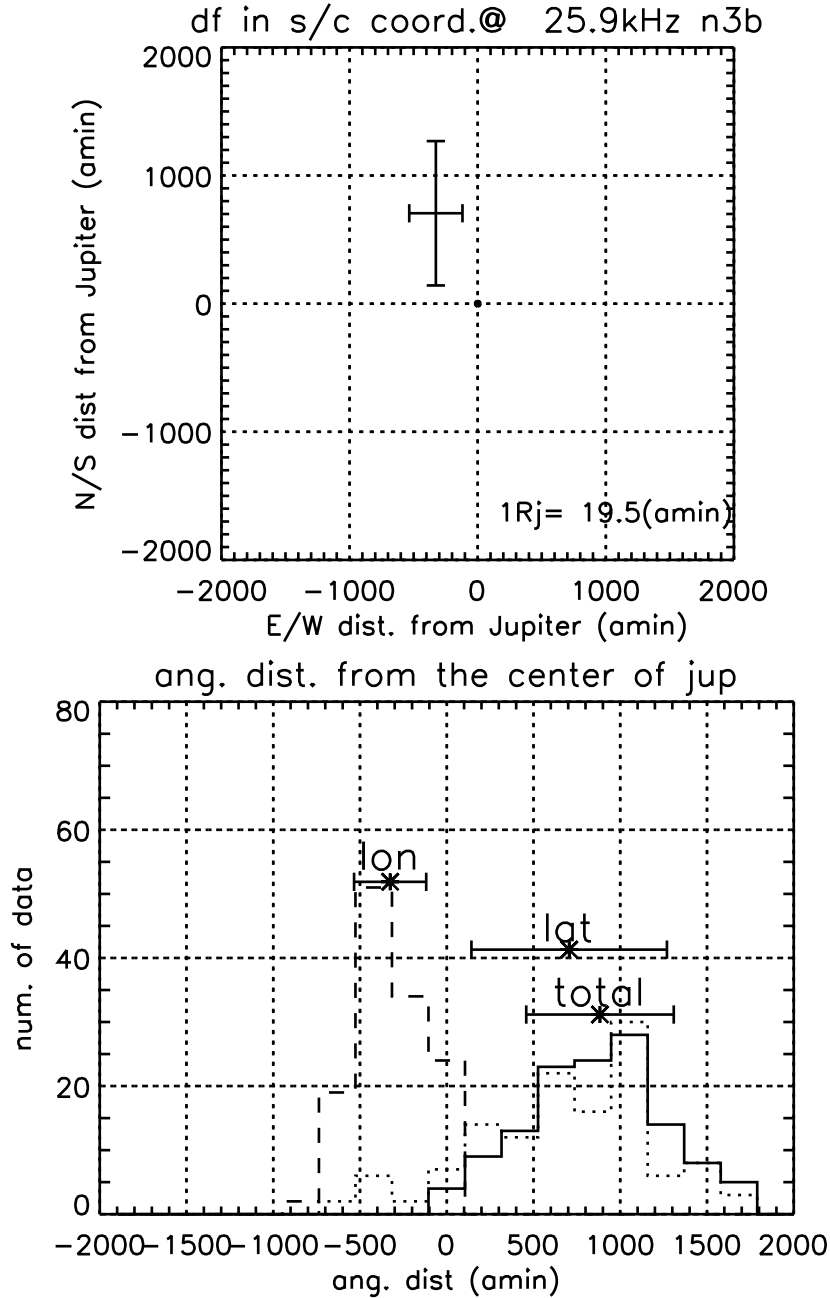


**Figure 4.24:** (top) A result of direction finding at 25.9 kHz performed at 1–2 h on 22 Dec. 2000, when Cassini was located at a distance of  $\sim 175$  R<sub>J</sub> from Jupiter in a local time of 13.3 h, corresponding to the event shown in Figures 4.14 and 4.15. Horizontal axis shows angular distances (arcmin) from Jupiter in the east-west direction and vertical axis is those in the north-south direction. Jupiter is located at the origin (0,0). One Jovian radii corresponds to an apparent diameter of 19.5 arcmin seen from Cassini. (bottom) Histograms showing the distribution of arrival directions at 25.9 kHz observed at 1–2 h on 22 Dec. 2000. Horizontal axis is angular distances between the arrival direction of rays and Jupiter in arcmin. Solid line indicates the total angular distances from Jupiter with the error bar annotated “total” corresponding to  $\pm 1\sigma$  and the average value of the arrival directions marked “\*”. Broken and dotted lines indicate the angular distances in the longitudinal and latitudinal directions (i.e., east-west and north-south directions), respectively.

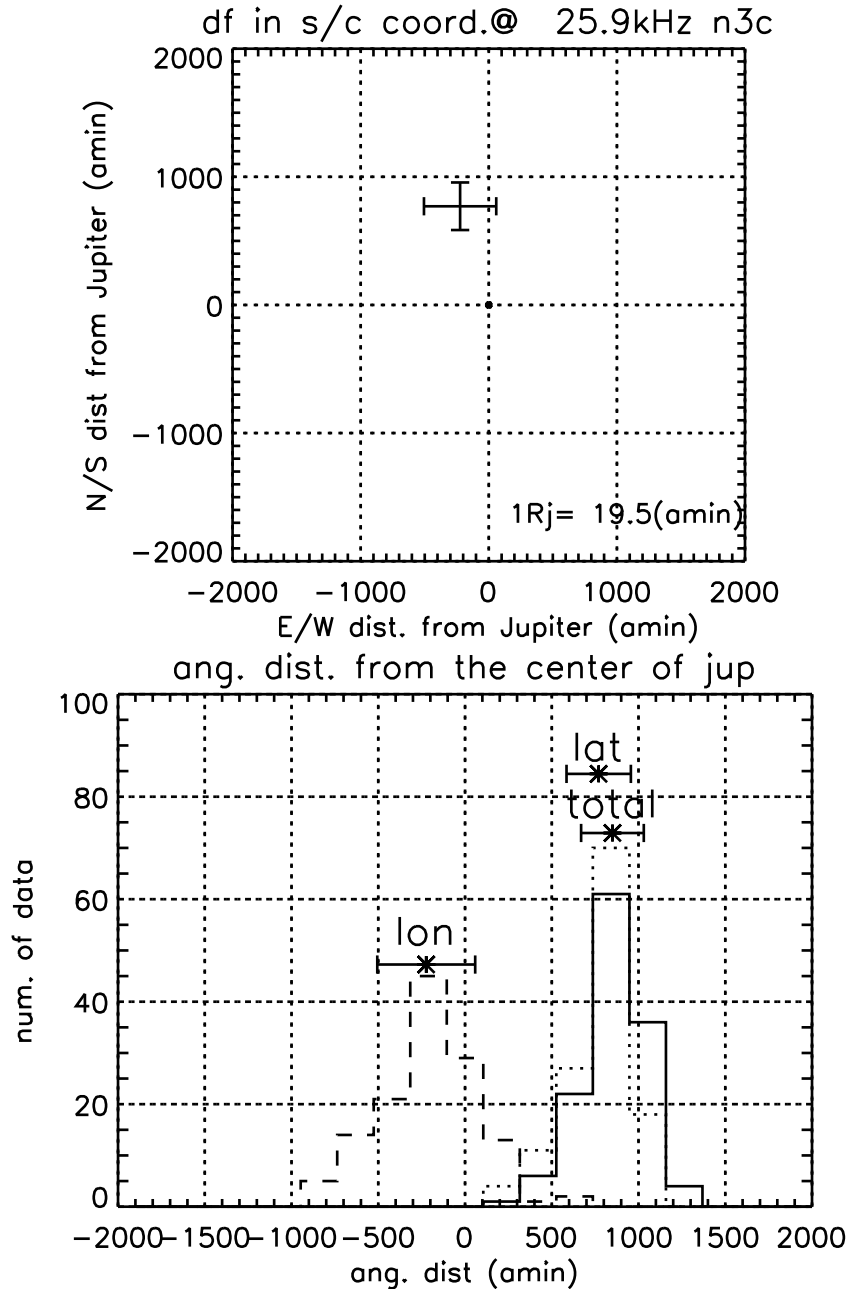


**Figure 4.25:** Direction finding results at 25.9 kHz observed on 22 Dec. 2000 with the same format as Figure 4.24. Note that the direction findings were performed assuming to be  $Q, U = 0$ : i.e., the received waves are completely circular polarized.

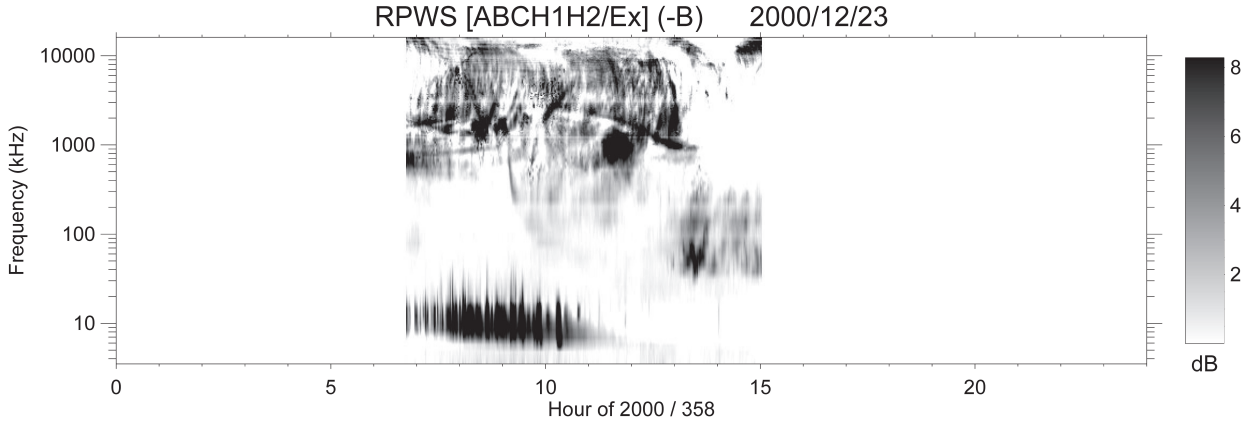


**Figure 4.26:** Dynamic spectra observed by RPWS on 23 Dec. 2000 when Cassini was located at a distance of 166 R<sub>J</sub> from Jupiter in a local time of 13.6 h.

We infer that this disagreement is possibly caused by the following reasons:

1. QP bursts propagating to high latitudes are refracted toward the equatorial region by the local plasmas in the magnetosphere, magnetosheath, and interplanetary space (e.g., *Hospodarsky et al.*, 2004)

and/or

2. QP bursts have the real source region at the magnetosheath where the local plasma frequency is comparable to the emission frequencies of QP bursts.

In Chapters 5 and 6, we investigate the refractive effects and generation in the magnetosheath based on the ray tracing method and theoretical approach, respectively.

## 4.4 Brief Summary

In this chapter, polarization properties and source directions of QP bursts were investigated based on the wave data observed by Ulysses at the northern high latitudes and Cassini at the low latitudes. It was indicated that:

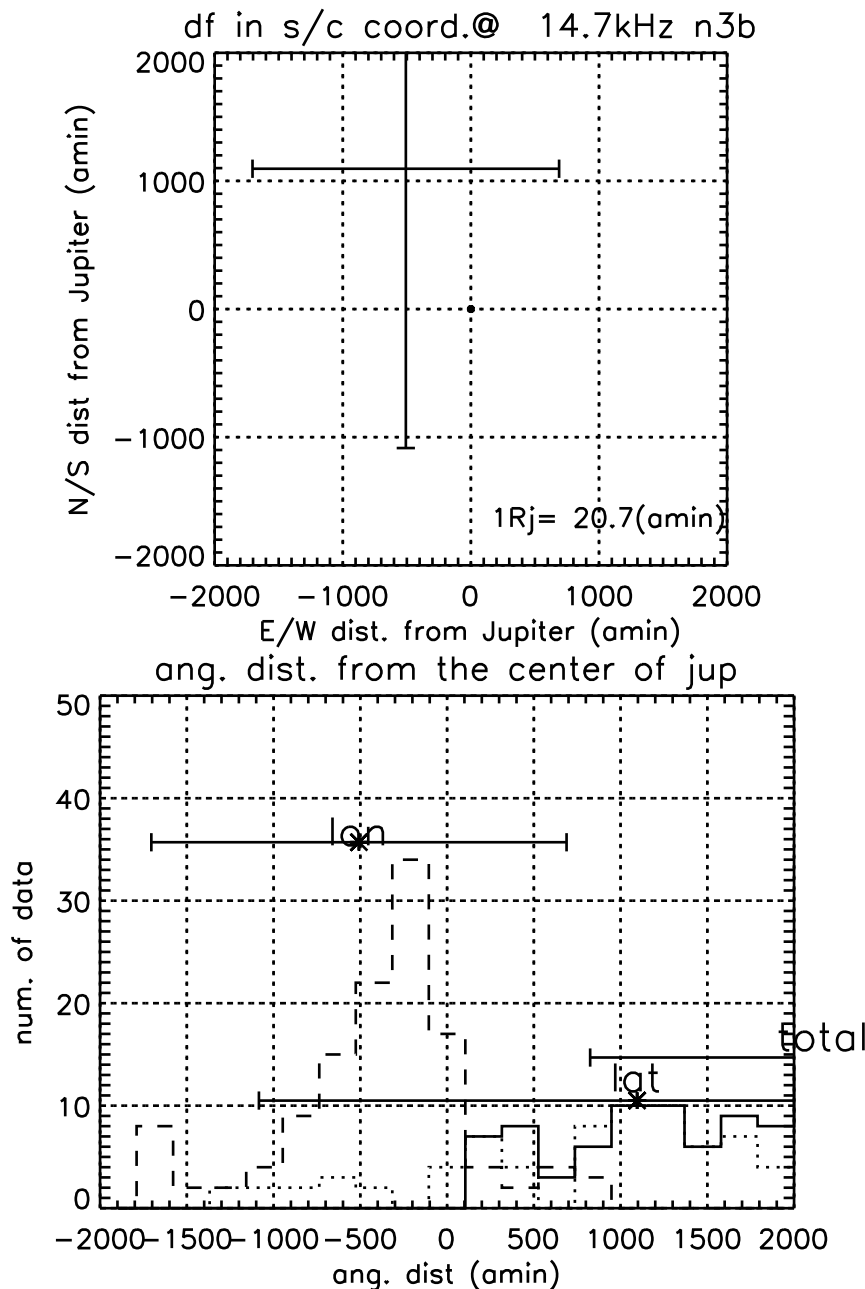


**Figure 4.27:** Results of the direction finding at 14.7 kHz performed at 8–9 h on 23 Dec. 2000 with the same format as that of Figure 4.24. One Jovian radii corresponds to an apparent diameter of 20.7 arcmin seen from Cassini.

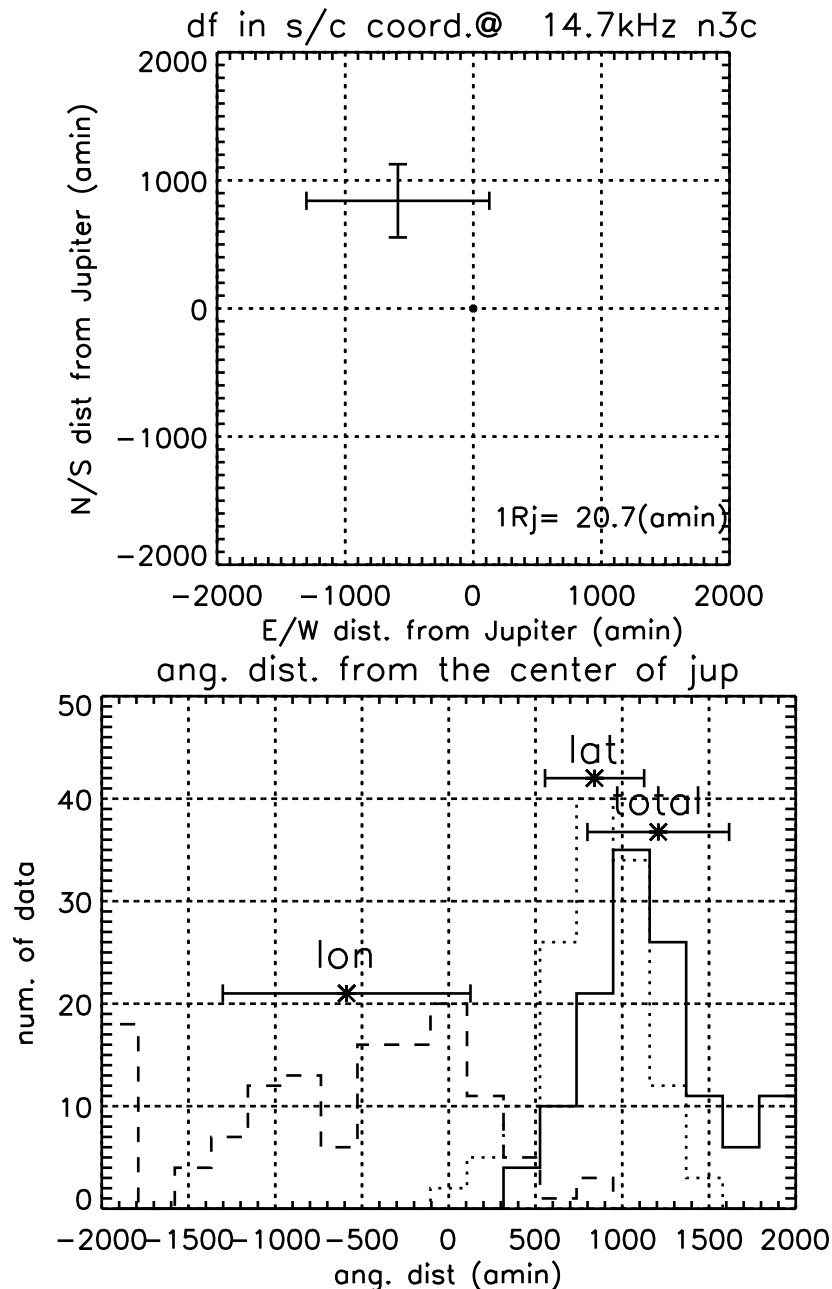


**Figure 4.28:** Direction finding results at 14.7 kHz at 8–9 h observed on 23 Dec. 2000 with the same format as Figure 4.24. Note that the direction findings were performed assuming to be  $Q, U = 0$ : i.e., the received waves are completely circular polarized.

1. QP bursts observed at the northern high latitudes are LH circular polarized waves ( $V = +0.7\text{--}+0.8$ ,  $Q = 0\text{--}+0.4$ , and  $U = 0\text{--}+0.2$ ), which are equivalent to L-O mode waves from the north polar region (Figures 4.6–4.13)
2. QP bursts observed at the low latitudes are statistically LH circular polarized ( $V = 0\text{--}0.6$ ,  $Q, U \sim 0$ ) without any dependence on CML and SSL (Figures 4.16–4.18)
3. Power of QP bursts observed by Cassini are dependent on SSL in the same manner as those observed by Galileo (Figure 4.18)
4. Apparent directions of QP bursts observed by Cassini are significantly more distant from Jupiter ( $\sim 50 R_J$ ) than the  $f_p$  and  $f_c$  surfaces ( $\sim 2 R_J$  and  $\sim 10 R_J$ , respectively) (Figures 4.25 and 4.28)

We interpreted the result (4) was caused by the following reasons:

- QP bursts propagating to the high latitudes are refracted toward the equatorial region by the local plasmas in the magnetosphere, magnetosheath, and interplanetary space and/or
- QP bursts have the real source region at the magnetosheath.

# Chapter 5

## Interpretation of Observational Results Based on Propagation Analysis

In this chapter, we interpret the observed characteristics obtained in the previous chapters using a three-dimensional ray tracing method, which can trace ray paths of electromagnetic waves propagating in magnetized plasma. The ray tracing gives information on the source location, directivity, and propagation of QP bursts which can reproduce the observed occurrence characteristics.

### 5.1 Description of Ray Tracing Method

#### 5.1.1 Ray Tracing Equations

The ray tracing calculates propagation paths of electromagnetic waves in magnetized cold plasma by sequentially solving the dispersion-relation of plasma waves, the *Appleton-*

*Hartree formula.* The formula is given as

$$n^2 = 1 - \frac{2X}{2 - \frac{Y^2 \sin^2 \theta}{1-X} + \rho \sqrt{\frac{Y^4 \sin^4 \theta}{(1-X)^2} + 4Y^2 \cos^2 \theta}} \quad (5.1)$$

where  $n$  is a refraction index of electromagnetic waves in magnetized plasma, expressed as  $n = c|\vec{k}|/\omega$ .  $\rho$  is set to be  $+1$  for L-O mode waves and  $-1$  for R-X mode waves.  $\theta$  is an angle between wave normal vector  $\vec{k}$  and the local magnetic field vector  $\vec{B}$ . The other parameters,  $X$  and  $Y$  are given as follows:

$$X = \left(\frac{\omega_p}{\omega}\right)^2, \quad (5.2)$$

$$Y = \frac{\omega_c}{\omega}, \quad (5.3)$$

where  $\omega$ ,  $\omega_p$  and  $\omega_c$  are frequency of waves, local plasma and cyclotron frequencies, respectively.

The dispersion relation of waves in magnetized cold plasma,  $D(t, \omega, \vec{r}, \vec{k})$  is defined as

$$D(t, \vec{r}, \omega, \vec{k}) = \left(\frac{c|\vec{k}|}{\omega}\right)^2 + \frac{2X}{2 - \frac{Y^2 \sin^2 \theta}{1-X} + \rho \sqrt{\frac{Y^4 \sin^4 \theta}{(1-X)^2} + 4Y^2 \cos^2 \theta}} - 1 = 0 \quad (5.4)$$

where  $\vec{r}$  and  $t$  indicates position of a ray path and time. We assume that Equation 5.4 is conserved during propagation of a ray. Introducing a new parameter  $\tau$  denoting a segment along the ray path, we obtain the derivation of  $D$  with respect to  $\tau$

$$\frac{dD}{d\tau} = \frac{\partial D}{\partial t} \frac{\partial t}{\partial \tau} + \frac{\partial D}{\partial \omega} \frac{\partial \omega}{\partial \tau} + \frac{\partial D}{\partial \vec{r}} \cdot \frac{\partial \vec{r}}{\partial \tau} + \frac{\partial D}{\partial \vec{k}} \cdot \frac{\partial \vec{k}}{\partial \tau} = 0. \quad (5.5)$$

By assuming that the magnetized media is under a temporally-steady state and the wave frequency is constant, we have the following relations:

$$\frac{\partial D}{\partial t} = \frac{\partial \omega}{\partial \tau} = 0 \quad (5.6)$$

Then, Equation 5.5 is expressed as

$$\frac{dD}{d\tau} = \frac{\partial D}{\partial \vec{r}} \cdot \frac{\partial \vec{r}}{\partial \tau} + \frac{\partial D}{\partial \vec{k}} \cdot \frac{\partial \vec{k}}{\partial \tau} = 0 \quad (5.7)$$

When parametric connections between  $\partial \vec{r}/\partial \tau$  and  $\partial D/\partial \vec{k}$  and those between  $\partial \vec{k}/\partial \tau$  and  $\partial D/\partial \vec{r}$  are considered, necessary and sufficient conditions for validity of Equation 5.7 are

$$\frac{\partial \vec{r}}{\partial \tau} = +\frac{\partial D}{\partial \vec{k}}, \quad \frac{\partial \vec{k}}{\partial \tau} = -\frac{\partial D}{\partial \vec{r}} \quad (5.8)$$

Using these conditions and Equation 5.5, similar conditions are obtained as

$$\frac{\partial t}{\partial \tau} = -\frac{\partial D}{\partial \omega}, \quad \frac{\partial \omega}{\partial \tau} = +\frac{\partial D}{\partial t} \quad (5.9)$$

From Equations 5.8 and 5.9,  $d\vec{r}$  and  $d\vec{k}$  are written as

$$d\vec{r} = \frac{\partial \vec{r}/\partial \tau}{\partial t/\partial \tau} \cdot dt = -\frac{\partial D/\partial \vec{k}}{\partial D/\partial \omega} \cdot dt \quad (5.10)$$

$$d\vec{k} = \frac{\partial \vec{k}/\partial \tau}{\partial t/\partial \tau} \cdot dt = +\frac{\partial D/\partial \vec{r}}{\partial D/\partial \omega} \cdot dt \quad (5.11)$$

Then,  $d\vec{r}$  and  $d\vec{k}$  can be obtained by estimating the derivation of  $D$  in Equation 5.10 and 5.11.

Finally, a full ray path is derived from a sequential integration of  $d\vec{r}$ . The differential equations of ray tracing in the present study is expressed as follows:

$$D_j = D(t, \omega, \vec{r}_j, \vec{k}_j) \quad (5.12)$$

$$d\vec{r}_{j+1} = -\frac{\partial D_j/\partial \vec{k}_j}{\partial D_j/\partial \omega} \cdot dt_j \quad (5.13)$$

$$d\vec{k}_{j+1} = +\frac{\partial D_j/\partial \vec{r}_j}{\partial D_j/\partial \omega} \cdot dt_j \quad (5.14)$$

$$\vec{r}_{j+1} = \vec{r}_j + d\vec{r}_{j+1} \quad (5.15)$$

$$\vec{k}_{j+1} = \vec{k}_j + d\vec{k}_{j+1} \quad (5.16)$$

$$D_{j+1} = D(t, \omega, \vec{r}_{j+1}, \vec{k}_{j+1}) \quad (5.17)$$

### 5.1.2 Parameters for Ray Tracing

#### Plasma model

In this calculation, *Divine and Garrett's* (1983) model was used as a model of the magnetospheric plasma distribution. For the case of emissions at low frequencies, plasma distribution model of the magnetosheath is also included, of which boundary surfaces are expressed as quadratic curves introduced by *Slavin et al.* (1985). Refraction in the magnetosheath is significant for the waves at lower frequency than the local plasma frequency  $f_p$  in the sheath. For example, left-handed ordinary (L-O) mode waves at frequencies of  $f < 12.7$  kHz are cut off in the magnetosheath with the electron density  $n_e \sim 2/\text{cc}$  because the emission frequency  $f$  is less than the local cut off frequency  $f_p$  of L-O mode wave which is defined as

$$f_p = \sqrt{\frac{e^2 n_e}{m_e \epsilon_0}} \quad (5.18)$$

where  $e$ ,  $m_e$ , and  $\epsilon_0$  are elementary charge, electron mass, and electric permissibility in vacuum, respectively.

Details of the magnetosheath plasma model in the present calculation are as follows:

- The boundaries of the bowshock and magnetopause are symmetric with respect to the Sun-Jupiter axis: i.e., they are expressed as "conics" in three dimensions
- The boundary surfaces are defined by the following function:

$$r = \frac{L}{1 + \epsilon \cos \theta} \quad (5.19)$$

where  $r$  is a distance between the conic focus and a point on the boundary,  $\epsilon$  is the

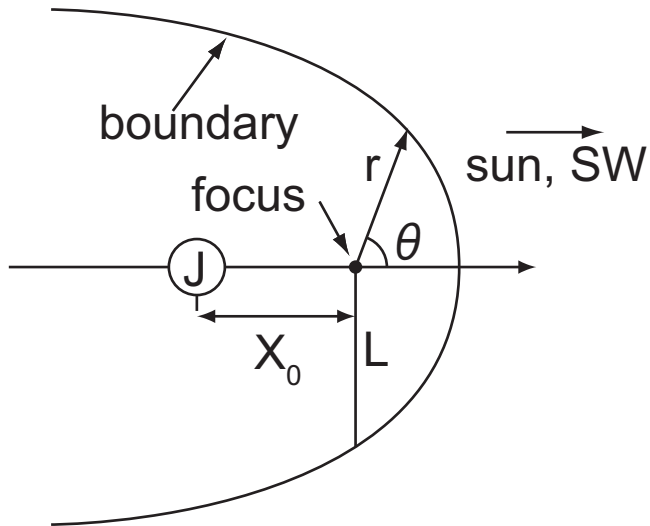


**Figure 5.1:** A schematic of a boundary defined by Equation 5.19.  $r$  is a distance between the conic focus and a point on the boundary,  $\epsilon$  is the eccentricity of the quadratic curve,  $L$  is the radius of the the conic's cross-section including the focus, and  $\theta$  is the angle between the position vector  $\vec{r}$  and the Sun-Jupiter axis. The conic focus is placed on the Sun-Jupiter axis at a distance of  $X_0$  from Jupiter.

eccentricity of the quadratic curve,  $L$  is the radius of the the conic's cross-section including the focus, and  $\theta$  is the angle between the position vector  $\vec{r}$  and the Sun-Jupiter axis. The conic focus is placed on the Sun-Jupiter axis at a distance of  $X_0$  from Jupiter (see also Figure 5.1).

- Values of  $\epsilon$ ,  $L$ , and  $X_0$  are adopted from Slavin et al. (1985). In Slavin et al. (1985), these values were obtained by the linear least square fitting of Equation 5.19 to the boundaries observed by Pioneers and Voyagers:  $(\epsilon, L, X_0) = (1.21, 156 \text{ R}_J, +10 \text{ R}_J)$  for the bowshock and  $(0.91, 101 \text{ R}_J, +9 \text{ R}_J)$  for the magnetopause.
- Solar wind plasma is filled between the bowshock and magnetopause surfaces with the linear gradient of electron density depending on  $r$ , which is defined by

$$n_e = n_0 \cdot \frac{r_{BS} - r}{r_{BS} - r_{MP}} + n_1 \quad (5.20)$$

where  $n_0$  is the density at the magnetopause,  $n_1$  is that at the bowshock,  $r_{BS}$  is the distance between the bowshock and focus, and  $r_{MP}$  is that between the magne-

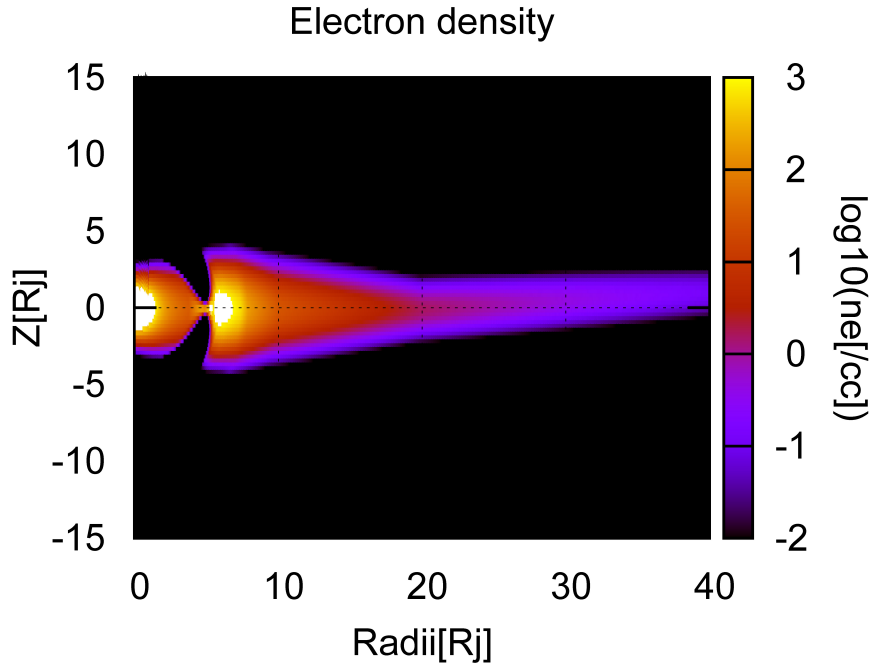


**Figure 5.2:** Meridional distribution of the electron density derived from the Divine-Garrett model (Divine and Garrett, 1983) used in the present ray tracing. Vertical axis is parallel to the spin axis and horizontal axis is included in the meridian plane of  $110^\circ$  System III longitude. Colors show the electron density (electrons/cc) in base ten logarithm.

topause and focus. Values of  $n_0$  and  $n_1$  were set to be  $1.08/\text{cc}$  and  $1/\text{cc}$ , respectively, corresponding to  $n_e = 2.08/\text{cc}$  and  $f_p \sim 13 \text{ kHz}$  at the magnetopause, and  $n_e = 1/\text{cc}$  and  $f_p \sim 9 \text{ kHz}$  at the bowshock. These densities are typical values when solar wind disturbances (e.g., the Corotating Interaction Region, CIR) arrive at Jupiter.

Figures 5.2 and 5.3 indicate electron density distributions from the plasma models for the magnetosphere and magnetosheath used in the present calculation.

### Magnetic field model

At high source altitudes in the polar region, from where rays are emitted in this calculation, the equatorial current sheet modifies the local magnetic field significantly. Thus, the VIP4 internal field model (Connerney et al., 1998) and the Euler potential model of current sheet (Khurana, 1997) were adopted as the magnetic field model (we call this combined

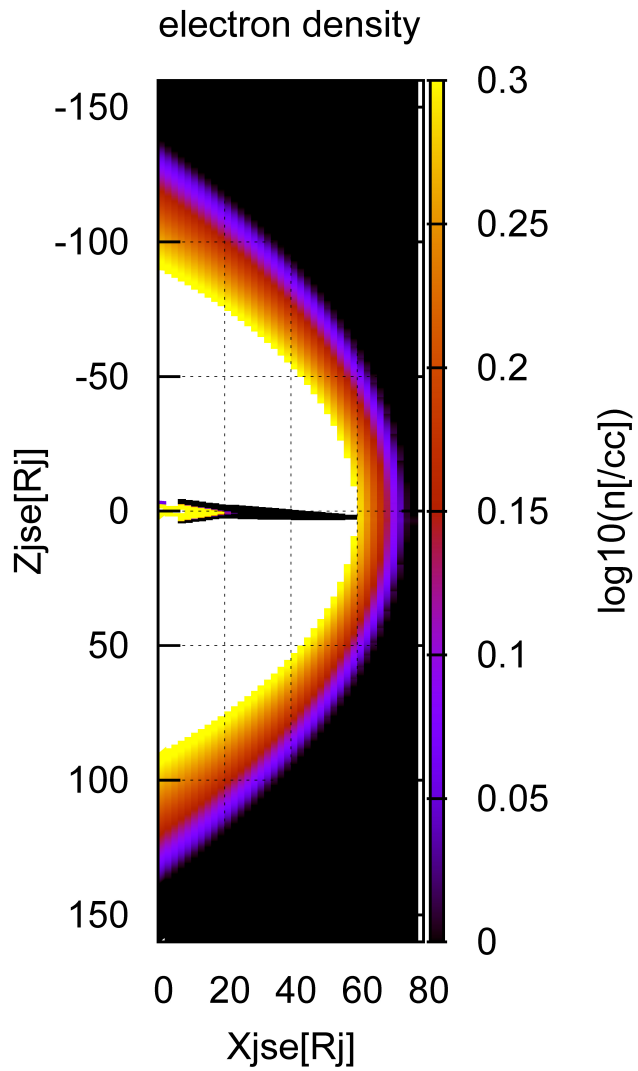


**Figure 5.3:** Meridional distribution of the electron density derived from the plasma model for the magnetosphere and magnetosheath (*Divine and Garrett, 1983; Slavin et al., 1985*) used in the present ray tracing. Horizontal axis is aligned to the Sun-Jupiter axis, and vertical axis is parallel to the spin axis. Colors show the electron density in base ten logarithm.

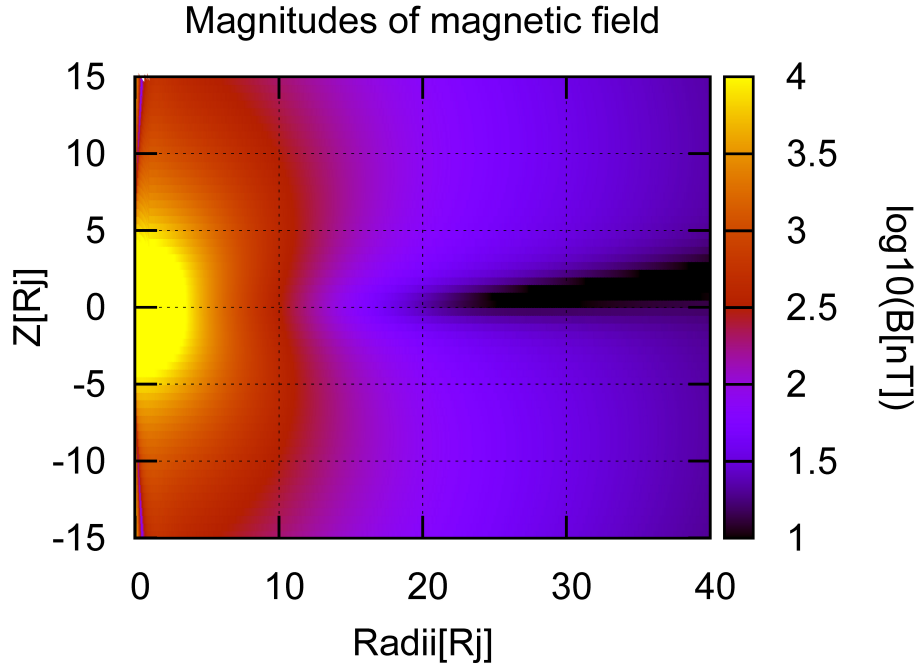


**Figure 5.4:** Meridional distribution of magnitudes of the magnetic field from the VIP4-CS model (Connerney et al., 1998; Khurana, 1997) used in the present ray tracing. Vertical axis is parallel to the spin axis and horizontal axis is included in the meridian plane of  $110^\circ$  System III longitude. Colors show the magnitude of the magnetic field in base ten logarithm.

model “VIP4-CS model” in this thesis). We calculated the propagation paths of electromagnetic waves in the magnetized plasma determined with the plasma and magnetic field models by solving Equations 5.12–5.17 sequentially. Figure 5.4 indicates magnitudes of the magnetic field from the VIP4-CS model in a meridian plane.

### Source parameters

The source parameters for the ray tracing are given as the wave mode, emission frequency, L-value of source field lines, a half-cone angle of hollow cones, and ratio of the emission frequency to the local cutoff frequency of the wave mode.

We calculated ray paths for both L-O mode waves and R-X mode waves. It was assumed that L-O mode waves are generated at a frequency near the local cutoff frequency (equivalent to the plasma frequency,  $f_p$ ) via the mode conversion process proposed in pre-

vious studies (e.g., Oya, 1974; Jones, 1977), whereas R-X mode waves were assumed to be generated via the cyclotron maser instability (CMI) (Wu and Lee, 1979) near the local cutoff frequency  $f_{RX}$  in the region where local cyclotron frequency  $f_c$  is much larger than  $f_p$  ( $f_p/f_c \sim 0.14$ , Hilgers, 1992). In such highly magnetized plasma, the local  $f_{RX}$  is close to local  $f_c$  ( $f_{RX} \sim f_c$ ) because  $f_{RX}$  is given by the following relation:

$$f_{RX} = \frac{f_c}{2} + \sqrt{f_p^2 + \left(\frac{f_c}{2}\right)^2} \quad (5.21)$$

Emission frequencies were set in a range of 3–300 kHz (LF and VLF range) because QP burst are observed most frequently in the range (e.g., MacDowall et al., 1993; detection criteria in Section 3.1 of the present thesis).

We defined the L-value source field lines from the internal magnetic field model (VIP4 model). After setting the source L-value by using only the VIP4 model, ray paths were calculated under the magnetic field from the VIP4-CS model.

A half-cone angle of the hollow cone is the angular distance between the initial k-vector direction and the local magnetic field line (derived from the VIP4-CS model). For example, an initial k-vector with a half-cone angle of  $0^\circ$  is directed outward from Jupiter and parallel to the tangential line to the local magnetic field line at the source. The range of a half-cone angle from  $0^\circ$  to  $90^\circ$  was examined in this calculation. Several theoretical works (e.g., L-O mode: Oya, 1974, R-X mode: Wu and Lee, 1979) predicted that planetary auroral radio emissions are generated with a large initial angle (up to  $90^\circ$ ). These generated emissions are immediately refracted around the source region and escape outward from the planet. Therefore the half-cone angle includes both effects of the theoretical initial angle and the refraction around the source.

The ratio of the emission frequency to the local cutoff frequency was defined as  $f/f_p$  for the L-O mode and  $f/f_{RX}$  for the R-X mode, where  $f$  is the emission frequency. These parameters are indices corresponding to the source altitude of the emission, i.e., the larger the ratios, the higher the source altitudes.

All the parameters used in the present ray tracing study are summarized in Table 5.1.

**Table 5.1:** Parameters for ray tracing**Plasma and magnetic field model**

plasma model	<i>Divine and Garrett</i> [1983] model (magnetosphere) and <i>Slavin et al.</i> (1985) model (magnetosheath)
magnetic field model	VIP4 ( <i>Connerney et al.</i> , 1998) model and the Euler potential model of current sheet ( <i>Khurana</i> , 1997)

**Source parameters**

parameter	content	comments
wave mode	L-O/R-X mode	Each mode is examined in the present study
emission frequency, $f$	free (3-300 kHz)	Emission frequency from the detection criteria in the data analysis for occurrence characteristics.
L-value of source	free	L-value of the source magnetic field line
a half-cone angle	free (0-90 deg)	An angular distance between the initial k-vector direction and the source field line
$f/f_p, f/f_{RX}$	free	Ratio of emission frequency to local cutoff frequency of L-O/R-X mode wave at the source point.

## 5.2 QP Bursts Observed by Ulysses at High Latitudes

### 5.2.1 Assumptions and Calculation Conditions

For the case of QP bursts observed at high latitudes, some assumptions and conditions were adopted as below. The examined emission frequencies were set to be  $f = 30, 100$ , and  $300$  kHz, which were in the frequency range observed by Ulysses (*MacDowall et al.*, 1993). The wave mode was chosen to be L-O mode on the basis of Ulysses' spectral and polarization measurements in the high latitude region indicated in Section 4.2 of this thesis and *MacDowall et al.* (1993). L-O mode waves are most efficiently converted from Z-mode waves at a half cone angle of  $90^\circ$  as shown in *Oya* (1974). Thus, assuming the mode conversion process, a half cone angle which is the initial ray direction with respect to the local magnetic field line was set to be  $90^\circ$ . The magnetic L-shell of the wave source was set to be  $L > 30$  ( $L = 30, 50, 70$ ) in consideration of the MeV electron outbursts with a quasi-periodicity of  $\sim 40$  minutes observed in  $L > 30$  region of the Jovian polar magnetosphere during Ulysses' first flyby (*McKibben et al.*, 1993). The local time of an observer was set to be 16 hours, which is the typical local time of Ulysses during the second encounter observations.

The parameter  $f/f_p$  is free, which is the ratio of emission frequency to the local plasma frequency at the source point. Source points were allocated on the northern and southern hemispheres. In the present case, we set System III longitudes of source magnetic field lines to be  $0^\circ$ – $360^\circ$ . This corresponds to that the source field lines of QP bursts are located in all longitudes

Ray paths for the QP radio emission were examined by varying the free parameters, and they were compared with the observations. Below, we show eight cases of the ray tracing results for discussing the source altitude, directivity, and dependence on the planetary rotational phase. Table 5.2 lists the simulation conditions for each ray tracing result. The calculated results for QP ray paths were plotted on maps with a similar format to that of Figure 3.3. The plotted rays indicate the “observable region” where an observer can detect

**Table 5.2:** Calculation conditions of the ray tracing for the case of Ulysses

case	figure	mode	$f$	$f/f_p, f/f_{RX}$	L	half-cone ang.	comments
case U1	5.5a	L-O	30 kHz	5.0	30	90°	
case U2	5.5b	L-O	30 kHz	1.3	30	90°	
case U3	5.5c	L-O	30 kHz	1.01-1.5	30	90°	
case U4	5.5d	L-O	30 kHz	1.01-1.5	30	90°	emit during 90°<SSL<300°
case U5	5.5e	L-O	30 kHz	1.3	30-70	90°	
case U6	5.5f	L-O	30 kHz	1.3	30	90°	longitudinally restricted source
case U7	5.5g	L-O	30–300 kHz	1.3	30	90°	
case U8	5.7	R-X	30 kHz	1.3	30	90°	

these rays.

### 5.2.2 Ordinary Mode

We analyzed the source altitude distribution for various  $f/f_p$  values for the case of L-O mode waves. The left panel in Figure 5.5a shows the observable region of the emission from a relatively higher source altitude: the emission frequency, ratio of  $f/f_p$ , and L shell of the source magnetic field were 30 kHz, 5.0, and 30, respectively (see Table 5.2, case U1). Here, we have assumed that the emissions are steady and continuous during one planetary rotation. The horizontal and vertical axes of the left panel in Figure 5.5a correspond to the CML and magnetic latitude of an observer, respectively, and the symbol “+” indicates the region where an observer can detect a ray emitted from the source region. The sources are uniformly distributed on all longitudes co-rotating with Jupiter. The right panel in Figure 5.5a shows an example of ray paths from a point source on the magnetic

field line in a meridional plane of System III longitude ( $110^\circ$ ). Regarding the latitudinal distribution shown in the left panel, results of the calculation shows that the latitudinal range of the observable region is broad (from  $+10^\circ$  to nearly  $+80^\circ$ ) when the observer is between  $\text{CML}=120^\circ\text{--}240^\circ$ , and the observer can detect these emissions even at relatively lower latitudes ( $< +30^\circ$ ) in cases of  $\text{CML}<120^\circ$  and  $\text{CML}>240^\circ$ . This result disagrees with the results of the occurrence probability distribution of the observed QP burst groups shown in Figure 3.3.

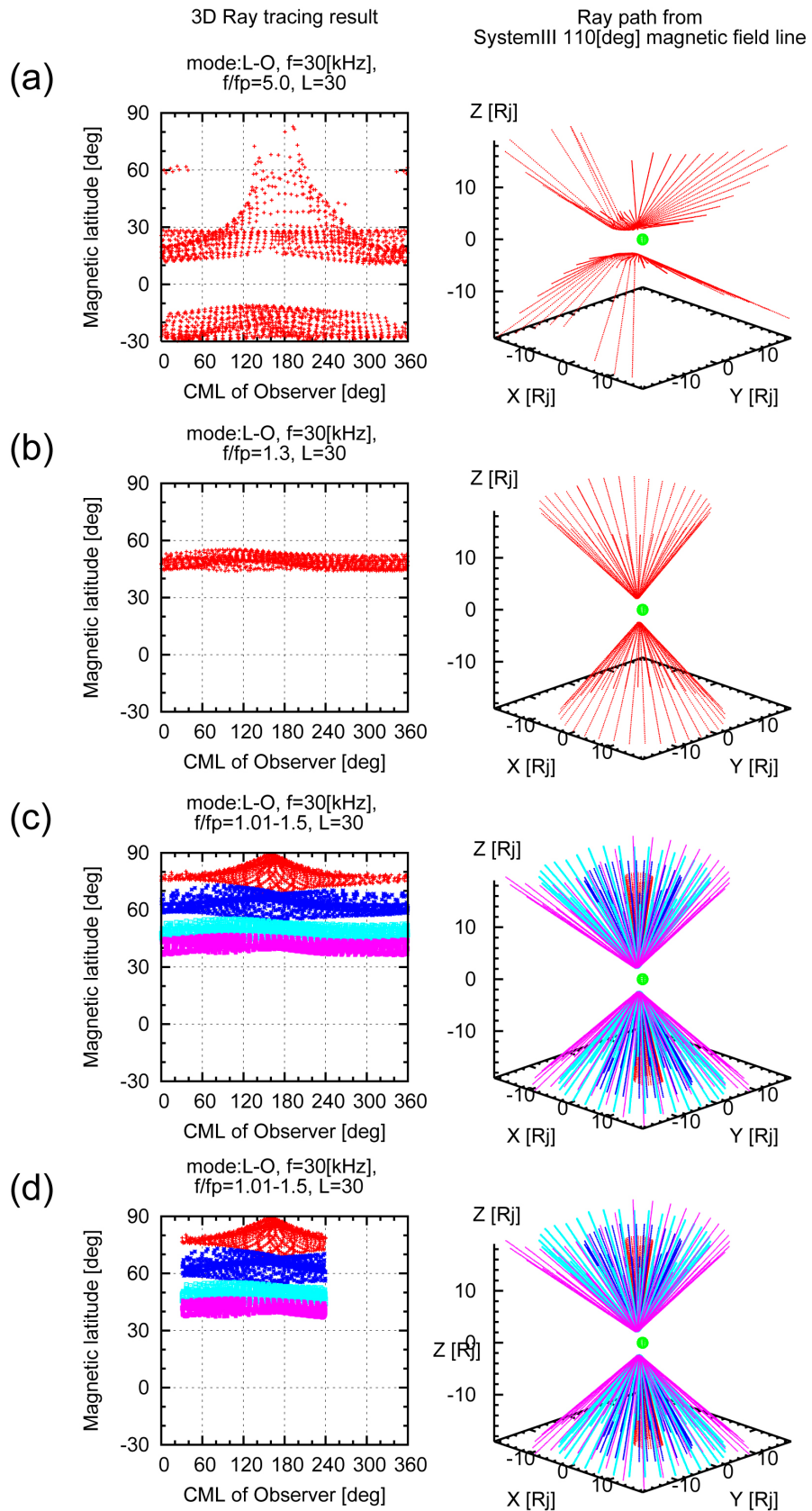


Figure 5.5:

**Figure 5.5:** (a) 3D ray tracing result for the case of  $f = 30$  kHz,  $f/f_p = 5.0$ , and  $L = 30$ . (left) Observable region map similar in format to Figure 3.3. The horizontal axis is the CML of the observer (deg), and the vertical axis is the magnetic latitude of the observer (deg). The symbol “+” indicates the point where an observer can detect the ray. (right) Ray path from a point source on the magnetic field line in the System III longitude  $110^\circ$  meridional plane. The X-axis is on the System III longitude  $0^\circ$  meridional plane, the Z-axis is parallel to the spin axis, and the Y-axis completes the right-handed triad. The green sphere is Jupiter. Emissions are excited steadily during one planetary rotation (see Table 5.2, case U1). (b) 3D ray tracing result with the same format as that of panel (a). The parameters are also the same as for (a), but with  $f/f_p = 1.3$  (case U2). (c) The ray tracing result in the case where the parameters are the same as the case of (b), but with  $1.01 < f/f_p < 1.5$  (case U3). The red, blue, light blue, and violet marks are for cases of  $f/f_p = 1.01, 1.1., 1.3$ , and  $1.5$ , respectively. (d) The ray tracing result with the same parameters as in (c) except that the emission is excited during a particular rotational phase ( $90^\circ < \text{SSL} < 330^\circ$ , case U4).

Figure 5.5b shows the case for a relatively lower source altitude, where  $f/f_p$  is equal to 1.3. The L-value of the source magnetic field line and allocation of the source point are the same as for Figure 5.5a (see Table 5.2, case U2). In this case, the observable region is restricted to a narrow latitudinal width and the observer can detect the emissions only at relatively higher latitudes. This result corresponds to the latitudinal distribution derived from the observations well. The low  $f/f_p$  value in the present case corresponds to a source altitude of  $1.4 R_J$  from the planetary surface. The most probable range of  $f/f_p$  ratio for reproducing the observed latitudinal range turns out to be 1.01–1.5 (see Table 5.2, case U3). This range is equivalent to an altitude of  $1.3\text{--}1.4 R_J$ . The results for this range are shown in Figure 5.5c. The distributions indicated by red, blue, light blue, and violet crosses correspond to observable regions when  $f/f_p = 1.01, 1.1., 1.3$ , and  $1.5$ , respectively. As is evident from Figure 5.5c, high latitudinal components observed at the latitudes of  $\text{MLAT} > +30^\circ$  corresponds to the radiation cone with broad beaming. This suggests that QP bursts observed at high latitude have so-called “filled cone” directivity.

Note that although Figure 5.5c reproduces the observed latitudinal distribution well, the longitudinal structure derived from the model calculation is very different from the observations. This implies that the observable latitudinal distribution is sensitive to the source altitude, but not to the longitudinal distribution.

### 5.2.3 Dependence on the Planetary Rotational Phase

In the previous section, ray tracing was performed under the condition that the emissions were steady and continuous during one planetary rotation, and hence, the results cannot describe the observed longitudinal structures. In this section, a time-dependent source is considered on the basis that the QP burst groups are related to the planetary rotational phase (Figure 3.3). Figure 5.5d is the ray tracing result calculated under the condition that the emissions are generated during a particular rotational phase of the planet, where the emission starts at  $\text{SSL} = 90^\circ$  and has a duration of 5.8 h. The L-value of the source magnetic field line, allocation of source points, emission frequency and range of  $f/f_p$  are similar to those in Figure 5.5c (case U4). The longitudinal and latitudinal structures in Figure 5.5d reproduce the observations very well. Therefore, to describe the observed longitudinal and latitudinal distributions of QP bursts, it can be considered that quasi-periodic bursts are excited recurrently, not continuously, and that they are correlated with the planetary rotational phase. This result in turn implies that the observed CML distributions in the case of QP occurrence are apparent ones caused by the rotational phase dependent excitation.

### 5.2.4 Dependence of the Observable Region on Other Parameters

We examined the dependence of the observable region on other parameters such as the L-value of the source magnetic field line, longitudinal expansion of the source region in the polar latitudes, and emission frequency (cases U5, U6, and U7 in Table 5.2). The ray tracing results (not shown) indicated that the L-value of the source is not important to the longitudinal and latitudinal distributions of the observable region (case U5). This may result from the fact that the magnetic field lines in the high latitudinal region ( $L > 30$ ) are rather vertical. The longitudinally restricted source region (case U6) showed that the distribution of the observable region is little responsive to the longitudinal expansion of the source. The dependence on the emission frequencies was also examined in the cases

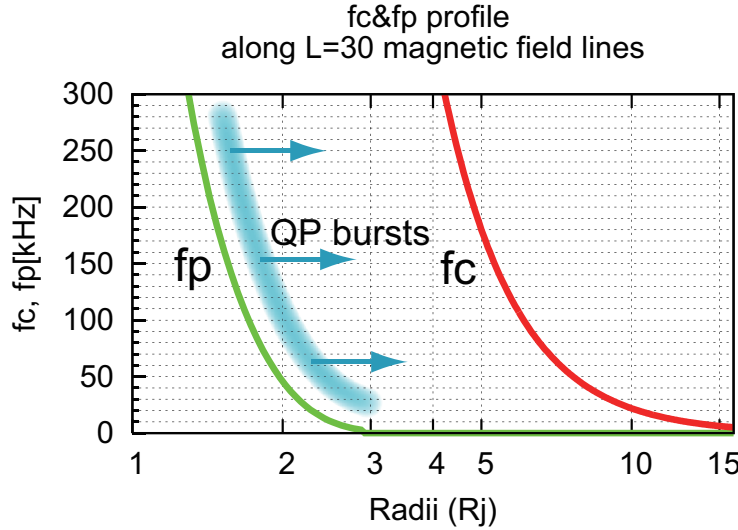


**Figure 5.6:** Profiles of plasma and cyclotron frequencies along the  $L = 30$  magnetic field line derived from the *Divine and Garrett* (1983) plasma model and the VIP4 magnetic field model. The horizontal axis indicates radius from center of the planet, and the vertical axis is cyclotron or plasma frequency. The green line shows the plasma frequency profile, and the red line represents the cyclotron frequency profile.

of  $f = 30, 100$ , and  $300$  kHz with a low  $f/f_p$  value (case U7), and the results showed that rays generated at these frequencies have similar directivity. This implies that the plasma density around the source region has a steep gradient with respect to altitude. Actually, as shown in Figure 5.6, the profile of the plasma frequency in the high latitudinal region, which is derived from the Divine and Garrett model, has a steep gradient. Thus, the waves generated close to the local  $f_p$  in these regions have similar directivity, and an observer would be able to detect them as a broad band emission.

The sensitivity of the ray tracing results to the magnetic field and plasma models was also examined, and it was found that the observable region is insensitive to changes in these models: e.g., if the magnetic field model is changed to a simple tilted dipole and the plasma density is rarefied to  $1/10$  of the Divine and Garrett model, the resultant observable region does not show significant changes more than  $\sim 10^\circ$  level in latitude and longitude. This deviation is not essential to the present observed distribution.

### 5.2.5 Summary and Discussion: Radiation Characteristics of QP bursts Observed at High Latitudes

The comparison of 3D ray tracing results with observations of occurrence probability maps provides some information on the generation of the QP bursts observed at high latitudes. Parametric surveys indicated that the source region of QP bursts is located at an altitude of  $1.3\text{--}1.4 R_J$ , wherein the emission frequency is nearly equal to the local plasma frequency ( $f/f_p \sim 1$ ). This result confirms that the assumed L-O mode waves for generation of QP bursts observed at high latitudes is reasonable, and it is consistent with the polarization measurement of QP bursts indicated in Section 4.2 and *MacDowall et al.* (1993). These results suggest that QP bursts are generated by the mode conversion process such as from Z-mode waves to electromagnetic L-O mode waves at  $f = f_p$  (e.g., *Oya*, 1974; *Iizima*, 1988). Such a source region is consistent with the broad frequency range QP bursts observed at high latitudes (1–200 kHz). If rays are generated at frequencies nearly equal to the local plasma frequency, then the source region will be restricted to a narrow range of altitude. For example, if the emission frequencies are 30–300 kHz and the ratio  $f/f_p$  is 1.3, each source region along the  $L=30$  magnetic field line is restricted to an altitude range of  $0.4\text{--}1.4 R_J$  (see  $f_p$  profile shown in Figure 5.6). The restricted source region provides the rays with similar directivities, and an observer can detect broad band radio emissions simultaneously.

On the other hand, if the emissions were generated near the local cyclotron frequency, the source expansion would be relatively broad: e.g., if  $f = 30\text{--}300$  kHz with  $f/f_{RX} = 1.3$ , the source region along the  $L=30$  magnetic field lines would expand to an altitude of  $3.7\text{--}8.7 R_J$  (see  $f_c(\sim f_{RX})$  profile shown in Figure 5.6). This source expansion would give the radiation various ray directions, which is in contrast to the present observations. This fact implies that the cyclotron maser instability (*Wu and Lee*, 1979) is not the generation process of QP bursts observed by Ulysses in the high-latitude region. Actually, the ray tracing results assuming R-X mode waves indicate an inconsistent observable region with the observed distribution: rays escape from the polar region toward the lower equatorial

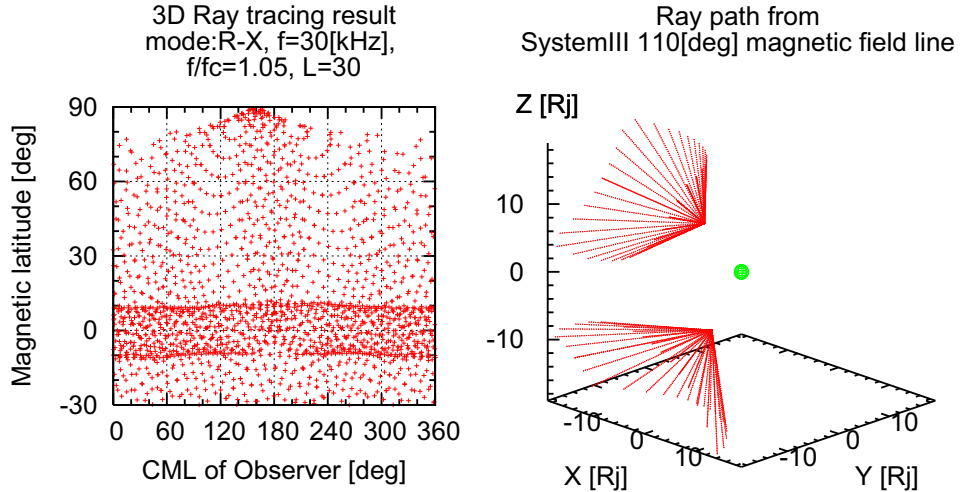


**Figure 5.7:** The ray tracing result for the case of R-X mode waves,  $f = 30$  kHz,  $f/f_{RX} = 1.05$ , and  $L = 30$ . The half cone angle is  $50^\circ$  (case U8 in Table 5.2).

region as shown in Figure 5.7. Instead, the R-X mode wave is reasonable for the QP bursts in the low latitudinal region that were observed by Galileo and Cassini as indicated in Chapter 3 and 4, and previous studies (e.g., Hospodarsky *et al.*, 2004).

Ray tracing results suggested that QP bursts beaming which can reproduce the high latitudinal components is significantly broadened, like “filled cone” shape (see Figure 5.5c and d). This radiation characteristic is opposite to those of other auroral radio components: e.g., Io-related Decametric radio emissions (Io-DAM), which has discrete thin beaming, so-called “hollow cone” shape (e.g., Kaiser *et al.*, 2000). These differences imply that each radio component has different generation mechanism and propagation process.

Parametric surveys suggested that the emission source is in a high L-value region, where magnetic field lines converge and are approximately vertical. This suggestion is consistent with the X-ray “hot spot” with 45-min quasi-periodicity observed by the Chandra X-ray Observatory (Gladstone *et al.*, 2002). Gladstone *et al.* (2002) reported that the location of the hot spot is restricted to a Jovicentric latitudinal range from  $+60^\circ$  to  $+70^\circ$  and longitudinal range from  $160^\circ$  to  $180^\circ$  in the Jovian polar cap region and that the source has a spot-like feature. Simultaneous observations made by Cassini/UVIS and Galileo/PWS also indicated that UV auroral signatures were correlated with QP radio bursts in the

Jovian polar region (*Pryor et al.*, 2005). Unfortunately, it is still unclear what type of UV aurora structure corresponds to the radio source. However, X-rays, UV emissions, and radio wave signatures are possibly evidence of particle acceleration above the polar region, and they might be helpful for understanding short period magnetic activities in the Jovian polar region.

## 5.3 QP Bursts Observed by Galileo at Low Latitudes

### 5.3.1 Assumptions and Calculation Conditions

In Section 3.3, a shadow zone was identified in a region of  $<30 R_J$  at  $|MLAT| < 10^\circ$ . In this section, we examine the source location, directivity, and propagation of QP bursts using three-dimensional ray tracing comparing with the observed shadow zone. We performed 3D ray tracing under the following assumptions: (1) rays propagate from a source region directly to an observer without reflection at the magnetosheath, and (2) radio sources maintain their condition in all longitudes and distribute symmetrically with respect to the magnetic axis.

We think that assumption (1) is reasonable because QP bursts' frequency detected in the present study is so higher than those of the trapped continuum, so, QP bursts would be free from the reflection at the magnetosheath.

Assumption (2) allows us to compare the observed distribution of QP bursts, which corresponds to longitudinally-averaged distribution of ray paths in a magnetic meridian plane, with the distribution of modeled rays emitted from a radio source on a magnetic field line. We selected the field line located in a meridian plane of System III longitude  $110^\circ$ , where the magnetic axis projected onto the meridian plane is almost parallel to the rotational axis. Rays are emitted from the source field line in a hollow cone shape, plotted in three dimensions, and projected onto the R-Z plane of  $110^\circ$ , where R is the distance from the magnetic axis and Z is parallel to the magnetic axis, with a similar format to that of Figure 3.5. This coordinate is the same as the magnetic coordinate. In the magnetic

**Table 5.3:** Calculation conditions of the ray tracing for the case of Galileo

case	figure	mode	$f$	$f/f_p, f/f_{RX}$	L	half-cone ang.
case G1	5.9a	L-O	10 kHz	1.05	16	30°
case G2	5.9b	L-O	10 kHz	1.05	16	60°
case G3	5.9c	L-O	10 kHz	1.05	16	90°
case G4	5.9d	L-O	10 kHz	1.05	12	30°
case G5	5.9e	L-O	10 kHz	1.05	12	60°
case G6	5.9f	L-O	10 kHz	1.05	12	90°
case G7	5.9g	L-O	10 kHz	1.05	32	30°
case G8	5.9h	L-O	10 kHz	1.05	32	60°
case G9	5.9i	L-O	10 kHz	1.05	32	90°
case G10	5.11a	R-X	10 kHz	1.05	32	30°
case G11	5.11b	R-X	10 kHz	1.05	32	40°
case G12	5.11c	R-X	10 kHz	1.05	32	50°
case G13	5.11d	R-X	10 kHz	1.05	32	60°

coordinate, magnetic field and plasma distribution are almost axisymmetric. Thus, we can regard the distribution of rays on the meridian plane of 110° as representative distribution of rays from all longitudes in the magnetic coordinate.

The emission frequency was set to 3–10 kHz by referring to the detection criteria for Galileo in Section 3.1. Ray paths at 3 kHz emit and propagate in the magnetosphere similarly to those at 10 kHz because QP bursts at 3 kHz are observed with those at 10 kHz simultaneously, forming impulsive bursts in dynamic spectrograms (see Figure 3.2).

The ratio of  $f/f_p$  was set to  $f/f_p = 1.01\text{--}1.1$  referring to the theoretical study by Oya (1974), who claimed that ordinary mode waves are effectively converted from Z mode waves at a frequency near the local  $f_p$  in a sharp density gradient region. The ratio of  $f/f_{RX}$  was set to  $f/f_{RX} = 1.01\text{--}1.1$  by following Wu and Lee (1979), who predicted that R-X mode waves are generated at a frequency near the local  $f_{RX}$  in strongly magnetized plasma ( $f_c \gg f_p, f_{RX} \sim f_c$ ).

Calculation conditions for each case are summarized in Table 5.3.

### 5.3.2 Ordinary Mode

Figure 5.8 indicates magnetic field lines and distribution of the fundamental parameters for the plasma wave propagation in the meridian plane of  $110^\circ$  System III longitude. The vertical and horizontal axes are parallel to the magnetic axis and the magnetic equator, respectively. The red and black contours show the distribution of local  $f_p$  and  $f_c$ , respectively, which are calculated from the plasma and magnetic field models. The values of each line are denoted in base ten logarithms. The blue broken lines are the magnetic field lines from the internal field model (VIP4), which are traced from the equatorial plane to the  $f_p$  surface where the emission source is located (in this figure,  $f = 10$  kHz,  $f/f_p = 1.05$ , and L-values of these field lines are 12, 16, 20, 24, 28, and 32, respectively). The green solid lines are the magnetic field lines from the VIP4-CS model, which are traced from the surface of  $f_p \sim 10$  kHz in the northern hemisphere toward the outer regions of the magnetosphere. Magnetic field tracing is stopped if a field line reaches  $150 R_J$  from Jupiter, which is regarded as “opened” to the interplanetary space in this calculation. All the magnetic field lines of  $L > 12$  in Figure 5.8 are “opened”, while those of the lower L-values ( $L = 12$  in Figure 5.8) extend from sources in the northern hemisphere toward the outermost magnetosphere but return to the southern Jovian surface, thus they are regarded as “closed” lines.

Figure 5.9a indicates the modeled ray paths projected onto a meridian plane in similar format to that of Figure 3.5. The green lines are modeled ray paths and the blue broken lines are the magnetic latitudes of  $\pm 10^\circ$ . The latitudinal range between two broken lines corresponds to the region where Galileo performed observations. The L-value of the source field line, a half-cone angle,  $f/f_p$ , and  $f$  were set to 16,  $30^\circ$ , 1.05, and 10 kHz, respectively (corresponding to the case G1 in Table 5.3). Although the initial half-cone angle was set to  $90^\circ$ , the L-O mode waves were significantly refracted around the source region and escaped toward the high latitudes. Figure 5.9b–i are also results of ray tracing (the cases G2–G9 in Table 5.3), which have the same format as that of Figure 5.9a. The L-value of the source field line, a half-cone angle,  $f/f_p$ , and  $f$  were set to 12–32,  $0^\circ$ – $90^\circ$ , 1.05, and 10 kHz, for these cases, respectively. One can see that the modeled rays for all the cases do not pass

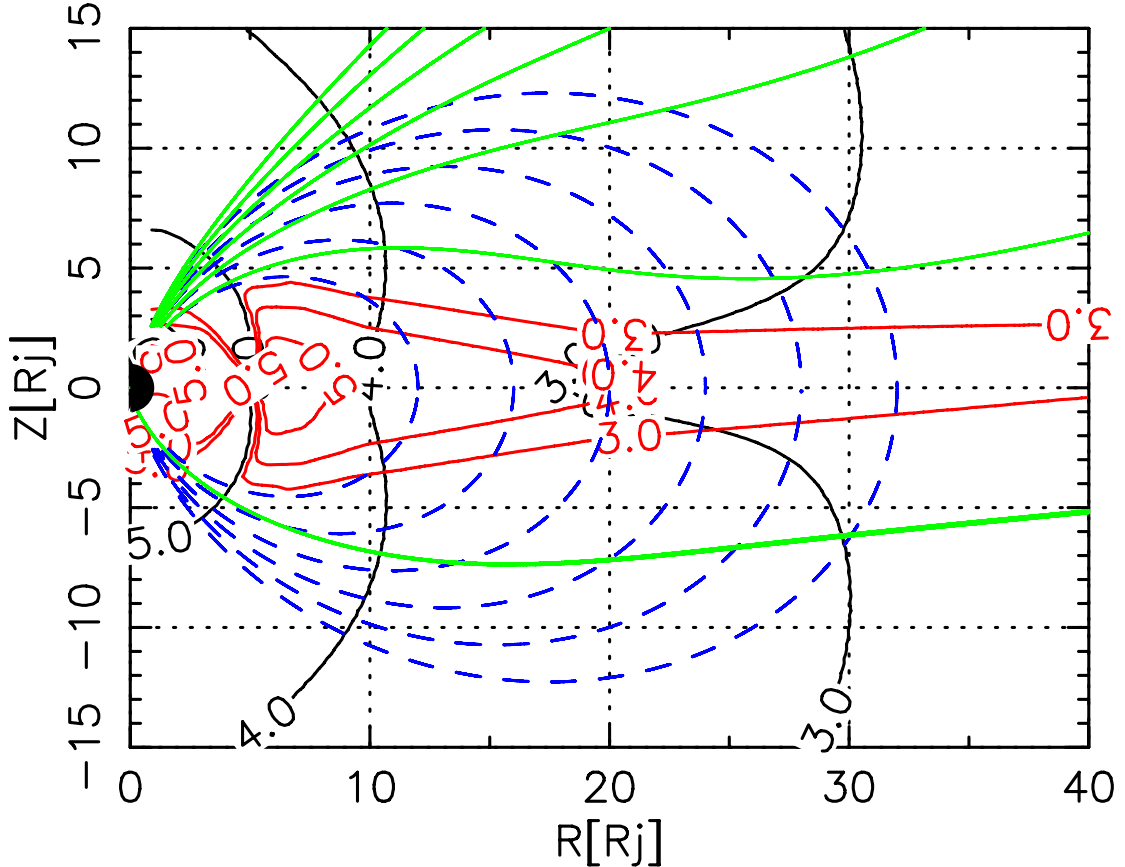


**Figure 5.8:** A plot of distribution of plasma parameters in a meridian plane of  $110^\circ$ . Vertical and horizontal axes are parallel to magnetic axis and magnetic equator. Red and black contours correspond to distribution of  $f_p$  and  $f_c$ , respectively. Values of each line are given in base ten logarithms of  $f_p$  and  $f_c$ . Blue broken lines are magnetic field lines given by the internal field model (VIP4), which are traced from the equatorial plane to the  $f_p$  surface where emission source is located (in this figure,  $f = 10$  kHz,  $f/f_p = 1.05$ , and L-values of these field lines are 12, 16, 20, 24, 28, and 32, respectively). Green solid lines are magnetic field lines from the internal and current sheet models, which are traced from the  $f_p$  surface in the northern hemisphere toward outer regions of magnetosphere.

across the observable region.

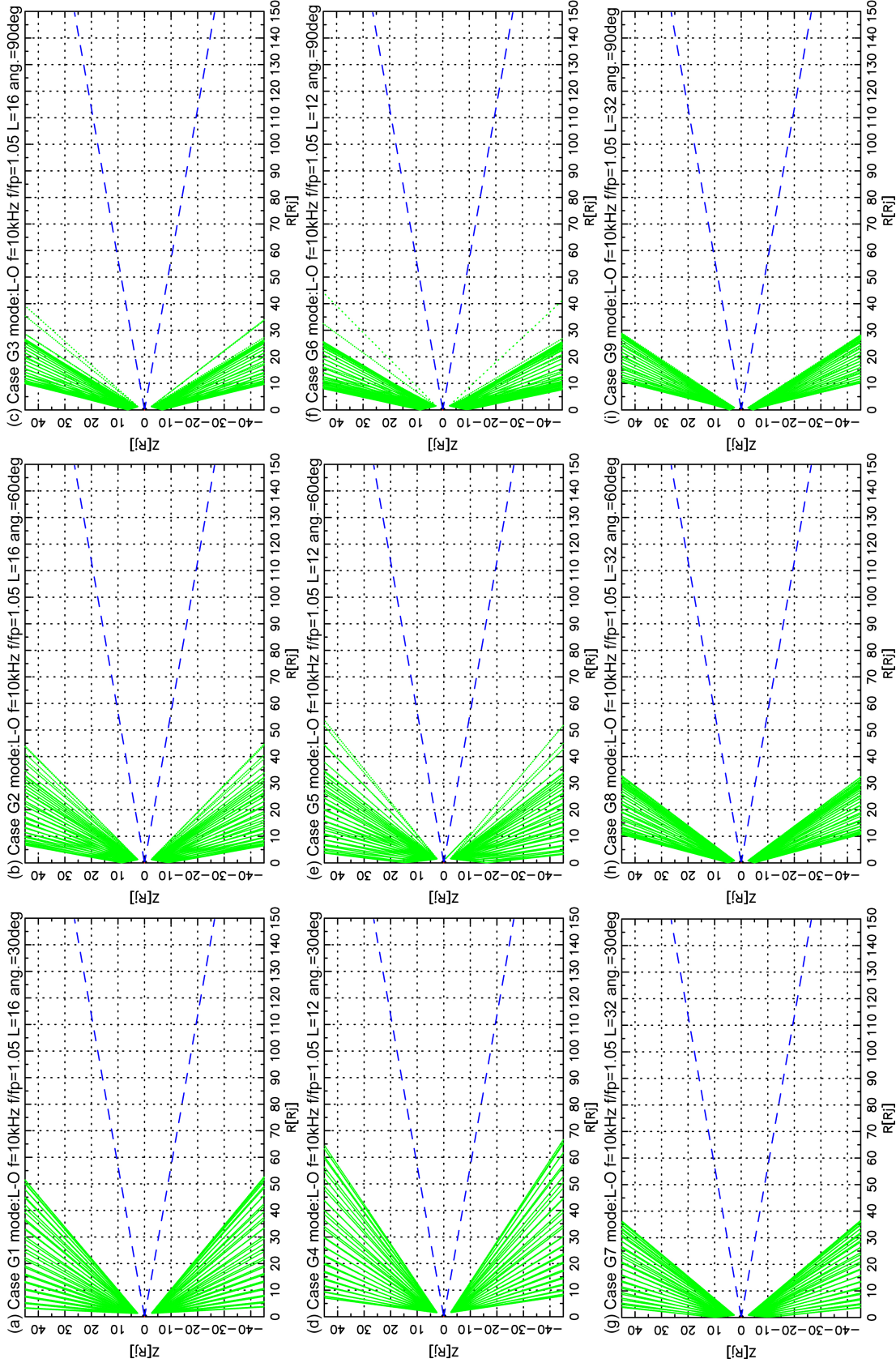
The modeled rays are still absent at low latitudes even if the ratio  $f/f_p$  is changed from 1.01 to 1.1 and  $f$  is changed from 3–10 kHz for all source L-values and initial half-cone angles. These results indicate that the L-O mode waves are not directed toward the equatorial region but the high latitudinal region because of the refraction near the source region. Thus, we conclude that QP bursts observed at low latitude, as shown in Figure 3.5, are not L-O mode waves.

### 5.3.3 Extraordinary Mode

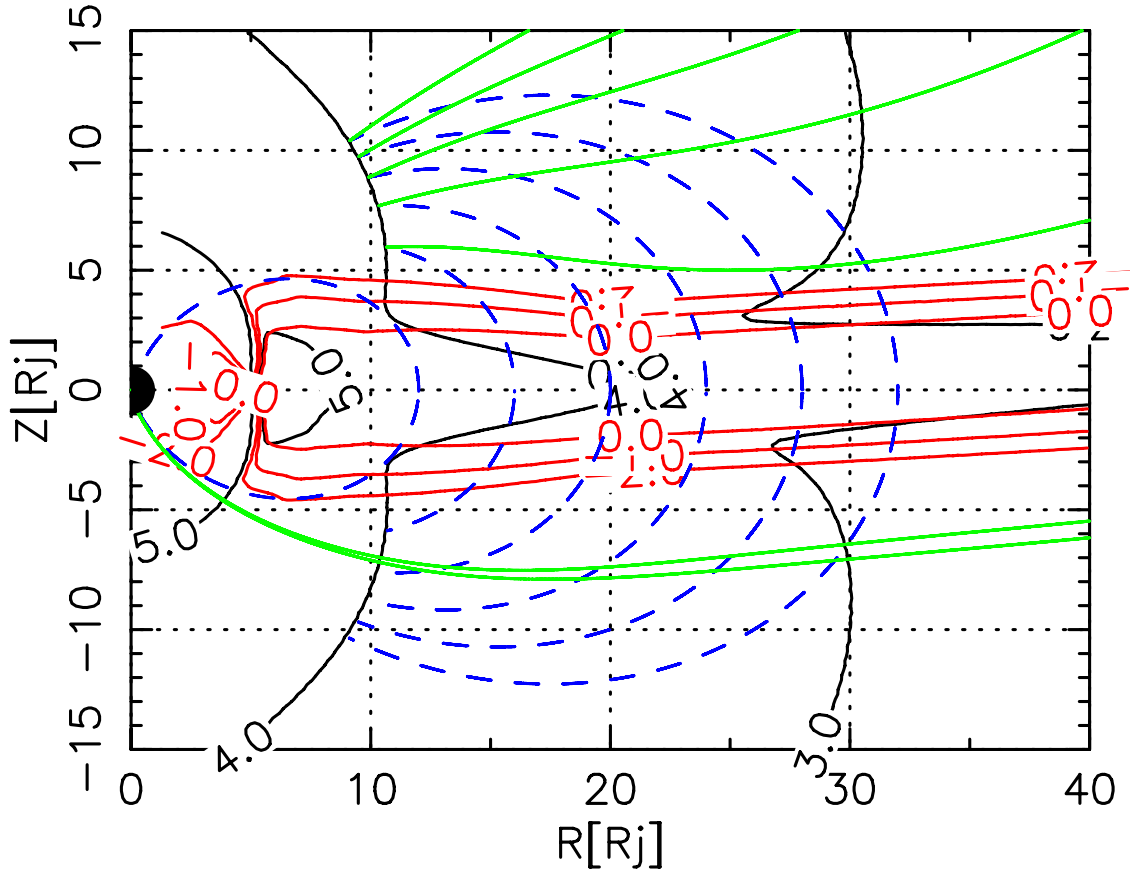
Figure 5.10 shows magnetic field lines and distribution of the fundamental parameters for the CMI process: the R-X mode cutoff frequency  $f_{RX}$  and the ratio  $f_p/f_c$ . Figure 5.10 has a similar format to that of Figure 5.8, but the black and red lines correspond to the distribution of  $f_{RX}$  and the ratio  $f_p/f_c$  in log scale, respectively. The magnetic field lines are traced similarly to those for the L-O mode waves, but their ends are located on the  $f_{RX}$  surface, where  $f$  and  $f/f_{RX}$  were set to 10 kHz and 1.05 in this figure, respectively. The field lines of higher L-values than 20 are “opened” in this figure.

Figure 5.10 indicates that the source region of R-X mode waves at 10 kHz is not located along field lines of  $L < 12$  because the local cutoff frequency  $f_{RX}$  is more than 10 kHz in the region. Thus, we conclude that the radio emissions at  $< 10$  kHz are not generated along the source field lines of  $L < 12$  via the CMI process.

Figure 5.11a–d are examples of the modeled ray paths in a meridian plane for  $L = 32$  (cases G10–G13 in Table 5.3) with the same format as that of Figure 5.9. A half-cone angle,  $f/f_{RX}$ , and  $f$  were set to  $30^\circ$ – $60^\circ$ , 1.05, and 10 kHz, respectively. The red lines correspond to the rays crossing the observable equatorial region of  $|MLAT| < 10^\circ$ . The source regions for these cases have locations appropriate for the CMI process: there is a region of  $f_p/f_c \ll 1$  on the surface of  $f_{RX} \sim 10$  kHz (see Figure 5.10). In Figure 5.11a–d, one can see that rays for all these cases can cross the observable region. In particular, those with cone angles less than  $50^\circ$  (Figure 5.11a and b) cross the region at a distance of  $> 30R_J$ . For  $L = 32$ , an



**Figure 5.9.** Plots of modeled ray paths projected onto the meridian plane in similar format to that of Figure 3.5. Green lines are modeled ray paths and blue broken lines are magnetic latitudes of  $\pm 10^\circ$ . L-value of source field line, half-cone angle,  $f/f_p$ , and  $f$  were set to be 12-32, 30°-90°, 1.05, and 10 kHz, respectively. Panels (a)-(i) correspond to the cases G1-G9 in Table 5.3.



**Figure 5.10:** A plot of distribution of plasma parameters in meridian plane of  $110^\circ$  in similar format to that Figure 5.8, but black and red lines correspond to distribution of  $f_{RX}$  and ratio  $f_p/f_c$  in log scale, respectively. The magnetic field lines are traced similarly to those for L-O mode waves, but their ends are located on  $f_{RX}$  surface, where  $f/f_{RX}$  and  $f$  were set to be 1.05 and 10 kHz in this figure, respectively.

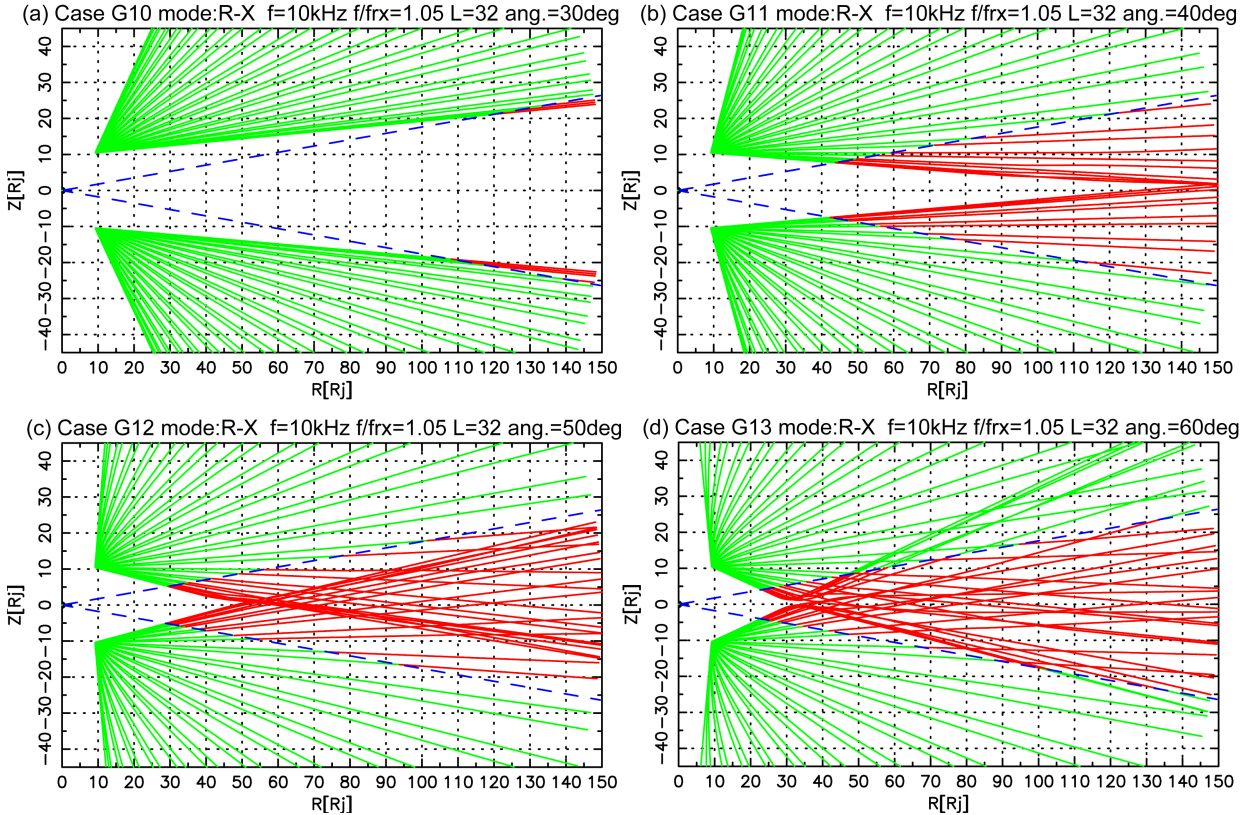


**Figure 5.11:** Examples of modeled ray paths in a meridian plane for  $L > 12$  (cases G10–G13 in Table 5.3) with same format as that of Figure 5.9. L-value, half-cone angle,  $f/f_{RX}$ , and f were set to be 32,  $30^\circ$ – $60^\circ$ , 1.05, and 10 kHz, respectively. Red lines corresponds to rays crossing observed equatorial region of  $|MLAT| < 10^\circ$ . Panels (a)–(d) correspond to the cases G10–G13 in Table 5.3.

angle less than  $50^\circ$  is a plausible condition for QP bursts observed in the equatorial region.

For various source L-values, we examined the relationship between a half-cone angle and the minimum radial distance at which rays cross the equatorial region where  $|MLAT| < 10^\circ$  (“minimum equatorial distance”, hereafter). The results are shown in Figure 5.12a, where  $f = 10$  kHz and  $f/f_{RX} = 1.05$ . The vertical axis is a half-cone angle and the horizontal is the minimum equatorial distance. The lines denoted by symbols represent the relationship between a half-cone angle and the minimum equatorial distance for each source L-value ( $L = 16, 20, 24, 28$ , and 32, respectively). When the rays cross the equatorial region at

a distance of  $>150R_J$  or propagate toward higher latitudes than  $|MLAT| = 10^\circ$ , symbols are plotted on the right axis in this figure. In such a case, rays are not observable from an observer in the equatorial region in the magnetosphere ( $<150R_J$ ). The hatched region corresponds to the “shadow zone” as indicated in Figure 3.5. Based on the observation, the rays were not detected in the shadow zone.

It is evident that rays with source field lines of  $L = 16$  (black line denoted by “+” in Figure 5.12a) can propagate into the shadow zone for almost all half-cone angles. This result is inconsistent with the observation result. Rays with higher source L-values than 16 are not extended into the shadow zone but detectable at an equatorial distance of more than  $30R_J$ . Thus, QP bursts at 10 kHz observed outside the shadow zone in the equatorial region need to have a higher latitudinal source than the field line of  $L \sim 16$ . According to the VIP4-CS models, field lines of  $L > \sim 16$  are extended to more than  $100R_J$  at the equatorial plane. This would correspond to the outermost region of the Jovian magnetosphere or opened to interplanetary space. The minimum value of possible source field lines does not change significantly with respect to the ratio  $f/f_{RX}$  ranging from 1.01 to 1.1 for all of source L-values and half-cone angles.

Figure 5.12b indicates the same relationship as that of Figure 5.12a but for  $f = 3$  kHz and  $f/f_{RX} = 1.05$ . When rays are stopped by the plasma torus or become evanescent before reaching latitudes of  $|MLAT| < 10^\circ$ , symbols are plotted on the left axis in this figure. One can see that the minimum L-value of possible source field lines is  $L > \sim 20$  for the case of  $f = 3$  kHz (the minimum value does not change significantly with respect to the ratio  $f/f_{RX}$  ranging from 1.01 to 1.1). These field lines are also extended to more than  $100R_J$  at the equatorial plane. It is required that QP bursts at 3 kHz and those at 10 kHz have similar source parameters and propagation processes because they were observed simultaneously at low latitudes forming impulsive bursts in dynamic spectrograms (see Figure 3.2). Thus, we conclude that QP bursts at 3–10 kHz observed in the equatorial region are emitted from  $f_{RX}$  surface along the field lines of  $L > \sim 20$ . According to the VIP4-CS and Divine-Garrett models, the  $f_{RX}$  surface corresponds to the altitudes of  $\sim 10\text{--}20R_J$  for  $f = 3\text{--}10$  kHz and

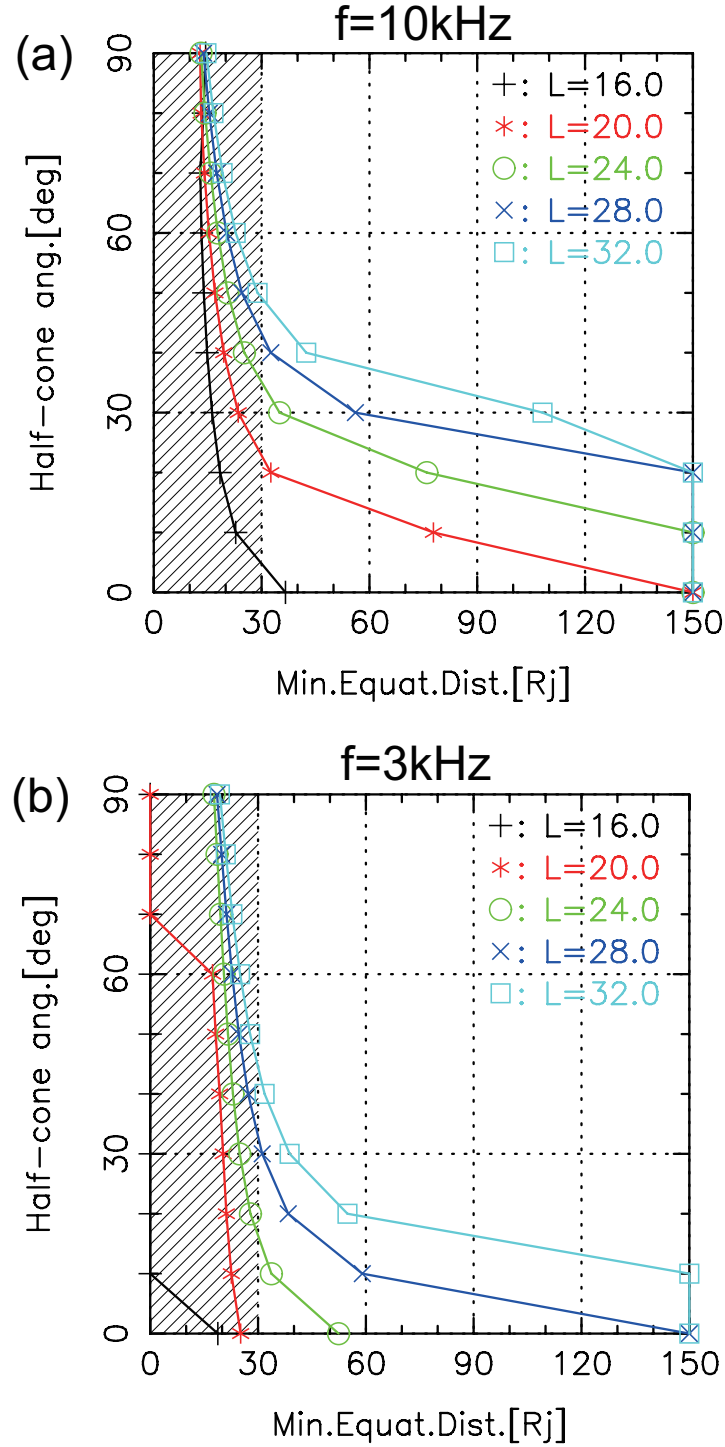


**Figure 5.12:** (a) A plot showing relationship between half-cone angles of modeled rays and minimum radial distances in equatorial region where an observer can detect rays.  $f/f_{RX}$  and  $f$  were set to be 1.05 and 10 kHz, respectively. Vertical axis is half-cone angles and horizontal is the minimum equatorial distance. Lines denoted by various symbols represent relationship between half-cone angles and the minimum equatorial distances for each source  $L$ -value ( $L = 16, 20, 24, 28$ , and  $32$ , respectively). When the rays cross the equatorial region at a distance of  $>150R_J$  or propagate toward higher latitudes than  $|MLAT| = 10^\circ$ , symbols are plotted on the right axis in this figure. (b) The same plot as panel (a) but for  $f = 3$  kHz. When rays are stopped by the plasma torus or become evanescent before reaching latitudes of  $|MLAT| < 10^\circ$ , symbols are plotted on the left axis in this figure.

$f/f_{RX} \sim 1$ . These results indicate that the source region of QP bursts is located above the polar auroral region.

As shown in Figure 5.12, the cone angle and source L-value, which are consistent with the observation results, were not uniquely determined from the ray tracing. However, we can see that cone angles of rays have relatively small values (less than  $40^\circ$  for all cases in Figure 5.12a). For example, the rays of  $f = 10$  kHz originated on  $L = 20$  have an angular range of less than  $20^\circ$  to be observable in a radial distance from  $30\text{--}150R_J$ . This tendency also does not change with respect to the ratio  $f/f_{RX}$  ranging from 1.01 to 1.1 and  $f$  from 3 to 10 kHz for all source L-values and half-cone angles.

### 5.3.4 Summary and Discussion: Radiation Characteristics of QP bursts Observed at Low Latitudes

Based on the ray tracing, we modeled ray paths at a VLF range ( $f = 3\text{--}10$  kHz) for surveys of the source parameters of QP bursts observed at low latitudes. The magnetic field and plasma distributions were determined based on the VIP4-CS and Divine-Garrett models. Rays emitted from a magnetic field line were modeled and projected onto a meridian plane. The observed shadow zone constrained the source location and beaming of rays in the model calculation.

Rays of the L-O mode waves were calculated for various L-values and cone angles under the condition of  $f/f_p = 1.01\text{--}1.1$  and  $f = 3\text{--}10$  kHz by assuming the mode conversion process. These results indicate that the rays emitted from the polar  $f_p$  surface are immediately refracted around the source and propagated to latitudes much higher than  $|\text{MLAT}| = 10^\circ$ . This is inconsistent with the observed occurrence distribution in a meridian plane. Thus, we concluded that L-O mode waves emitted from the polar  $f_p$  surface are unreasonable for QP bursts observed at low latitudes.

Rays of R-X mode waves were calculated under the condition of  $f/f_{RX} = 1.01\text{--}1.1$  and  $f = 3\text{--}10$  kHz for various L-values and cone angles by assuming the CMI process. From the shadow zone observed at less than  $30 R_J$ , it is concluded that QP bursts observed in the

equatorial region are emitted from the polar  $f_{RX}$  surface (corresponding to the altitudes of  $\sim 10\text{--}20 R_J$  for emissions at  $f = 3\text{--}10 \text{ kHz}$  and  $f/f_{RX} \sim 1$ ) along field lines of  $L > \sim 20$ . This result indicates that the source region of QP bursts is located above the polar auroral region.

In addition, we indicated the relationship between a half-cone angle and the minimum equatorial radial distance. This suggests two possible radiation characteristics for QP bursts: (1) they have beaming angles like “filled cones” emitted from source field lines in a restricted L-value range (e.g., the rays at 10 kHz from  $L = 20$  field lines with a half-cone angle ranging from  $0^\circ$  to  $20^\circ$  can cross the magnetic equator from 30 to  $150 R_J$ ), or (2) they have a large source L-value range with beaming angles like “hollow cones” (e.g., the rays at 10 kHz from the  $L = 20\text{--}32$  field lines with a half-cone angle of  $20^\circ$  can cross the equator from 30 to  $150 R_J$ ). As introduced in the Section 1.3.3, the X-ray “hot spot” pulsating with 45-min periodicity has the polar source region restricted in particular longitudes and latitudes (Jovigraphic latitude:  $+60^\circ\text{--}+70^\circ$ , System III longitude:  $160^\circ\text{--}180^\circ$ ). This implies that QP bursts have similar restricted source field lines to those of the “hot spot”. Thus, we conclude that QP bursts observed at low latitudes would have beaming angles like “filled cones” emitted from source field lines in a restricted L-value range.

*Hospodarsky et al. (2004)* reported that same QP burst events were observed by Galileo and Cassini, which were placed at different distances from Jupiter and different local time sectors in the equatorial region. We need to further investigate what beaming is consistent with the results in *Hospodarsky et al. (2004)* based on ray tracing analysis assuming three dimensional conditions (e.g., restricted longitudinal distribution of radio source).

According to the VIP4-CS model, source field lines of  $L > 20$  extend to  $> 100 R_J$  at the equatorial plane. It should be noted, however, that no external field model other than the current sheet is included in the magnetic field model in this study. Thus, the magnetospheric region corresponding to QP bursts are not exactly determined. Leastwise, it was concluded that source field lines of QP bursts observed at low latitudes correspond to the outermost region of the Jovian magnetosphere or opened to interplanetary space.

This is consistent with the quasi-periodic aurora and relativistic particle bursts, which are possibly related to QP bursts: the X-ray aurora with 45-min periodicity (*Gladstone et al.*, 2002) and relativistic electron populations accompanied with QP40 bursts detected along the field lines connected to the equatorial region of more than  $30 R_J$  (*McKibben et al.*, 1993). All these phenomena imply that the quasi-periodic particle acceleration process is associated with the boundary region between the outer magnetosphere and interplanetary space.

Based on theoretical approaches, *Bunce et al.* (2004) predicted that intermittent reconnections at the dayside magnetosphere generate a sufficient field-aligned current at the polar cusp responsible for relativistic particle accelerations as mentioned above if fast solar wind flows inducing large polar cap potentials are assumed. It is still unknown whether the quasi-periodic phenomena (e.g., QP bursts, relativistic electron, and X-ray aurora) originate from the cusp process or a process of other regions. It is necessary to investigate responses of these phenomena to solar wind parameters (e.g., density, velocity, reconnection rate, dynamic pressure, etc.) and to other magnetospheric fluctuations (e.g., ULF waves in the magnetosphere). In Chapter 6, relationships between QP bursts, the solar wind, and magnetospheric fluctuations are discussed based on the solar wind, magnetospheric fields, and radio emissions data observed by Ulysses and Galileo.

We suggested that QP bursts observed at low latitudes are R-X mode waves excited at the polar  $f_{RX}$  surface in a particular rotational phase (i.e.,  $SSL=300^\circ-480^\circ$ , see Figure 3.4). On the other hand, in Section 5.2, it was indicated that QP bursts observed at the northern high latitudes ( $MLAT > +30^\circ$ ) are L-O mode waves excited at the polar  $f_p$  surface at  $SSL= 90^\circ - 300^\circ$ . We interpret those results as meaning that QP bursts have two kinds of sources: one has higher altitudes ( $f_{RX}$  surface) emitting R-X mode waves and the other has lower altitudes ( $f_p$  surface) emitting L-O mode waves. This interpretation leads to the prediction that QP bursts previously observed at low latitudes (e.g., *Kurth et al.*, 1989; QP15 bursts in *MacDowall et al.*, 1993; *Hospodarsky et al.*, 2004; this section) are R-X mode waves and those at high latitudes (e.g., QP40 bursts in *MacDowall et al.*,

1993; Section 5.2 in this thesis) are L-O mode waves. Some polarization measurements at high latitudes support this idea: QP bursts observed at high latitudes are suggested to be L-O mode waves (Section 4.2 in this thesis; *MacDowall et al.*, 1993).

## 5.4 QP Bursts Observed by Cassini at Low Latitudes

### 5.4.1 Assumptions and Calculation Conditions

In Section 4.3, the direction finding analyses found that QP bursts have apparent arrival directions of  $\sim 50 R_J$  distant from Jupiter seen from Cassini in the interplanetary space (see Figure 4.25 and 4.28). These apparent heights are significantly higher than the characteristic height,  $f_p$  and  $f_c$  surface, which are expected to be a few and  $\sim 10 R_J$  height for VLF radio emissions. We interpreted that this disagreement is possibly caused by the two reasons:

1. QP bursts propagating to high latitudes are refracted toward the equatorial region by the local plasmas in the magnetosphere, magnetosheath, and interplanetary space and/or,
2. QP bursts have the real source region at the magnetosheath where the local plasma frequency is comparable to the emission frequencies of QP bursts.

In this section, the refraction effect suggested by the reason (1) was estimated based on the ray tracing analysis.

In the present analysis, it was assumed that L-O and R-X mode waves are emitted from the source region which were suggested in Sections 5.2 and 5.3 and propagate through the magnetosphere, magnetosheath, and the interplanetary space plasmas defined by the *Divine-Garrett* and *Slavin* models indicated in Section 5.1.2. In the magnetosheath model, the maximum plasma frequency of the magnetosheath is equivalent to  $f_p \sim 12.98$  kHz. Thus, L-O mode waves at 13 kHz is quite close to the cutoff, while R-X mode waves at 13 kHz are completely cutoff because the magnetosheath is weakly magnetized, and

**Table 5.4:** Calculation conditions of the ray tracing for the case of Cassini

case	figure	mode	$f$	$f/f_p, f/f_{RX}$	L	half-cone ang.
case C1	5.13a	L-O	26 kHz	1.05	32	90°
case C2	5.13b	L-O	13 kHz	1.05	32	90°
case C3	5.14a	R-X	26 kHz	1.05	32	50°
case C4	5.14b	R-X	14 kHz	1.05	32	50°

$f_{RX}$  is slightly higher than 12.98 kHz. Rays are supposed to be refracted significantly near their cutoff frequencies (i.e.,  $f/f_p, f/f_{RX} \sim 1$ ). To estimate the refraction effects by the magnetosheath, the emission frequencies were set to be 13 kHz and two times higher frequency of 26 kHz for L-O mode waves, and those for R-X mode waves were set to be 14 and 26 kHz. The ratios of  $f/f_p$  and  $f/f_{RX}$  at the source region were set to  $f/f_p = 1.01\text{--}1.1$  and  $f/f_{RX} = 1.01\text{--}1.1$ , respectively, for the same reasons as shown in Section 5.3. Half-cone angles and source field lines were determined to be typical values suggested in Sections 5.2 and 5.3. Calculation conditions for each case are summarized in Table 5.4.

### 5.4.2 Ordinary mode

Figure 5.13 indicates ray tracing results for L-O mode waves with similar formats to Figure 5.9. Blue lines are the ray paths traced from the polar region to a distance of 200  $R_J$  from Jupiter, and red contours represent the plasma density structure derived from the *Divine-Garrett* and *Slavin* model. Cross-sections of hollow cone are plotted in a meridian plane including the Sun-Jupiter axis. The symbol “★” roughly denotes the radial distance of Cassini (166–175  $R_J$ ) when the direction findings were performed (see Section 4.3.2).

Figure 5.13a represents a result for the case of L-value of source field line, half-cone angle,  $f/f_p$ , and  $f$  which were set to be 32, 90°, 1.05, and 26 kHz, respectively (Case C1 in Table 5.4). The rays propagate from the polar region toward high latitudes without significant refraction because the emission frequency is sufficiently higher than the local plasma frequency of the magnetosheath. In Figure 5.13b, all of the parameters are the same

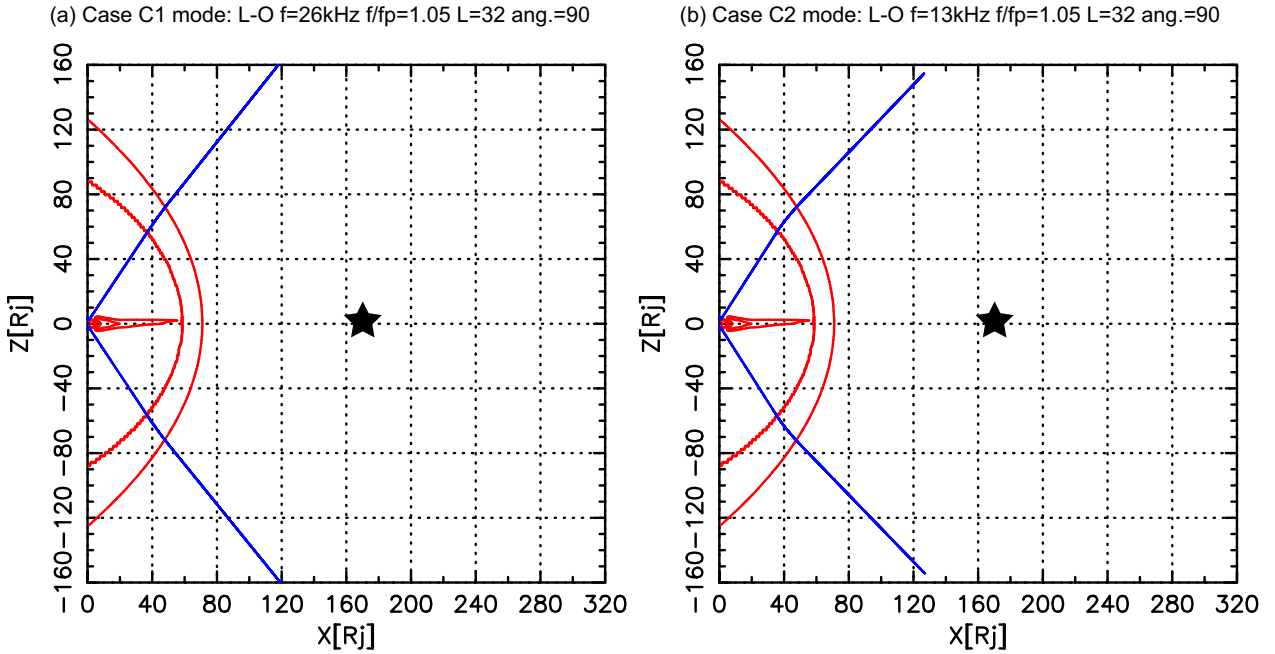


**Figure 5.13:** Ray tracing results for the case of L-O mode waves with similar formats to Figure 5.9. Blue lines are the ray paths traced from the polar region to a distance of  $200 R_J$  from Jupiter, and red contours represent the plasma density structure derived from the *Divine-Garrett* and *Slavin* model. Cross-sections of the hollow cone are plotted in a meridian plane including the Sun-Jupiter axis. Symbol “★” roughly denotes the radial distance of Cassini ( $166\text{--}175 R_J$ ) when the direction findings were performed (see Section 4.3.2). (a) L-value of source field line, half-cone angle,  $f/f_p$ , and  $f$  were set to be 32,  $90^\circ$ , 1.05, and 26 kHz, respectively (Case C1 in Table 5.4). (b) All of the parameters are the same as Case C1, except for  $f$  which was set to be 13 kHz (Case C2).

as Case C1, except for  $f$  which was set to be 13 kHz (Case C2). Even the emission frequency is quite close to the local  $f_p$  at the magnetosheath, rays are not refracted significantly by the magnetosheath toward the equatorial region.

Both cases indicate that the assumed magnetosheath plasma cannot refract rays significantly toward the position of Cassini in the equatorial region. Thus, we conclude that L-O mode waves, which are emitted from the polar region toward high latitudes, could not have the apparent arrival directions at a distance of  $\sim 50 R_J$  from Jupiter by the refraction under the assumption of the *Slavin* magnetosheath model.

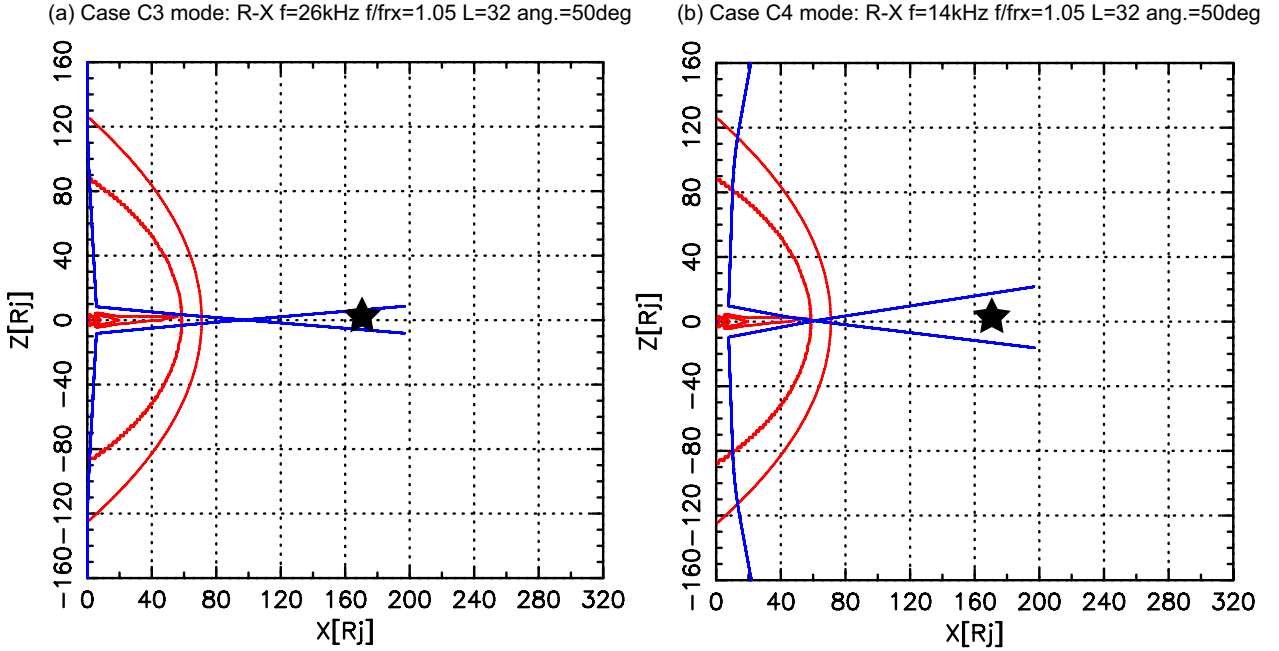


**Figure 5.14:** Ray tracing results for the case of R-X mode waves with the same format as Figure 5.13. (a) L-value of source field line, half-cone angle,  $f/f_{RX}$ , and  $f$  were set to be 32, 50°, 1.05, and 26 kHz, respectively (Case C3 in Table 5.4). (b) All of the parameters are the same as Case C3, except for  $f$  which was set to be 14 kHz (Case C4).

### 5.4.3 Extraordinary mode

Figure 5.14 indicates ray tracing results for R-X mode waves with the same format to Figure 5.13. Figure 5.14a is a result for the case of L-value of source field line, half-cone angle,  $f/f_{RX}$ , and  $f$  set to be 32, 50°, 1.05, and 26 kHz, respectively (Case C3). The parameters for the case of Figure 5.14b (Case C4) are same as those for Case C3, except for  $f$  which was set to be 14 kHz.

These results indicate that R-X mode waves can propagate from the polar region to the equatorial region, however, the refraction at the magnetosheath is insignificant, and the apparent diameter between the arrival directions of rays and Jupiter are much less than  $\sim 50 R_J$  seen from the observer at “★”. Consequently, we conclude that R-X mode waves also could not have the arrival directions of  $\sim 50 R_J$  by the refraction under the assumption of the *Slavin* magnetosheath model.

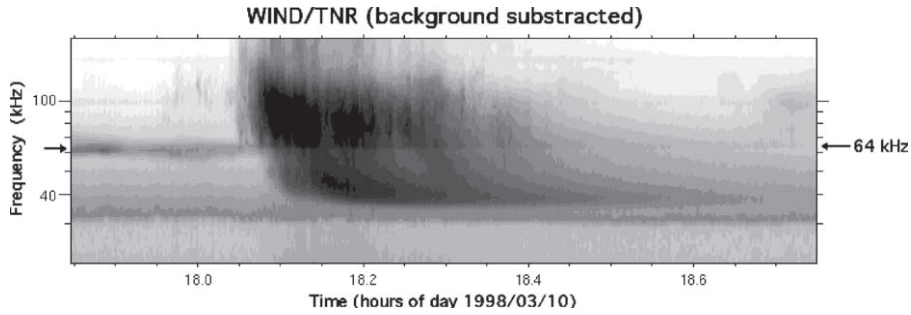


**Figure 5.15:** The dynamic spectrum showing a typical event of LF bursts observed by the WIND satellite (*Steinberg et al.*, 2004).

#### 5.4.4 Summary and Discussion: Propagation of QP bursts in the Magnetosheath and Interplanetary Space

The examinations by the ray tracing method concluded that both of L-O and R-X mode waves cannot have the apparent arrival directions  $\sim 50 R_J$  from Jupiter by the refraction of the *Slavin* magnetosheath model. However, it is still possible to direct the rays emitted from the polar region toward the equatorial region by another refraction process: the wave scattering by density fluctuations at a spacial scale comparable to the wavelength in the magnetosheath and interplanetary space plasmas.

*Steinberg et al.* (2004) performed the ray tracing for “LF bursts”, which are emitted from the terrestrial magnetosphere at LF range (see Figure 5.15 for a typical example), assuming the density fluctuations in the solar wind plasma referring to the spectral analysis of the density fluctuations performed by *Lacombe et al.* (1988, 1997). They assumed that a ray propagates with an angular deviation  $\delta\theta$  over a step of length  $\delta S$ , which is defined by

$$\langle \Delta\theta^2 \rangle = b(f)\Delta S. \quad (5.22)$$

The coefficient  $b(f)$  is the scattering coefficient given by the following equation in *Lacombe et al.* (1997)

$$b(f) = \frac{\sqrt{\pi}}{2\mu^4} \frac{f_p^4}{f^4} \frac{1}{h} \left[ \frac{\delta n_e}{n_e} \right]^2 \quad (5.23)$$

where  $\mu = \sqrt{1 - f_p^2/f^2}$  is the refractive index at the frequency  $f$  and the plasma frequency  $f_p$ , and  $\delta n_e$  is the variance in electron densities at the Gaussian scale  $h$ . Equation 5.23 is expressed simply by its value at  $2f_p$ :

$$b(f) = b(2f_p) \frac{9}{\mu^4} \frac{f_p^4}{f^4}. \quad (5.24)$$

where  $b(2f_p)$  is the scatter coefficient in the magnetosheath, which was set to be in Steinberg et al. (2004). Steinberg et al. (2004) set  $\Delta\theta \leq 0.1$  rad and a constant step  $\Delta S = 200$  km for  $b(2f_p) = 1-2 \times 10^{-10} \text{ rad}^2/\text{m}$ . Figure 5.16 represents the ray tracing results in Steinberg et al. (2004). The left panels (a and c) indicate the ray paths in the  $x$ - $z$  plane of the GSE coordinate at frequencies of  $f = 1.3f_p$  and  $1.9f_p$  where  $f_p$  is the local plasma frequency of the solar wind. The right panels (b and d) show the number of rays which cross the sphere of radius  $R = 400R_E$ , indicating the dispersions of rays by the solar wind scattering. As is evident from Figure 5.16, rays are significantly refracted by the density fluctuations in the solar wind plasma even at high frequencies, e.g., two times higher than the local  $f_p$  of the solar wind.

At Jupiter, QP bursts emitted from altitudes of a few to  $10 R_J$  at VLF-LF range could be also scattered significantly by the fluctuations in the magnetosheath and solar wind and reach to the high arrival directions of  $\sim 50 R_J$ . Thus, we reinterpret the direction finding results in Section 4.3.2 resulted from the following causes:

1. QP bursts emitted from the polar region (a few to  $10 R_J$  altitudes) were scattered and directed to the apparent altitudes of  $\sim 50 R_J$  by the local density fluctuations in the magnetosheath and interplanetary space plasmas

and/or,

2. QP bursts have the real source region at the magnetosheath where the local plasma frequency is comparable to the emission frequencies of QP bursts.

In Chapter 6, we examine the cause (2) based on the theoretical approach on the wave generation mechanisms.

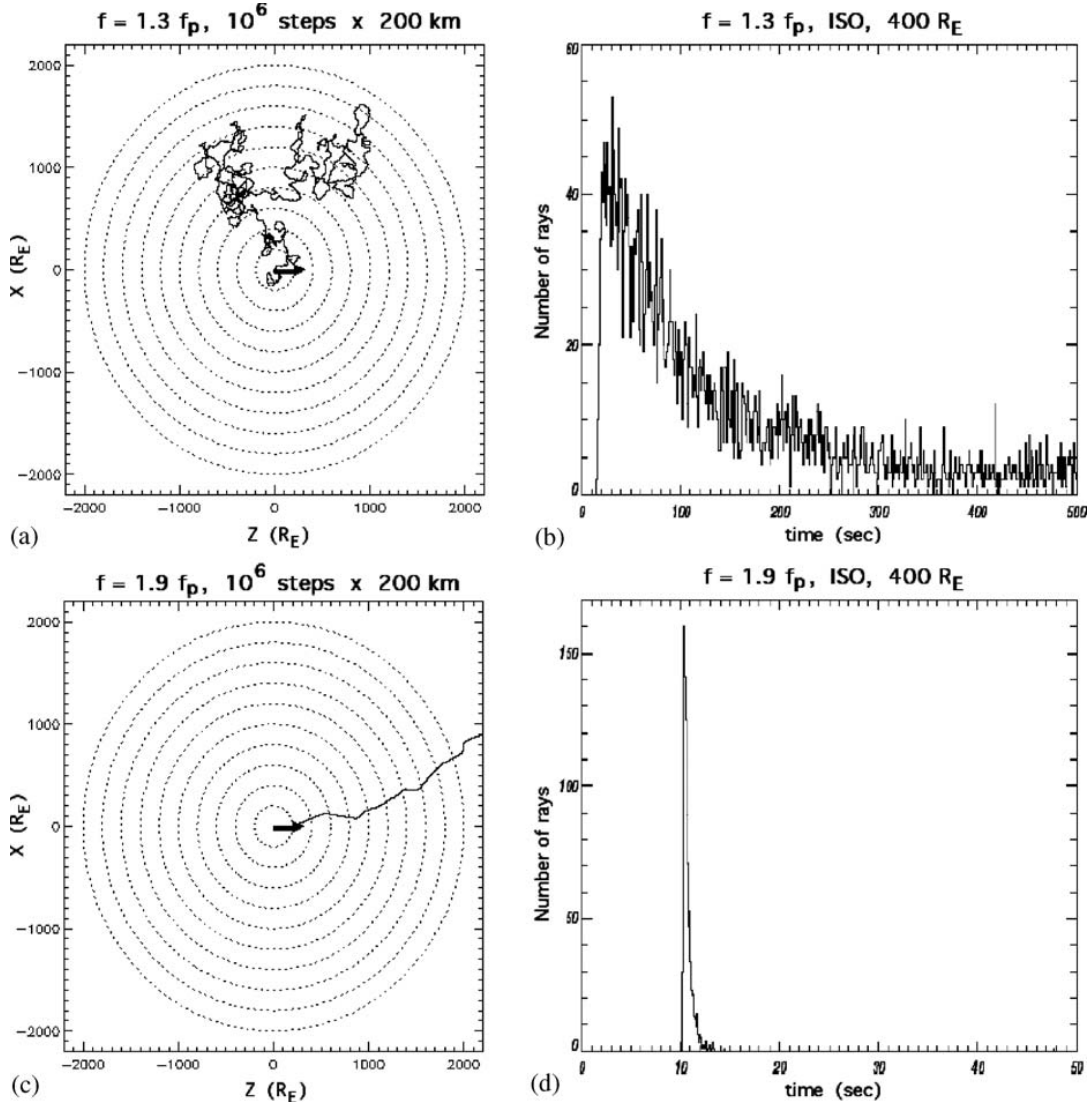


**Figure 5.16:** Results of the ray tracing (after Steinberg et al., 2004). Left panels: the path of a ray in the  $x$ - $z$  plane in the GSE coordinate at  $f = 1.3f_p$  and at  $1.9f_p$  where  $f_p$  is the local plasma frequency of the solar wind. Right panels: the number  $N_r(t)$  of rays which cross the sphere of radius  $R = 400R_E$  (outward and inward), as a function of time, at  $1.3f_p$  and  $1.9f_p$ .

## 5.5 Brief Summary

In this chapter, the observation results in Chapters 3 and 4 were interpreted based on the ray tracing analysis, and we discussed the source location, directivity, and propagation process of QP bursts at all geometries. The parametric survey comparing with the observations at the high latitudes suggested that:

1. QP bursts observed at the high latitudes have the source region located at an altitude of  $1.3\text{--}1.4 R_J$  along high latitudinal field lines, wherein the emission frequency is nearly equal to the local plasma frequency ( $f/f_p \sim 1$ ) (Figure 5.5)
2. QP bursts observed at the northern high latitudes are L-O mode waves with significantly broadened beaming patterns, like “filled cone” shape (Figure 5.5)
3. QP bursts at the high latitudes are generated during a particular rotational phase ( $\text{SSL}=90^\circ\text{--}300^\circ$ ), forming the longitudinal structure of high occurrence probabilities (Figure 5.5d)

On the other hand, the ray tracing performed for the QP bursts observed at the low latitudes suggested that:

4. QP bursts at 3–10 kHz observed in the equatorial region are emitted from a  $f_{RX}$  surface at  $\sim 10\text{--}20 R_J$  along the field lines of  $L > \sim 20$  (Figures 5.11 and 5.12)
5. QP bursts observed at the low latitudes would have beaming angles like “filled cones” emitted from source field lines in a restricted L-value range, forming the “shadow zone” in the equatorial region (Figure 5.12)

Those results were interpreted as meaning that:

6. QP bursts have two kinds of sources: one has higher altitudes ( $f_{RX}$  surface) emitting R-X mode waves and the one has lower altitudes ( $f_p$  surface) emitting L-O mode waves (Discussion in Section 5.3.4)

Based on the ray tracing with the magnetosheath plasma model, we reinterpreted the direction finding results by Cassini were resulted from the following causes:

- QP bursts from the polar region (a few to 10  $R_J$  altitudes) were scattered and reached to the apparent altitudes of  $\sim 50 R_J$  by the local density fluctuations in the magnetosheath and interplanetary space (Figures 5.13–5.16)

and/or,

- QP bursts have the real source region in the magnetosheath



# Chapter 6

## Generation Mechanism of Quasi-Periodic Bursts

In Chapter 5, ray tracing analyses were made to investigate the source location, directivity, and wave modes of QP bursts, comparing with the occurrence characteristics, polarization, and direction findings performed by Ulysses, Galileo, and Cassini. In this chapter, two possible microscopic generation mechanisms of QP bursts are discussed based on theoretical approaches under the observational constraints obtained in the previous chapter. Besides, two macroscopic scenarios for the quasi-periodic particle acceleration process are proposed and verified based on the observation of QP bursts, magnetic fields, and solar wind by Ulysses and Galileo.

### 6.1 Microscopic Generation Mechanisms of Quasi-Periodic Bursts

We propose two possible scenarios for the microscopic generation process of QP bursts: the direct generation so-called “Cyclotron Maser Instability (CMI)” (*Wu and Lee, 1979*) and indirect generation called “Mode Conversion Process” (*Oya, 1974; Jones, 1976*). In the CMI process, free-space electromagnetic waves directly resonate with the electrons ac-

companying unstable structures of particle distribution functions in the velocity space, e.g., loss-cone or horseshoe distributions. In the mode conversion process, free-space waves are converted from the local plasma waves (e.g., Z mode waves) at discontinuity of plasma densities. These two processes are investigated as possible generation mechanisms of QP bursts based on the theories of each process established by previous studies with the observational constraints obtained by the ray tracing in this study.

### 6.1.1 Scenario 1: Direct Generation

#### Description of Direct Generation Scenario

Firstly, we examine the “direct generation scenario” that QP bursts are excited via the CMI process. Figure 6.1 indicates a flow diagram showing the direct generation scenario. In this scenario, QP radio bursts are assumed to be generated via the CMI process induced by unstable structures of the quasi-periodic electron outbursts with relativistic energies, which were observed by Ulysses at high latitudes (*McKibben et al.*, 1993; *Zhang et al.*, 1995). We investigated the possibility that free-space electromagnetic waves are generated by the observed electron outbursts based on numerical calculations of the linear wave growth rate (note that, hereafter, ion dynamics are neglected).

Some previous theoretical studies developed evaluation methods of the linear growth rate of cyclotron resonance waves, which include contribution of suprathermal electrons as energy sources for these waves (e.g., *Baldwin et al.*, 1969; *Lee et al.*, 1979). The formulation of the growth rate is expressed as integrations for gradient of the electron distribution functions  $f$  along the “resonance curve”, which is defined by the delta function  $\delta(\gamma\omega - k_{\parallel}u_{\parallel} - n\Omega_e)$  in the phase space of specific momentum  $\mathbf{u} \equiv \gamma\mathbf{v}$  (see Figure 6.2 and 6.8 for instance), where  $k$  is the wave number at a complex frequency  $\omega$ ,  $\Omega_e$  is the local electron cyclotron frequency,  $n$  is the resonance order, and  $\gamma \equiv (1 + u^2/c^2)^{1/2}$  is the Lorentz factor at a particle velocity of  $\mathbf{v}$ . The mark “ $\parallel$ ” denotes a parallel component with respect to the background magnetic field lines, and, “ $\perp$ ” is a perpendicular component. The complex frequency is defined as  $\omega \equiv \omega_r + i\omega_i$  where  $\omega_r$  is a real part of  $\omega$  and an imaginary part  $\omega_i$

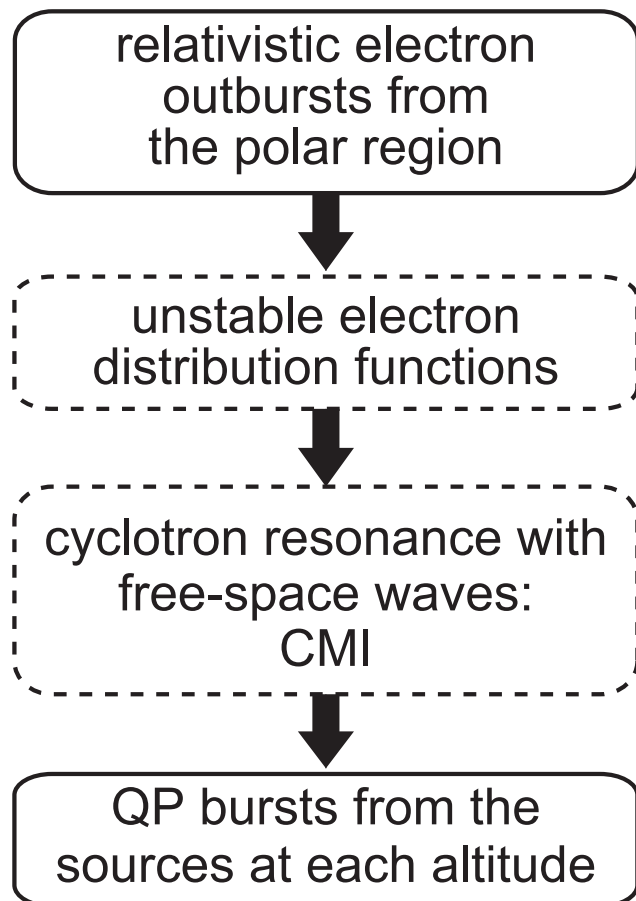


**Figure 6.1:** A flow diagram showing a possible scenario for QP bursts' generation termed the “direct generation scenario”. In this scenario, QP bursts are assumed to be generated via the CMI process induced by unstable structures of the quasi-periodic electron outbursts. The processes framed by broken lines indicate that these processes have not been identified in observations or verified by wave generation theories.

is the wave growth rate. With reference to *Nishimura et al.* (2007), the linearized growth rate  $\omega_i$ , is written as

$$\omega_i = \omega_r \sum_s \frac{2\pi^2 \omega_{ps}^2}{G \omega^2 n_s} \int \int \int d\mathbf{u} \sum_{n=0}^{\infty} \frac{u_{\perp} n \Omega_e}{\gamma k_{\perp}} (\alpha_1 J_n^2 + \alpha_2 J_n J_{n+1} + \alpha_3 J_{n+1}^2) \cdot \left( n \Omega_e \frac{\partial}{\partial u_{\perp}} + k_{\parallel} u_{\perp} \frac{\partial}{\partial u_{\parallel}} \right) f_s(u_{\perp}, u_{\parallel}) \cdot \delta(\gamma \omega - k_{\parallel} u_{\parallel} - n \Omega_e) \quad (6.1)$$

where  $\omega_p$  is the local plasma frequency,  $n_s$  is electron densities of  $s$ -th species ( $s$ : hot and cold plasma), and  $J_n = J_n(b)$  is the  $n$ -th order Bessel function depending on  $b \equiv k_{\perp} u_{\perp} / \Omega_e$ . It should be noted that Equation 6.1 is derived under the assumptions of  $\omega_i \ll \omega_r$  and  $k_{\perp} u_{\perp} / \Omega_e \ll 1$ . The assumption of  $\omega_i \ll \omega_r$  indicates that the instabilities induced by the suprathermal plasma do not contribute significantly to the wave dispersion relations but serve as free energy sources for waves in the cold plasma. The second assumption of  $k_{\perp} u_{\perp} / \Omega_e \ll 1$  corresponds to the relation that cyclotron radii of the electrons are sufficiently smaller than the wavelengths of the waves generated by the instabilities. This ensures that the electrons feel the spatially-uniform electric fields of these waves at any gyro phases, i.e., the gyro radii are not modulated by the wave electric fields. The parameters  $\alpha_i$  ( $i = 1, 2, 3$ ) are the nondimensional coefficients defined by

$$\alpha_1 = \frac{n \Omega_e}{k_{\perp} u_{\perp}} (\psi_{11} + \psi_{22} + \psi_{12}) + \frac{k_{\perp} u_{\parallel}^2}{n \Omega_e u_{\perp}} \psi_{33} + \frac{u_{\parallel}}{u_{\perp}} (\psi_{13} - \psi_{23}) \quad (6.2)$$

$$\alpha_2 = -2\psi_{22} - \psi_{12} + \frac{k_{\perp} u_{\parallel}}{n \Omega_e} \psi_{23} \quad (6.3)$$

$$\alpha_3 = \frac{k_{\perp} u_{\perp}}{n \Omega_e} \psi_{22} \quad (6.4)$$

with  $\psi_{ij}$  ( $i, j = 1, 2, 3$ ) which is expressed as

$$\psi_{11} \equiv N^4 \sin^2 \theta - N^2 (\epsilon \sin^2 \theta + \eta) + \epsilon \eta \quad (6.5)$$

$$\psi_{22} \equiv -N^2 (\epsilon \sin^2 \theta + \eta \cos^2 \theta) + \epsilon \eta \quad (6.6)$$

$$\psi_{33} \equiv N^4 \cos^2 \theta - N^2 \epsilon (1 + \cos^2 \theta) + \epsilon^2 - g^2 \quad (6.7)$$

$$\psi_{13} \equiv 2N^2(N^2 - \epsilon) \sin \theta \cos \theta \quad (6.8)$$

$$\psi_{12} \equiv 2g(\eta - N^2 \sin^2 \theta) \quad (6.9)$$

$$\psi_{23} \equiv 2N^2 g \sin \theta \cos \theta \quad (6.10)$$

where  $N$  is a refraction index of plasma waves and  $\theta$  is a propagation angle. The parameters  $\epsilon$ ,  $g$ , and  $\eta$  are given by

$$\epsilon \equiv 1 - \omega_p^2 / (\omega_r^2 - \Omega_e^2) \quad (6.11)$$

$$g \equiv \omega_p^2 \Omega_e / \omega_r (\omega_r^2 - \Omega_e^2) \quad (6.12)$$

$$\eta \equiv 1 - \omega_p^2 / \omega_r^2. \quad (6.13)$$

The coefficient  $G$  in Equation 6.1 is derived from partial differentiation of the dispersion relation of the cold plasma  $\text{Re}(\Lambda^t(\mathbf{k}, \omega_r))$  with respect to  $\omega_r$ , that is,

$$\begin{aligned} G &\equiv \omega_r \frac{\partial}{\partial \omega_r} [\text{Re}(\Lambda^t(\mathbf{k}, \omega_r))] \\ &= 2N^4 \left[ \frac{\omega_r^2 \omega_p^2 \sin^2 \theta}{(\omega_r^2 - \Omega_e^2)^2} + \frac{\omega_p^2 \cos^2 \theta}{\omega_r^2} \right] \\ &\quad + 4N^2 \left[ \frac{\omega_p^2 (\omega_p^2 - \Omega_e^2)}{(\omega_r^2 - \Omega_e^2)^2} - 1 - \frac{\omega_p^2 \Omega_e^2 \sin^2 \theta}{2(\omega_r^2 - \Omega_e^2)^2} \right] \\ &\quad + 2 \left[ \left( 2 - \frac{\omega_p^2}{\omega_r^2} \right) \left( 1 - \frac{\omega_p^2}{\omega_r^2 - \Omega_e^2} \right)^2 - \frac{\omega_p^4 \Omega_e^2}{\omega_r^2 (\omega_r^2 - \Omega_e^2)^2} + 2 \left( 1 - \frac{\omega_p^2}{\omega_r^2} \right)^2 \frac{\omega_r^2 \Omega_e^2}{(\omega_r^2 - \Omega_e^2)^2} \right] \end{aligned} \quad (6.14)$$

In this study, the electron distribution function of hot components is given by the following formula

$$f_h(u_{\parallel}, u_{\perp}) = \frac{n_h}{\sqrt{\pi^3} a_{\parallel} a_{\perp}^2 c^3} \exp \left( -\frac{1}{a_{\perp}^2} \frac{(u_{\perp} - u_{\perp 0})^2}{c^2} - \frac{1}{a_{\parallel}^2} \frac{(u_{\parallel} - u_{\parallel 0})^2}{c^2} \right) \quad (6.15)$$

which corresponds to the Maxwellian distribution with mean parallel and perpendicular

**Table 6.1:** Characteristics of the quasi-periodic electron outbursts in a relativistic energy range

particle flux	315/cm <sup>2</sup> /sec at R~54R <sub>J</sub> ( $E > 16$ MeV)*
duration	120 sec*
anisotropy	outbursts from the Jovian polar region*
total energy	$2.9 \times 10^{12}$ W*

\*: after McKibben *et al.* (1993) and Zhang *et al.* (1995)

	R~10R <sub>J</sub> ( $E > 16$ MeV)	R~2R <sub>J</sub> ( $E > 16$ MeV)
particle flux	$\sim 9.5 \times 10^4$ /cm <sup>2</sup> /sec	$\sim 9.5 \times 10^6$ /cm <sup>2</sup> /sec
number density $n_b$	$\sim 3.2 \times 10^{-6}$ /cc	$\sim 3.2 \times 10^{-4}$ /cc
background density $n_{BG}$	$\sim 1.1 \times 10^{-5}$ /cc	$\sim 120$ /cc
$n_b/n_{BG}$	$\sim 3.2 \times 10^{-1}$	$\sim 2.6 \times 10^{-6}$

momentums of  $u_{\parallel 0}$  and  $u_{\perp 0}$ .  $a_{\parallel}$  and  $a_{\perp}$  denote parallel and perpendicular temperatures of the Maxwellian distribution.

### Assumptions and Conditions

Characteristics of the distribution function in Equation 6.15 were determined based on the observation results of relativistic electron outbursts with 40 minutes quasi-periodicity (McKibben *et al.*, 1993; Zhang *et al.*, 1995). McKibben *et al.* (1993) estimated the particle flux of these electron outbursts in an energy range of more than 16 MeV to be 315/cm<sup>2</sup>/sec from the *in-situ* observations by Ulysses/COSPIN at a radial distance of  $\sim 54R_J$  from Jupiter. The duration and total energy of the electron outbursts were also found to be 120 sec and  $2.9 \times 10^{12}$  W by these studies. These characteristics of the electron outbursts are summarized in Table 6.1.

In this study, it was assumed that total flux contents conserve along the flux tube where the quasi-periodic electron outbursts and QP radio bursts are occurring. The observed characteristics of the outbursts were extrapolated to those at the altitudes of  $\sim 2$  and  $10R_J$ , where QP radio bursts are possibly excited as suggested by the ray tracing results in Section 5.2 and 5.3. The extrapolated parameters are also summarized in Table 6.1. We postulated the background density of cold plasma by the plasma distribution model adopted for the

ray tracings.

These results indicate that densities of the relativistic electron outbursts are sufficiently lower than those of the background plasma at both of the source altitudes. This implies that the wave dispersion relations at each altitude are dominated by the cold plasma, and the hot plasma (suprothermal electrons) contributes only as free energy sources for the cold plasma waves. Thus, the linear growth rate governed by Equation 6.1 can be applied to QP bursts.

In Section 5.4, we suggested a possibility that the QP bursts observed in the interplanetary space have real sources at the magnetosheath. In the present analysis, growth rates at the magnetosheath were also calculated. The extrapolation of the outbursts' characteristics was not performed for the magnetosheath because the flux tube contents are possibly changed drastically at the magnetopause. However, densities of the electron outbursts are plausibly smaller than the local plasma densities at the magnetosheath; i.e., the cold plasma is dominant. This is because plasma densities of the magnetosheath are sufficiently larger than those at  $10 R_J$  and cross sections of the flux tube are also larger than those at  $10 R_J$ . Thus, the linear growth rate in Equation 6.1 is also applicable at the magnetosheath. For instance, the ratio of  $n_b/n_{BG}$  was set to be  $10^{-3}$  in the present calculations.

Parameters of waves and those of the distribution function in Equation 6.15 are free for growth rate calculations: wave mode (O or X modes), resonance order  $n$ , mean parallel and perpendicular momentums  $u_{\parallel 0}$  and  $u_{\perp 0}$ , and parallel and perpendicular temperatures  $a_{\parallel}$  and  $a_{\perp}$  are all free. The wave growth rates were calculated at each of possible source altitudes, where the background plasmas are characterized by the parameter of  $\omega_p/\omega_c = 10^{-3}$  at  $10R_J$ ,  $\omega_p/\omega_c = 10^{-2}$  at  $2R_J$ , and  $\omega_p/\omega_c \sim 42$  at the magnetosheath. We investigated the appropriate parameters of the distribution function which can reproduce the observed characteristics of QP radio bursts. It should be noted that  $e$ -folding time of the wave growth, when wave amplitudes are amplified to  $e$  times larger than the initial amplitudes, was required to be less than 120 sec, which is equivalent to the duration of the periodic electron outbursts. Besides, the resonance order was set to be  $n = 1$  or  $n = 2$  because

**Table 6.2:** Calculation conditions for the linear wave growth rate

case	figure	mode	$\omega_p/\omega_c$	$n$	$u_{\parallel 0}$ (keV)	$u_{\perp 0}$ (keV)	$a_{\parallel}$ (keV)	$a_{\perp}$ (keV)
case H1	6.3	O	$10^{-3}$	2	1016	0	308	308
case H2	6.4	X	$10^{-3}$	2	1016	0	308	308
case H3	6.5	O	$10^{-3}$	1	15489	0	308	308
case H4	6.6	X	$10^{-3}$	1	15489	0	308	308
case H5	6.9	O	$10^{-3}$	1	15489	3837	308	308
case H6	6.10	X	$10^{-3}$	1	15489	3837	308	308
case L1	6.12	O	$10^{-2}$	1	15489	3837	308	308
case L2	6.13	X	$10^{-2}$	1	15489	3837	308	308
case S1*	6.14	X	42	1	15489	3837	308	308

$\omega_p$ : local plasma frequency,  $\omega_c$ : local cyclotron frequency,  $n$ : resonance order

$u_{\parallel 0}, u_{\perp 0}$ : parallel and perpendicular mean momentums of the distribution function

$a_{\parallel}, a_{\perp}$ : parallel and perpendicular temperatures of the distribution function

\* the ratio of beam densities to background densities  $n_b/n_{BG}$  was set to be  $10^{-3}$

growth rates are generally larger at low resonance order than those at higher order. Calculation conditions for the growth rate indicated in the figures are summarized in Table 6.2.

### Calculation Results: Polar High Altitudes–Parallel Beam

First, growth rates were calculated assuming the distribution function to be the “parallel beam” distribution as shown in Figure 6.2, which corresponds to the Maxwellian shifted in parallel directions in the momentum space. It should be noted that parallel mean energy of the outward beam was set to be positive with respect to the background field line direction; i.e., the source region is located at the northern hemisphere. Figure 6.3 is a result of the growth rate calculation for the O mode waves generated by the parallel beam distribution at high source altitudes in the northern hemisphere, corresponding to the QP bursts observed by Galileo at low latitudes (Section 5.3). The free parameters of  $\omega_p/\omega_c$ ,  $n$ ,  $u_{\parallel 0}$ ,  $u_{\perp 0}$ ,  $a_{\parallel}$ , and  $a_{\perp}$  were set to be  $10^{-3}$ , 2,  $\sim 1$  MeV, 0 eV,  $\sim 300$  keV, and  $\sim 300$  keV, respectively (case H1 in Table 6.2). The top panel represents dependence of the growth rate with respect to

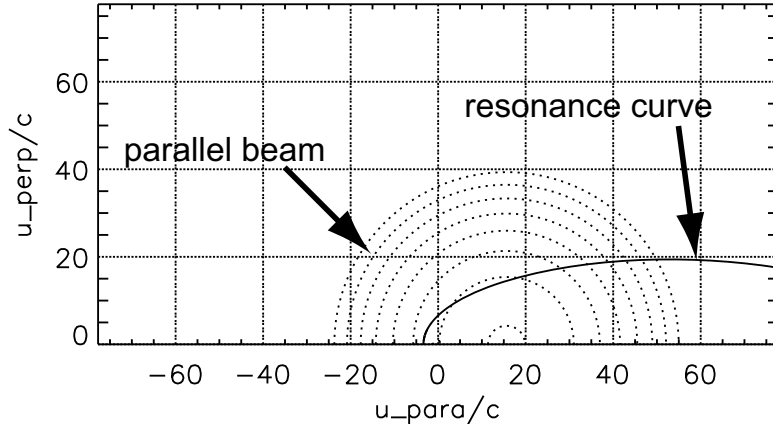


**Figure 6.2:** A schematic showing distribution function and resonance curve in a momentum space. Contours show phase space densities of the distribution function corresponding to an electron parallel beam, and solid curve is the resonance curve. Horizontal and vertical axes indicate the parallel and perpendicular specific momentums normalized by the light speed.

wave frequencies and propagation angles. The vertical and horizontal axes show the wave frequencies  $\omega_r$  normalized by the local cyclotron frequency  $\omega_c$  and wave propagation angles  $\theta$ , respectively. The gray shade indicates the growth rate  $\omega_i$  normalized by  $\omega_c$ . The bottom left panel is the maximum growth rates in an angular range of  $\theta = 0^\circ$ – $180^\circ$  as a function of the frequencies  $\omega_r/\omega_c$ . The vertical and horizontal axes indicate  $\omega_i/\omega_c$  and  $\omega_r/\omega_c$ . The bottom right panel is the maximum growth rates in a frequency range of  $\omega_r/\omega_c = 0$ – $2$  as a function of the propagation angles  $\theta$ . The vertical and horizontal axes indicate  $\omega_i/\omega_c$  and  $\theta$ . The horizontal broken lines show the level corresponding to the  $e$ -folding time of 120 sec.

As is evident in the top panel of Figure 6.3, O mode waves are weakly generated with broadband frequencies and broad beaming patterns above and below the local cyclotron frequency. Because the background plasma is strongly magnetized ( $\omega_p/\omega_c = 10^{-3}$ ), these O mode waves are free-space electromagnetic waves (L-O mode). These characteristics are qualitatively similar to those of the QP bursts observed by Galileo. However, the growth rate is insufficient to amplify these waves within the duration time of the electron out bursts.

Figure 6.4 is a calculation result for the case of X mode (Case H2) where the parameters

fc: 30.0kHz, mode:01, wp/wc: 0.001, n : 2,  
 $u_{x0}$ : 1016.keV,  $u_{y0}$ : 0.keV,  $a_x$ : 308.keV,  $a_y$ : 308.keV

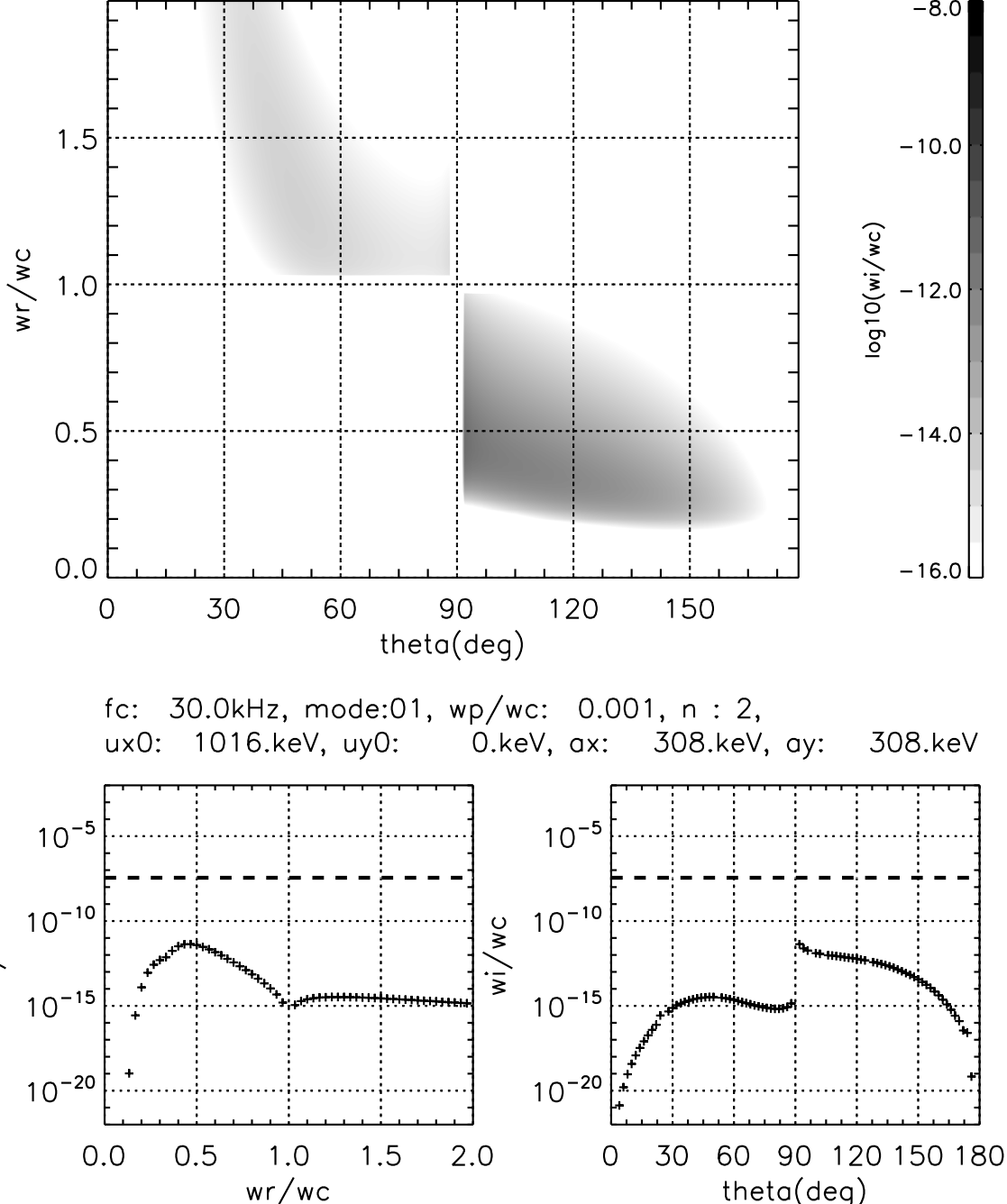
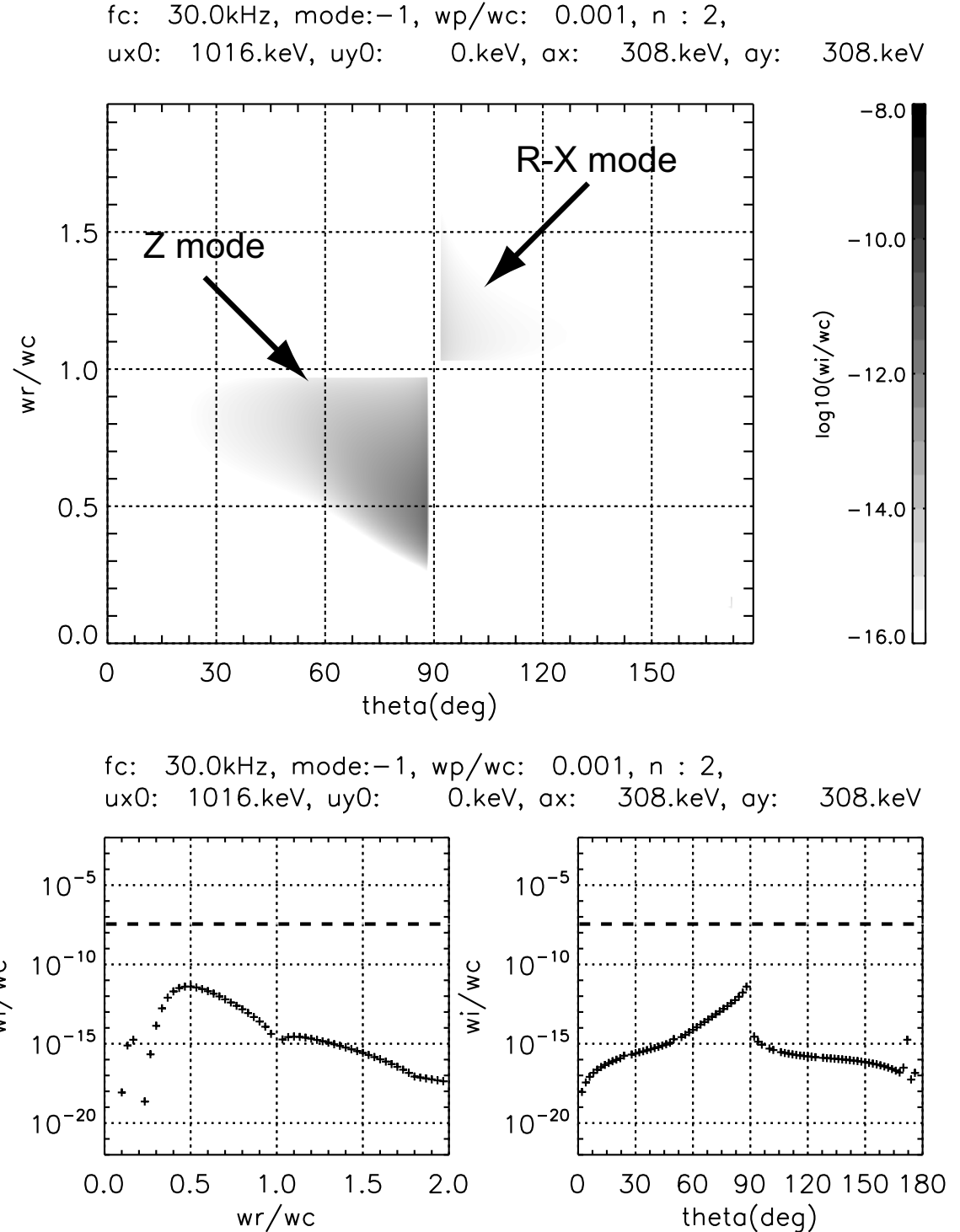


**Figure 6.3:** Growth rate for the case of O mode waves where  $\omega_p/\omega_c = 10^{-3}$ ,  $n = 2$ ,  $u_{\parallel 0} \sim 1$  MeV,  $u_{\perp 0} = 0$  eV, and  $a_{\parallel} = a_{\perp} \sim 300$  keV (case H1 in Table 6.2). (top) Dependence of the growth rate with respect to wave frequencies and propagation angles. Vertical and horizontal axes show the wave frequencies  $\omega_r$  normalized by the local cyclotron frequency  $\omega_c$  and wave propagation angles  $\theta$ , respectively. Gray shade indicates the growth rate  $\omega_i$  normalized by  $\omega_c$ . (bottom left) Maximum growth rates in an angular range of  $\theta = 0^\circ$ – $180^\circ$  as a function of the frequencies  $\omega_r/\omega_c$ . Vertical and horizontal axes indicate  $\omega_i/\omega_c$  and  $\omega_r/\omega_c$ . (bottom right) Maximum growth rates in a frequency range of  $\omega_r/\omega_c = 0$ – $2$  as a function of the propagation angles  $\theta$ . Vertical and horizontal axes indicate  $\omega_i/\omega_c$  and  $\theta$ . Horizontal broken lines show the level corresponding to the  $e$ -folding time of 120 sec when waves are amplified to  $e$  times larger than the initial amplitudes.

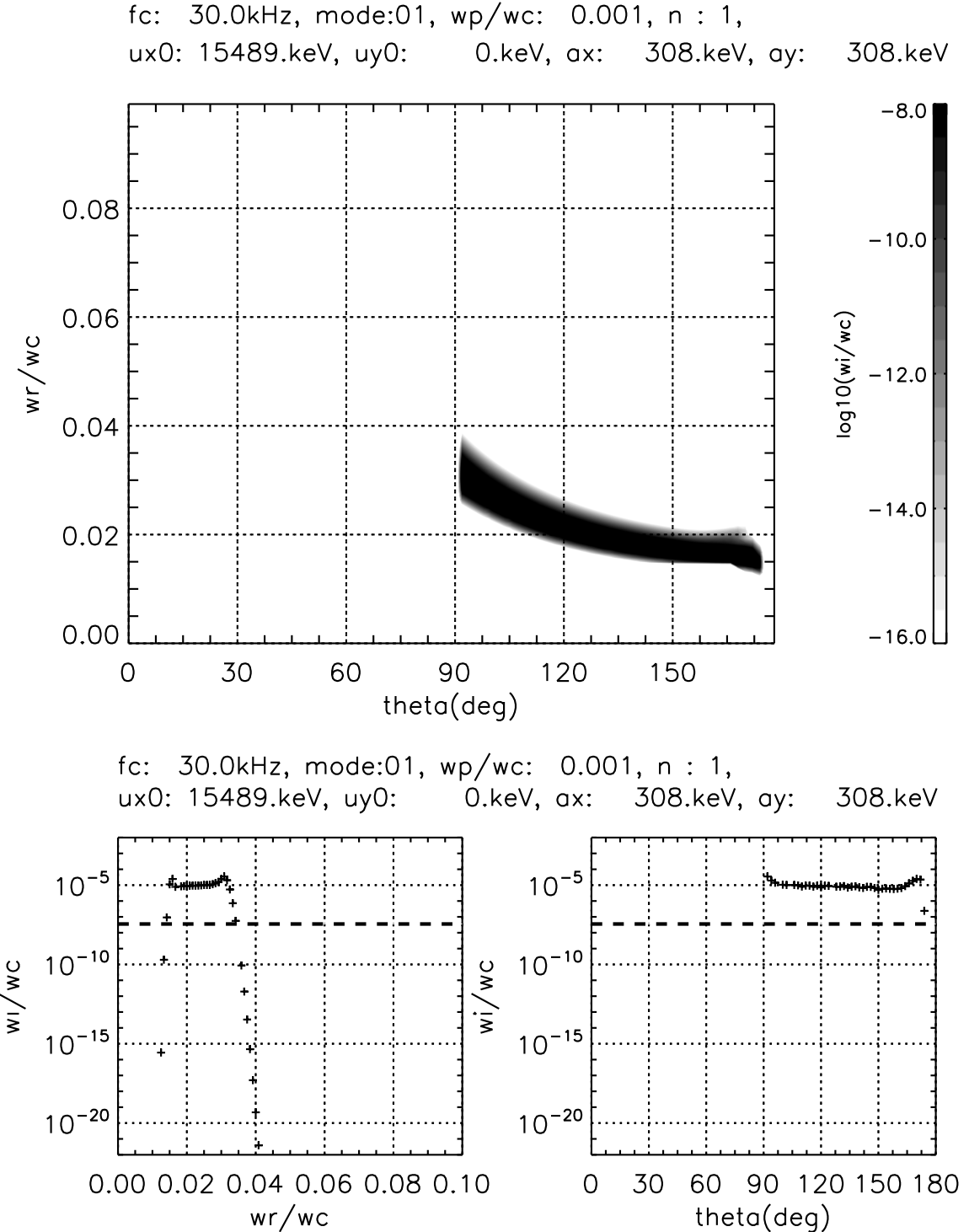
are the same as those in Case H1 except for the wave mode. Formats are the same as those of Figure 6.3. Above the local cyclotron frequency, free-space waves (R-X mode) are generated broadly in anti-parallel directions with respect to the background field. However, growth rates are insufficient as well as Case H1 at any frequencies and propagation angles. It should be noted that the local Z mode waves propagating parallel to the background are also excited below the cyclotron frequency.

Figure 6.5 and 6.6 indicate results for the cases of higher mean parallel energies of electron beams. The mean parallel energies were set to be  $\sim 15$  MeV which is comparable to the energy range where the periodic electron outbursts were detected, and the other parameters are the same as those in Case H1 and H2. Figure 6.5 is the result for O mode waves indicating the significantly large growth rate of  $\omega_i/\omega_c \sim 10^{-5}$  at  $\omega_r/\omega_c = 0.015 - 0.03$  and  $\theta = 90^\circ - 180^\circ$ . This large growth rate corresponds to the *e*-folding time of 0.5 sec, which is consistent with the observations of the electron outbursts and QP bursts. However, beaming patterns of the calculation result disagree with those of QP bursts suggested by the ray tracing analysis. In the present calculation, the excited waves are directed in anti-parallel directions of the local magnetic field and electron beam, i.e., toward Jupiter. This tendency is opposite to the suggested beaming patterns by the ray tracing, which have the broad beaming patterns directed outward from Jupiter (see Figures 5.11 and 5.12 in Section 5.3). It was found that X mode waves are also excited strongly in anti-parallel directions as shown in Figure 6.6 (Case H4). The maximum growth rate is comparable to that of O mode in Case H3 at propagation angles of  $100^\circ - 160^\circ$ . However, the frequencies, where growth rate is significantly larger than the *e*-folding time of 120 sec, are quite smaller than the local cyclotron frequency (less than  $\sim 0.06 f_c$  for Case H4). This means that the excited waves are Z mode waves propagating to opposite directions of the electron beam and background field. Thus, free-space X mode waves are not excited in  $< 120$  sec.

Above characteristics remain to be almost the same even if we change the resonance order, temperatures, and mean energies in the relativistic energy ranges. Therefore, we conclude that the parallel beam cannot generate the free-space electromagnetic waves signifi-



**Figure 6.4:** Growth rate for the case of X mode where  $\omega_p/\omega_c = 10^{-3}$ ,  $n = 2$ ,  $u_{\parallel 0} \sim 1$  MeV,  $u_{\perp 0} = 0$  eV, and  $a_{\parallel} = a_{\perp} \sim 300$  keV (case H2). Formats are the same as those of Figure 6.3.



**Figure 6.5:** Growth rate for the case of O mode where  $\omega_p/\omega_c = 10^{-3}$ ,  $n = 1$ ,  $u_{\parallel 0} \sim 15$  MeV,  $u_{\perp 0} = 0$  eV, and  $a_{\parallel} = a_{\perp} \sim 300$  keV (case H3). Formats are the same as those of Figure 6.3.

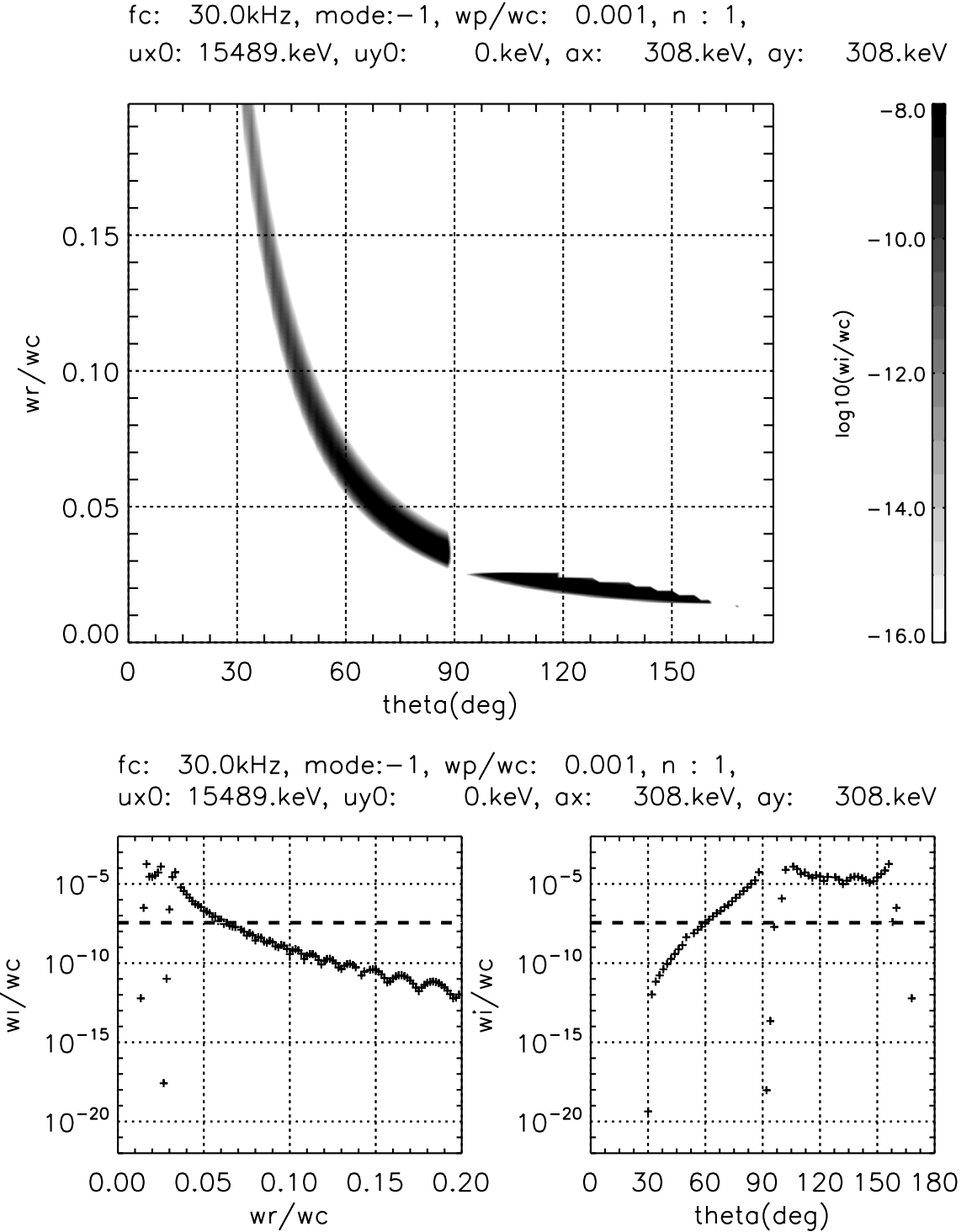


**Figure 6.6:** Growth rate for the case of X mode where  $\omega_p/\omega_c = 10^{-3}$ ,  $n = 1$ ,  $u_{\parallel 0} \sim 15$  MeV,  $u_{\perp 0} = 0$  eV, and  $a_{\parallel} = a_{\perp} \sim 300$  keV (case H4). Formats are the same as those of Figure 6.3.

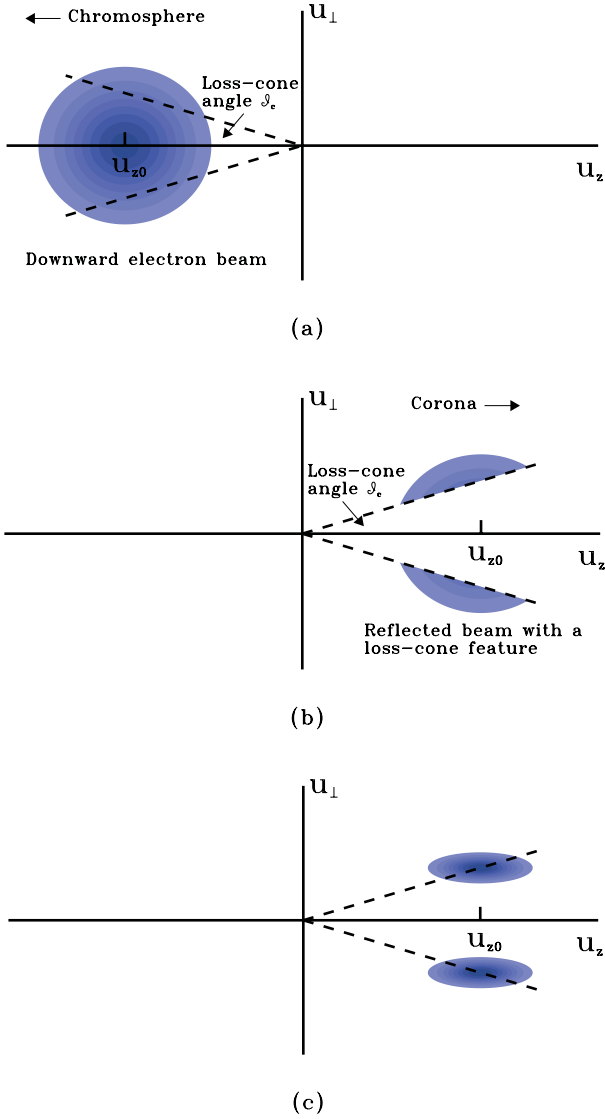
cantly, which are consistent with the ray tracing results, at any frequencies and propagation angles in the high altitude source region.

### **Calculation Results: Polar High Altitudes–Ring Beam**

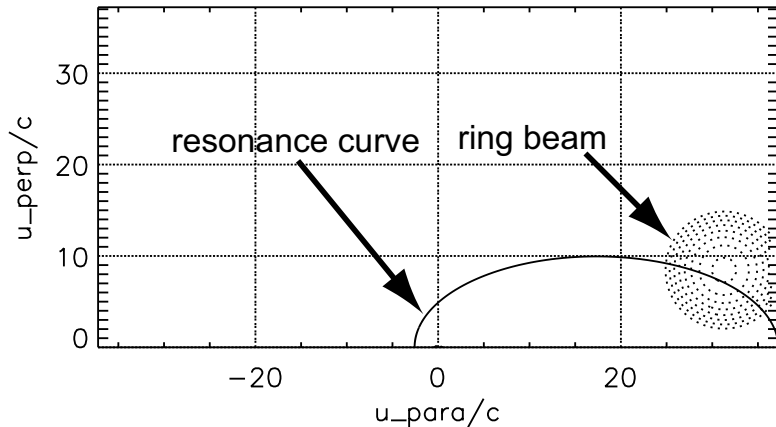
Secondly, we assumed the distribution function to be so-called the “ring beam” distribution referring to the previous studies which addressed the solar Type III bursts based on the CMI theory (e.g., *Wu et al.*, 2002, 2005; *Yoon et al.*, 2002; *Chen et al.*, 2002). These studies calculated the linear growth rates of the waves generated via the CMI process assuming the ring beam distribution as indicated in Figure 6.7. They postulated a generation site above an active region in the solar corona, where electron beams are precipitating toward the chromosphere. The electron beams are reflected at the mirror point and escape outward from the chromosphere accompanying the loss cone structures, which finally form the ring beam distribution and generate free-space waves via the CMI process. They obtained the result that the ring beam distribution could directly generate free-space waves in O and X modes with significant growth rates. The present study also assumes the ring beam distribution based on Equation 6.15, which is equivalent to the Maxwellian shifted in parallel and perpendicular directions in the momentum space (see Figure 6.8).

Figure 6.9 and 6.10 indicate the growth rate derived from the ring beam distribution. The mean parallel and perpendicular energies correspond to  $\sim 15$  MeV and  $\sim 4$  MeV, respectively (Case H5 and H6). The other parameters are the same as those in Case H1 and H2. The bottom right panel of Figure 6.9 indicates that the growth rate of O mode wave reaches at the level of 120 sec *e*-folding time at a broad angular range of  $40^\circ$ – $170^\circ$ . This result qualitatively agrees with the observations and ray tracing results. For the X mode case in Figure 6.10, free-space waves are not excited significantly while Z mode waves are strongly excited similar to the case for the X mode waves generated by the energetic parallel beam (Case H4).

These characteristics remain to be almost the same even if we change the resonance order, temperatures, and mean energies in relativistic energy ranges. Thus, it is concluded



**Figure 6.7:** Momentum distribution function of a beam of electrons viewed from a generation site above an active region (after Wu et al., 2005);  $u_{\perp}$  and  $u_z$  denote the components of momentum per unit mass perpendicular and parallel to the ambient magnetic field, respectively. Displayed are (a) the downward beam electrons, (b) the reflected electrons with a loss-cone feature, and (c) ring beam feature. Darker color marks higher population of electrons.



**Figure 6.8:** A schematic showing a distribution function and resonance curve in a momentum space with the same format as Figure 6.2. Contours show phase space densities of the distribution function which corresponds to an electron ring beam.

that unstable structures of the relativistic ring beams can generate the O mode free-space waves within 120 sec with broad beaming patterns at high source altitudes. As indicated in Figure 6.9, the frequency range of O mode wave is narrow at a source region. For example, the bandwidth where the *e*-folding time is less than 120 sec is  $\omega_r/\omega_c = 0\text{--}0.1$  for Case H5. However, if the ring beams maintain their instabilities along the source flux tube, broadband O mode waves are emitted from the flux tube. These results suggest that the relativistic electron outbursts with quasi-periodicity have unstable structures like ring beams in their momentum distribution, and QP radio bursts are generated via the CMI process induced by these structures.

It should be noted that the ray tracing analysis in Section 5.3 suggested that the R-X mode waves emitted from the high altitudes are consistent with the observed shadow zone. The present theoretical study indicated that R-X mode waves are not excited at the high altitudes. Thus, we conclude the observed shadow zone is not formed by the R-X mode waves. However, the ray tracing suggests that the L-O mode waves excited below the local  $f_c$  at high altitudes (e.g.,  $f < 0.1f_c$ , see Figure 6.9) can propagate in similar paths to those of the R-X mode waves. Figure 6.11 shows propagation paths of L-O and R-X mode waves emitted from high altitudes, where the background conditions are similar to those in the

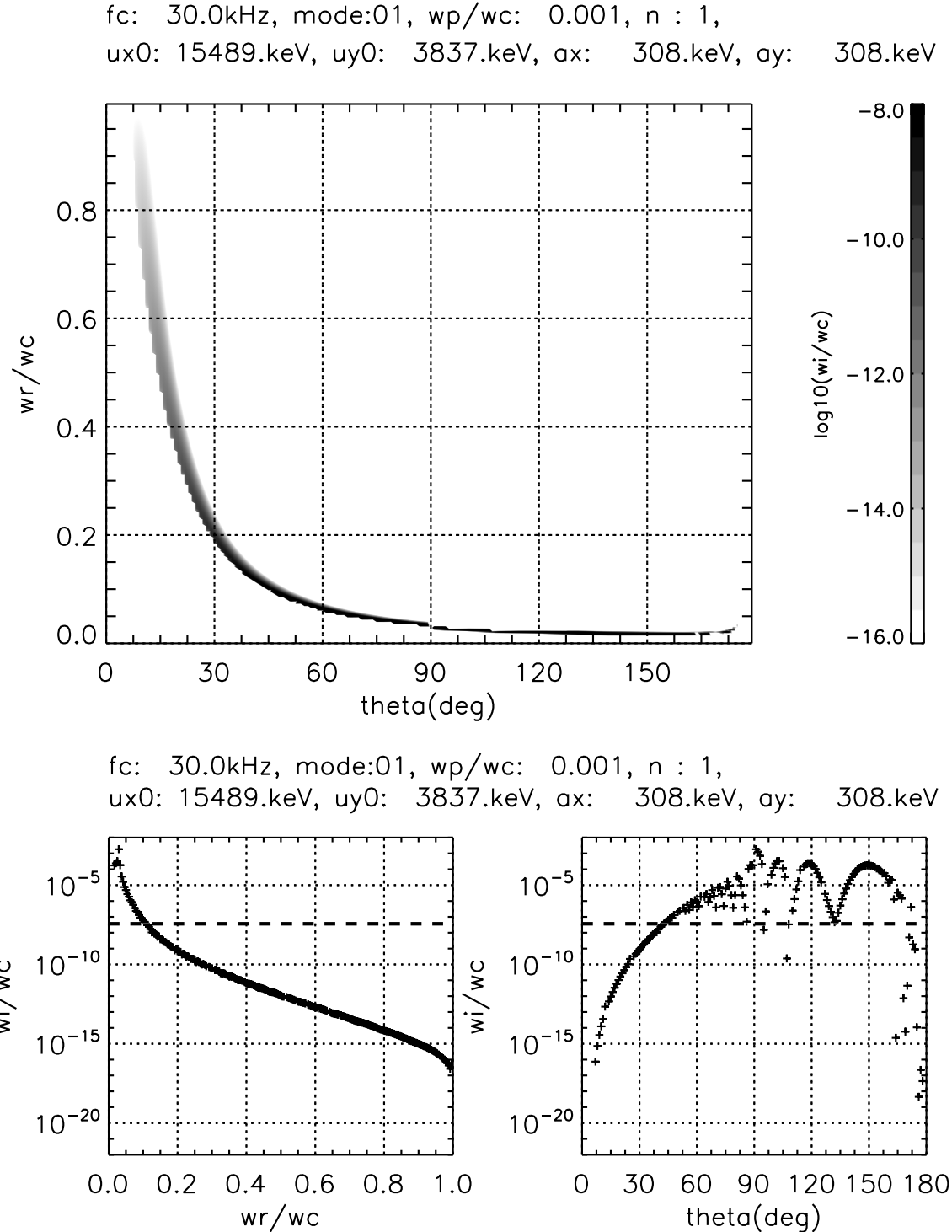


**Figure 6.9:** Growth rate for the case of O mode where  $\omega_p/\omega_c = 10^{-3}$ ,  $n = 1$ ,  $u_{\parallel 0} \sim 15$  MeV,  $u_{\perp 0} \sim 4$  eV, and  $a_{\parallel} = a_{\perp} \sim 300$  keV (case H5). Formats are the same as those of Figure 6.3.

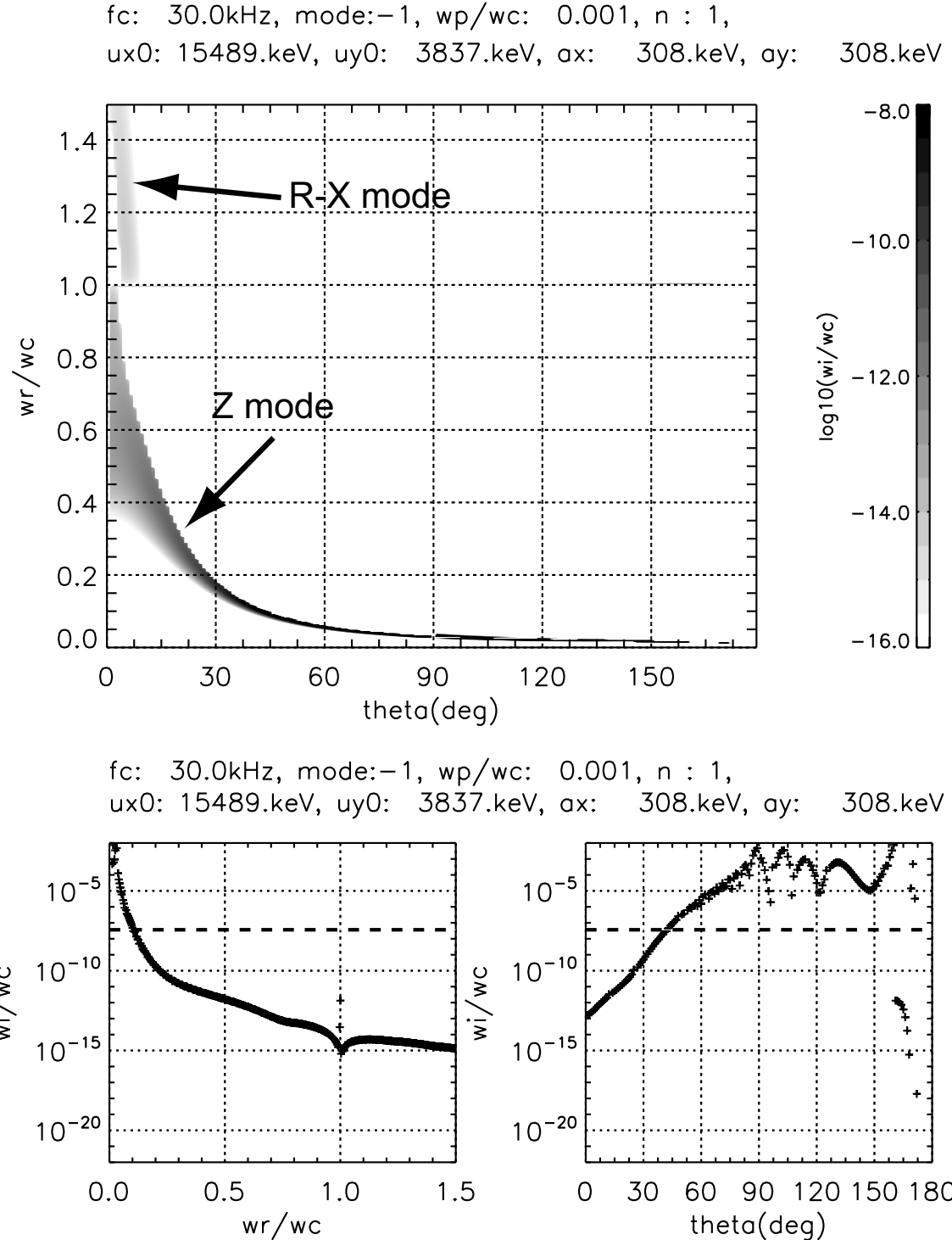


**Figure 6.10:** Growth rate for the case of X mode where  $\omega_p/\omega_c = 10^{-3}$ ,  $n = 1$ ,  $u_{\parallel 0} \sim 15$  MeV,  $u_{\perp 0} \sim 4$  MeV, and  $a_{\parallel} = a_{\perp} \sim 300$  keV (case H6). Formats are the same as those of Figure 6.3.

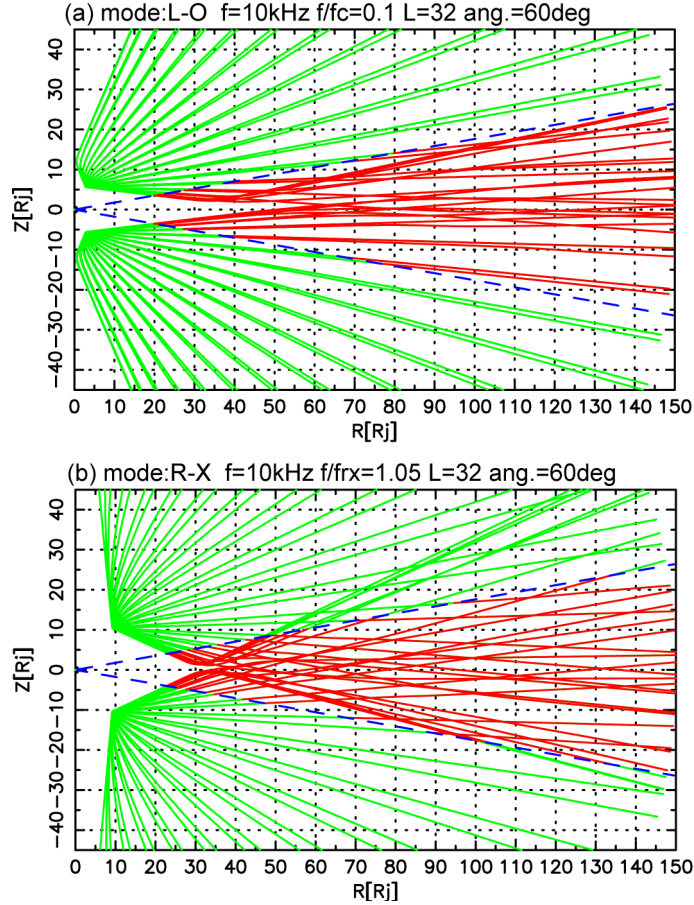


**Figure 6.11:** Ray tracing results for the cases of L-O and R-X mode waves from high source altitudes. (a) A result of L-O mode waves where source L-value, half-cone angle,  $f/f_c$ , and  $f$  were set to be 32,  $60^\circ$ , 0.1, and 10 kHz, respectively. (b) A result of R-X mode waves where source L-value, half-cone angle,  $f/f_c$ , and  $f$  were set to be R-X mode, 32,  $60^\circ$ , 1.05, and 10 kHz, respectively.

growth rate calculations. This result indicates that waves in both modes can propagate from the polar sources to the equatorial region forming the shadow zone. Thus, we can infer that the L-O mode waves excited by the relativistic beams form the observed shadow zone.

### Calculation Results: Polar Low Altitudes

We also investigated growth rates of the waves emitted from the polar low altitudes ( $\sim 2 R_J$ ), corresponding to the QP bursts observed by Ulysses at high latitudes (Section

5.2). The background plasma is characterized by the parameter of  $\omega_p/\omega_c = 10^{-2}$ . Figure 6.12 indicates a result for the case of O mode waves at the polar low altitudes, where the free parameters of  $\omega_p/\omega_c$ ,  $n$ ,  $u_{\parallel 0}$ ,  $u_{\perp 0}$ ,  $a_{\parallel}$ , and  $a_{\perp}$  were set to be  $10^{-2}$ , 1,  $\sim 15$  MeV,  $\sim 4$  MeV,  $\sim 300$  keV, and  $\sim 300$  keV, respectively (case L1 in Table 6.2). In Case L1, the ring beam distribution was also assumed. Similar to the result in Case H5, O mode waves are excited significantly with broad beaming patterns as shown in Figure 6.12. Figure 6.13 represents the growth rate of the X mode waves at polar low altitudes (Case L2). The free parameters are the same as Case L1 except for the wave mode. This result is also similar to that for Case H6, which indicated that free-space waves are not generated because of smaller growth rates relative to Z mode waves by the ring beam at high altitudes.

From these results, we conclude that O mode waves are generated with broad beaming patterns at low altitudes by the ring beams. This implies that the QP bursts observed by Ulysses at high latitudes are the L-O mode waves generated by the CMI process. However, the second generation scenario, the mode conversion process, is also feasible because Z mode waves propagating toward Jupiter are generated (see Figure 6.13) and possibly converted to free-space mode waves at boundaries below  $\sim 2 R_J$ . In Section 6.1.2, we discuss the process for converting Z mode waves to L-O mode waves based on the previous theoretical studies.

### Calculation Results: Magnetosheath

We found no solution for the cases in which growth rates of free-space waves become positive at the magnetosheath. This means that free-space waves are dumped by the background plasma which is almost unmagnetized in the magnetosheath ( $\omega_p/\omega_c \sim 42$  in the present calculation). At the magnetosheath, particular kinds of local plasma waves are generated around the local cyclotron frequency. Figure 6.14 indicates the generation of whistler mode waves below the local cyclotron frequency (Case S1). In this case, the ratio  $n_b/n_{BG}$  was set to be  $10^{-3}$  for a case study, which is possibly quite higher than the true value. Whistler mode waves are excited at a frequency range of  $\omega_r/\omega_c=0.2\text{--}0.8$  and an

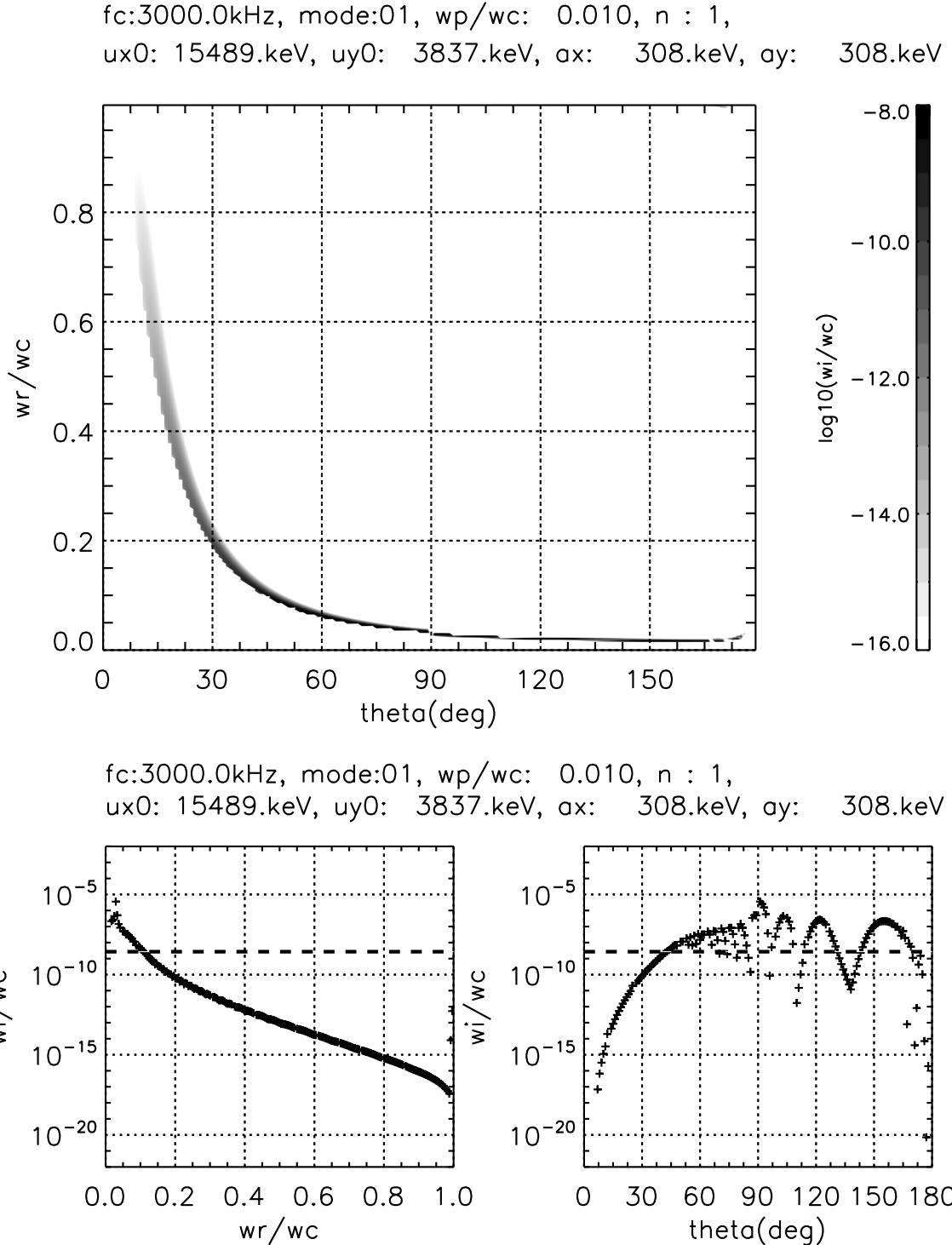


**Figure 6.12:** Growth rate for the case of O mode where  $\omega_p/\omega_c = 10^{-2}$ ,  $n = 1$ ,  $u_{\parallel 0} \sim 15$  MeV,  $u_{\perp 0} \sim 4$  MeV, and  $a_{\parallel} = a_{\perp} \sim 300$  keV (case L1). Formats are the same as those of Figure 6.3.

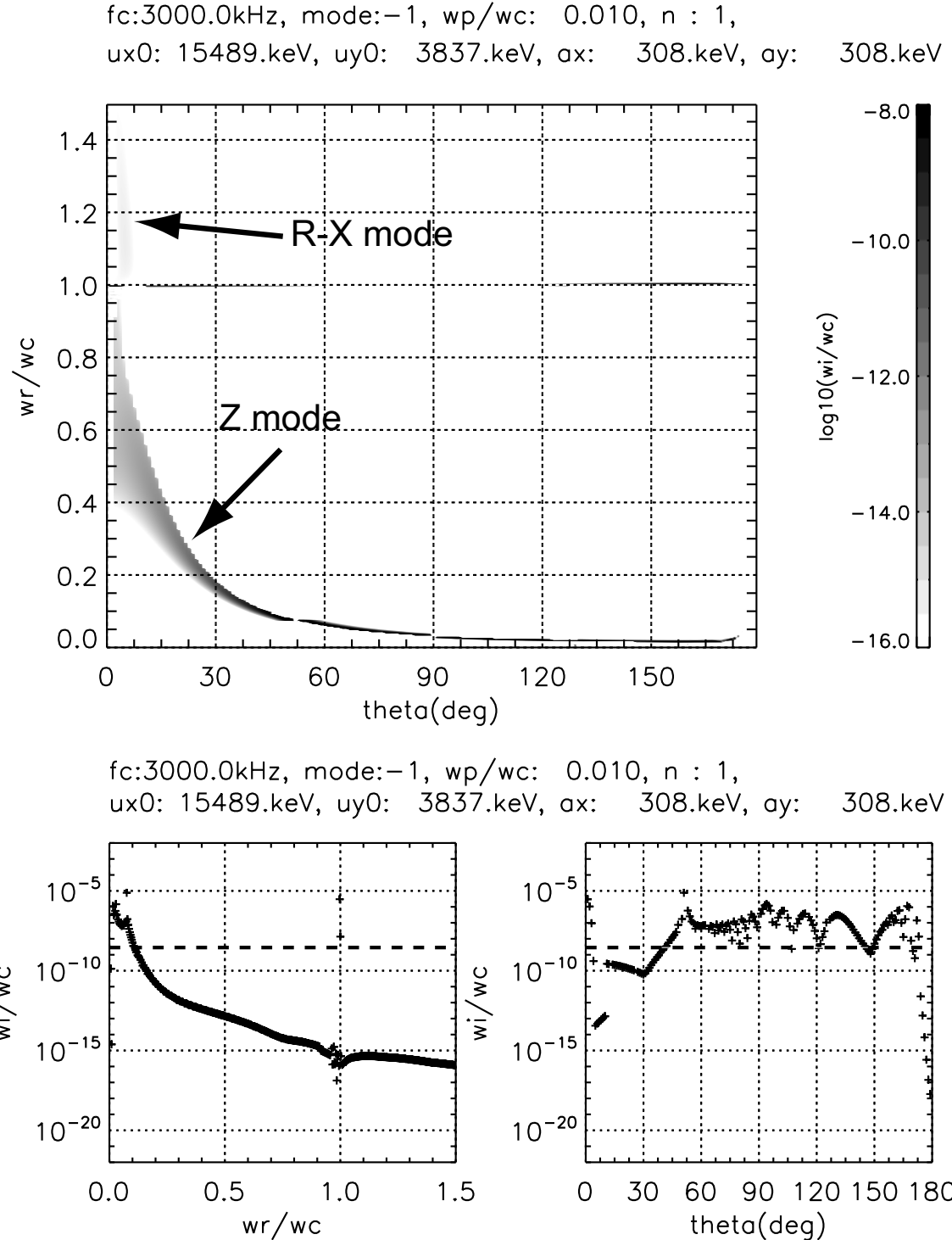


**Figure 6.13:** Growth rate for the case of X mode where  $\omega_p/\omega_c = 10^{-2}$ ,  $n = 1$ ,  $u_{\parallel 0} \sim 15$  MeV,  $u_{\perp 0} \sim 4$  MeV, and  $a_{\parallel} = a_{\perp} \sim 300$  keV (case L2). Formats are the same as those of Figure 6.3.

fc: 0.3kHz, mode:-1, wp/wc: 42.423, n : 1,  
 $u_{x0}$ : 15489.keV,  $u_{y0}$ : 3837.keV,  $a_x$ : 308.keV,  $a_y$ : 308.keV

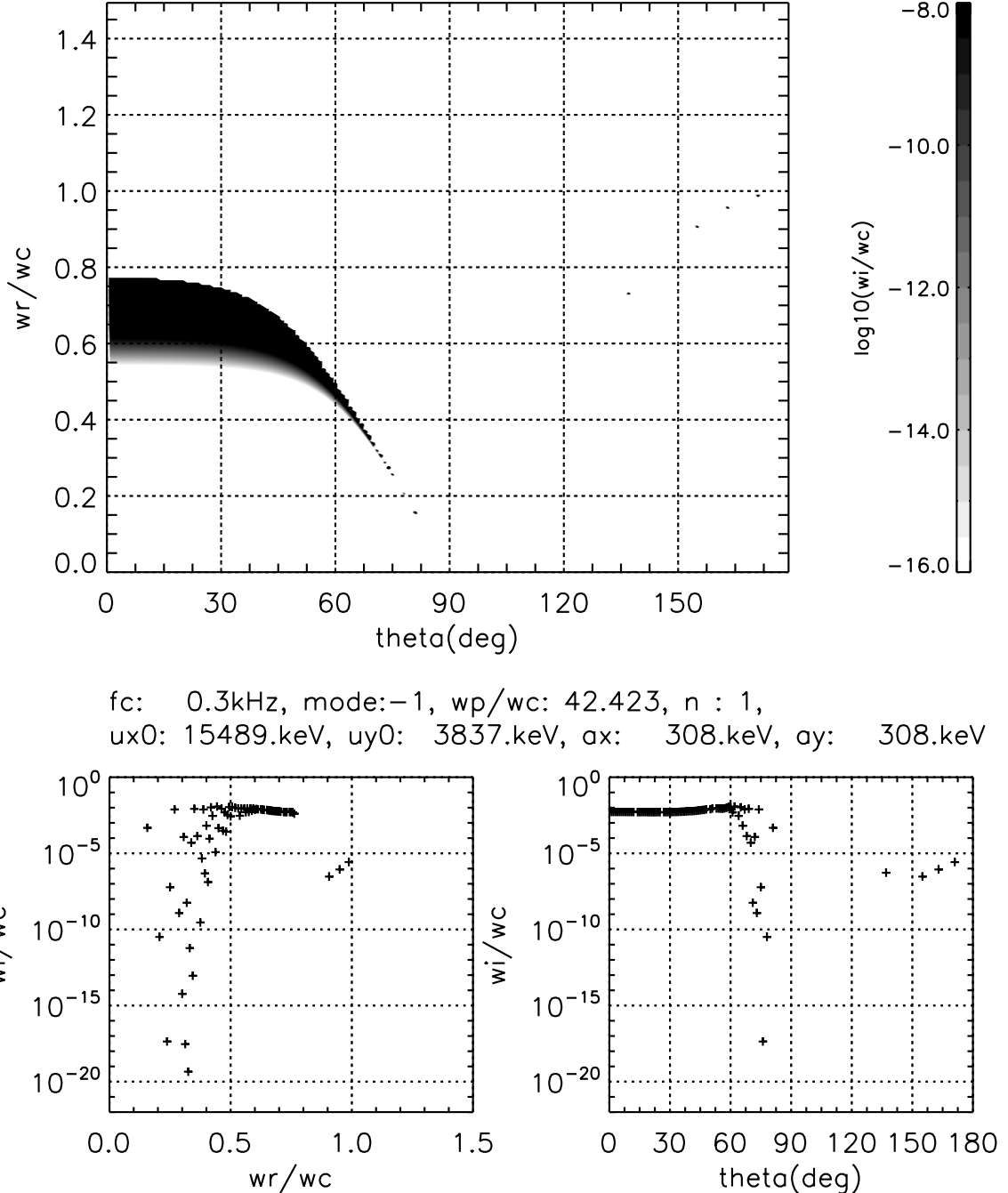


**Figure 6.14:** Growth rate for the case of X mode where  $\omega_p/\omega_c \sim 42$ ,  $n = 1$ ,  $u_{\parallel 0} \sim 15$  MeV,  $u_{\perp 0} \sim 4$  MeV, and  $a_{\parallel} = a_{\perp} \sim 300$  keV (case S1). Formats are the same as those of Figure 6.3. The ratio  $n_b/n_{BG}$  was set to be  $10^{-3}$ .

angular range of  $0^\circ$ – $70^\circ$ . It should be noted that absolute values of growth rates include uncertainty because of the ambiguous ratio of electron beam densities to the background densities.

From these results, we conclude that free-space waves are not generated directly by the relativistic electron beams at the magnetosheath. In addition, the mode conversion process is also unreasonable at the magnetosheath because the local plasma waves as the sources for free-space waves are not excited. These results reject the second possible interpretation of the direction finding by Cassini in Section 5.4, here we denote it again,

2. QP bursts have the real source region at the magnetosheath where the local plasma frequency is comparable to the emission frequencies of QP bursts.

Thus we adopt the first interpretation as the most plausible interpretation,

1. QP bursts emitted from the polar region (a few to  $10 R_J$  altitudes) were scattered and directed to the apparent altitudes of  $\sim 50 R_J$  by the local density fluctuations in the magnetosheath and interplanetary space plasmas

### 6.1.2 Scenario 2: Indirect Generation

#### Description of Indirect Generation Scenario

We examined the second scenario, the “indirect generation scenario”, in which QP bursts are excited via the mode conversion process. Figure 6.15 indicates a flow diagram showing the indirect generation scenario. In this scenario, QP radio bursts are assumed to be converted from the local plasma waves (e.g., Z mode waves) at discontinuity of plasma densities. Z mode waves are supposed to be generated via the cyclotron resonance process as indicated in Section 6.1.1, where these local plasma waves are induced by unstable structures of the quasi-periodic electron outbursts with relativistic energies. We discussed the possibility that free-space electromagnetic waves are converted from Z mode waves based on the results of *Oya* (1974) who performed numerical calculations of the energy conversion rate from Z mode waves to free-space waves.

*Oya* (1974) postulated the Cartesian coordinate at the plasma discontinuity as indicated in Figure 6.16 for numerical calculations of the conversion rates. The media with high plasma densities  $n_1$  (media 1) contacts with the low density media ( $n_2$ , media 2) at the  $x$ - $y$  plane, and the  $z$ -axis is parallel to the boundary normal direction. The ambient magnetic field  $\mathbf{B}_0$  is penetrating the density boundary with an angular distance  $\theta_H$  to the  $z$ -axis. The incident extraordinary mode waves (IE), which are corresponding to the local Z mode waves, enter the boundary with an incident angle  $\theta_{IE}$ . These waves are reflected or transmitted at the boundary and converted to free-space waves in X and O modes. The reflected O and X mode waves are denoted as REO and REE, and the transmitted waves are denoted as TEO and TEE, respectively. See *Oya* (1974) for detailed formulations of the energy conversion rates.

#### Assumptions and Conditions

In the present study, we postulated a simple model of the wave generation site which is located in the northern polar magnetosphere, where magnetic fields are approximately perpendicular to the steep density gradient of the polar plasma (see Figure 5.8). A schematic

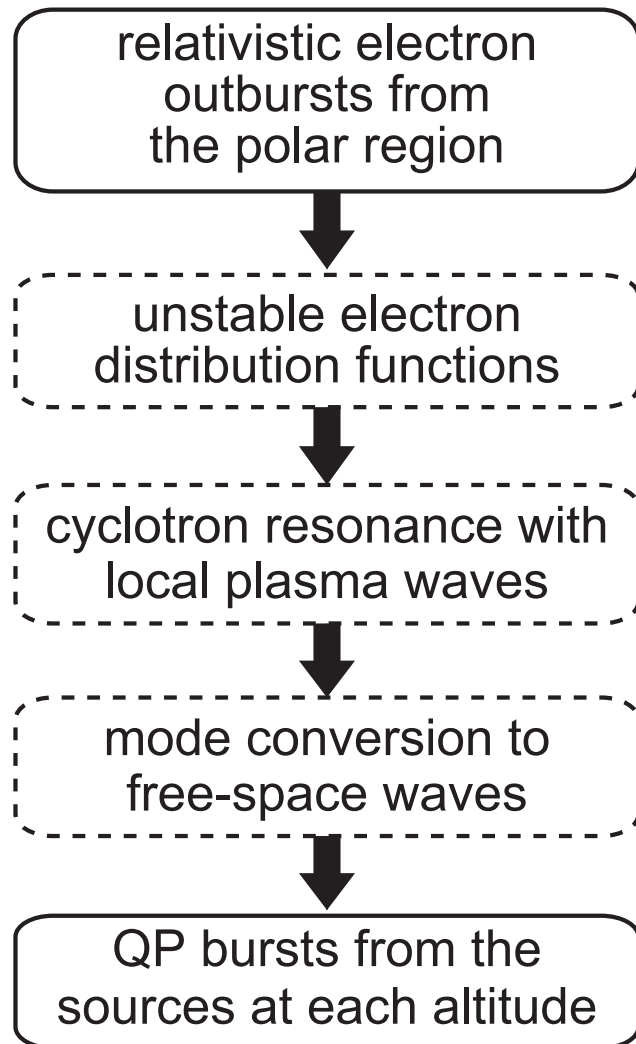


**Figure 6.15:** A flow diagram showing a possible scenario for QP bursts' generation termed the “indirect generation scenario”. In this scenario, QP bursts are assumed to be generated via the mode conversion process. The processes framed by broken lines indicate that these processes have not been identified in observations or verified by wave generation theories.

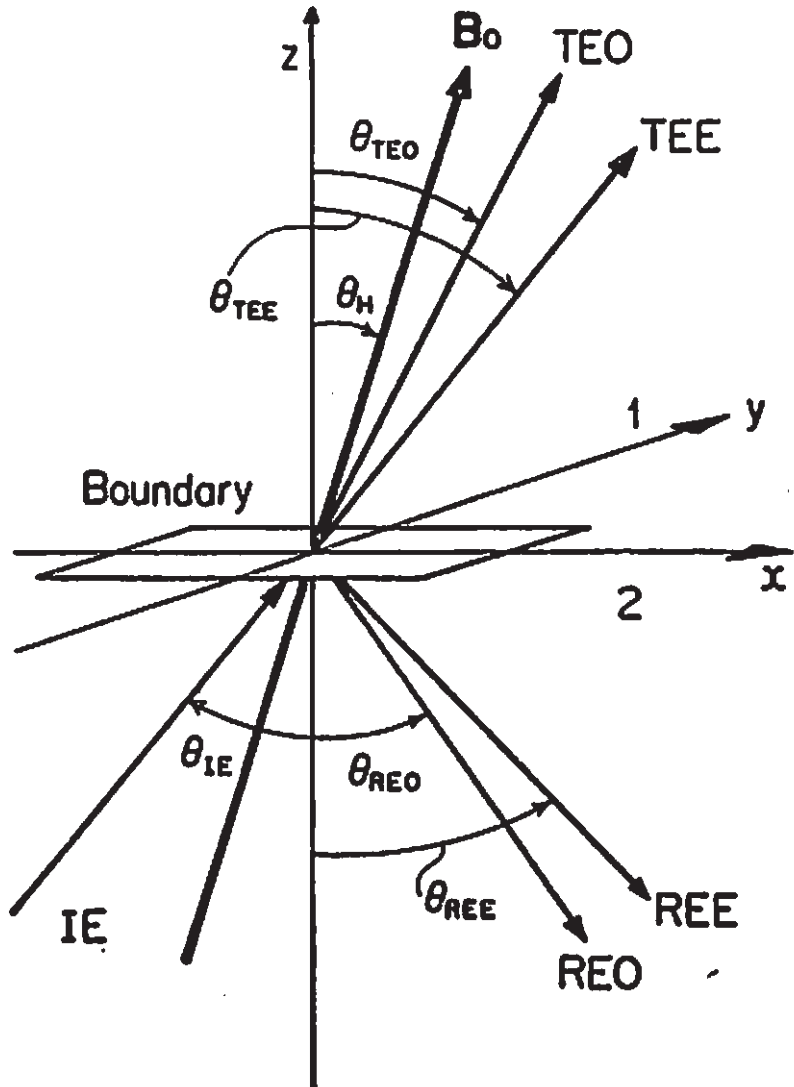


**Figure 6.16:** Sharp boundary between the media 1 and 2 with Cartesian coordinate \$(x, y, z)\$ whose \$z\$-axis coincides with the normal direction of the boundary (after Oya, 1974). Densities of the media 1 and 2 are \$n\_1\$ and \$n\_2\$ (\$n\_1 > n\_2\$), respectively. The extraordinary mode incident wave \$IE\$ is split into the reflected ordinary mode wave \$REO\$, the reflected extraordinary mode wave \$REE\$, the transmitted ordinary mode wave \$TEO\$, and the transmitted extraordinary mode wave \$TEE\$. \$\mathbf{B}\_0\$ is the magnetic field with an angular distance \$\theta\_H\$ to the \$z\$-axis. This boundary region is supposed to be located at the southern polar region.

of the generation site model is indicated in Figure 6.17. In this model, incident X mode waves are the Z mode waves which are excited via the cyclotron resonance with the relativistic electron outbursts as demonstrated in Section 6.1.1. The ambient magnetic field is supposed to be parallel to the boundary normal direction. The propagation angle of the generated Z mode waves is annotated as  $\theta_{IE}$  corresponding to an incident angle to the density boundary. It should be noted that the plasma media 1 and 2 are opposite to those in Figure 6.16 because this boundary region is supposed to be located at the northern hemisphere. The reflected O mode waves are the free-space waves (i.e., L-O mode waves) converted from the incident X mode waves at a reflection angle of  $\theta_{REO}$ .

It was found that the plasma density boundary is available in the polar magnetosphere based on the analysis of the magnetic and plasma distribution models adopted in the ray tracing. Figure 6.18 indicates profiles of the local cyclotron and plasma frequencies along the magnetic field line whose apex is located at a equatorial distance of  $30 R_J$  from Jupiter. The horizontal and vertical axes represent radial distances from the center of Jupiter and the frequencies in logarithmic scales, respectively. Solid and broken lines are profiles of the local cyclotron and plasma frequencies, respectively, which were derived from the plasma and magnetic field models used in the ray tracing (see Section 5.1.2). The  $f_p$  profile indicates the steep density gradients of polar plasma at radial distances less than  $4 R_J$ . Figure 6.19 represents magnitudes of the density gradients derived from the plasma distribution model with similar formats to those of Figure 6.18. The density gradients are given in the unit of /cc/km. In Oya (1974), the boundary density gap is characterized by the “step ratio”  $\alpha \equiv n_1/n_2 - 1$ . The ratio was found to be  $\sim 10^{-4}$  at  $2 R_J$  in the present study.

## Discussions

Oya (1974) calculated the conversion rates for Jovian decametric radio emissions emitted from topside of the polar ionosphere, which corresponds to the “boundary” of plasma densities for the incident Z mode wave. The calculation results are shown in Figures 6.20–6.22. Figure 6.20 indicates the energy conversion rates at different step ratios ( $\alpha = 0.01$ –

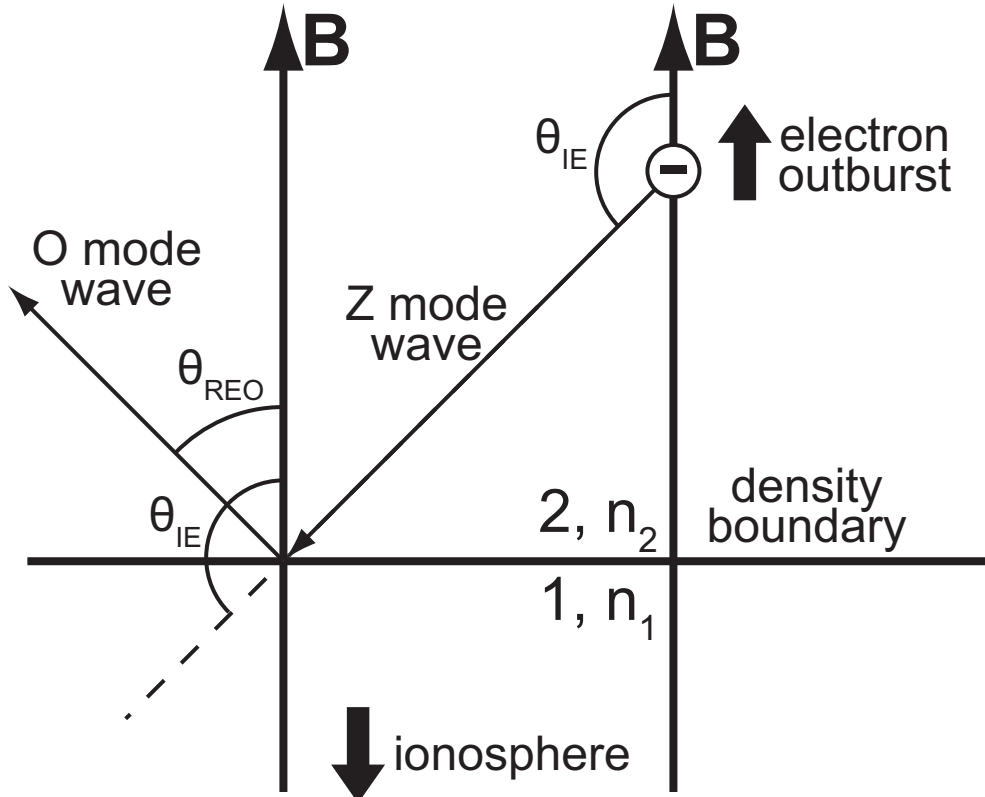


**Figure 6.17:** A schematic of the mode conversion model in the present study. The ambient magnetic field is directed outward from the ionosphere and parallel to the boundary normal direction. Z mode waves are excited by the relativistic electron outbursts with the propagation angle of  $\theta_{IE}$ , which is equivalent to an incident angle at the density boundary between the media 1 and 2. Plasma densities of each medium are denoted  $n_1$  and  $n_2$  ( $n_1 > n_2$ ), respectively. It should be noted that the plasma media 1 and 2 are opposite to those in Figure 6.16 because this boundary region is supposed to be located at the northern hemisphere. The reflected O mode waves are converted from the incident extraordinary mode (Z mode) waves at a reflection angle of  $\theta_{REO}$ .

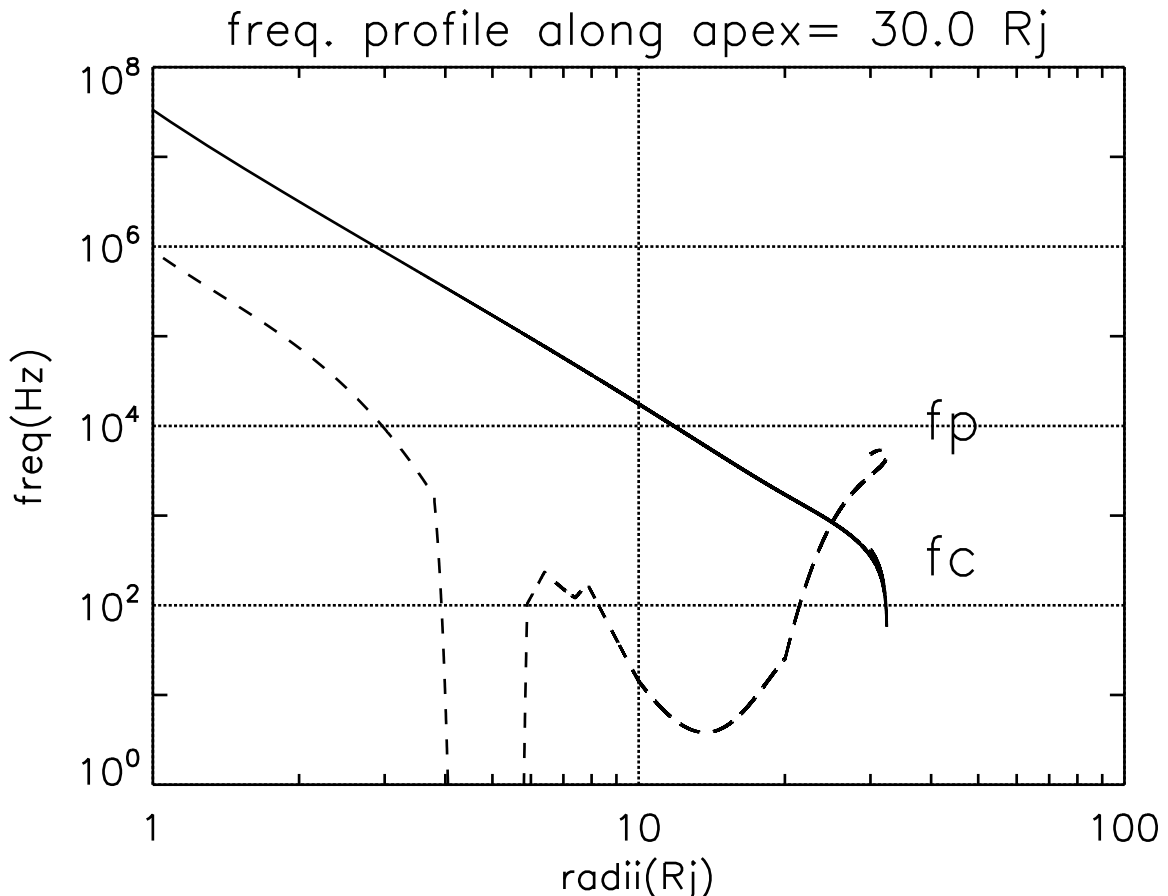


**Figure 6.18:** A plot showing the profiles of plasma and cyclotron frequencies along the field line whose apex is located at a equatorial distance of  $30.0 R_j$  from Jupiter. Horizontal and vertical axes represent radial distances from the center of Jupiter and the frequencies in logarithmic scales. Solid and broken lines are profiles of the local cyclotron and plasma frequencies, respectively, which were derived from the plasma and magnetic field models used in the ray tracing (see Section 5.1.2).

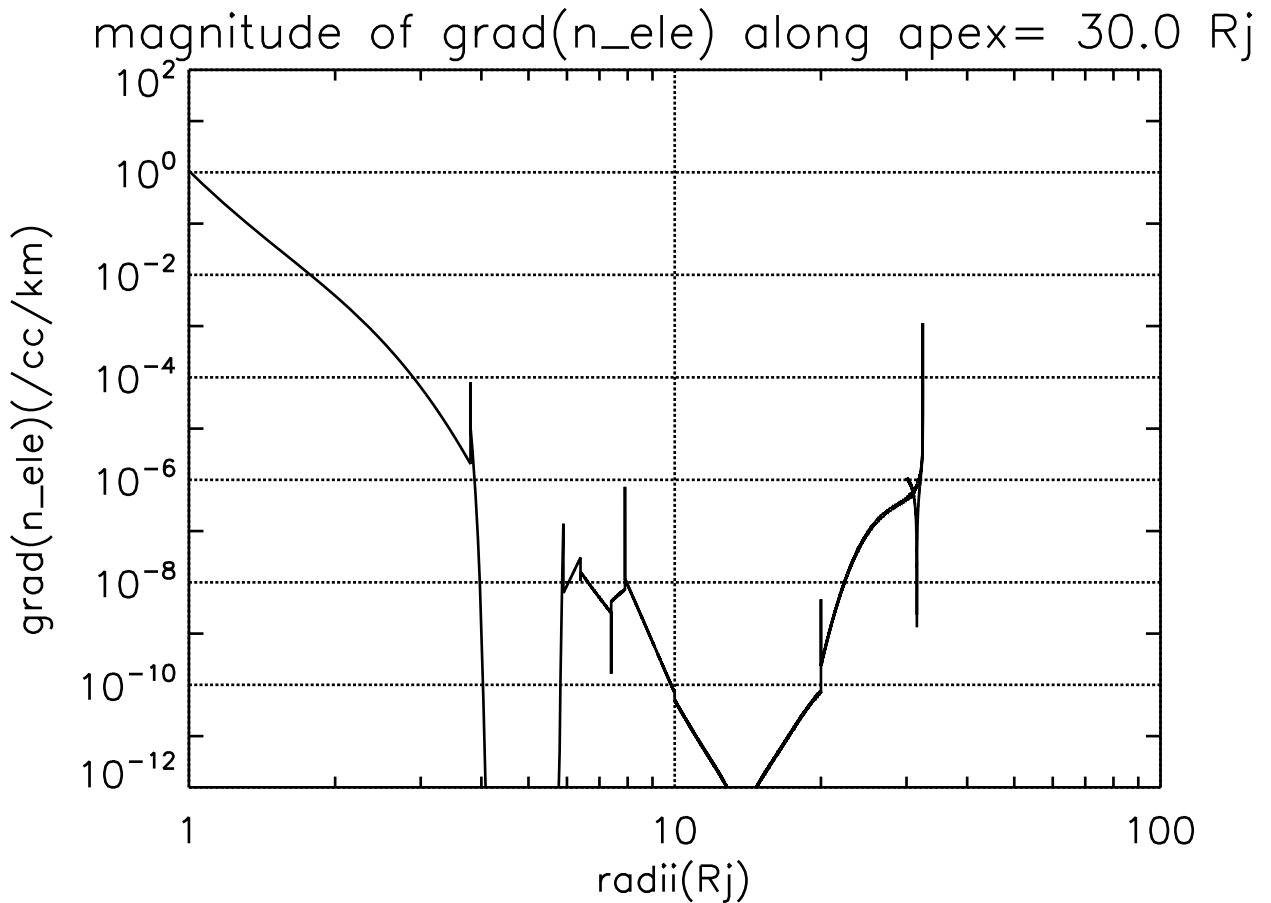


**Figure 6.19:** A plot showing the profile of electron density gradients along the field line whose apex is located at a equatorial distance of 30  $R_J$  from Jupiter. Horizontal and vertical axes represent radial distances from the center of Jupiter and density gradients in logarithmic scales. The density gradients are given in the unit of /cc/km, which were derived from the plasma and magnetic field model used in the ray tracing (see Section 5.1.2).

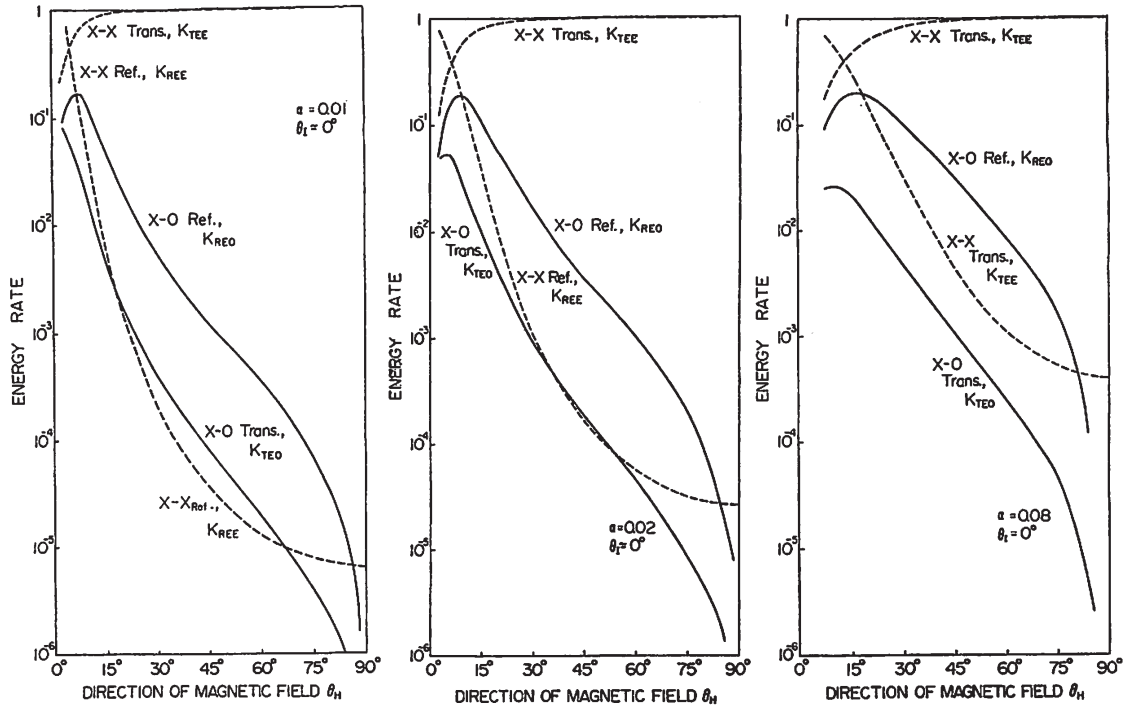


**Figure 6.20:** Energy conversion rate of  $K_j$  ( $j = \text{REO, REE, TEO, and TEE}$ ) vs the angle  $\theta_H$  between the magnetic field and boundary normal direction (after Oya, 1974). The calculation has been made for  $\theta_I = 0^\circ$  and  $\alpha = 0.01$  (left),  $0.02$  (middle), and  $0.08$  (right), respectively. Here,  $\theta_I$  is an incident angle of the X (Z) mode wave.

0.08) as functions of  $\theta_H$ . This result implies that the maximum conversion rate of  $K_{\text{REO}}$  is not significantly dependent on the step ratio: e.g.,  $K_{\text{REO}}$  increases up to an order of 10 % in a range of small  $\theta_H$  in each case of Figure 6.20.

Also at the polar high altitudes, the local Z mode waves can regard the steep density gradients as the “boundary” (see Figure 6.19). For example, at a radial distance of  $\sim 2R_J$ , Z mode waves at a frequency close to the local  $f_p$  ( $\sim 100$  kHz) have a wavelength  $\lambda \sim 3$  km because phase velocities are close to the light speed. On the other hand, density gradients are equal to  $\sim 10^{-2}/\text{cc/km}$  at  $2R_J$ , which corresponds to the density gap of  $0.03/\text{cc}$  over a wavelength of 3 km (i.e.,  $\alpha \sim 10^{-4}$ ). This means that the steep gradient in the polar region works as the density boundary for the Z mode waves near the local  $f_p$ . From these results,

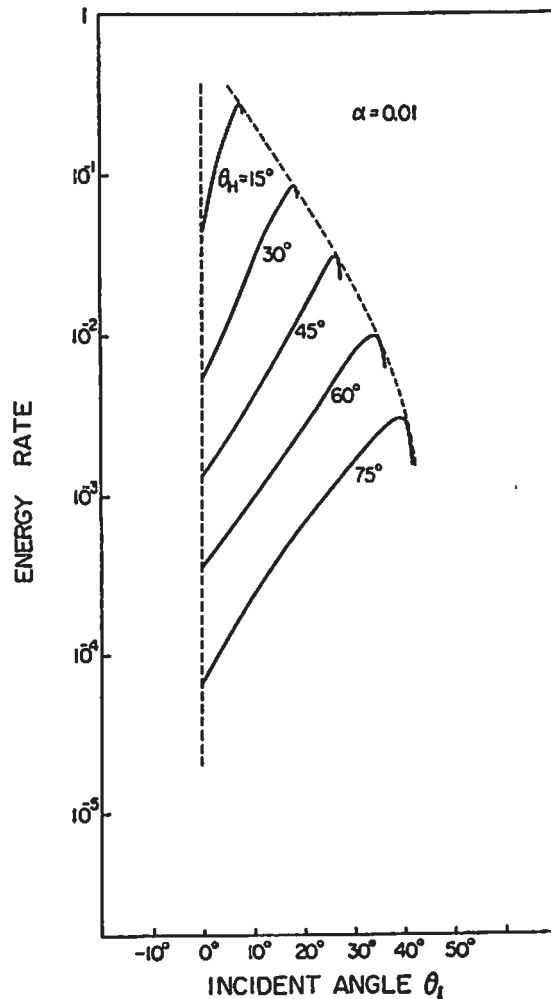
we conclude that the conversion rates even for the small step ratios in the present study represent similar parameter dependences to those in *Oya* (1974).

Figure 6.21 represents the dependence of the conversion rates on the incident angle  $\theta_I$  of the X (Z) mode waves for  $\alpha = 0.01$  at each  $\theta_H$ . This result indicates that the conversion rates have the maximum at small incident angles when the angles  $\theta_H$  are set to be small values. For example, the conversion rate  $K_{REO}$  has the maximum of tens of percent around  $\theta_I \sim 10^\circ$  for  $\theta_H = 15^\circ$ . The generation site model of the present study has the similar situations because the ambient magnetic field is approximately perpendicular to the boundary, and Z mode waves could have perpendicular incidence to the boundary with anti-parallel propagation angles as shown in Figures 6.6, 6.10, and 6.13. This suggests that also in the present simple model, free-space O mode waves are converted from the Z mode waves generated in the polar magnetosphere at the maximum rate of tens of percent. This effective conversion achieves the intense L-O mode emissions which is comparable to those excited via the direct generation process.

Figure 6.22 shows the polar diagram of the conversion rates of free-space O mode waves in *Oya* (1974). The maximum conversion rate corresponds to dominant ray directions of the free-space waves, which propagate quasi-perpendicular with respect to the background magnetic field. Although the initial propagation angles are quasi-perpendicular, the emitted rays are expected to be refracted significantly by the ambient polar plasma and finally escape from the source region with smaller propagation angles with respect to the source field line as shown in the ray tracing analyses in Chapter 5. If these conversion sites are supposed to be located continuously along the source field lines, the total angular range of the free-space O mode waves is broadened like the filled-cone shape, which is consistent with the occurrence statistics and ray tracing results in Sections 3.2.1 and 5.2.

From the above discussions, we conclude that the following mode conversion scenario is possible in the polar magnetosphere:

1. Z mode waves are excited via the cyclotron resonance process at frequencies of  $< 0.1f_c$  with broad propagation angles by the parallel or ring beam of relativistic electrons,



**Figure 6.21:** Energy conversion rate of the reflected ordinary mode wave  $K_{REO}$  vs the incident angle  $\theta_I$  of the extraordinary mode wave for  $\alpha = 0.01$  taking the magnetic field angles  $\theta_H$  as parameters (after Oya, 1974).

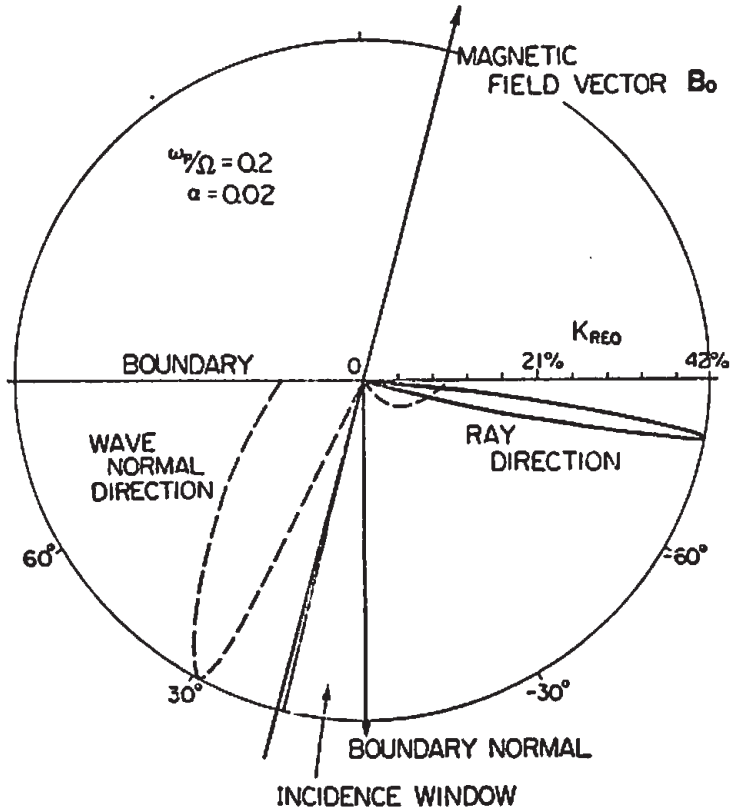


**Figure 6.22:** Polar diagram to indicate the  $K_{REO}(\theta)$  as the function of  $\theta$  (after Oya, 1974). The angle  $\theta$  is taken in two ways; one is for the ray direction angle  $\theta_R$  of the reflected REO wave (solid lines) and the other is for the wave normal angle  $\theta_{REO}$  of the REO wave (dashed curves). The result is obtained for the plasma parameter  $\omega_p/\Omega = 0.2$ . The angle range of the incidence waves corresponding to the obtained  $K(\theta_R)$  and  $K(\theta_{REO})$  is indicated by the “incidence window”.

2. the Z mode waves propagating downward from the source region enter the density boundary where their frequencies are close to the local  $f_p$  at the boundary,
3. the Z mode waves are finally converted to the free-space O mode waves.

This process is applicable not only to the Z mode waves generated at the low altitudes ( $\sim 2 R_J$ ), but also to those at the high altitudes ( $\sim 10 R_J$ ) if they can propagate downward from  $\sim 10 R_J$  to the density boundary at low altitudes. Figure 6.23 is a schematic of the mode conversion process suggested by the present discussions.

As a further step of this study, it is required to estimate the energy conversion rates quantitatively based on the realistic plasma density, magnetic field, and characteristics of Z mode waves. For the quantitative estimation, we need *in-situ* observations of the polar plasma and evaluation for the temporal evolution and propagation process of the Z mode waves.

### 6.1.3 Brief Summary

In this section, we proposed two possible scenarios for the microscopic generation mechanism of QP bursts and examined these scenarios based on the theoretical approaches taking into account of the relativistic beam. One is the “direct generation scenario” where free-space waves are generated directly from the instabilities of electron velocity distributions (Figure 6.1), and the other is the “indirect generation scenario” where free-space waves are converted from the local plasma waves (Figure 6.15).

The growth rate calculations were performed to examine the direct generation scenario at low ( $\sim 2 R_J$ ) and high ( $\sim 10 R_J$ ) source altitudes. The results suggested that:

1. The relativistic ring beams can generate significant O mode free-space waves with broad beaming patterns at high source altitudes in *e*-folding time less than the electron outbursts’ duration ( $\sim 120$  sec) (Figure 6.9)
2. Free-space X mode waves are not excited effectively by the relativistic electron beams

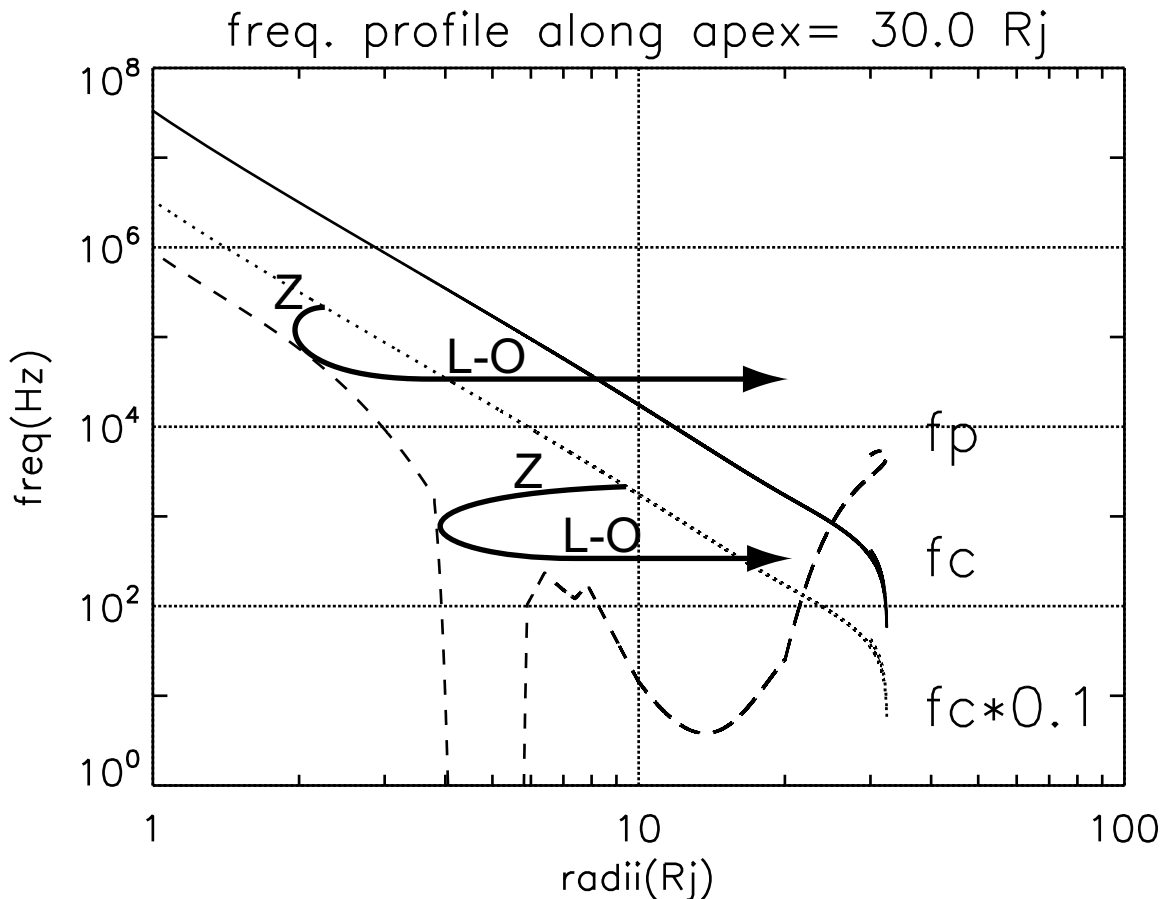


**Figure 6.23:** The frequency profiles showing the conversion process of free-space O mode (L-O mode) waves from Z mode waves with similar formats to Figure 6.18. Z mode waves are excited by the cyclotron resonance process at the altitudes where their frequencies are less than one tenth of the local cyclotron frequencies (see Figure 6.6, 6.10, and 6.13). They propagate to the boundary of plasma densities where frequencies of the generated Z mode waves are close to the local plasma frequencies. These waves are converted to L-O mode waves at the density boundary.

3. The excited O mode waves could propagate similarly to those of the R-X mode waves as indicated in Section 5.3, forming the observed shadow zone
4. Frequency range of the O mode waves is narrow at the source altitudes (e.g., the bandwidth where the *e*-folding time is less than 120 sec is  $\omega_r/\omega_c = 0\text{--}0.1$  in Figure 6.9)
5. Broadband QP bursts in O mode are emitted from the source flux tube if the ring beams maintain their instabilities along the flux tube
6. Free-space O mode waves are also excited at low altitudes with similar characteristics to those at high altitudes (Figure 6.12)

The growth rate calculation under conditions of the magnetosheath revealed that:

7. Both of the direct and indirect processes are unreasonable in the magnetosheath because the free-space waves and local plasma waves are not excited effectively

Thus, we adopted the first interpretation for the result of the direction finding by Cassini in Section 5.4:

8. QP bursts from the polar region (a few to 10  $R_J$  altitudes) were scattered and reached to the apparent altitudes of  $\sim 50 R_J$  by the local density fluctuations in the magnetosheath and interplanetary space

We examined the indirect generation scenario referring to the previous theoretical study (Oya, 1974). It was concluded that the following mode conversion scenario is possible at low and high source altitudes:

9. Z mode waves propagating toward Jupiter are excited at low and high altitudes at frequencies less than  $0.1 f_c$  by the cyclotron resonance with the parallel or ring beams (Figures 6.6, 6.10 and 6.13)
10. The Z mode waves are converted to the free-space O mode waves with the energy conversion rates of tens of percents in the density boundary region where their frequencies are close to the local  $f_p$  (Figure 6.20–6.23)

## 6.2 Macroscopic Generation Process of Quasi-Periodic Phenomena

In this section, we examine two possible scenarios of the relativistic energization process, which would strongly accelerate particles along field lines in the polar magnetosphere with quasi periodicity accompanied with the “QP phenomena”: the periodic radio bursts and auroral emissions. The two scenarios were briefly verified based on the *in-situ* and wave observations by Galileo and Ulysses.

### 6.2.1 Scenario 1: External Process

#### Flux Transfer Event Scenario

Firstly, we introduce the “flux transfer event (FTE)” scenario as one of the drivers for the QP phenomena. Bunce *et al.* (2004) represented a conceptual model of the cusp process, which generates field aligned currents above the cusp region via intermittent reconnections, i.e., the flux transfer event.

In the model, a pair of vortexes is assumed to be imposed in the polar ionosphere by pulsed reconnection at the open-closed field line boundary as indicated in the top panel of Figure 6.24. The top panel in Figure 6.24 indicates the twin vortex of ionospheric flow. If the ionospheric magnetic field is frozen-in and threaded perpendicular to the conductivity layer uniformly (i.e.,  $\mathbf{B}_i = B_i \hat{z}$ ), the flow pattern is equivalent to the equipotential lines of the electrostatic field formulated by

$$\mathbf{E}_i = -\nabla\Phi_i = -\mathbf{V}_i \times \mathbf{B}_i \quad (6.16)$$

where  $\mathbf{E}_i$  is the ionospheric electric field,  $\Phi_i$  is the electrostatic potential, and  $\mathbf{V}_i$  is the ionospheric plasma velocity. The total ionospheric currents  $\mathbf{i}$  consist of the Pedersen currents

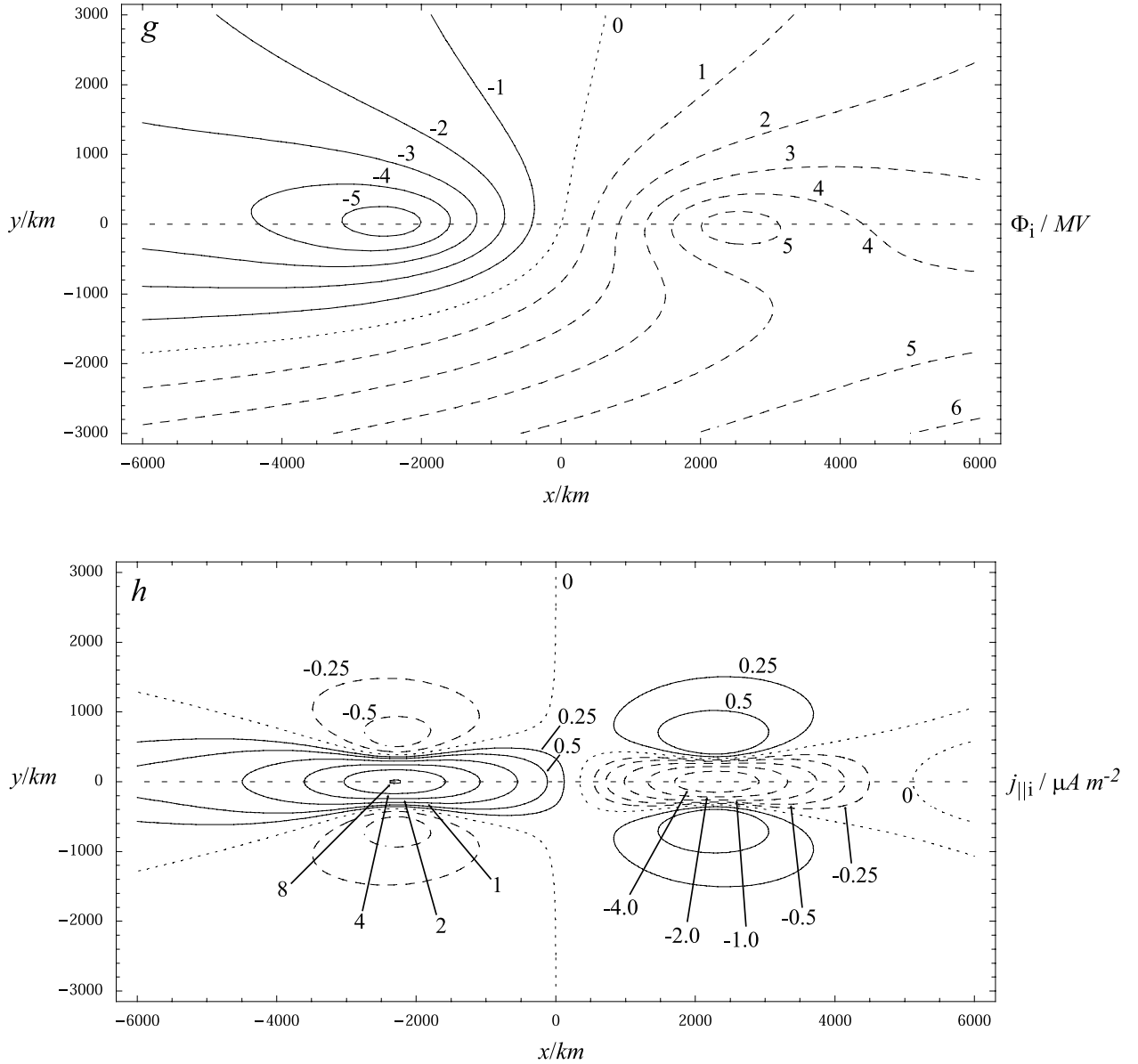


**Figure 6.24:** (top) Contours of the electrostatic potential, i.e., streamlines of the plasma flow, are shown on a grid of -3000–3000 km in *y* and -6000–6000 km in *x*. The short dashed line at *y* = 0 indicates the open-closed field line boundary. The dotted line depicts zero electrostatic potential. The solid lines show contours of negative electrostatic potential. Contours are labeled in steps of 0.5 MV. The bottom panel shows contours of the field-aligned current density over the same area as the top panel. Similarly, the short dashed line at *y* = 0 shows the open-closed field line boundary. Dotted lines indicate contours of zero field-aligned current density. Solid lines indicate the regions of upward directed field-aligned current density, while the dashed lines indicate the regions of downward directed field-aligned current density. Contours are labeled 0.25, 0.5, 1.0, etc., in units of  $\mu Am^{-2}$  (after Bunce et al., 2004).

$\mathbf{i}_P$  and Hall currents  $\mathbf{i}_H$  written as

$$\mathbf{i} = \mathbf{i}_P + \mathbf{i}_H = \Sigma_P \mathbf{E}'_i + \Sigma_H \hat{\mathbf{B}}_i \times \mathbf{E}'_i \quad (6.17)$$

where  $\Sigma_P$  and  $\Sigma_H$  are height-integrated Pedersen and Hall conductances, respectively, and  $\mathbf{E}'_i$  is the electric field in the neutral atmosphere rest frame given by

$$\mathbf{E}'_i = -(\mathbf{V}_i - \mathbf{V}_n) \times \mathbf{B}_i \quad (6.18)$$

where  $\mathbf{V}_n$  is the velocity of the neutral atmosphere.

Finally, the field aligned current is derived from the divergence of the ionospheric currents:

$$j_{||i} = -\nabla \cdot \mathbf{i} \quad (6.19)$$

Substituting Equations 6.17 and 6.18 into Equation 6.19 yields

$$j_{||i} = -\nabla \cdot (\mathbf{i}_P + \mathbf{i}_H) \quad (6.20)$$

$$= -\nabla \cdot \mathbf{i}_P \quad (6.21)$$

$$= \nabla \cdot (\Sigma_P (\mathbf{V}_i - \mathbf{V}_n) \times \mathbf{B}_i) \quad (6.22)$$

$$= \Sigma_P \mathbf{B}_i \cdot (\nabla \times \mathbf{V}_i) \quad (6.23)$$

where we assumed that  $\mathbf{V}_n$ ,  $\Sigma_P$  and  $\Sigma_H$  are all constants,  $\mathbf{B}_i$  is rotation- and divergence-free, and the neutral atmosphere is rigidly corotating (i.e., moving eastward uniformly with  $\nabla \times \mathbf{V}_n = 0$ ). It should be noted that the Hall currents  $\mathbf{i}_H$  do not contribute to the divergence because they are flowing along the equipotential lines closing in the ionosphere. With use of the divergence of Equation 6.16, Equation 6.23 is rewritten as

$$j_{||i} = \Sigma_P \nabla^2 \Phi_i \quad (6.24)$$

In *Bunce et al. (2004)*, the field aligned current density was calculated assuming the flow

velocities and the height-integrated Pedersen conductances in the polar ionosphere. The bottom panel of Figure 6.24 indicates the field aligned current densities for the case of “fast flow” model where the interplanetary magnetic field (IMF) has high densities, thus, the polar ionospheric flow (the top panel) is fast because of the high reconnection rate. Upward and downward field aligned currents are generated above the twin-vortex at the open-closed boundary.

The field aligned potential drop was derived from the current densities based on the work by *Knight* (1973), who related the field aligned currents  $j_{\parallel}$  to potential drop  $\Phi_{\parallel}$  theoretically. *Bunce et al.* (2004) estimated that the strong potential drop of  $\sim 5$  MV is achieved in the *downward* current region along the closed field lines for the case of “fast flow” model. This strong potential could accelerate electrons up to relativistic energies directed *outward* from Jupiter as observed by Ulysses at southern high latitudes (*McKibben et al.*, 1993; *Zhang et al.*, 1995). *Bunce et al.* (2004) also suggested that UV auroral flare or X-ray “hot spot” (*Waite et al.*, 2001; *Gladstone et al.*, 2002) could be sufficiently brightened due to energetic particle precipitations by the upward/downward currents above the cusp. Figure 6.25 summarizes the scenario for the particle accelerations by the FTE.

We verified the “FTE scenario” based on the observations of magnetic field performed by Galileo at the magnetopause and those of the QP bursts’ response to the solar wind detected by Ulysses in the interplanetary space.

### **Validation: Flux Transfer Event at the Magnetopause**

The FTE scenario predicts that at the magnetopause, there exist the pulse reconnections with similar quasi-periodicity to that of QP phenomena: e.g., the “40 minutes” periodicity for QP radio bursts as shown in Figure 3.9. magnetic field data at the magnetopause were converted to the components in “boundary-normal coordinates” to detect the FTE signals. In the present analysis, three-dimensional vector components  $(b_L, b_M, b_N)$  in boundary-normal coordinates are defined as follows:

1.  $\hat{N}$  vector is perpendicular to the boundary (magnetopause) and directed outward

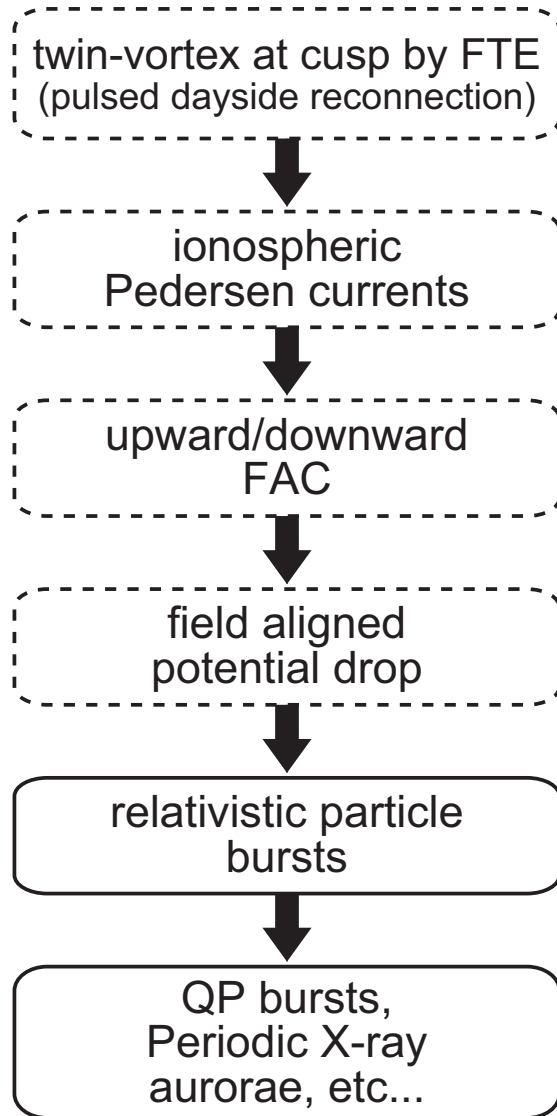


**Figure 6.25:** A flow diagram showing a possible scenario for the Jovian relativistic particle acceleration process with quasi-periodicity, which is proposed by *Bunce et al. (2004)*. In this scenario, the driver of the particle acceleration is assumed to be the flux transfer event in the cusp region. The processes framed by broken lines indicate that these process have not been identified in observations.

from Jupiter

2.  $\hat{M}$  vector is derived from cross product of  $\hat{N}$  and the normalized position vector of spacecraft  $\hat{r}$  (i.e.,  $\hat{M} = \hat{N} \times \hat{r}$ , approximately equivalent to azimuthal components in the Jovigraphic coordinate).
3.  $\hat{L}$  vector completes the right-handed triad (i.e.,  $\hat{M} = \hat{N} \times \hat{L}$ , approximately equivalent to north-south component in the Jovigraphic coordinate).
4. each boundary-normal component is derived from projections of observed magnetic field vectors to  $\hat{L}$ ,  $\hat{M}$ , and  $\hat{N}$ .

The boundary normal components were determined by applying the “minimum variance method” to the magnetic field signals observed around magnetopause crossings of Galileo. The minimum variance method detects the normal vector to the plane on which the observed vectors have the largest variance. The projections of magnetic field vector to the normal vector correspond to the  $N$  components in boundary-normal coordinates. For details of above data processing, see also, e.g., Sonnerup and Cahill (1967).

Cowley (1982) depicted morphology of the FTE as shown in Figure 6.26. It is expected that if the FTEs are occurring on the magnetopause with similar morphology to that in Figure 6.26, they are observed as pulsed signals in boundary-normal components  $b_N$ .

Figure 6.27 indicates the magnetic field components in boundary-normal coordinates observed by Galileo on 24 Oct. 2001, when it was passing through the magnetopause at a distance of 78 R<sub>J</sub> from Jupiter in a local time of 14.3 h. From the top panel,  $L$ ,  $M$ ,  $N$  components and magnitude of the magnetic field in boundary-normal coordinates are plotted. Horizontal axes show time and vertical axes show magnetic field of each component in nT. Vertical broken lines indicate the boundaries of the magnetopause and bowshock, respectively, which were determined based on the magnetic field and wave data. A pulse signal was observed at 18:35 in  $N$  components of panel (c) just before the escape of Galileo from the magnetosheath to the interplanetary space. This result indicates that the pulse was a significant FTE signal, however, not periodic like QP phenomena. No

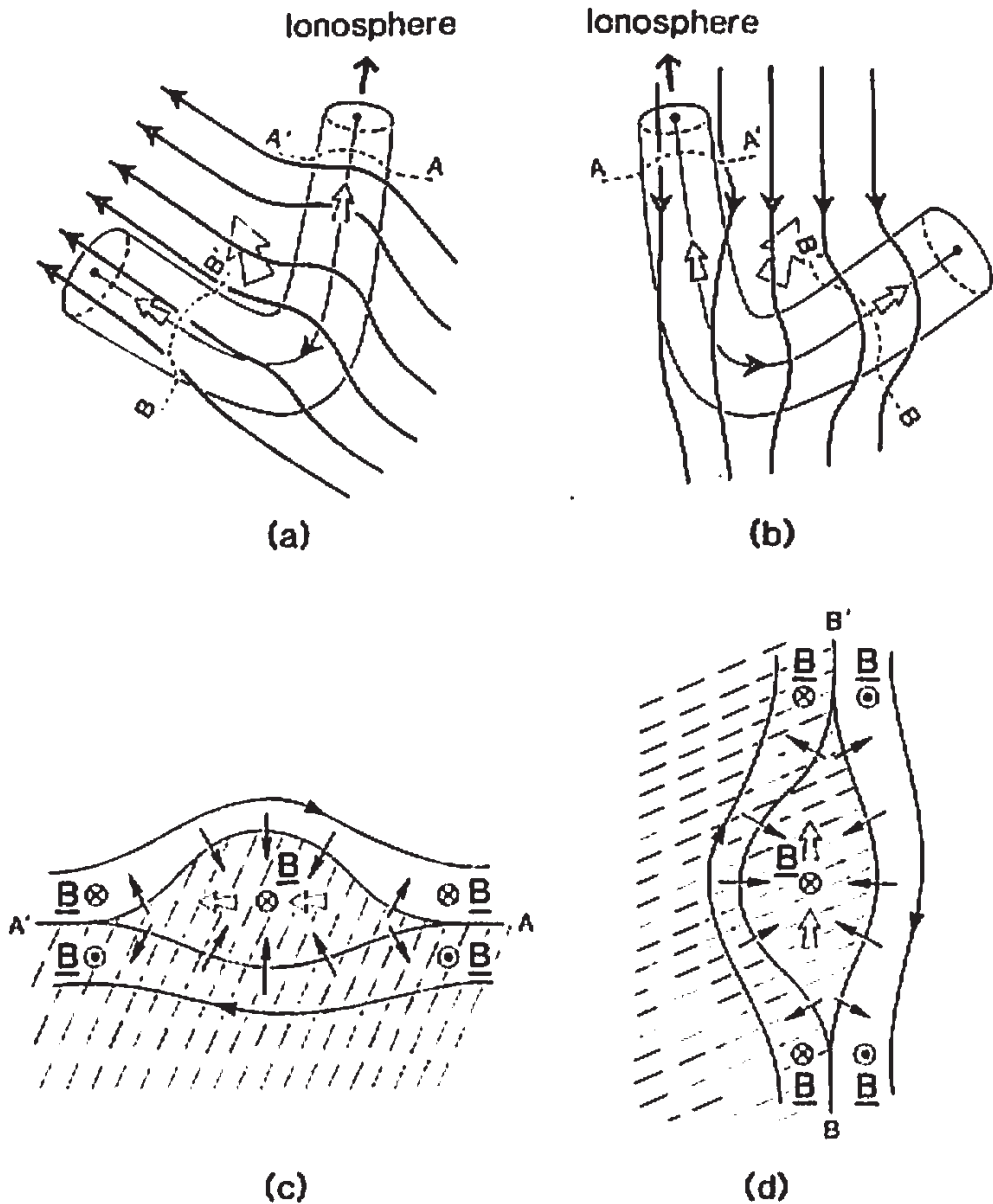


**Figure 6.26:** (a) Front (solar) and (b) back (Jupiter) view and (c,d) cross sections of a northward moving flux transfer event at Jupiter (after Cowley, 1982). Solid arrows indicate the interplanetary magnetic field (IMF). Jupiter's intrinsic field points southward, and the IMF is assumed to have a northward component. The IMF, also, is assumed to have an east-west component pointing toward dawn. Figure (c) is the cross section along A'A and (d) is that along B'B.

FTE signal with tens of minutes period was found from the Galileo/MAG data around its magnetopause crossing. These characteristics were always observed in the magnetic field data. Thus, we conclude that the FTE signals at Jupiter were not accompanied with periodic features similar to the QP phenomena. This observational results disagree with the FTE scenario described above.

### **Validation: Solar Wind Response**

Going back to the concept of the FTE scenario, it also predicts that the field aligned currents were considerably controlled by the IMF and solar wind plasma: if the IMF is directed northward, the reconnection rate increases, followed by the enhancement of the field aligned currents. We examined this prediction based on the solar wind and wave data observed by Ulysses.

Occurrence probabilities of QP bursts were compared with the magnitude of the IMF, velocity and dynamic pressure of solar wind, and the “reconnection voltage”. The reconnection voltage is the production rate of open flux tube by the dayside reconnections. An empirical formula for the voltage was developed by previous studies (e.g., Akasofu, 1978). The low-latitude dayside reconnection voltage  $\phi_L$  is given by

$$\phi_L = v_{sw} B_\perp L_o \cos^4 \left( \frac{\theta}{2} \right) \quad (6.25)$$

where  $v_{sw}$  is the velocity of the solar wind,  $B_\perp$  is the magnitude of the IMF component perpendicular to  $v_{sw}$ , and  $L_o$  is the characteristic length of reconnection on the magnetopause which is perpendicular to  $B_\perp$ . The parameter  $\theta$  is the “clock angle” between the IMF vector and Jupiter’s magnetic axis projected onto a plane perpendicular to the Sun-Jupiter direction. The high-latitude reconnection voltage  $\phi_H$  is given with a similar formulation to  $\phi_L$

$$\phi_H = \frac{1}{2} v_{sw} B_\perp L_o \sin^4 \left( \frac{\theta}{2} \right) \quad (6.26)$$

where the magnitude of  $\phi_H$  is empirically estimated to be a half of the high-latitude recon-

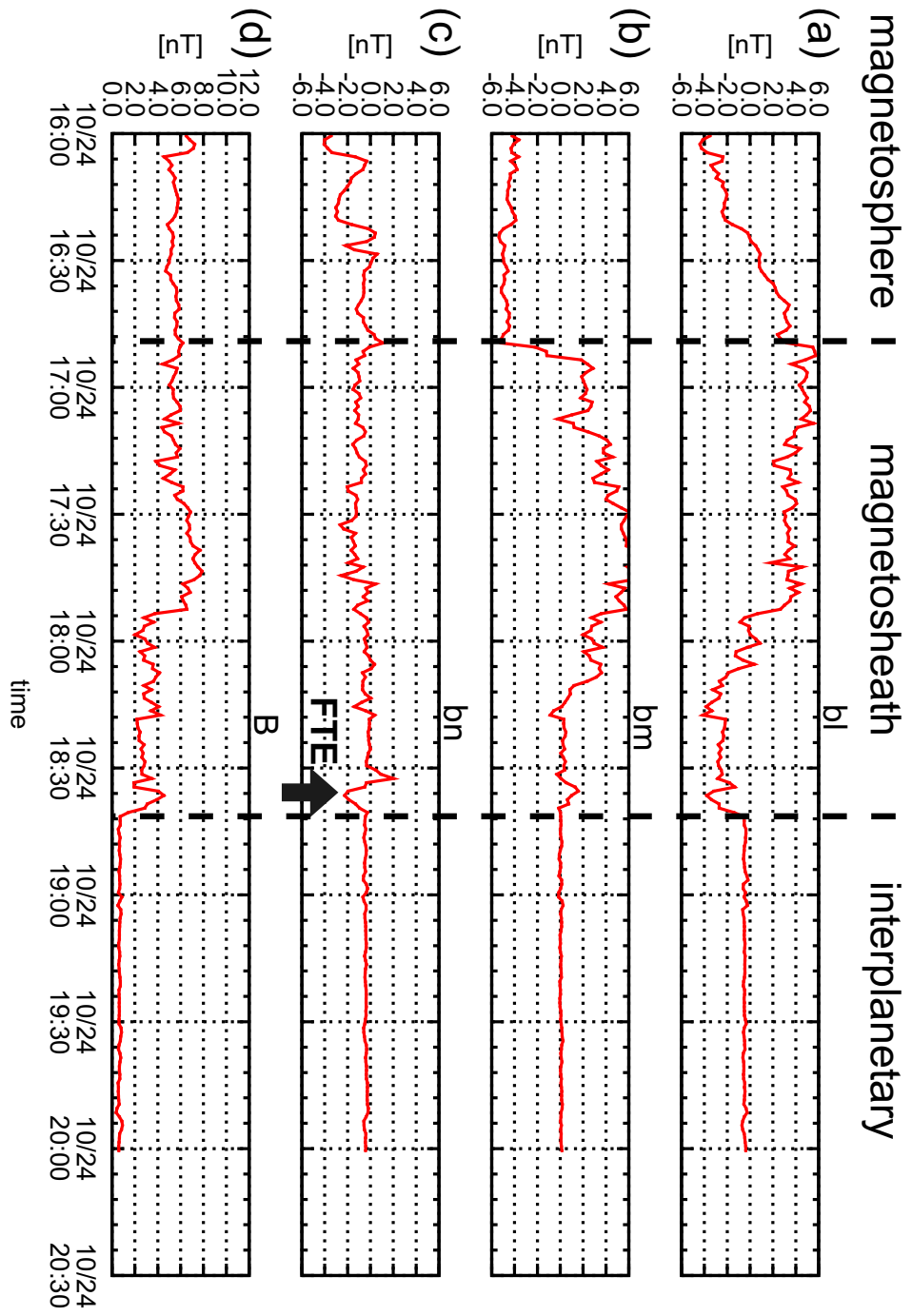


**Figure 6.27:** Magnetic field components in boundary-normal coordinates observed by Galileo/MAG at 16–20 h on 24 Oct. 2001, when Galileo was located at a distance of  $78 R_J$  from Jupiter in a local time of 14.3 h. Horizontal axes show time and vertical axes show magnetic field of each component in nT. (a)  $N$  components which are perpendicular to the boundary (magnetopause) and directed outward from Jupiter (b)  $L$  components which are the projections of the north-south components of magnetic field vector into the boundary plane (c)  $M$  components which complete the right-handed triad (i.e.,  $\hat{M} = \hat{N} \times \hat{L}$ , approximately equivalent to azimuthal components in the Jovigraphic coordinate). (d) Magnitudes of the magnetic fields. Vertical broken lines indicate the time when Galileo passed the magnetopause or bowshock. Vertical arrow annotated “FTE” in the boundary normal components ( $b_n$ ) corresponds to the signal of flux transfer event.

nexion voltage. In the present analysis, the reconnection channel  $L_0$  was set to be  $\sim 37$   $R_J$ , which is a half width of the typical diameter of Jovian magnetosphere's cross-section. Other parameters  $v_{sw}$ ,  $B_\perp$ , and  $\theta$  were derived from the measurements of the solar wind and IMF by SWOOPS and FGM/VHM onboard Ulysses.

Figure 6.28 is a plot showing the solar wind parameters and occurrence probabilities of QP bursts observed Ulysses at high latitudes during its second encounter with Jupiter in 2004. The horizontal axes show the time of 6 months from 1 Nov. 2003 with orbital parameters of Ulysses. In Figure 6.28a–e, the magnitude of the IMF ( $|B_{IMF}|$ ), high- and low-latitude reconnection voltages ( $\Phi_h$  and  $\Phi_l$ ), radial velocity of solar wind ( $V_r$ ), and dynamic pressure of solar wind ( $P_{dyn}$ ) are plotted. Panel (f) indicates the occurrence probabilities of QP bursts of every 10 hours, which were detected based on the criteria described in Section 3.1: i.e., events in the panel (f) are the same as those in Figure 3.3. Figure 6.28 indicates that solar wind disturbances like the corotating interaction region (CIR) or coronal mass ejection (CME) accompanying with the enhancements in the solar wind parameters were arriving at Jupiter. The occurrence probabilities of QP bursts gradually declined as Ulysses flew down to low latitudes.

Figures 6.29a-d represent the cross correlation coefficients between QP bursts' occurrence and the four solar wind parameters. These cross correlation coefficients are functions of lag time between QP bursts and solar wind parameters, which were derived from the same data sets in Figure 6.28. However, it should be noted that because QP bursts' occurrence are strongly dependent on the magnetic latitudes (see Figure 3.3), the periods when QP bursts are absent due to the latitudinal effect ( $MLAT < +30^\circ$ ) were excluded. In Figure 6.29, horizontal axes show the lag time and vertical axes are the cross correlation coefficients, which were calculated from logarithmic values of the occurrence probabilities and solar wind parameters. These figures indicate that correlations between QP bursts and the solar wind are insignificant even for the reconnection voltage, which is supposed to control the QP phenomena in the FTE scenario.

Responses of another radio component to the solar wind were also investigated in the

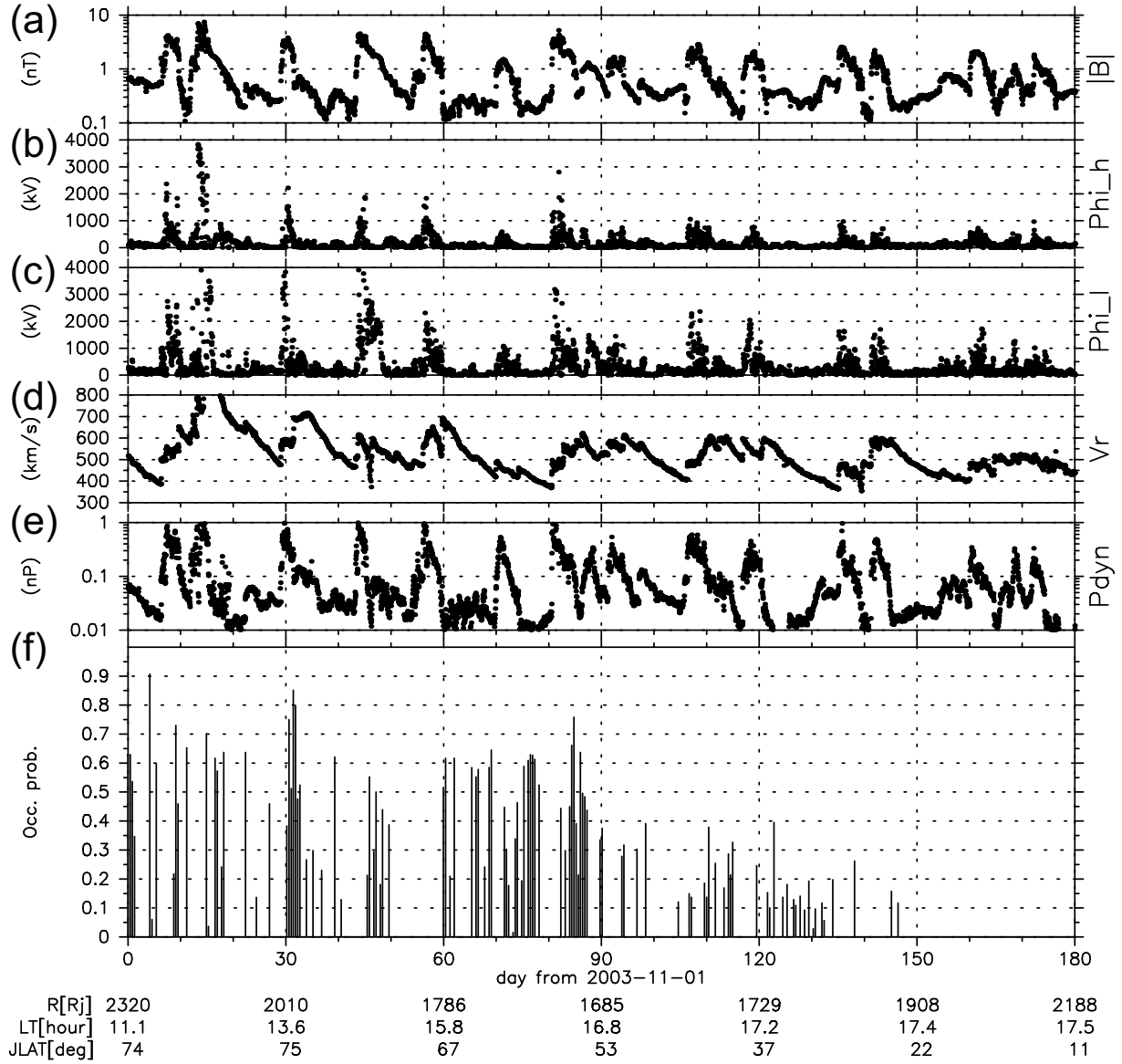


**Figure 6.28:** Solar wind parameters and the QP bursts' occurrence probabilities observed by Ulysses during its second encounter with Jupiter in 2004. Horizontal axes show days from 1 Nov. 2003. (a) Magnitude of the interplanetary magnetic field observed with FGM/VHM onboard Ulysses. (b) High-latitude and (c) low-latitude reconnection voltages, which correspond to the production rates of open flux tube by reconnections at the planetary magnetopause (see text). (d) Solar wind radial velocities from SWOOPS in the RTN coordinate where Sun is located at the origin and radial components are parallel to the Sun-Ulysses axis. (e) Dynamic pressure of solar wind plasma observed by SWOOPS. (f) Occurrence probabilities of QP bursts of every 10 hours, which were detected based on the criteria in Section 3.1. Orbital parameters of Ulysses are displayed at the bottom of the horizontal axis.

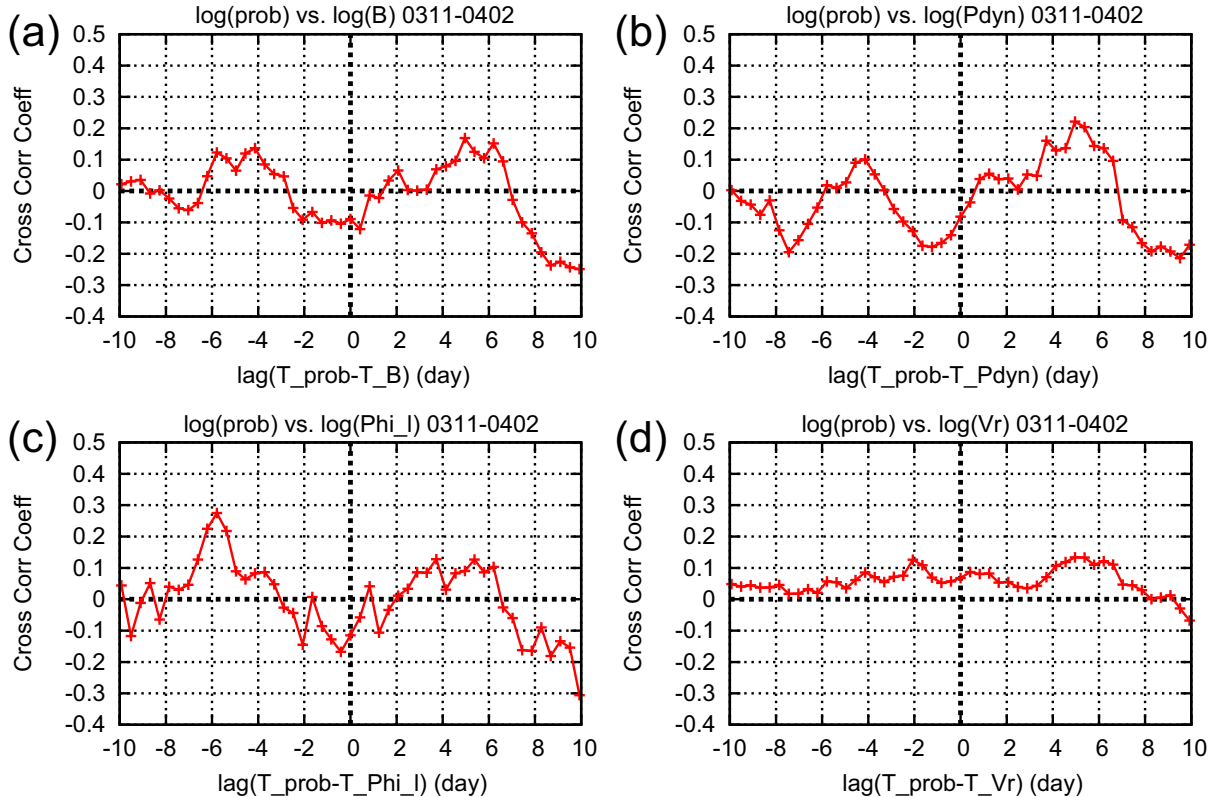


**Figure 6.29:** Cross correlation coefficients between solar wind parameters and QP bursts' occurrence probabilities as functions of lag time. Data of the solar wind and QP bursts were observed from Nov. 2003 to Feb. 2004 by Ulysses at northern high latitudes during its second encounter with Jupiter. Horizontal axes are the lag time between the QP bursts' data and solar wind data, and vertical axes are the cross correlation coefficients which were calculated from logarithmic values of the occurrence probabilities and solar wind parameters. (a) Correlation function between the occurrence probabilities and magnitude of the interplanetary magnetic field  $|B_{IMF}|$ , (b) that between the occurrence probabilities and dynamic pressure of solar wind plasma  $P_{dyn}$ , (c) that between the occurrence probabilities and low-latitude reconnection voltage  $\Phi_l$ , and (d) that between the occurrence probabilities and radial velocity of solar wind  $V_r$ .

same analysis period. Figure 6.30 indicates the solar wind parameters and received power of high-latitude bKOM, which was observed at high latitudes ( $MLAT > +30^\circ$ ) by Ulysses during the second encounter. Its source and radiation characteristics were described in detail by Kimura *et al.* (2008a). The received power of high-latitude bKOM was averaged in a frequency range of 40–50 kHz and normalized to the power at  $1R_J$  from the radio source.

Figure 6.31 draws cross correlation functions between the power of high-latitude bKOM and the four solar wind parameters. Formats of this figure is the same as Figure 6.29. It is notable that the received power of bKOM were positively correlated with  $|B_{IMF}|$ ,  $P_{dyn}$ , and  $\Phi_l$  in a time lag from  $<10$  h to  $\sim 1$  day. These results strongly suggest that fluctuations of high-latitude bKOM is partially controlled by the solar wind.

Thorough surveys for the responses of Jovian radio components including the other emissions to the solar wind were performed based on the data from Ulysses during the first and second encounters to Jupiter. The responses of nKOM and HOM were investigated based on the data set observed at low latitudes during the inbound phase of the first encounter. The results are summarized in Table 6.3. Note that, in this analysis, we regarded “correlated” with the solar wind for the case that correlation coefficients show only one peak with the value of  $>+0.3$  within  $\pm 5$  days lag, while the correlation coefficients of  $< +0.3$  and/or multiple peaks within  $\pm 5$  days lag were regarded as “uncorrelated”. Table 6.3 indicates that the QP bursts do not respond significantly to any solar wind parameters compared to the other radio components. Consequently, we confirmed that there is no observational evidence supporting the FTE scenario in the present analysis. Thus, we conclude that the FTE scenario is not feasible for the relativistic particle acceleration process of QP phenomena.

Changing the subject, surprisingly, the Jovian radio components other than QP bursts respond to the solar wind in a characteristic manner: the radio emissions whose source is related to the outer magnetosphere show sensitive responses to many solar wind parameters, on the other hand, those related to the inner magnetosphere indicate insensitive

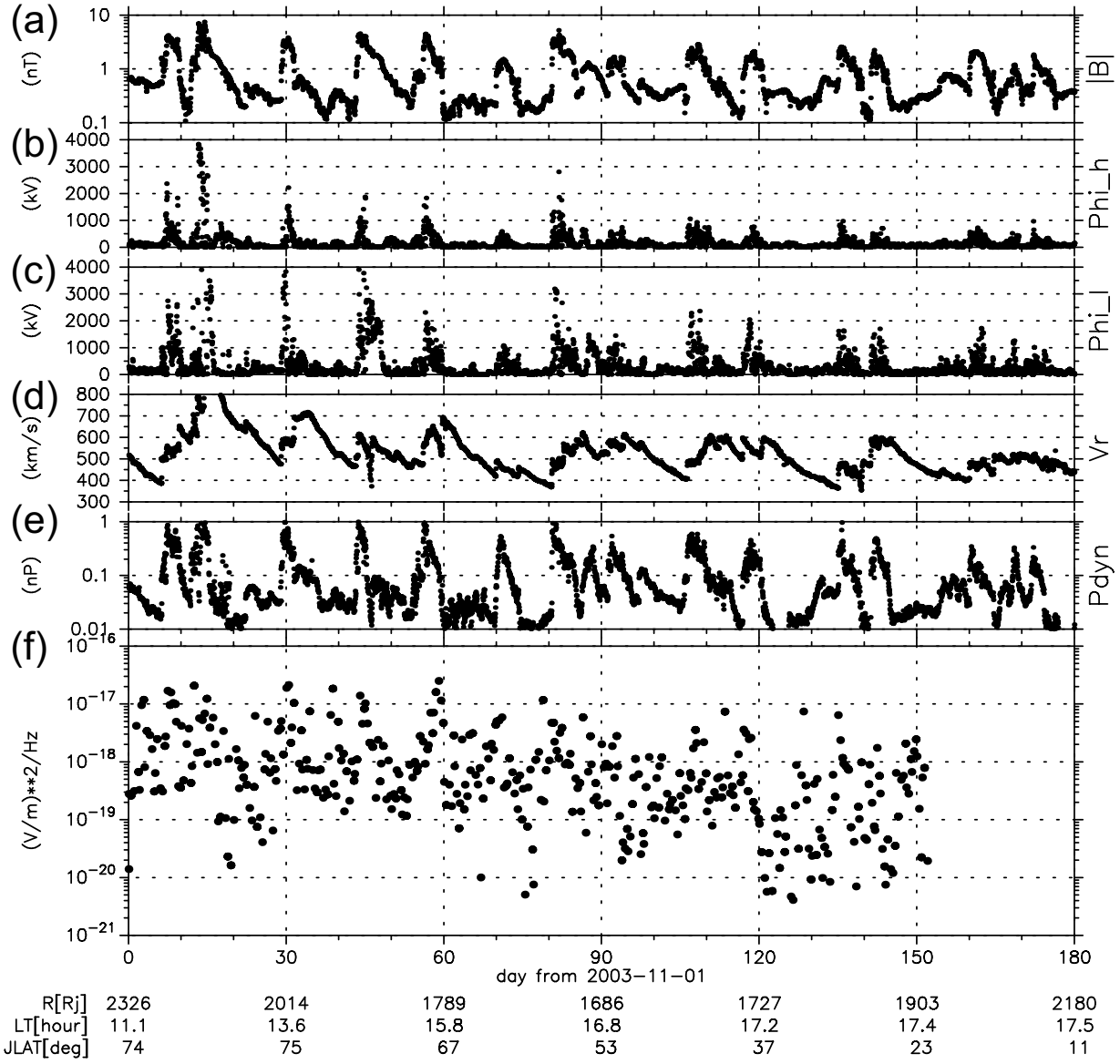


**Figure 6.30:** The solar wind parameters and intensities of bKOM observed by Ulysses at high latitudes during its second encounter with Jupiter in 2004. Formats are the same as Figure 6.28 except for panel (f), which indicates the received power of bKOM averaged at 40–50 kHz and normalized to the power at  $1R_J$  from the radio source. Plotted events of the high-latitude bKOM were observed during the Jovian rotational phase of  $SSL=180^\circ\text{--}270^\circ$ .

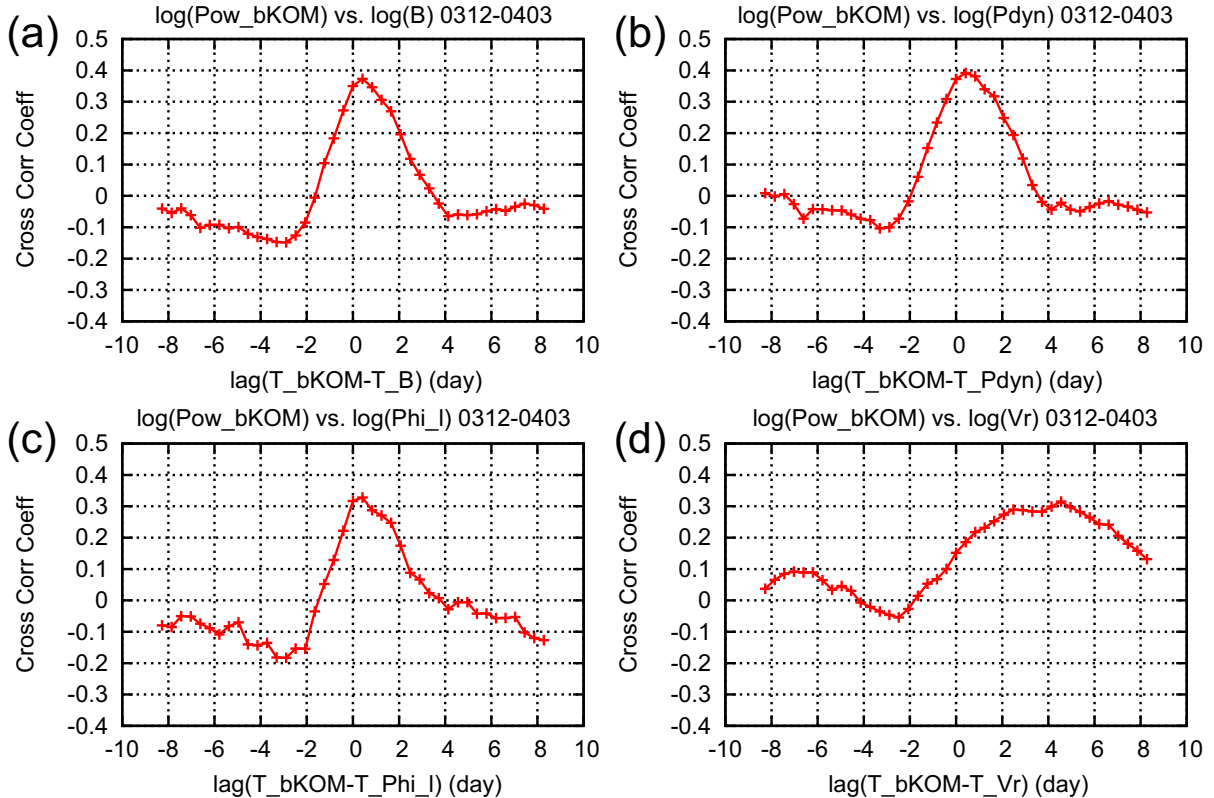


**Figure 6.31:** Cross correlation coefficients between the solar wind parameters and received power of bKOM as functions of lag time. Data of solar wind and bKOM were observed from Dec, 2003 to Mar, 2004. Formats are the same as Figure 6.29. The received power of bKOM was averaged at 40–50 kHz and corrected to the power at  $1R_J$  from the radio source. Events of the high-latitude bKOM were observed during the Jovian rotational phase of  $\text{SSL}=180^\circ\text{--}270^\circ$ .

**Table 6.3:** Responses of Jovian radio components to the solar wind

	nKOM	HOM	bKOM	QPB
related to	inner MS	middle MS	open-closed boundary	outer or external MS
$ \mathbf{B}_{IMF} $	✓	✓	✓	N/A
$P_{dyn}$	N/A	✓	✓	N/A
$\Phi_l$	N/A	N/A	✓	N/A
$V_r$	N/A	N/A	N/A	N/A
time lag	10 h >	10 h >	10 h – 1 day	N/A

✓: one peak correlation with the coefficient of  $>+0.3$  within  $\pm 5$  days lag (e.g., Figure 6.31a–c)

N/A : insignificant correlation (correlation coefficients  $< +0.3$ ) and/or multiple peaks within  $\pm 5$  days lag

$|\mathbf{B}_{IMF}|$ : magnitude of the IMF,

$P_{dyn}$ : dynamic pressure of solar wind,

$\Phi_l$ : low-latitude reconnection voltage,

$V_r$ : radial velocity of solar wind,

MS: magnetosphere

responses. In addition, the time lag of each response is quite short: less than 1 day, which is a few times larger than the solar wind travel time from the magnetopause to the inner magnetosphere. These characteristics possibly corresponds to the simultaneous response of the Jovian magnetospheric activities to the solar wind. The fast responses suggests that the disturbances induced by the solar wind propagates rapidly inward from the external to internal magnetosphere, generating particle accelerations at each magnetospheric region. Good correlations between the radio components and magnitude of the IMF (or the dynamic pressure) imply that these propagating disturbances could be compressional wave: e.g., the magnetosonic wave.

### 6.2.2 Scenario 2: Internal Process

#### Field Line Resonance Scenario

We propose the second scenario for the Jovian quasi-periodic particle accelerations based on the analogy of those at the terrestrial magnetosphere: the “field line resonance” (FLR) process. In the terrestrial magnetosphere, global standing Alfvén waves are excited along

dipole-like field lines at the magnetospheric boundary by wave coupling process with the compressional waves generated by the Kelvin-Helmholtz (K-H) instabilities at the magnetopause. These standing waves are observed at eigenfrequencies of the field lines in a particular L-shell. (see, e.g., *Southwood (1974)* for a theory of generation mechanisms). This process is named the “field line resonance process”. Frequencies of geomagnetic oscillations by the standing waves are from 1 to 4 mHz ( $\sim$ 4–16 minutes), which have been historically classified as “Pc 5 pulsations”. Some previous studies suggested that the FLR process is followed by the periodic particle acceleration process accompanying the periodic auroral pulsations and relevant variations of radio emissions (auroral kilometric radiations, AKR) at the frequencies of Pc 5 pulsations.

*Hanasz et al. (2006)* reported that the periodic pulsating AKR emissions were observed by the Interball satellite as indicated in Figure 6.32. The top panel represents the dynamic spectra and integrated intensity variations observed on 6 August 1997 by Polrad onboard Interball. The bottom panel is the Lomb periodgram derived from the integrated intensities (see Section 3.5 for the definition of the Lomb periodgram). These figures indicate the AKR emissions were pulsating at the significant frequency of 2.1 mHz corresponding to  $\sim$ 8 minutes period, which is close to the periods of FLR. *Hanasz et al. (2006)* also performed direction findings of the pulsating AKR by Interball with simultaneous ground-based observations of geomagnetic fields. These observations allowed to compare the periods of the pulsating AKR with those of the FLR pulsations possibly occurring along the source field lines of the pulsating AKR. Figure 6.33 shows a scatter plot showing relations between the periods of AKR and FLR pulsations. The horizontal and vertical axes are the frequencies of the pulsating AKR and FLR estimated by the Lomb periodgram, respectively. The open circles are the secondary peaks of the periodgrams which were not included for the linear fitting in the scatter plot. This results indicate that the periods of the AKR and FLR are almost the same, thus, suggesting that the electron precipitations generating the pulsating AKR are modulated by the FLR process.

Some other previous studies reported observational evidences of the periodic particle

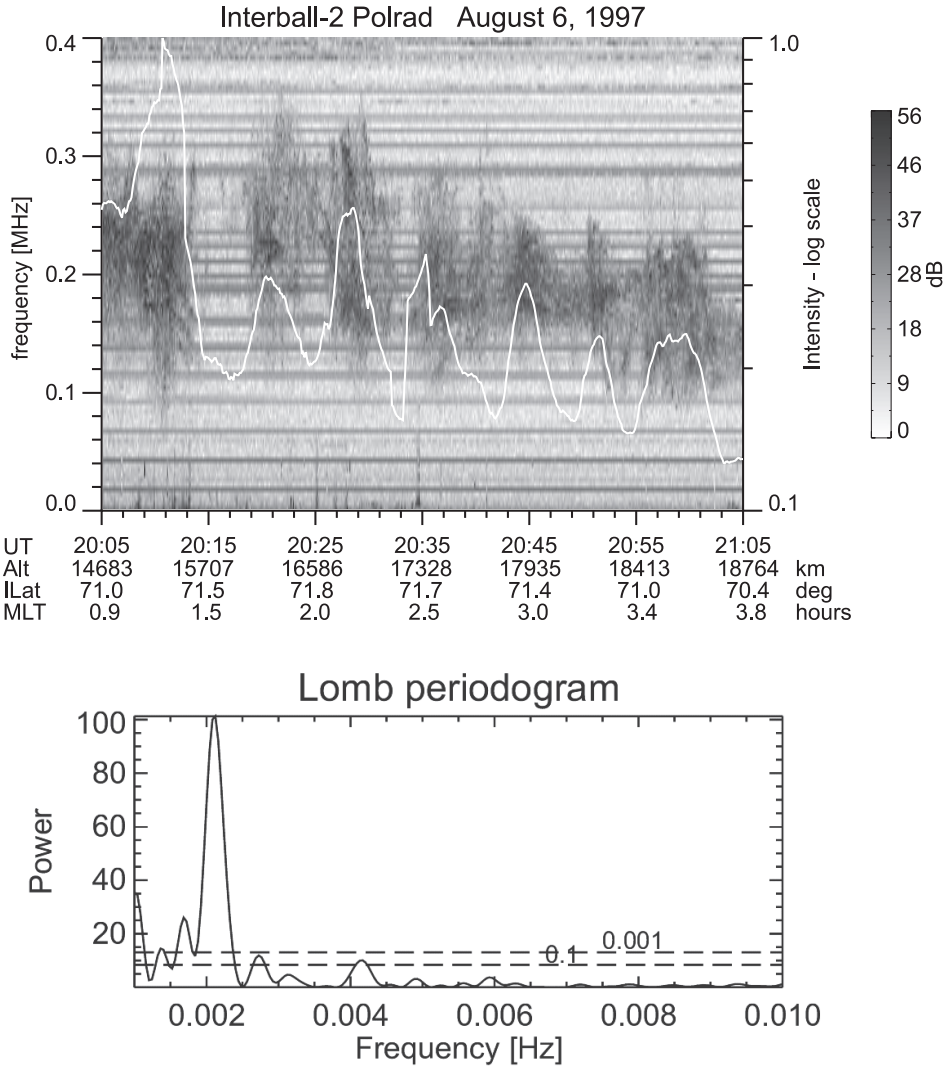


**Figure 6.32:** Example of a pulsating AKR event on 6 August 1997 2005–2105 UT, recorded by Interball-2 (Polrad) (after Hanasz et al., 2006). (top) Interball spectrogram. Superimposed white line is a plot of the AKR intensity variations in a logarithmic scale (rightside scale). (bottom) Lomb periodogram of the intensity variations (arbitrary units). The power levels of periodic signals corresponding to false alarm probability (FAP) = 0.001 and 0.1 are also shown. Smaller values of FAP indicate higher probability of distinct signal presence. The peak of the main feature indicates the dominating pulsation frequency of 2.1 mHz (~8 minutes).

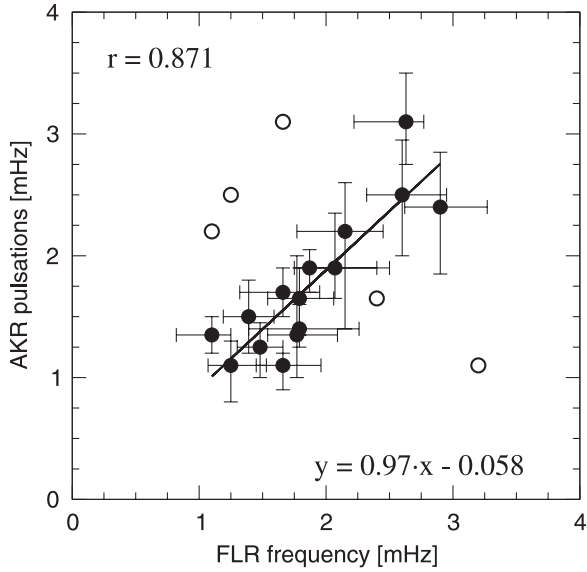


**Figure 6.33:** Correlation between AKR pulsation frequencies and FLRs frequencies for 15 cases detected in Hanasz *et al.* (2006). The secondary peaks in the periodgram at non correlated frequencies are marked with open circles.

accelerations by the FLR process. Figure 6.34 shows the variations of magnetic fields, riometer, and ELF–VLF wave data indicating the periodic electron precipitations accompanied with the Pc 5 geomagnetic pulsations (Nosé *et al.*, 1998). Cosmic Noise Absorption (CNA) was observed as pulsating signals in the riometer data, which correspond to the electron density modulations in the ionosphere by electron precipitations. The magnetic field data in Figure 6.34 indicate that Pc 5 pulsations were observed simultaneously with the CNA pulsations. Spanswick *et al.* (2005) took the occurrence statistics of the CNA pulsation and compared with those of Pc 5 magnetic pulsations based on magnetic field and riometer data. Figure 6.35 represents the statistical distribution showing the occurrence probabilities of CNA and magnetic Pc 5 pulsations. It was confirmed that CNA pulsations, which correspond to the periodic electron precipitations, are excited at the same region as the Pc 5 pulsations. At the earth, the region corresponds to flank regions of the magnetosphere, where the K-H instabilities are induced by interactions between the magnetopause and the solar wind flow. These observation results suggest that the periodic particle accelerations are generated by the FLR process. Some theoretical studies predicted that the

FLR accelerations are resulted from inertial Alfvén waves in the polar region, which propagate obliquely with respect to magnetic fields and could have parallel electric fields varying periodically (e.g., Wright *et al.*, 2002, 2003).

We applied the concept of the FLR process to the Jovian quasi-periodic phenomena because electron and proton outbursts (see Chapter 1) could be generated by the standing Alfvén waves with intrinsic periods at particular magnetic field lines. Figure 6.36 represents the FLR scenario in the Jovian magnetosphere proposed by this study.

### **Validation: Magnetic Field Spectra in the Magnetosphere**

We surveyed supporting evidences for our FLR scenario based on the observations of magnetic fields performed by Galileo. The magnetic fields observed at the outer and middle magnetosphere were analyzed based on the results in the previous chapters which suggested that source field lines of QP radio bursts are connected to the outer or external part of the magnetosphere. Observed magnetic fields were converted to the perturbation fields in “field-aligned coordinates” to detect Alfvénic fluctuations. Field-aligned coordinates are defined as follows:

1.  $\hat{z}$  vector is parallel to the background magnetic fields determined by 2nd order polynomial fitting (see below)
2.  $\hat{y}$  vector is derived from cross product of  $\hat{z}$  vector and normalized position vector of spacecraft  $\hat{r}$  in the Jovigraphic coordinates (i.e.,  $\hat{y} = \hat{z} \times \hat{r}$ , approximately equivalent to azimuthal components in the Jovigraphic coordinate).
3.  $\hat{x}$  vector completes the right-handed triad (i.e.,  $\hat{x} = \hat{y} \times \hat{z}$ , approximately equivalent to north-south components in the Jovigraphic coordinate).

The background and perturbation fields were determined in the way similar to that adopted by Khurana and Kivelson (1989) and Wilson and Dougherty (2000):

1. Observed magnetic field data were averaged to 1-minute resolutions.

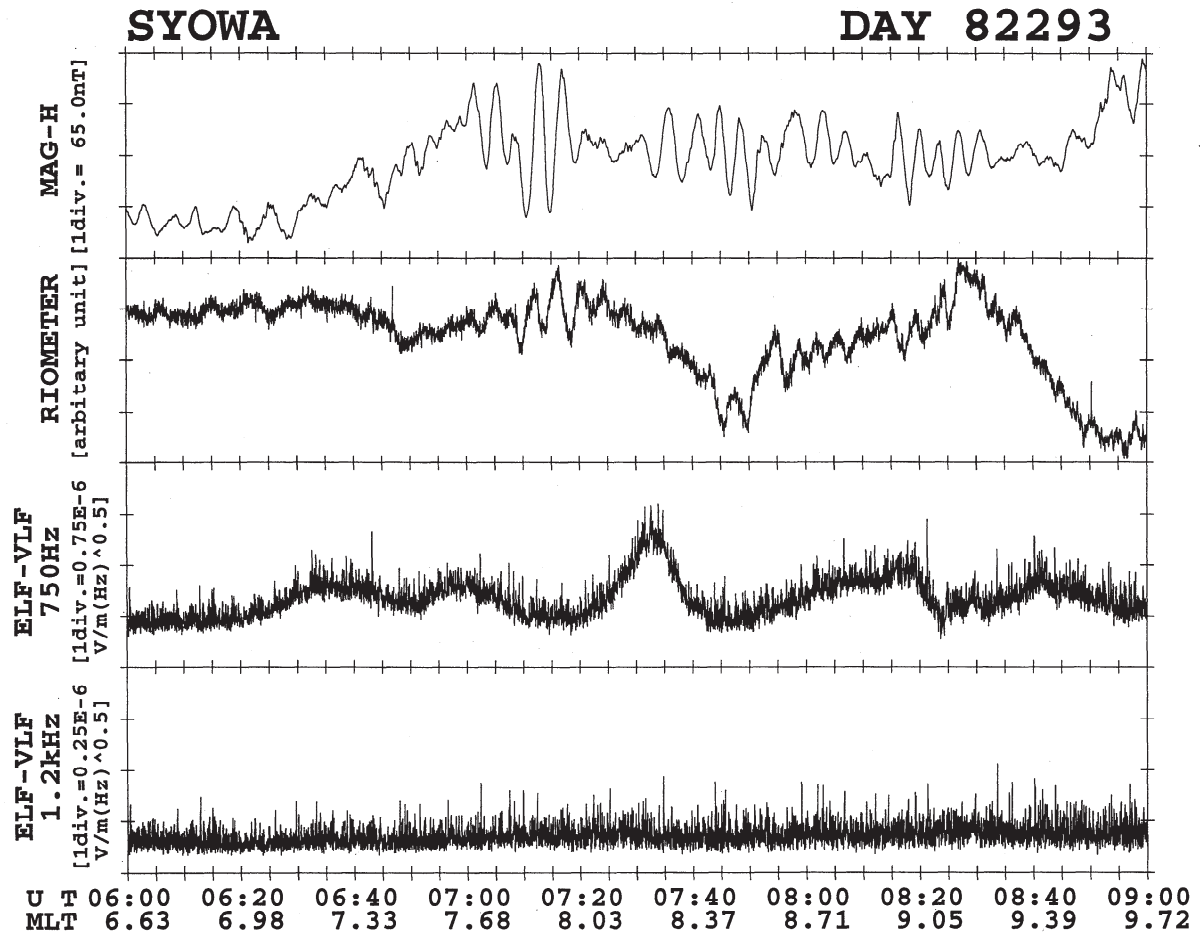


**Figure 6.34:** Magnetic field, riometer, and ELF–VLF wave data presented by Nosé et al. (1998). The first and second panels from the top give the H-component magnetic field data and the 30 MHz riometer data at Syowa Station. The lower two panels present the ELF–VLF wave intensities at the frequency band of 750 Hz and 1.2 kHz.

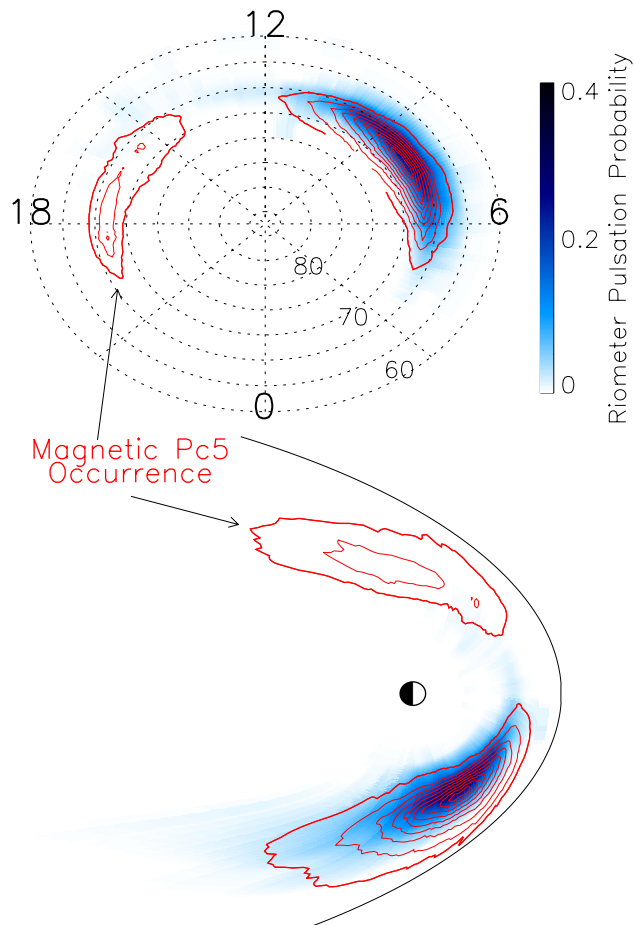


**Figure 6.35:** Occurrence probabilities of magnetic and riometer Pc5 pulsations (Spanswick et al., 2005). Top figure is the polar plot of these occurrence probabilities, and bottom figure shows the distribution of the probabilities in the magnetosphere. The color level plot indicates the probability of observing a riometer pulsation with a magnetic pulsation. Contours of magnetic Pc5 occurrence (from Baker et al., 2003) are shown in red.

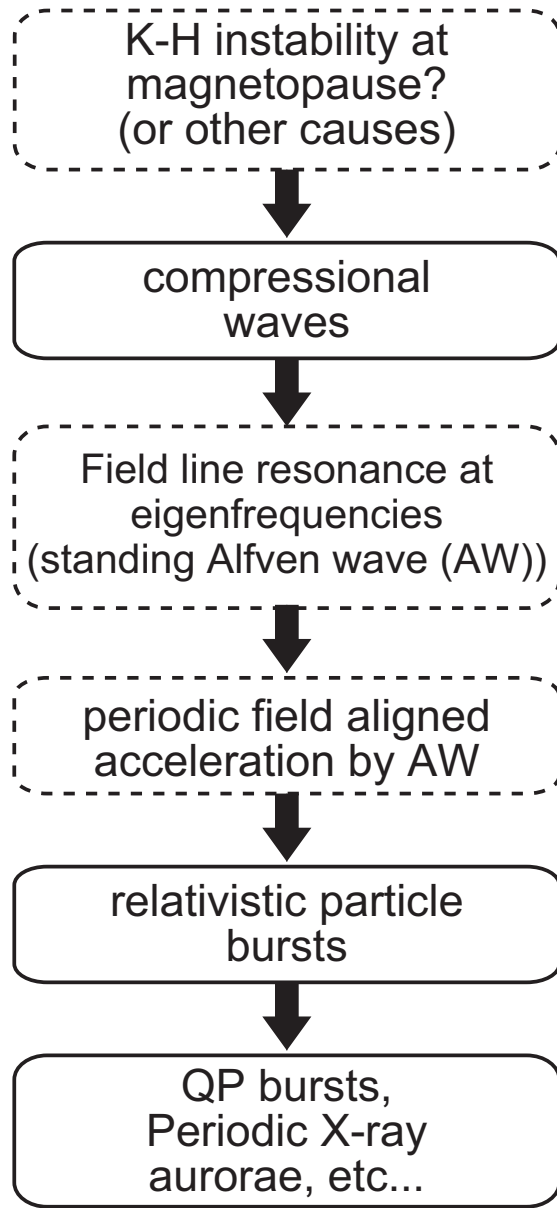


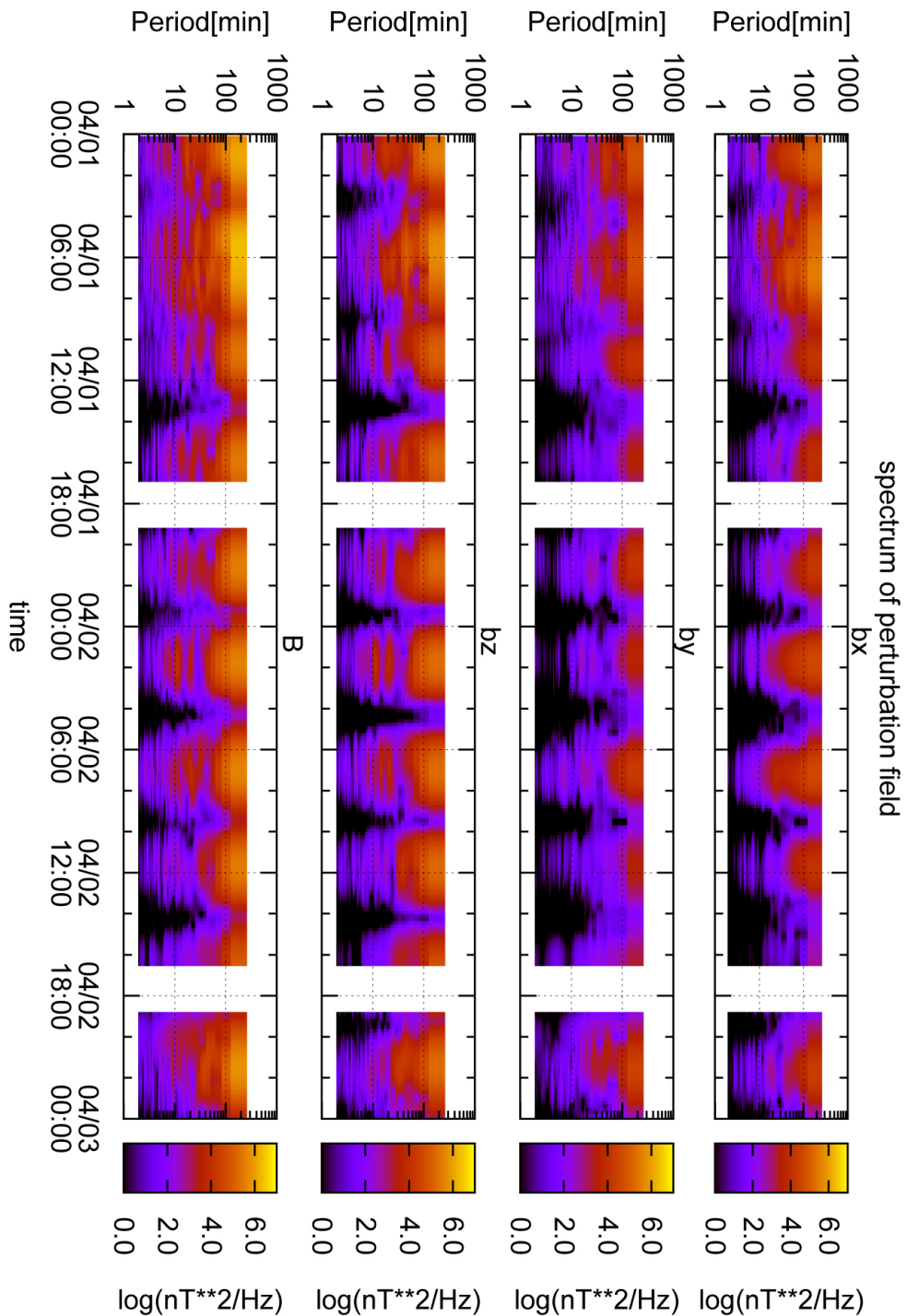
**Figure 6.36:** A flow diagram of a possible scenario for the Jovian relativistic particle acceleration process with quasi-periodicity, which is proposed in the present study. In this scenario, the driver of the particle acceleration is assumed to be the field line resonance: i.e., Alfvén waves standing along a particular field line between the northern and southern polar ionospheres. The processes framed by broken lines indicate that these processes have not been identified in observations at Jupiter.

2. A background field at an observed data point was determined by 2nd order polynomial fitting to the data within  $\pm 64$  minutes from the data point
3. A perturbation field was derived from subtracting the background field from the observed field.
4. Three-dimensional components were derived from projections of the perturbation field to  $\hat{x}$ ,  $\hat{y}$ , and  $\hat{z}$ .

Firstly, to detect the relation to the QP phenomena, we investigated periodicity of the perturbation field by using Fast Fourier Transfer (FFT) method because the vast amount of MAG data was sampled at a fixed time interval during the Real-Time Survey mode. Figure 6.37 plots power spectra of the perturbation fields in field-aligned coordinates observed by Galileo on 1–3 April 1997, when it was located at a distance of 38.2–21.2  $R_J$  from Jupiter in a local time of 5.3–7.2 h. Horizontal axes show the time from 0 h on 1 April, and vertical axes show periods of fluctuations in minutes. Colors indicate the spectral power of the magnetic perturbation fields estimated by FFT. It should be noted that spectral power in the all components has significant enhancements every  $\sim 5$  hours. These enhancements correspond to the large amplitude fluctuations observed when Galileo crossed the current sheet in the middle magnetosphere. Around the crossings, multiple periodicities were detected with the large spectral power in the dynamic spectra.

Figure 6.38 indicates the spectra averaged over 2 hours from 7 h on 1 April during a current sheet crossing. Horizontal axes show periods in minutes at the left panel and frequencies in mHz at the right panel. Vertical axes are spectral power in units of  $nT^2/Hz$  estimated by FFT. The averaged spectra of each component in the magnetic perturbation fields are plotted: red solid lines are spectra of  $b_x$ , green broken lines are those of  $b_y$ , pink dotted lines are  $b_z$ , and right blue dotted-broken lines are  $b_{perp} = \sqrt{b_x^2 + b_y^2}$ . The spectra of  $b_y$ ,  $b_z$ , and  $B_{perp}$  are multiplied by 10, 100, and 1000, respectively. Vertical solid lines are periods of interest (5, 10, 20, and 40 minutes), which are comparable to those of QP bursts obtained in Section 3.5. It was confirmed that during the current

**Figure 6.37:** Dynamic spectra of the perturbation fields in field-aligned coordinates observed on 1–3 Apr. 1997 by MAG onboard Galileo, when it was located at a distance of  $38.2\text{--}21.2 R_j$  from Jupiter in a local time of 5.3–7.2 h. From the top panel,  $b_x$ ,  $b_y$ ,  $b_z$  components, and magnitude of the perturbation fields are plotted. In field-aligned coordinates,  $z$  axis is parallel to the background field which determined by temporally-averaged data of magnetic fields, and  $x$ ,  $y$  components are included in the plane perpendicular to  $z$  axis (see text for detailed definitions). Horizontal axes show the time from 0 h on 1 Apr, and vertical axes show periods of fluctuations in minutes. Colors indicate the spectral power of the magnetic perturbation fields calculated by Fast Fourier Transfer (FFT).



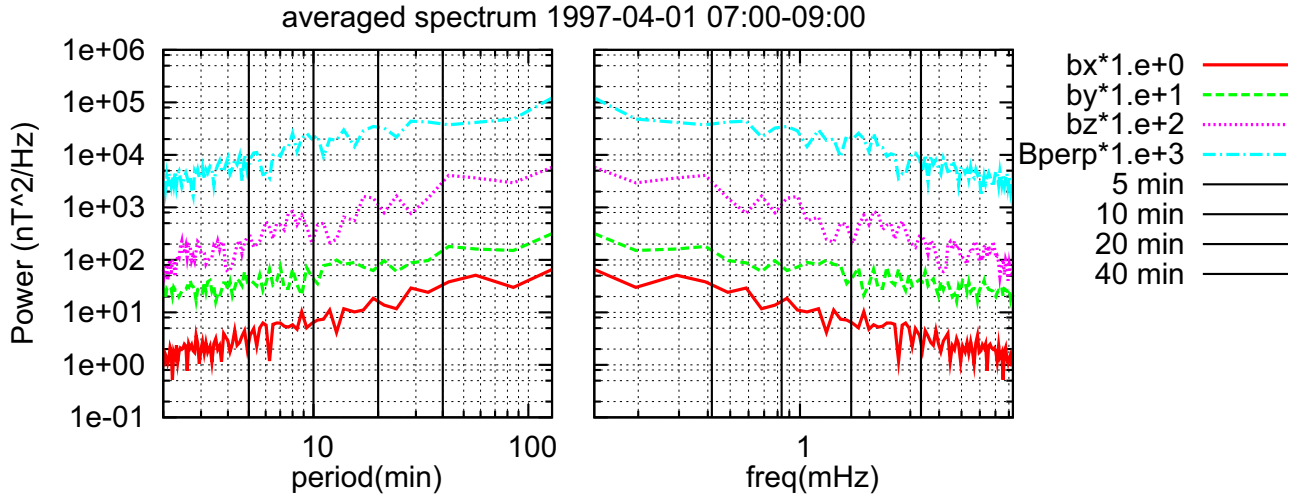


**Figure 6.38:** Averaged spectra of the perturbation fields in the field aligned coordinates observed at 7–9 h on 1 Apr. 1997. Vertical axes indicate the spectral power of the perturbation fields, and horizontal axes show the periods of fluctuations in minutes (left panel) and mHz (right panel). Solid, broken, dotted, and dotted-broken lines are the spectra of  $b_x$ ,  $b_y$ ,  $b_z$ , and  $B_{perp} = \sqrt{b_x^2 + b_y^2}$ , respectively. Spectra of  $b_y$ ,  $b_z$ , and  $B_{perp}$  are multiplied by 10, 100, and 1000, respectively. Vertical solid lines correspond to the periods of 5, 10, 20, and 40 min.

sheet crossings, multiple periods were detected in each component without characteristic frequencies like “40 minutes” in QP bursts. These characteristics are different from those of the FLR process at the earth, which shows at characteristic frequencies (1–4 mHz) corresponding to the eigenfrequencies of field lines at the magnetospheric boundaries. The multiple periodicity was also detected even in the outer magnetosphere. We conclude that monochromatic oscillations of magnetic fields, which correspond to eigenfrequencies at particular L-shells, were not detected in the outer and middle Jovian magnetosphere.

### Validation: Polarization of Magnetic Fields

Even though no monochromatic oscillation was detected in the magnetic field spectra, we found Alfvénic fluctuations at similar frequencies to QP phenomena by application of band-pass filtering to the observed signals. Figure 6.39 is a hodograph showing the polarization of the perturbation field vectors at 40 minutes frequency, which was derived

from band-pass filtering of the magnetic field signals observed at 8–9 h on 1 April 1997, when Galileo was located at  $\sim 30 R_J$  from Jupiter and a northern height of  $\sim 6 R_J$  from the magnetic equator in a local time of 5.5 h. (the same event as Figure 6.37 and 6.38). The left panel indicates the polarization of the perturbation fields in a plane perpendicular to background fields. The horizontal and vertical axes show  $b_x$  and  $b_y$  of the magnetic perturbation fields in nT, respectively. The right figure represents temporal variations of the polarization.  $x$  and  $y$  axes are equivalent to those in the left panel, and  $z$  axis indicates the time from 8 h to 9 h. The green line shows the background magnetic field. Although  $b_x$  and  $b_y$  signals were filtered independently, these components have a particular phase relation: right-handed circular polarization with respect to the background field. This characteristic corresponds to those of Alfvén waves.

The minimum variance analysis was performed again to detect the phase propagation angle which is an angular distance between the background field and wave number vector  $\vec{k}$ . The wave number vector was regarded as the normal vector of the plane where magnetic field signals have the maximum variance. The phase propagation angle was found to be  $\sim 25^\circ \pm 180^\circ$  for this case. It should be noted that ambiguity of  $180^\circ$  is included because the minimum variance analysis detects only polarization planes from fixed-point observations by one observer. Also, the Poynting vector, which indicates propagation directions of wave energy, cannot be determined because a set of electric and magnetic field data had not been observed with high-time resolutions during all periods of the Galileo mission.

At least, the minimum variance analysis found the phase propagation angle to be quasi-parallel direction with respect to the background field. In addition, amplitudes of the perturbation fields were found to be  $\sim 1\%$  of the background. This means that the amplitudes were small enough to regard the observed Alfvén waves as linear waves. These characteristics were frequently detected at northern- and southern-side of the current sheet region in the middle magnetosphere with tens of minutes periodicity. This result suggests that linear Alfvén waves at multiple periods are propagating toward and/or outward from the current sheet. Besides, one can infer that these waves propagate to the polar magnetosphere where

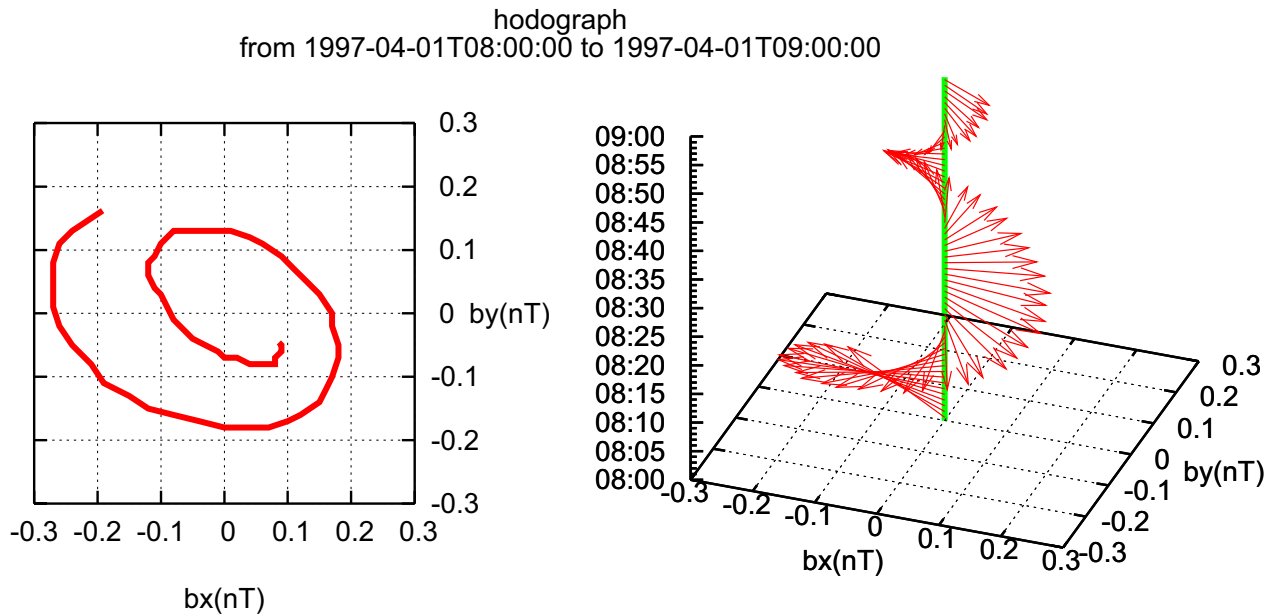


**Figure 6.39:** Hodograph of the perturbation field vector observed by Galileo at 8–9 h on 1 Apr. 1997, when it was located at a radial distance of  $\sim 30 R_J$  from Jupiter and  $\sim 6 R_J$  north from the magnetic equator. Left panel indicates the polarization of the perturbation fields in the plane perpendicular to the background fields. Horizontal and vertical axes show the  $b_x$  and  $b_y$  of the magnetic perturbation fields in nT, respectively. Right figure represents temporal variations of the polarization.  $x$  and  $y$  axes are equivalent to those in the left panel, and  $z$  axis indicates the time from 8 h to 9 h. Green line shows the background magnetic field. Polarization of this event is right-handed circular with respect to the background field.

QP phenomena are generated.

In fact, Ohgawara (1999) reported that Ulysses observed the Alfvénic fluctuations accompanied with the QP phenomena in the southern polar region during its first encounter with Jupiter. Figure 6.40 shows dynamic spectra of relativistic electron count rates and  $b_{perp}^2$  in field-aligned coordinates derived from the data of COSPIN and URAP observed on 12 Feb. 1992, when Ulysses was at a distance of  $\sim 75 R_J$  in the southern high latitudinal region ( $MLAT \sim -27^\circ$ ) of the dusk terminator. The event in Figure 6.40 corresponds to that in Figure 1.21 (McKibben *et al.*, 1993). Quasi-periodic electron outbursts accompanying QP radio bursts at 40 minutes period were observed at 2–5 h, followed by Alfvénic fluctuations with similar periodicity at 4–5 h. A hodograph of the magnetic perturbation fields is plotted in Figure 6.41, indicating partially left-handed circular polarization of the magnetic fields observed at 5.8–6.4 on 12 February 1992. These result also suggests the strong relation between Alfvén waves and QP phenomena.

From these results, we conclude that the Alfvén waves, which are propagating between the equatorial and polar region with periodic variations of field-aligned electric fields, could be a generator of QP accelerations in the Jovian polar region. This is also consistent with the proton outbursts observed by Ulysses (McKibben *et al.*, 1993; Zhang *et al.*, 1995), which could be energized by upward electric fields of the Alfvén waves. Although frequencies of the Alfvén waves are not monochromatic, i.e., they are not standing at a particular L-shell, this process is similar to the concept of the FLR at the terrestrial magnetosphere (Southwood, 1974). Thus, in this study, we term this Alfvénic accelerations still the “FLR scenario”.

Despite the detailed discussions as indicated above, many problems are still remaining in the FLR scenario:

- Why “40-minutes period” is selected as the periodicity of the QP phenomena while there exist the multiple periods in the equatorial region ?
- Can the Alfvén waves possess sufficient energy to accelerate particles up to relativistic energy range in the polar region ?

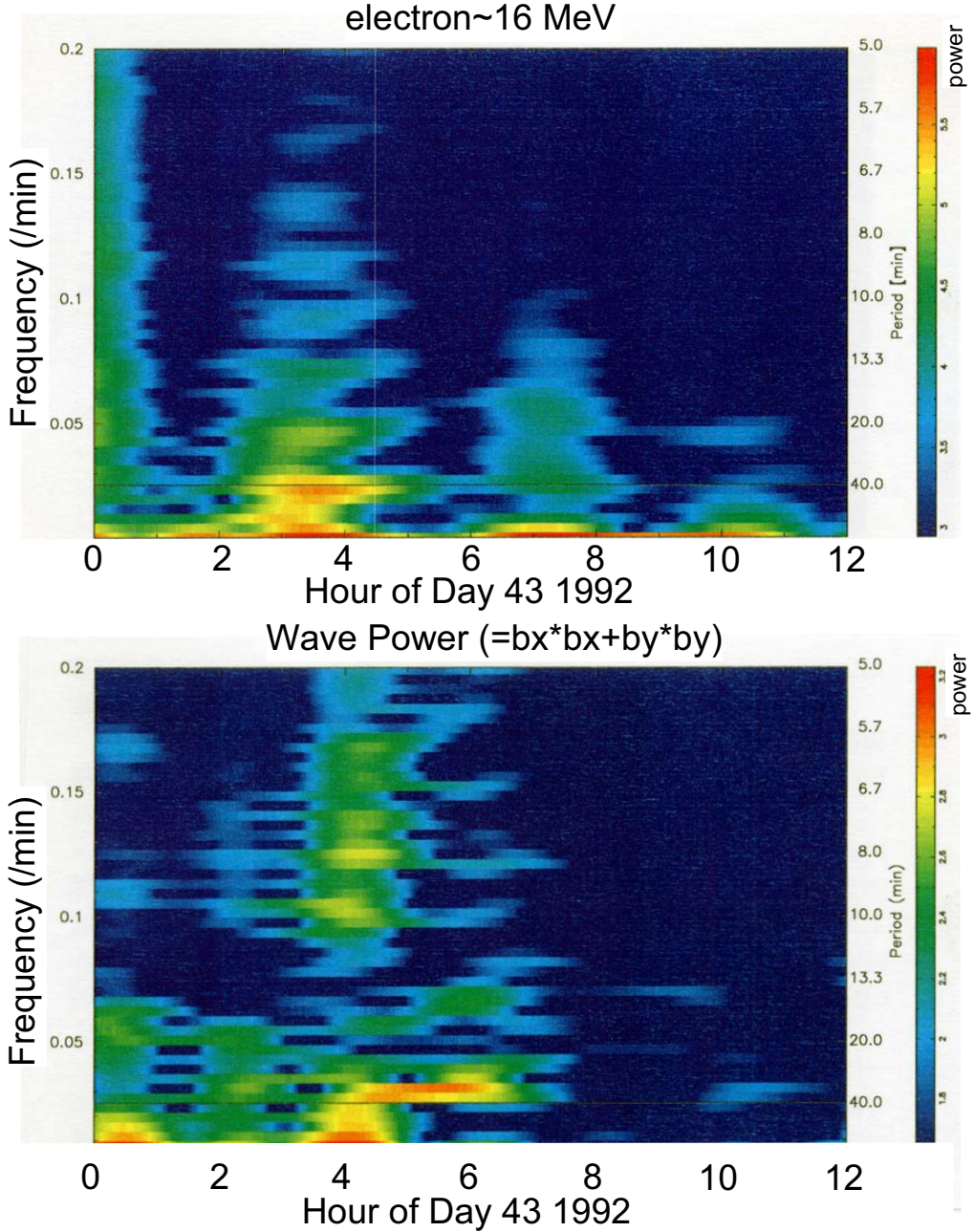


**Figure 6.40:** Dynamic spectra of the magnetic perturbation fields and relativistic electron count rates observed by Ulysses during its first encounter with Jupiter (after Ohgawara, 1999). This event corresponds to that in Figure 1.21 (McKibben et al., 1993), which represents the quasi-periodic electron outbursts accompanying QP radio bursts observed on 12 Feb (Day 43), 1992, when Ulysses was at a distance of  $\sim 75 R_J$  in the southern high latitudinal region (MLAT  $\sim 27^\circ$ ) of the dusk terminator. Top panel is the dynamic spectra of electron count rates in an energy range of  $>16$  MeV observed by COSPIN onboard Ulysses. Bottom panel shows the spectra of  $b_x^2 + b_y^2$  of the magnetic perturbation fields in field-aligned coordinates observed by FGM/VHM. Horizontal axes show the time from 0 h on Day 43, and vertical axes show frequencies. Colors show the spectral powers of the magnetic fields and electron count rates.

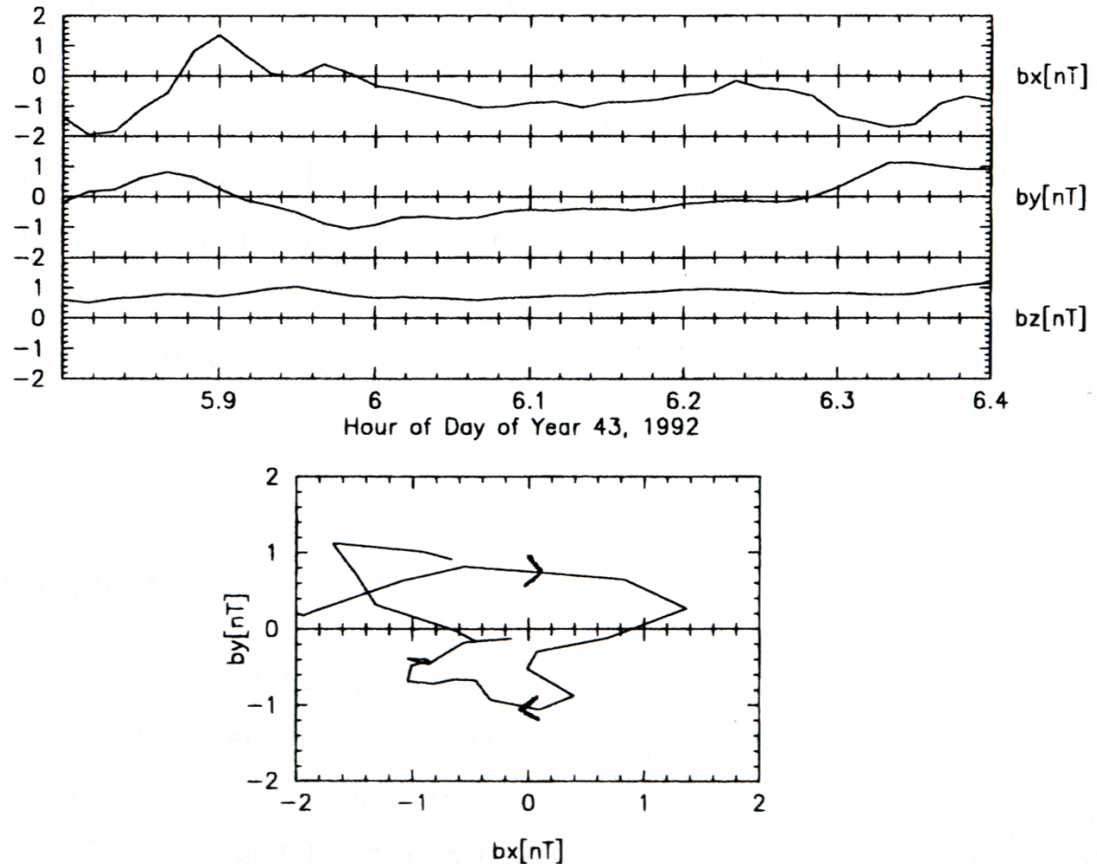


**Figure 6.41:** Hodograph of the perturbation field vector at 5.8–6.4 h on 12 Feb (Day 43), 1992 (after Ohgawara, 1999), corresponding to the same event in Figure 1.21 and 6.40.  $b_x$ ,  $b_y$ , and  $b_z$  components in field-aligned coordinates are plotted in top panel. Bottom panel depicts the hodograph showing the polarization of the magnetic perturbation field vector in the  $x$ - $y$  plane of field-aligned coordinates.

- Can the K-H instabilities become the energy source for the Alfvén waves in the FLR scenario ?
- If that's the case, why QP radio bursts are uncorrelated with velocities of the solar wind which drive the K-H instabilities (see Figure 6.29) ?

To solve these problems, it is required to perform thorough observations of particle, wave, and electromagnetic fields with high time resolutions in the polar region where QP phenomena are supposed to be generated (e.g., a few to  $\sim 10 R_J$  altitudes for QP radio bursts). See Chapter 7 for details of the still-outstanding problems and observational requirements to solve them.

### 6.2.3 Brief Summary

In this section, we proposed two possible scenarios for the relativistic particle acceleration process of the quasi-periodic phenomena. The two scenarios were examined based on *in-situ* and remote observations of plasma, magnetic field, and wave data performed by Galileo and Ulysses.

One of the scenarios is the “flux transfer event (FTE) scenario” where field aligned currents are generated above the cusp region via intermittent reconnections (Figure 6.25), and another one is the “field line resonance (FLR) scenario” where global standing Alfvén waves at eigenfrequencies, which are generated along source field lines at the magnetospheric boundary, are accompanied with periodic field aligned accelerations (Figure 6.36).

The FTE scenario was examined in two ways: analyses of magnetic field in the boundary normal coordinate at the magnetopause and those of QP bursts’ response to some solar wind parameters (i.e., magnetic fields of the IMF, dynamic pressure, reconnection voltage, and solar wind velocity). From these analyses, we confirmed that

1. FTE signals at Jupiter’s magnetopause were not accompanied with similar periodic features to the QP phenomena (Figure 6.27)

2. QP bursts do not respond significantly to any solar wind parameters compared with the other radio components (Figure 6.29 and Table 6.3)

Thus, it was concluded that

3. The FTE scenario is not feasible for the relativistic particle acceleration process of QP phenomena

The FLR scenario was investigated based on the *in-situ* magnetic field data in the middle and outer magnetospheres. The results indicated that

4. Linear Alfvén waves with a period of tens of minutes were found to be propagating in quasi-parallel with field lines in the middle magnetosphere (Figure 6.39).
5. The Alfvén waves are possibly propagating to the polar region accompanied with the relativistic electron outbursts and QP radio bursts (Figures 6.40 and 6.41)

Thus, we concluded that

6. The Alfvén waves propagating between the equatorial and polar region could be a generator of QP accelerations in the Jovian polar region

However, some problems are still outstanding in the FLR scenario of the quasi-periodic particle accelerations:

- Why is “40-minutes period” selected as the periodicity of the QP phenomena while there exist multiple periods in the equatorial region ?
- Can the Alfvén waves possess sufficient energy to accelerate particles up to relativistic energies ?
- Can the K-H instabilities become the energy source for the Alfvén waves ?
- Why QP radio bursts are uncorrelated with velocities of the solar wind which drive the K-H instabilities (see Figure 6.29) ?

# Chapter 7

## Summary and Conclusions

### 7.1 Summary and Conclusions

This thesis addressed the propagation and generation processes of quasi-periodic radio bursts, which are possibly relevant to the periodic particle acceleration process in the Jovian polar region. We also discussed the magnetospheric dynamics responsible for the particle acceleration process based on the radio emission studies.

#### Occurrence Characteristics

In Chapter 3, occurrence characteristics of QP bursts were investigated based on the wave data observed by Ulysses at the northern high latitudes and Galileo at the low latitudes. It was indicated that the occurrence probabilities of QP bursts have dependence on geometric parameters (latitudes, longitudes, and radial distance):

1. QP bursts are frequently observed in the northern latitudinal ranges ( $+30^\circ$  to  $\sim +90^\circ$ )
2. QP bursts are excited in a particular rotational phase (SSL= $90^\circ$ – $300^\circ$  at the high latitudes and  $300^\circ$ – $480^\circ$  at the low latitudes), corresponding to the so-called “clock modulations” which are internally driven in a particular rotational phase with a similar manner to the phenomena found in Saturn’s magnetosphere (Figures 3.3 and

3.4)

3. QP bursts have the “shadow zone” ( $<30 R_J$  at  $|MLAT| < 10^\circ$ )

Statistics based on the Lomb-Scargle analysis presented the remarkable characteristic of QP bursts’ periodicity:

4. The period of “ $\sim 40$  min” is the most dominant in amplitudes at all latitudes, which is possibly the key periodicity for QP bursts and relevant phenomena

## **Polarization Properties**

In Chapter 4, polarization properties and source directions of QP bursts were investigated based on the wave data observed by Ulysses at the northern high latitudes and Cassini at the low latitudes. It was indicated that:

1. QP bursts observed at the northern high latitudes are LH circular polarized waves ( $V = +0.7 \text{--} +0.8$ ,  $Q = 0 \text{--} +0.4$ , and  $U = 0 \text{--} +0.2$ )
2. QP bursts observed at the low latitudes are statistically LH circular polarized ( $V = 0 \text{--} 0.6$ ,  $Q, U \sim 0$ )
3. Power of QP bursts observed by Cassini are dependent on SSL in the same manner as those observed by Galileo (SSL=300°–480°)
4. Apparent directions of QP bursts observed by Cassini are significantly more distant from Jupiter ( $\sim 50 R_J$ ) than the  $f_p$  and  $f_c$  surfaces

## **Interpretation of the Observations Based on the Ray Tracing**

In Chapter 5, the observation results in Chapters 3 and 4 were interpreted based on the ray tracing analysis, and we discussed the source location, directivity, and propagation process of QP bursts observed at the high and low latitudes. The parametric surveys comparing with the observations at the high latitudes suggested that:

1. QP bursts observed at the high latitudes have the source region located at  $f_p$  surface ( $1.3\text{--}1.4 R_J$ ) along high-latitudinal field lines
2. QP bursts observed at the northern high latitudes are L-O mode waves with significantly broadened beaming patterns like a “filled cone”
3. QP bursts at the high latitudes are generated during a particular rotational phase ( $\text{SSL}=90^\circ\text{--}300^\circ$ )

On the other hand, the ray tracing performed for QP bursts observed at the low latitudes suggested that:

4. QP bursts observed in the equatorial region are emitted from the  $f_{RX}$  surface ( $\sim 10\text{--}20 R_J$ ) along high-latitudinal field lines ( $L > \sim 20$ )
5. QP bursts observed at the low latitudes would have ‘a ‘filled cone’’ like beaming angles emitted from the restricted L-value range

Those results were interpreted as meaning that:

6. QP bursts have two kinds of sources: one has higher altitudes ( $f_{RX}$  surface) emitting R-X mode waves and the other has lower altitudes ( $f_p$  surface) emitting L-O mode waves

Based on the ray tracing with the magnetosheath plasma model, we reinterpreted the direction finding results by Cassini were resulted from the following causes:

- QP bursts from the polar region were scattered and reached to the apparent altitudes ( $\sim 50 R_J$ ) by the local density fluctuations in the magnetosheath and interplanetary space

and/or,

- QP bursts have the real source region in the magnetosheath

## **Microscopic Generation of Quasi-Periodic Bursts**

In Section 6.1, we proposed two possible scenarios for the microscopic generation mechanism of QP bursts (the “direct generation scenario” and “indirect generation scenario”) and examined these scenarios based on the theoretical approaches.

The growth rate calculations were performed to examine the direct generation scenario at low ( $\sim 2 R_J$ ) and high ( $\sim 10 R_J$ ) source altitudes. The results suggested that:

1. The relativistic ring beams can generate significant O mode free-space waves with broad beaming patterns at high source altitudes
2. Free-space X mode waves are not excited effectively by the relativistic electron beams
3. The excited O mode waves could propagate similarly to those of the R-X mode waves as indicated in Section 5.3, forming the observed shadow zone
4. Frequency range of the O mode waves is narrow at the source altitudes
5. Broadband QP bursts in O mode are emitted from the source flux tube if the ring beams maintain their instabilities along the flux tube
6. Free-space O mode waves are also excited at low altitudes with similar characteristics to those at high altitudes

The growth rate calculation under conditions of the magnetosheath revealed that:

7. Both of the direct and indirect processes are unreasonable in the magnetosheath

Thus, we interpreted the direction finding by Cassini in Section 5.4 as the following causes:

8. QP bursts from the polar region were scattered and reached to the high apparent altitudes ( $\sim 50 R_J$ ) by the local density fluctuations in the magnetosheath and interplanetary space

We examined the indirect generation scenario referring to the previous theoretical study. It was concluded that the following mode conversion scenario is possible at low and high source altitudes:

9. Z mode waves propagating toward Jupiter are excited at low and high altitudes via the cyclotron resonance induced by the parallel or ring beams
10. The Z mode waves are converted to free-space O mode waves at the density boundary where  $f \sim f_p$

## **Macroscopic Generation of QP Phenomena**

In Section 6.2, we proposed two possible scenarios for the relativistic particle acceleration process of the quasi-periodic phenomena (the “flux transfer event (FTE) scenario” and “field line resonance (FLR) scenario”). The two scenarios were examined based on *in-situ* and remote observations of plasma, magnetic field, and wave data performed by Galileo and Ulysses.

The FTE scenario was examined based on observations of magnetic fields, solar wind, and QP bursts. We confirmed that

1. FTE signals at Jupiter’s magnetopause were not accompanied with periodic features similar to the QP phenomena
2. QP bursts do not respond significantly to any solar wind parameters compared with the other radio components

Thus, it was concluded that

3. The FTE scenario is not feasible for the relativistic particle acceleration process of QP phenomena

The FLR scenario was investigated based on the *in-situ* magnetic field data in the middle and outer magnetospheres. The results indicated that

4. Linear Alfvén waves with a period of tens of minutes were found to be propagating quasi-parallel with the background field lines in the middle magnetosphere
5. The Alfvén waves are possibly propagating to the polar region accompanied with the relativistic electron outbursts and QP radio bursts

Thus, we concluded that

6. The Alfvén waves propagating between the equatorial and polar region could be a generator of QP accelerations in the Jovian polar region

## **Picture of QP Phenomena**

From these conclusions, this thesis proposes a picture of generation process for the Jovian quasi-periodic phenomena as shown in Figure 7.1. The QP phenomena could be excited in the following sequence: (a) Alfvén waves propagating toward the polar region are excited by the clock like disturbances, which are initiated once a rotation by internal processes of the Jovian magnetosphere such as the Vasyliunas cycle, (b) field aligned electric fields of the Alfvén waves accelerate particles (electrons, protons, and heavy magnetospheric ions) upward and downward with a period of “~40 min”, followed by the relativistic particle outbursts and precipitations, (c) multispectral auroras (X-ray, UV, and IR) and Z mode waves are excited in the polar region by the energetic particles, and finally, (d) free-space L-O mode waves are converted from the downward Z mode waves and are also excited directly from the electron outbursts. The excited free-space waves are QP radio bursts, which propagate toward high and low latitudes with circular polarization, and those at low frequencies are scattered by the magnetosheath and interplanetary medium.

## **7.2 Open Issues and Requirements**

There still remain some unsolved problems to justify the picture of the Jovian QP phenomena:

- What internal disturbance initiates the Alfvén waves ?
- Why is “40-minutes period” selected as the periodicity of the QP phenomena while there exist multiple periods in the equatorial region ?

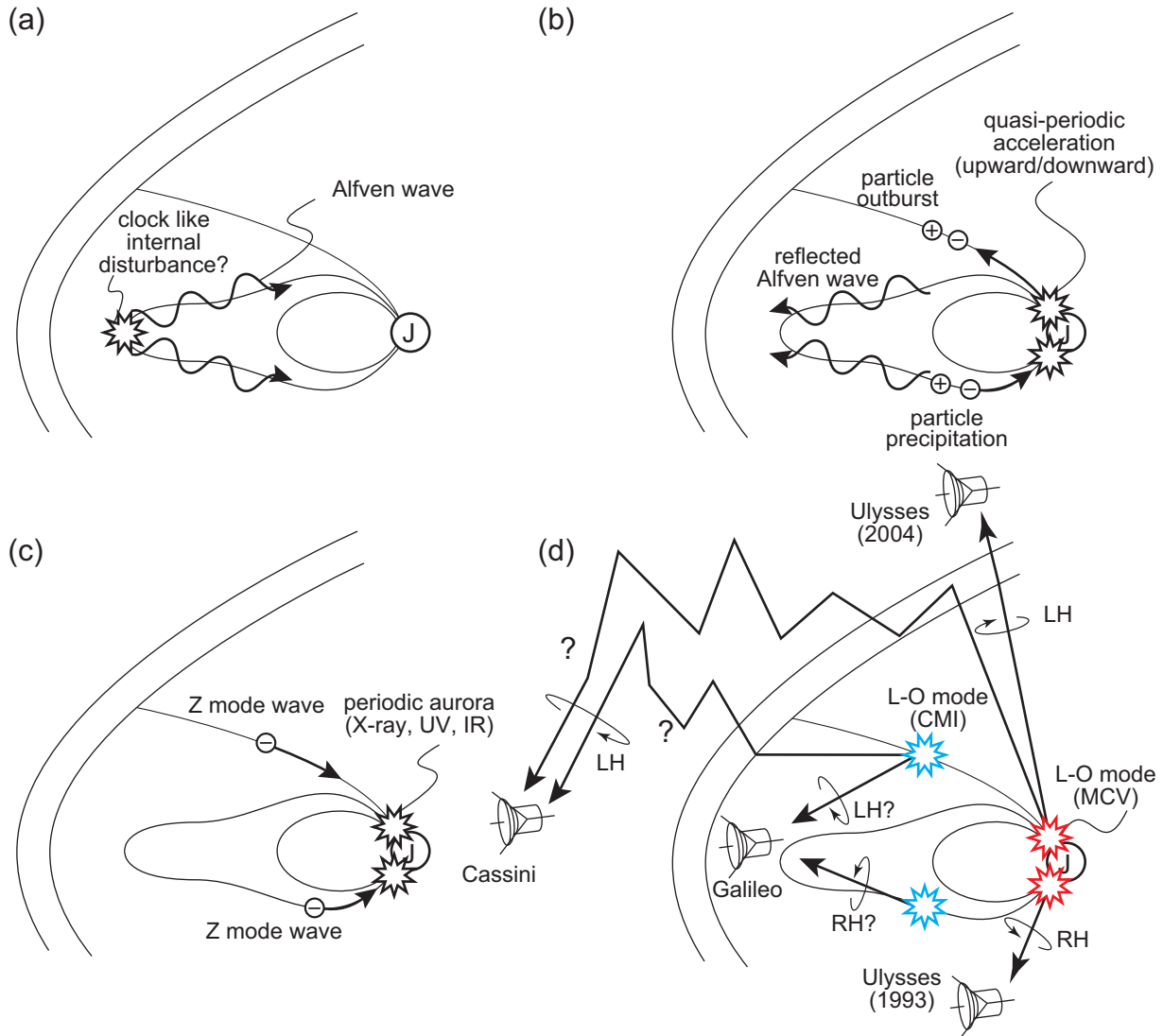


**Figure 7.1:** A picture of Jovian quasi-periodic phenomena obtained by this thesis. (a) Clock like internal disturbances initiate Alfvén waves propagating toward the polar region. (b) Alfvén waves accelerate particles (electrons, protons, and heavy magnetosospheric ions) upward and downward with periods of a few to tens of minutes, followed by the relativistic particle outbursts and precipitations. (c) Multispectral auroras (X-ray, UV, and IR) and Z mode waves are excited in the polar region by the energetic particles. (d) Free-space L-O mode waves are converted from the downward Z mode waves (denoted MCV) and are also excited directly from the electron outbursts (denoted CMI). The excited free-space waves are QP radio bursts, which propagate toward high and low latitudes with circular polarization, and those at low frequencies are scattered by the magnetosheath and interplanetary medium.

- Can the Alfvén waves possess sufficient energy to accelerate particles up to relativistic energies ?
- Can the K-H instabilities become the energy source for the Alfvén waves ?
- Why QP radio bursts are uncorrelated with velocities of the solar wind which drive the K-H instabilities ?
- Which is more significant, directly-generated L-O mode waves or indirectly-generated L-O mode waves ?

Some additional studies are necessary to solve these problems: e.g., numerical simulations for the interactions between energetic particles and wave electromagnetic fields. The simulations solve electromagnetic fields induced by the relativistic electrons, which are energized by periodically-varying parallel electric fields relevant to Alfvén waves. This approach is expected to associate physical properties of the electron outbursts with the Alfvén waves and QP radio bursts quantitatively. The source simulations and ray tracing analyses can achieve comprehensive numerical modelings for generation and propagation of QP bursts and other planetary radio emissions.

Finally, this thesis proposes observational requirements to solve the problems. The observations should be performed by multi-spacecraft exploration with a full set of equipments. Hereafter, we suppose two spacecraft in two kinds of orbital regimes.

One regime is termed the “polar regime” where spacecraft #1 performs *in-situ* and remote observations around the magnetopause and cusp region at high latitudes, and spacecraft #2 performs observations in the polar region at the magnetic footprint of spacecraft #1. Based on these observations, we further investigate the FTE scenario, relating the accelerations and field aligned currents in the polar region to reconnection processes at the cusp and magnetopause.

The other regime is termed the “equatorial regime” where spacecraft #1 performs *in-situ* and remote observations in the equatorial distant tail region where the x-lines of the Vasyliunas cycle are possibly initiated, and spacecraft #2 observes in the polar region at

the magnetic footprint of the x-lines. The FLR scenario is investigated by this regime, relating the Alfvén waves accompanied with the QP phenomena in the polar region to the clock like internal disturbance in the magnetosphere.

In both regimes, spacecraft #2 is supposed to be performing *in-situ* observations in the source region of the periodic particle accelerations and/or QP radio bursts. This observations reveal the generation mechanisms of QP radio bursts directly.

Equipments of these spacecraft require high specifications for complete observations to solve the problems. This thesis requires a particle detector with energy ranges from cold components to more than 10 MeV because mean energies of the periodic electron outbursts could be around 10 MeV. Energy resolutions of the detector  $\delta E/E$  should be  $\sim 1$  MeV/10 MeV, that is 10 % at  $E \sim 10$  MeV, where growth rates of QP bursts are significantly dependent on mean energies of the electron beams (e.g., see Figures 6.3 and 6.5). Pitch angle resolutions  $\delta\theta$  are estimated to be less than  $\sim \arctan(u_{\perp 0}/u_{\parallel 0}) \sim \arctan(4\text{MeV}/16\text{Mev}) \sim 14^\circ$  to resolve the characteristics of ring and parallel beams which can generate intense free-space waves (e.g., Figure 6.9). We also require ion mass spectrometers which can resolve the magnetospheric heavy ions (O, S) for direct detections of the source particles responsible for the X-ray hot spot.

Magnetometer should have comparable capabilities to those onboard Galileo or Cassini. It measures three-dimensional field components with high time resolutions (e.g., less than 24 sec in the survey mode).

We need specifications of a wave experiment which are comparable to those of the RPWS. The experiment is required to measure electric fields in a frequency range from direct-current to more than 16 MHz (higher than the maximum frequency of DAM) with capabilities for the three-dimensional direction finding and polarization measurement. Time resolution should be comparable to that of the RPWS (0.1 to 10 sec per one complete spectrum). The experiment is also required to measure a set of magnetic and electric fields at low frequencies to detect Poynting flux of the Alfvén waves.

Remote imaging and spectroscopy for the auroral emissions are need to be performed in multispectral wavelengths. Simultaneous imaging in X-ray, UV, and IR with high time resolutions (less than a few minutes) is expected to detect coincidence of the hot spots in multispectral wavelength. This observation directly reveals the source field lines of QP phenomena which are possibly connected to the cusp, distant tail, or other regions. In addition, spectroscopy in each wavelength provides further information on compositions and characteristic energies of the each kind of precipitating particles (heavy ions, protons, and electrons).

These observational requirements are summarized in Table 7.1.

**Table 7.1:** Observational requirements proposed by the present thesis

Orbital regime		
regime	S/C #1	S/C #2
polar regime	cusp and magnetopause at high lat.	polar region
equatorial regime	distant tail region	polar region
Specifications of equipments		
equipment	specifications	
particle detector	energy range from cold to $\sim 10$ MeV (electron) $\delta E/E \sim 10\%$ at $E \sim 10$ MeV (electron) $\delta\theta \sim \arctan(u_{\perp 0}/u_{\parallel 0}) \sim 14^\circ$ (electron) ion mass spectrometer	
magnetometer	three-dimensional components with high time resolution (e.g., <24 sec)	
wave experiment	frequency range from DC to more than 16 MHz direction finding and polarization high time res. (0.1 to 10 sec per spectrum) Poynting flux measurement	
imaging and spectroscopy	multispectral imaging (X-ray, UV, IR) spectroscopy in each wavelength high time res. (less than a few minutes)	



# References

- Akasofu, S.-I., The interaction between a magnetized plasma flow and a magnetized celestial body: a review of magnetospheric studies, *Space Sci. Rev.*, **21**, 489–526, 1978.
- Andrews, D. J., E. J. Bunce, S. W. H. Cowley, M. K. Dougherty, G. Provan, and D. J. Southwood, Planetary period oscillations in Saturn's magnetosphere: Phase relation of equatorial magnetic field oscillations and Saturn kilometric radiation modulation, *J. Geophys. Res.*, **113**, A09205, 2008.
- Baker, G. J., E. F. Donovan, and B. J. Jackel, A comprehensive survey of auroral latitude Pc5 pulsation characteristics, *J. Geophys. Res.*, **108**, 1384, 2003.
- Baldwin, D. E., I. B. Bernstein, and M. P. H. Weenink , Kinetic Theory of Plasma Waves in a Magnetic Field, in *Advances in Plasma Physics*, Ed. A. Simon, Interscience Publishers, 1969.
- Balogh, A., T. J. Beek, R. J. Forsyth, P. C. Hedgecock, R. J. Marquedant, E. J. Smith, D. J. Southwood, and B. T. Tsurutani, The magnetic field investigation on the Ulysses mission: instrumentation and preliminary scientific results, *Astron. Astrophys. Suppl. Ser.*, **92**, 221–236, 1992.
- Bame, S. J., D. J. McComas, B. L. Barraclough, J. L. Phillips, K. J. Sofaly, J. C. Chavez, B. E. Goldstein, and R. K. Sakurai, The Ulysses solar wind plasma experiment, *Astron. Astrophys. Suppl. Ser.*, **92**, 237–265, 1992.
- Bunce, E. J., S. W. H. Cowley, and T. K. Yeoman, Jovian cusp process: Implications for

- the polar aurora, *J. Geophys. Res.*, **109**, A09S13, 2004.
- Carbary, J. F., Mitchell, D. G., Brandt, P., Paranicas, C., Krimigis, S. M., ENA periodicities at Saturn. *Geophys. Res. Lett.*, **35**, L07102, 2008.
- Carbary, J. F., Mitchell, D. G., Krimigis, S. M., Hamilton, D. C., Krupp, N., Charged particle periodicity in Saturn's outer magnetosphere, *J. Geophys. Res.*, **112**, A06246, 2007.
- Carbary, J. F., S. M. Krimigis, D. G. Mitchell, C. Paranicas, P. Brandt, Energetic neutral atom (ENA) and charged particle periodicities in Saturn's magnetosphere, *Adv. Space Res.*, **44**, 483–493, 2009.
- Cecconi, B., and P. Zarka , Model of a variable radio period for Saturn, *J. Geophys. Res.*, **110**, A12203, 2005.
- Chen, Y. P., Zhou, G. C., Yoon, P. H., and Wu, C. S., A beam-maser instability: Direct amplification of radiation, *Phys. Plasmas*, **9**, 2816, 2002.
- Clarke, J. T., D. Grodent, S. W. H. Cowley, E. J. Bunce, P. Zarka, J. E. P. Connerney, and T. Satoh, Jupiter's aurora, in *Jupiter*, edited by F. Bagenal, T. E. Dowling, and W. B. McKinnon, Cambridge University Press, 639–670, 2004.
- Connerney, J. E. P., M. H. Acuña, N. F. Ness, and T. Satoh, New models of Jupiter's magnetic field constrained by the Io flux tube footprint, *J. Geophys. Res.*, **103**, 11929–11939, 1998.
- Cowley, S. W. H. and E. J. Bunce, Origin of the main auroral oval in Jupiter's coupled magnetosphere-ionosphere system, *Planet. Space Sci.*, **49**, 1067–1088, 2001.
- Cowley, S. W. H., The causes of convection in the Earth's magnetosphere: a review of developments during the IMS, *Rev. Geophys. and Space Phys.*, **20**, 531–565, 1982.
- Cravens, T. E., J. H. Waite, T. I. Gombosi, N. Lugaz, G. R. Gladstone, B. H. Mauk, and R. J. MacDowall, Implications of Jovian X-ray emission for magnetosphere-ionosphere coupling, *J. Geophys. Res.*, **108**, A12, 1465, 2003.

- Divine, N., and H. B. Garrett, Charged particle distributions in Jupiter's magnetosphere, *J. Geophys. Res.*, **88**, 6889–6903, 1983.
- Elsner, R. F., N. Lugaz, J. H. Waite Jr., T. E. Cravens, G. R. Gladstone, P. Ford, D. Grodent, A. Bhardwaj, R. J. MacDowall, M. D. Desch, and T. Majeed, Simultaneous Chandra X ray, Hubble Space Telescope ultraviolet, and Ulysses radio observations of Jupiter's aurora, *J. Geophys. Res.*, **110**, A01207, 2005.
- Flasar, F. M., et al., An intense stratospheric jet on Jupiter, *Nature*, **427**, 132–135, 2004.
- Gladstone, G. R., J. H. Waite Jr., D. Grodent, W. S. Lewis, F. J. Crary, R. F. Elsner, M. C. Weisskopf, T. Majeed, J.-M. Jahn, A. Bhardwaj, J. T. Clarke, D. T. Young, M. K. Dougherty, and S. A. Espinosa, A pulsating auroral X-ray hot spot on Jupiter, *Nature*, **415**, 1000–1003, 2002.
- Goldreich, P., and J. Farmer, Spontaneous axisymmetry braking of the external magnetic field at Saturn, *J. Geophys. Res.*, **112**, A05225, 2007.
- Grodent, D., J.-C. Gérard, J. T. Clarke, G. R. Gladstone, and J. H. Waite Jr., A possible auroral signature of a magnetotail reconnection process on Jupiter, *J. Geophys. Res.*, **109**, A05201, 2004.
- Gurnett et al., THE CASSINI RADIO AND PLASMAWAVE INVESTIGATION, *Space Sci. Rev.*, **114**, 396–463, 2004.
- Gurnett, D. A., A. M. Persoon, W. S. Kurth, J. B. Groene, T. F. Averkamp, M. K. Dougherty, and D. J. Southwood, The variable rotation period of the inner region of Saturn 's plasma disk, *Science*, **316**, 442–445, 2007.
- Gurnett, D. A., Shawhan, S. D., and Shaw, R. R., Auroral hiss, Z mode radiation, and auroral kilometric radiation in the polar magnetosphere — DE 1 observations, *J. Geophys. Res.*, **88**, 329–340, 1983.
- Gurnett, D. A., W. S. Kurth, R. R. Shaw, A. Roux, R. Gendrin, C. F. Kennel, F. L. Scarf, and S. D. Shawhan, The Galileo plasma wave investigation, *Space Sci. Rev.*, **60**, 341–355, 1992.

- Hanasz, J., H. de Feraudy, R. Schreiber, and M. Panchenko, Pulsations of the auroral kilometric radiation, *J. Geophys. Res.*, **111**, A03209, 2006.
- Hilgers, A., The auroral radiating plasma cavities, *Geophys. Res. Lett.*, **19**, 237–240, 1992.
- Hill, T. W., Inertial limit on corotation, *J. Geophys. Res.*, **84**, 6554–6558, 1979.
- Hoang, S., Meyer-Vernet, N., Bougeret, J.-L., Harvey, C.C., Lacombe, C., Mangeney, A., Moncuquet, M., Perche, C., Steinberg, J.-L., MacDowall, R.J., Stone, R.G., Solar wind thermal electrons in the ecliptic plane between 1 and 4 AU: preliminary results from the Ulysses radio receiver, *Geophys. Res. Lett.*, **19**, 1295–1298, 1992.
- Horne, J. H., and S. L. Baliunas, A prescription for period analysis of unevenly sampled time series, *ApJ*, **302**, 757–763, 1986.
- Hospodarsky, G. B., W. S. Kurth, B. Cecconi, D. A. Gurnett, M. L. Kaiser, M. D. Desch, and P. Zarka, Simultaneous observations of Jovian quasi-periodic radio emissions by the Galileo and Cassini spacecraft, *J. Geophys. Res.*, **109**, A09S07, 2004.
- Iizima, M., Generation and Propagation of Electro-Magnetic Waves Relation to Mode Conversion Processes in Cosmical Plasma., *Ph.D. thesis*, Tohoku University, 1988.
- Jones, D., Mode-coupling of Z-mode waves as a source of Terrestrial kilometric and Jovian decametric radiations, *Astron. and Astrophys.*, **55**, 245–252, 1977.
- Kaiser, M. L., M. D. Desch, and W. M. Farrell, Clock-like behavior of Jovian continuum radiation, *Planet. Space Sci.*, **41**, 1073–1077, 1993b.
- Kaiser, M. L., P. Zarka, W. S. Kurth, G. B. Hospodarsky, and D. A. Gurnett, Cassini and Wind stereoscopic observations of Jovian nonthermal radio emissions: Measurement of beam widths, *J. Geophys. Res.*, **105**, 16,053–16,062, 2000.
- Kaiser, M. L., Time-variable magnetospheric radio emissions from Jupiter, *J. Geophys. Res.*, **98**, 18,757–18,765, 1993.
- Kaiser, M. L., W. M. Farrell, M. D. Desch, G. B. Hospodarsky, W. S. Kurth, and D.

- A. Gurnett, Ulysses and Cassini at Jupiter: Comparison of the quasi-periodic radio bursts, in *Planetary Radio Emissions V*, 41–48, 2001.
- Khurana, K. K., Euler potential models of Jupiter's magnetospheric field, *J. Geophys. Res.*, **102**, 11,295–11,306, 1997.
- Khurana, K. K., Influence of solar wind on Jupiter's magnetosphere deduced from currents in the equatorial plane, *J. Geophys. Res.*, **106**, 25999–26016, 2001.
- Khurana, K. K., M. G. Kivelson, V. M. Vasyliunas, N. Krupp, J. Woch, A. Lagg, B. H. Mauk, and W. S. Kurth, The configuration of Jupiter's magnetosphere, in *Jupiter*, edited by F. Bagenal, T. E. Dowling, and W. B. McKinnon, Cambridge University Press, 593–616, 2004.
- Khurana, K. K., and M. G. Kivelson, Ultralow frequency MHD waves in Jupiter's magnetosphere, *J. Geophys. Res.*, **94**, 5241–5254, 1989.
- Kimura, T., F. Tsuchiya, H. Misawa, A. Morioka, and H. Nozawa, Occurrence statistics and ray tracing study of Jovian quasi-periodic radio bursts observed from low latitudes, *J. Geophys. Res.*, in press, 2009.
- Kimura, T., F. Tsuchiya, H. Misawa, A. Morioka, and H. Nozawa, Occurrence and source characteristics of the high-latitude components of Jovian broadband kilometric radiation, *Planetary and Space Sci.*, **56**, 1155–1168, 2008a.
- Kimura, T., F. Tsuchiya, H. Misawa, A. Morioka, and H. Nozawa, Radiation characteristics of quasi-periodic radio bursts in the Jovian high-latitude region, *Planetary and Space Sci.*, **56**, 1967–1976, 2008b.
- Kivelson, M. G., K. K. Khurana, J. D. Means, C. T. Russell, and R. C. Snare, The Galileo magnetic field investigation, *Space Sci. Rev.*, **60**, 357–383, 1992.
- Kivelson, M. G., and C. T. Russell, A brief history of solar-terrestrial physics, in *Introduction to space physics*, Cambridge University Press, 1995.
- Knight, S., Parallel electric fields, *Planet. Space Sci.*, **21**, 741–750, 1973.

- Koen, C., Significance testing of periodogram ordinates, *ApJ*, **348**, 700–702, 1990.
- Kraus, J. D., Chapter 4. Wave polarization, in *Radio astronomy* (2nd edition), Cygnus-Quasar Books, 1982.
- Krupp, N., J. Woch, A. Lagg, B. Wilken, S. Livi, and D. J. Williams, Energetic particle bursts in the predawn jovian magnetotail, *Geophys. Res. Lett.*, **25**, 1249–1253, 1998.
- Krupp, N., V. M. Vasyliunas, J. Woch, A. Lagg, K. K. Khurana, M. G. Kivelson, B. H. Mauk, E. C. Roelof, D. J. Williams, S. M. Krimigis, W. S. Kurth, L. A. Frank, W. R. Paterson, Dynamics of the Jovian magnetosphere, in *Jupiter*, edited by F. Bagenal, T. E. Dowling, and W. B. McKinnon, Cambridge University Press, 617–638, 2004.
- Kunde, V. G., et al., Jupiter's Atmospheric Composition from the Cassini Thermal Infrared Spectroscopy Experiment, *Science*, **305**, 1582, 2004.
- Kurth, W. S., Continuum radiation in planetary magnetospheres, Rucker, H. O., Bauer, S. J., Kaiser, M. L. (Eds.), *Planetary Radio Emissions*, III, Austrian Academic Science Press, Vienna, Austria, 329–350, 1992b.
- Kurth, W. S., Gurnett, D. A. and Scarf, F. L., Jovian type III bursts. *J. Geophys. Res.*, **94**, 6917–6924, 1989.
- Lacombe, C., Harvey, C. C., Hoang, S., Mangeney, A., Steinberg, J. -L., Burgess, D., ISEE observations or radiation at twice the solar wind plasma frequency., *Ann. Geophysicae*, **6**, 113–128, 1988.
- Lacombe, C., Steinberg, J. -L., Harvey, C. C., Hubert, D., Moncuquet, M., Density Buctuations measured by ISEE 1-2 in the Earth's magnetosheath and the resultant scattering of radio waves, *Ann. Geophysicae*, **15**, 387–396, 1997.
- Ladreiter, H. P., P. Zarka, A. Lecacheux, W. Macher, H. O. Rucker, R. Manning, D. A Gurnett, and W. S. Kurth, Analysis of electromagnetic wave direction finding performed by spaceborne antennas using singular-value decomposition techniques, *Radio Sciencce*, **30**, 1699-1712, 1995.

- Ladreiter, H. P., P. Zarka, and A. Lecacheux, Direction finding study of Jovian hectometric and broad kilometric radio emissions: evidence for their auroral origin, *Planet. Space. Sci.*, **42**, 919–931, 1994.
- Ladreiter, H. P., and Y. Leblanc, Modeling of the Jovian hectometric radiation: a three-dimensional study, *Ann. Geo.*, **8**, 477–488, 1990b.
- Ladreiter, H. P., and Y. Leblanc, Prediction of the Ulysses Jovian hectometric observations, *J. Geophys. Res.*, **96**, 21,207–21,212, 1991.
- Ladreiter, H. P., and Y. Leblanc, Source location of the Jovian hectometric radiation via ray-tracing technique, *J. Geophys. Res.*, **95**, 6423–6435, 1990a.
- Lee, L. C., C. S. Wu, H. P. Freund, D. Dillenburg, and J. Goedert, Excitation of high-frequency waves with mixed polarization by streaming energetic electrons, *J. Plasma Phys.*, **22**, 277–288, 1979.
- Louarn., P., B. H. Mauk, M. G. Kivelson, W. S. Kurth, A. Roux, C. Zirnmer, D. A. Gurnett, and D. J. Williams, A multi-instrument study of a jovian magnetospheric disturbance, *J. Geophys. Res.*, **106**, 29883–29898, 2001.
- MacDowall, R. J., M. L. Kaiser, M. D. Desch, W. M. Farrell, R. A. Hess, and R. G. Stone, Quasiperiodic Jovian radio bursts: observations from the Ulysses Radio and Plasma Wave Experiment, *Planet. Space. Sci.*, **41**, 1059–1072, 1993.
- McKibben, R. B., J. A. Simpson, and M. Zhang, Impulsive bursts of relativistic electrons discovered during Ulysses' traversal of Jupiter's dusk-side magnetosphere, *Planet. Space. Sci.*, **41**, 1041–1058, 1993.
- Morioka, A., H. Nozawa, H. Misawa, F. tsuchiya, Y. Miyoshi, T. Kimura, and W. Kurth, Rotationally driven quasi-periodic radio emissions in the Jovian magnetosphere, *J. Geophys. Res.*, **111**, A04223, 2006.
- Morioka, A., T. Yuasa, Y. S. Miyoshi, F. Tsuchiya, and H. Misawa, Source characteristics and radiation mechanism of Jovian anomalous continuum, *J. Geophys. Res.*, **109**, A06206, 2004.

- Morioka, A., and F. Tsuchiya, Solar wind control of Jovian electron flux: Pioneer 11 analysis, *Geophys. Res. Lett.*, **23**, 2963–2966, 1996.
- Nakagawa, F., Study on source characteristics of Jovian hectometric radio emissions, *Ph.D. thesis*, Tohoku University, 2001.
- Nishimura, Y., T. Ono, M. Iizima, A. Shinburi, and A. Kumamoto, Generation mechanism of Z-mode waves in the equatorial plasmasphere, *Earth Planets Space*, **59**, 1027–1034, 2007.
- Nosé, M., T. Iyemori, M. Sugiura, J. A. Slavin, R. A. Hoffman, J. D. Winningham, and N. Sato, Electron precipitation accompanying Pc 5 pulsations observed by the DE satellites and at a ground station, *J. Geophys. Res.*, **103**, 17,587–17,604, 1998.
- Nozawa, H., H. Misawa, S. Takahashi, A. Morioka, S. Okano, and R. Sood, Long-term variability of [SII] emissions from the Io plasma torus between 1997 and 2000, *J. Geophys. Res.*, **109**, A07209, 2004.
- Oya, H., Origin of Jovian decameter wave emissions-conversion from the electron cyclotron plasma wave to the ordinary mode electromagnetic wave, *Planet. Space. Sci.*, **22**, 687–708, 1974.
- Prangé, R., G Chagnon, M. G. Kivelson, T. A. Livengood, and W. Kurth, Temporal monitoring of Jupiter's auroral activity with IUE during the Galileo mission. Implications for magnetospheric processes, *Planet. Space. Sci.*, **49**, 405–415, 2001.
- Provan, G., D. J. Andrews, C. S. Arridge, A. J. Coates, S. W. H. Cowley, S. E. Milan, M. K. Dougherty, and D M. Wrigh, Polarization and phase of planetary-period magnetic field oscillations on high-latitude field line in Saturn's magnetosphere, *J. Geophys. Res.*, **114**, A02225, 2009.
- Pryor, W. R., et al., Cassini UVIS observations of Jupiter's auroral variability, *Icarus*, **178**, 312–326, 2005.
- Reiner, M. J., J. Fainberg, R. G. Stone, M. L. Kaiser, M. D. Desch, R. Manning, P. Zarka, and B. -M. Pedersen, Source characteristics of Jovian narrow-band kilometric radio

- emissions. *J. Geophys. Res.*, **98**, 13,163–13,176, 1993.
- Scargle, J. D., Studies in astronomical time series analysis. II. Statistical aspects of spectral analysis of unevenly spaced data, *ApJ*, **263**, 835–853, 1982.
- Schardt, A. W., F. B. McDonald, and J. H. Trainor, Energetic particles in the predawn magnetotail of Jupiter, *J. Geophys. Res.*, **86**, 8413–8428, 1981.
- Slavin, J. A., E. J. Smith, J. R. Spreiter, and S. S. Stahara, Solar wind flow about the outer planets: gas dynamic modeling of the Jupiter and Saturn bow shocks, 1985.
- Sonnerup, B. U. O., and L. J. Chahill, Jr., Magnetopause, structure and attitude from Explorer 12 observations, *J. Geophys. Res.*, **72**, 171–183, 1967.
- Southwood, D. J., Some features of field line resonances in the magnetosphere, *Planet. and Space Sci.*, **22**, 483–491, 1974.
- Southwood, D. J., and M. G. Kivelson, Saturnian magnetospheric dynamics: Elucidation of a camshaft model, *J. Geophys. Res.*, **112**, A12222, 2007.
- Spanswick, E., E. Donovan, and G. Baker, Pc5 modulation of high energy electron precipitation: particle interaction regions and scattering efficiency, *Annales Geophys.*, **23**, 1533–1542, 2005.
- Steinberg, J.-L., Lacombe. C., Zarka, P., et al., Terrestrial low frequency bursts: escape paths of radio waves through the bow shock, *Planet. Space Sci.*, 643–660, 2004.
- Stone, R. G., J. L. Bougeret, J. Caldwell, P. Canu, Y. de Conchy, N. Cornilleau-Wehrlin, M. D. Desch, J. Fainberg, K. Goetz, M. L. Goldstein, C. C. Harvey, S. Hoang, R. Howard, M. L. Kaiser, P. J. Kellogg, B. Klein, R. Knoll, A. Lecacheux, D. Lengyel-Frey, R. J. MacDowall, R. Manning, C. A. Meetre, A. Meyer, N. Monge, S. Monson, G. Nicol, M. J. Reiner, J. L. Steinberg, E. Trres, C. de Villedary, F. Wouters, and P. Zarka, The unified radio and plasma wave investigation, *Astron. Astrophys. Suppl. Ser.*, **92**, 291–316, 1992.
- Vasyliunas, V. M., Plasma distribution and flow, in *Physics of the Jovian Magnetosphere*, A. J. Dessler (ed.), Cambridge University Press, 395–453, 1983.

- Vogl, D. F., et al., In-flight calibration of the Cassini-Radio and Plasma Wave Science (RPWS) antenna system for direction-finding and polarization measurements, *J. Geophys. Res.*, **109**, A09S17, 2004.
- Waite Jr., J. H., et al., An auroral flare at Jupiter. *Nature*, **410**, 787–789, 2001.
- Wilson, R. J., and M. K. Dougherty, Evidence provided by Galileo of Ultra Low Frequency waves within Jupiter's middle magnetosphere, *Geophys. Res. Lett.*, **27**, 835–838, 2000.
- Woch, J., N. Krupp, A. Lagg, B. Wilken, S. Livi, and D. J. Williams, Quasi-periodic modulations of the jovian magnetotail, *Geophys. Res. Lett.*, **25**, 1253–1256, 1998.
- Woodward, R. C., Jr., F. Scherb, F. L. Roesler, and R. J. Oliversen, Periodic intensity variation in sulfur emissions from the Io plasma torus, *Icarus*, **111**, 45–64, 1994.
- Woodward, R. C., Jr., The sulfur emission and periodicity of the Jupiter plasma torus in 1988, *Ph.D. thesis*, University of Wisconsin–Madison, 1992.
- Wright, A. N., W. Allan, M. S. Ruderman, and R. C. Elphic, The dynamics of current carriers in standing Alfvén waves: Parallel electric fields in the auroral acceleration region, *J. Geophys. Res.*, **107**, A7, 1120, 2002.
- Wright, A. N., W. Allan, and P. A. Damiano, Alfvén wave dissipation via electron energization, *Geophys. Res. Lett.*, **30**, 1847, 2003.
- Wu, C. S., C. B. Wang, G. C. Zhou, S. Wang, and P. H. Yoon, Altitude-dependent emission of Type III solar radio bursts, *ApJ*, **621**, 1129–1136, 2005.
- Wu, C. S., Wang, C. B., Yoon, P. H., Zheng, H., and Wang, S., Generation of Type III solar radio bursts in the low corona by direct amplification, *ApJ*, **575**, 1094–1103, 2002.
- Wu, C. S., and L. C. Lee, A theory of the terrestrial kilometric radiation, *Astrophys. J.*, **230**, 621–626, 1979.
- Yoon, P. H., Wu, C. S., and Wang, C. B., Generation of Type III solar radio bursts in the

- low corona by direct amplification II Further numerical study, *ApJ*, **576**, 552–560, 2002.
- Zarka, P., L. Lamy, B. Cecconi, R. Prange, and H. O. Rucker, Modulation of Saturn's radio clock by solar wind speed, *Nature*, **450**, 265–267, 2007.
- Zarka, P., Radio and plasma waves at the outer planets, *Adv. Space Res.*, **433**, 2045–2060, 2004.
- Zhang, M., R. B. McKibben, J. A. Simpson, S. W. H. Cowley, K. Staines, J. D. Anglin, R. G. Marsden, T. R. Sanderson, and K.-P. Wenzel, Impulsive bursts of energetic particles in the high-latitude duskside magnetosphere of Jupiter, *J. Geophys. Res.*, **100**, 19,497–19,512, 1995.
- 大河原千晶, 木星磁気圏における高エネルギー粒子準周期的バースト現象の研究, 修士論文 (東北大学), 1999.